SYNTHESIS, ADSORPTION AND CATALYSIS OF LARGE PORE METAL PHOSPHONATES

Gordon Michael Pearce

A Thesis Submitted for the Degree of PhD
at the
University of St. Andrews

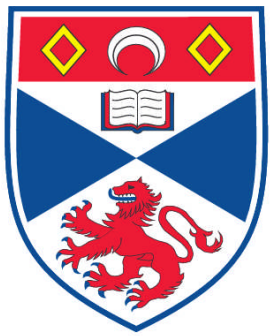

2009

Synthesis, Adsorption and Catalysis of Large Pore Metal Phosphonates

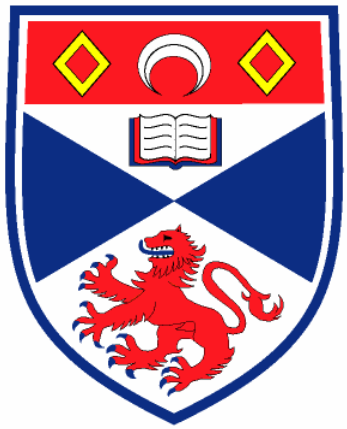

University
of
St Andrews

A thesis presented for the degree of
Doctor of Philosophy
in the Faculty of Science of the University of St Andrews

by

Gordon Michael Pearce BSc (Hons)

October 2009

Declaration

1. I, Gordon Michael Pearce, hereby certify that this thesis, which is approximately 50000 words in length, has been written by me, that it is a record of work carried out by me and that it has not been submitted in any previous application for a higher degree.

Date…… Signature of the candidate……

2. I was admitted as a research student in October, 2005 and as a candidate for the degree of PhD in October, 2006; the higher study for which this is a record was carried out in the University of St Andrews between 2005 and 2009.

Date…… Signature of the candidate……

3. I hereby certify that the candidate had fulfilled the conditions of the Resolution and Regulations appropriate for the degree of PhD in the University of St Andrews and that the candidate is qualified to submit this thesis in application for that degree.

Date…… Signature of the supervisor……..

4. In submitting this thesis to the University of St Andrews we understand that we are giving permission for it to be made available for use in accordance with the regulations of the University Library for the time being in force, subject to any copyright vested in the work not being affected thereby. We also understand that the title and the abstract will be published, and that a copy of the work may be made and supplied to any bona fide library or research worker, that this thesis will be electronically accessible for personal or research use, and that the library has the right to migrate this thesis into new electronic forms as required to ensure continued access to the thesis. We have obtained and third-party copyright permissions that may be required in order to allow such access and migration.

The following is an agreed request by candidate and supervisor regarding the electronic publication of this thesis:

Access to Printed copy and electronic publication of thesis through the University of St Andrews.

Date…… Signature of the candidate……

Date…… Signature of the supervisor……..

Abstract

The synthesis and properties of metal phosphonates prepared using piperazine-based bisphosphonic acids have been investigated. The ligands N,N'-piperazinebis(methylenephosphonic acid) (H_4L), and the 2-methyl (H_4L-Me) and 2,5-dimethyl (H_4L 2,5-diMe) derivatives have been prepared using a modified Mannich reaction. Hydrothermal reaction of gels prepared from metal (II) acetates and the bisphosphonic acids results in the synthesis of four structures: STA-12, Ni VSB-5, Co $H_2L.H_2O$ and Mg H_2L.

STA-12, synthesised by reaction of Mn, Fe, Co or Ni acetate with H_4L or H_4L-Me, has been investigated further. STA-12 crystallises in the space group $R\bar{3}$, and Ni STA-12 is the most crystalline version. Its structure was solved from synchrotron data (a = b = 27.8342(1) Å, c = 6.2421(3) Å, α = β = 90°, γ = 120°), and it has large 10 Å hexagonal shaped pores. Helical chains of Ni octahedra are coordinated by the ligands, resulting in phosphonate tetrahedra pointing towards the pore space. Water is present, both coordinated to the Ni^{2+} cations and physically adsorbed in the pores. Mixed metal structures based on Ni STA-12, where some Ni is replaced in the gel by another divalent metal (Mg, Mn, Fe or Co) can also be synthesised.

Dehydration of STA-12 results in two types of behaviour, depending on the metal present. Rhombohedral symmetry is retained on dehydration of Mn and Fe STA-12, the a cell parameter decreasing compared to the as-prepared structures by 2.42 Å and 1.64 Å respectively. Structure solution of dehydrated Mn STA-12 indicates changes in the torsion angles of the piperazine ring bring the inorganic chains closer together. Fe and Mn STA-12 do not adsorb N_2, which is thought to be due to the formation of an amorphous surface layer.

Dehydration of Ni and Co STA-12 causes crystallographic distortion. Three phases were isolated for Ni STA-12: removal of physically adsorbed water results in retention of rhombohedral symmetry, while dehydration at 323 K removes some coordinated water forming a triclinic structure. A fully dehydrated structure (dehydrated at 423 K) was solved from synchrotron data (a = 6.03475(5) Å, b = 14.9156(2) Å, c = 16.1572(7) Å, α = 112.5721(7)°, β = 95.7025(11)°, γ = 96.4950(11)°). The dehydration mechanism, followed by UV-vis and Infra-red spectroscopy, involves removal of water from the Ni^{2+} cations and full coordination of

two out of three of the phosphonate tetrahedra forming three crystallographically distinct Ni and P atoms. No structural distortion takes place on dehydration of Ni and Co STA-12 prepared using the methylated bisphosphonate, and the solids give a higher N_2 uptake as a result.

Dehydrated Ni and Co STA-12 were tested for adsorption performance for fuel related gases and probe molecules. Investigations were undertaken at low temperature with H_2, CO and CO_2, and ambient temperature with CO_2, CH_4, CH_3CN, CH_3OH and large hydrocarbons. Due to the presence of lower crystallinity, Co STA-12 has an inferior adsorption performance to Ni STA-12, although it has similar adsorption enthalpies for CO_2 at ambient temperature (-30 to -35 kJ mol^{-1}). Ni STA-12 adsorbs similar amounts of CO_2 and N_2 at low temperature, indicating the adsorption mechanisms are similar. Also, it adsorbs 10 × more CO_2 than CH_4 at low pressure, meaning it could be used for separation applications.

Ni STA-12 adsorbs 2 mmol g^{-1} H_2 with an enthalpy of -7.5 kJ mol^{-1}, the uptake being due to adsorption on only one-third of the Ni^{2+} cations. The uptake for CO is 6 mmol g^{-1}, with adsorption enthalpies ranging from -24 to -14 kJ mol^{-1}. This uptake is due to adsorption on all the Ni^{2+}, meaning the adsorption enthalpies are high enough to allow the structure to relax. This is also observed for adsorption of CH_3CN and CH_3OH, where there is a return to rhombohedral symmetry after uptake.

The adsorption sites in dehydrated Ni and Co STA-12 were investigated via Infra-red spectroscopic analysis of adsorbed probe molecules (H_2, CO, CO_2, CH_3CN and CH_3OH). The results indicate the adsorption sites at both low and ambient temperature are the metal cations and the P=O groups. The metal cation sites are also characterised as Lewis acids with reasonable strength.

STA-12 was shown to have acidic activity for the liquid phase selective oxidations of 1-hexene and cyclohexene, although there is evidence active sites are coordinated by products and/or solvents during the reaction. STA-12 also demonstrates basic activity for the Knoevenagel condensation of ethyl cyanoacetate and benzaldehyde. Modification of STA-12 by adsorption of diamine molecules causes a slight increase in the basicity, and the highest conversions are where water and diamine molecules are both present.

Acknowledgements

Firstly I would like to thank Dr Paul A Wright for his supervision over the course of my PhD studies. He has been an enormous help and has always been available with lots of enthusiastic ideas. The help I have received from members of the Wright group, especially Dr Stuart Miller, on a day to day basis in the lab, along with any constructive comments and criticisms, has also been very useful.

The support of my family – my mother, father and older brother Ian – has been invaluable in helping me to complete my studies, especially when things haven't been going well. I would also like to acknowledge the support and unwavering love of my fiancée Rachel to whom I got engaged during the course of my research – it is a reassuring thing to know all the time she has spent waiting around for me to finish will have been worth it!

During an interesting and fruitful month spent in Turin in the summer of 2007 I was welcomed and helped immensely in the running and devising of Infra-red experiments by Prof Silvia Bordiga, Dr Laura Regli and Dr Francesca Bonino. I enjoyed my time immensely in what is a beautiful city, and I look forward to visiting again sometime in the future.

The hard working technicians in the Chemistry department, especially Sylvia Williamson, Ross Blackley and Peter Pogorzelec, are also to be acknowledged for running samples and providing advice and instruction about operating various expensive pieces of machinery which I have used over the course of my work.

Although too numerous to name individually, I would also like to take this opportunity to thank my friends and acquaintances over the past few years, especially those involved with the University Music Society Chorus and Windband – they have allowed me to unwind and relax whenever I have been away from the Chemistry department!

Lastly, without the support of funding from the University of St Andrews it would not have been possible for me to even contemplate doing further study after my undergraduate degree, so I would like to thank them for providing the means.

Dedication

This thesis is dedicated to one special person.

To my fiancée Rachel – never did I think I would be embarking on the journey of life with such an amazing person to travel with. This is for you.

Publications from this work

Structural Transformation and Adsorption of Fuel-Related Gases of a Structurally Responsive Nickel Phosphonate Metal–Organic Framework, Ni STA-12, S. R. Miller, G. M. Pearce, P. A. Wright, F. Bonino, S. Chavan, S. Bordiga, I. Margiolaki, N. Guillou, G. Férey, S. Bourrelly and P. L. Llewellyn, *J. Am. Chem. Soc.*, 2008, **130**, 15967

Contents

	Page number
Chapter 1: Introduction	**1**
1.1 Microporous Materials	**1**
1.2 Hydrothermal Synthesis	**4**
1.3 MOF crystal growth and synthesis	**4**
1.4 Carboxylate Metal Organic Frameworks	**8**
1.5 Porous Phosphonate Frameworks	**18**
1.6 Gas adsorption in microporous materials	**30**
1.7 Catalysis using microporous materials	**31**
1.8 Microporous hybrid solids as catalysts	**32**
1.9 Aims of thesis	**39**
1.10 References	**40**
Chapter 2: Characterisation Techniques	**46**
2.1 Introduction	**46**
2.2 Basic Crystallography	**46**
2.2.1 Crystals	**46**
2.2.2 Seven Crystal Systems	**47**
2.2.3 Miller Indices	**50**
2.3 X-ray Diffraction	**50**
2.3.1 X-Rays	**50**
2.3.2 Diffraction of X-rays by crystals	**52**
2.3.3 X-ray powder diffraction	**53**
2.3.4 Structure solution using X-ray powder diffraction	**54**
2.3.5 Phase identification using X-ray powder diffraction	**56**
2.4 Gas and Vapour Adsorption	**58**
2.4.1 Introduction	**58**
2.4.2 Determination of specific surface area and porosity	**60**
2.4.3 Differential heats of adsorption – microcalorimetry	**60**
2.5 Solid State Infra-red (IR) spectroscopy	**61**

2.5.1 Vibrating diatomic molecules **61**
2.5.2 Vibrations of polyatomic molecules **63**
2.5.3 Combinations of vibrations in polyatomic molecules **65**
2.5.4 Solid State Fourier Transform Infra-red Spectroscopy **67**
2.6 Solid State UV-Visible (UV-vis) Spectroscopy **68**
2.6.1 Background to UV-vis **68**
2.6.2 Analysis using UV-vis spectroscopy **70**
2.7 Scanning Electron Microscopy (SEM) and Energy Dispersive X-ray Spectroscopy (EDX) **71**
2.8 Thermogravimetric Analysis **72**
2.9 Organic Elemental Microanalysis **73**
2.10 References **73**

Chapter 3: Synthesis of MOFs **75**

3.1 Introduction **75**
3.2 Experimental and Characterisation Techniques **75**
3.3 Synthesis of phosphonate ligands **76**
3.3.1 Product Characterisation **79**
3.4 Synthesis of bisphosphonates **80**
3.5 Structure 1 – STA-12 **81**
3.5.1 Characterisation **81**
3.5.2 Structure solution of Ni STA-12 **83**
3.5.3 Description of high resolution structure of Ni STA-12 **84**
3.5.4 Structural studies of other STA-12 structures **88**
3.5.4.1 H_4L ligand **88**
3.5.4.2 H_4L-Me ligand **92**
3.6 Structure 2 – Ni + H_4L 2,5-diMe **94**
3.7 Structure 3 – $CoH_2L.H_2O$ **96**
3.8 Structure 4 – Mg H_2L **98**
3.9 Synthesis of mixed metal STA-12 samples **100**
3.10 Synthesis of CPO-27 **104**
3.11 Synthesis of MIL structures **105**
3.11.1 Synthesis of MIL-47 **106**

3.11.2 Synthesis of MIL-53 **107**
3.11.3 Synthesis of MIL-68 **108**
3.11.4 Synthesis of MIL-100 **109**
3.12 Conclusions about MOF syntheses **110**
3.13 References **112**

Chapter 4: STA-12 – Dehydration Studies **114**

4.1 Introduction **114**
4.2 Experimental and Characterisation Techniques **114**
4.3 Dehydration of Ni STA-12 **115**
4.3.1 Nitrogen adsorption - Ni STA-12 **118**
4.3.2 Structure solution of dehydrated forms of Ni STA-12 **118**
4.3.3 Description of dehydrated Ni STA-12 structures **120**
4.3.4 Infra-red study of dehydration mechanism for Ni STA-12 **125**
4.3.4.1 Description of spectra produced **125**
4.3.4.2 Interpretation of dehydration/hydration mechanism from Infra-red spectra **127**
4.4 Dehydration of Ni Me STA-12 **128**
4.4.1 Nitrogen adsorption - Ni Me STA-12 **131**
4.5 Comparison of dehydration behaviour of Ni STA-12 and Ni Me STA-12 **131**
4.6 Dehydration of Co STA-12 **133**
4.6.1 Nitrogen adsorption – Co STA-12 **137**
4.6.2 UV-vis-NIR study of Co STA-12 dehydration **138**
4.6.3 Infra-red study of dehydration mechanism for Co STA-12 **140**
4.7 Dehydration of Co Me STA-12 **141**
4.7.1 Nitrogen adsorption – Co Me STA-12 **144**
4.8 Dehydration of Mn STA-12 **145**
4.8.1 Structural study of dehydrated Mn STA-12 and description of structure **147**
4.8.2 Infra-red study of dehydration mechanism for Mn STA-12 **151**
4.9 Dehydration of Fe STA-12 **152**
4.10 Conclusions of STA-12 dehydration studies **156**
4.11 References **158**

Chapter 5: Gas and Vapour Adsorption **160**

5.1 Introduction **160**

5.2 Experimental and Characterisation Techniques **160**

5.3 Low temperature adsorption + investigation of interaction sites in STA-12 **162**

5.3.1 Hydrogen adsorption **162**

5.3.2 H_2 adsorption and calorimetry **163**

5.3.2.1 Ni STA-12 **163**

5.3.2.2 Co STA-12 **167**

5.3.3 Carbon monoxide adsorption **168**

5.3.4 CO adsorption and calorimetry **169**

5.3.4.1 Ni STA-12 **169**

5.3.4.2 Co STA-12 **171**

5.4 Ambient temperature adsorption + investigation of interaction sites **172**

5.4.1 Carbon dioxide and methane adsorption **172**

5.4.2 Low pressure CO_2 adsorption **174**

5.4.3 CO_2 and CH_4 adsorption and calorimetry **175**

5.4.3.1 Ni STA-12 **175**

5.4.3.2 Co STA-12 **179**

5.4.4 Acetonitrile adsorption **181**

5.4.5 CH_3CN adsorption **182**

5.4.5.1 Ni STA-12 **182**

5.4.5.2 Co STA-12 **186**

5.4.6 Methanol adsorption **188**

5.4.6.1 Ni STA-12 **188**

5.4.6.2 Co STA-12 **192**

5.4.7 Methanol and water adsorption – Ni STA-12 **193**

5.4.8 Hydrocarbon adsorption **195**

5.4.8.1 Adsorption of hydrocarbons onto Ni STA-12 and Ni CPO-27 **196**

5.5 Conclusions about gas and vapour adsorption **197**

5.6 References **199**

Chapter 6: Catalysis Over Large Pore MOFs **202**

6.1 Introduction to catalysis using microporous materials **202**

6.2 Selective oxidation reactions **202**

6.2.1 Background **202**

6.2.2 Reactive intermediates in liquid phase selective oxidation reactions **205**

6.2.3 Experimental and Characterisation Techniques **206**

6.2.4 Reactions using STA-12 as catalysts **207**

6.2.5 Reactions using mixed metal STA-12 as catalysts **213**

6.2.6 Reactions using MIL-*n* structures as catalysts **215**

6.3 Base catalysis – Knoevenagel condensation **219**

6.3.1 Background to Knoevenagel condensation reaction **219**

6.3.2 Modification of STA-12 with diamines **221**

6.3.3 Experimental and Characterisation Techniques **223**

6.3.4 Results for Knoevenagel condensation reactions **224**

6.3.4.1 Unmodified STA-12 **224**

6.3.4.2 STA-12 modified with diamines **225**

6.4 Other catalytic reactions – Ni STA-12 + 20% Mn – CO activation **228**

6.5 Conclusions from catalysis **230**

6.6 References **231**

Chapter 7: General Conclusions and Future Work **233**

7.1 General Conclusions **233**

7.2 Possible future work **235**

7.3 References **236**

Appendix 1 – Ni STA-12 as-prepared – Atomic coordinates (High resolution) **237**

Appendix 2 – Ni STA-12 as-prepared – Atomic coordinates (Lab resolution) **238**

Appendix 3 - Ni STA-12 dehydrated 323 K – Atomic coordinates **239**

Appendix 4 - Ni STA-12 fully dehydrated – Atomic coordinates **240**

Appendix 5 - STA-12 – Rietveld refinements **242**

Appendix 6 - Mn STA-12 dehydrated 423 K - Atomic coordinates **244**

Appendix 7 - Ni STA-12 + acetonitrile heated 343 K - Atomic coordinates **245**

Appendix 8 - GC traces and calculations – Selective oxidation reactions **246**

Appendix 9 - GC traces and calculations – Knoevenagel reactions **248**

Chapter 1: Introduction

1.1 Microporous Materials

During the past 25 years there has been an enormous interest in the synthesis of novel microporous materials, ranging from crystalline aluminosilicates to metal organic framework solids (MOFs). In general, microporous materials are structurally diverse and contain channels and pores in the size range 2.5 to 20 Å. Chemical species can interact with the materials via surface interaction with the pore walls, which allows shape and size selectivity to be imparted to reactions and adsorptions. Microporous materials demonstrate useful properties for many applications such as gas storage, molecular sieving and catalysis, and are subsequently of great interest to industry.[1-3]

Zeolites, derived from the Greek for 'boiling stones', are naturally occurring minerals which lose water on heating.[4] They are defined as porous and crystalline aluminosilicates, with tetrahedral connectivity between the individual metal atoms in the framework via O atoms. The connectivity allows rings to form, creating pores and channels throughout the material. Tetrahedral aluminosilicates can be thought of as silica frameworks substituted by aluminate tetrahedra. The substitution of aluminium into the framework imparts a negative charge due to the difference in the charge between Si^{4+} and Al^{3+}. Therefore, to allow for the framework to be electrically neutral, additional cations have to be incorporated to allow the charge to balance. The number of these cations present depends on the amount of aluminium in the framework, and the charge of the additional cations. Often the additional cations do not form part of the framework, and these non-framework cations are usually in the pores or cavities where they can be relatively easily replaced or exchanged.

In the middle of the 19th century the first synthetic zeolite homologue, levynite, was synthesised.[5] This gave birth to a new genre of inorganic chemistry, and in 1932 the term 'molecular sieve' was introduced to describe microporous zeolites and carbons.[6] It took until the 1940s before significant attempts at making synthetic zeolites were

undertaken, and Union Carbide found the first industrial use in 1948.[7] Barrer and Milton also synthesised the first novel synthetic aluminosilicate zeolites at this time, and they are commonly referred to as the founding fathers of zeolite chemistry.[8, 9]

In the early 1980s, Flanigen and co-workers demonstrated the synthesis of aluminophosphate analogues of aluminosilicate zeolites.[10] Aluminophosphates have no need for extra framework cations for charge balancing, as the negative charge on each $[AlO_{4/2}]^-$ tetrahedron is balanced by the positive charge on each $[PO_{4/2}]^+$ tetrahedron. This work indicated phosphorus could be used within the frameworks of porous structures, and it inspired the synthesis of a large number of novel open framework materials (over 165 frameworks now known[11]). The classical definition of a zeolite was modified to accommodate this, with a zeolite-like material (zeotype) defined as a highly crystalline, tetrahedrally-coordinated solid oxide structure with defined pore structures and topologies.[2]

Metal organic framework solids (MOFs) are a class of porous solids which have rapidly expanded in number in the last 10 years.[12-15] For purely inorganic zeotypic structures the pore sizes are limited to *ca.* 10 Å, so an alternative synthetic strategy was formulated. This involved using organic molecules within the framework structure itself in an attempt to both increase the size of the pores and create novel channel topologies.[16] MOFs can be considered as hybrid materials where metal cations or oxymetal clusters are connected to each other via organic linker molecules. Regular arrays form, resulting in porous frameworks which in some cases have very low densities. Metal cations can coordinate to organic molecules in a number of ways, leading to formation of a large number of topologies and novel structures which can be tailored for use in possible applications.

A timeline outlining the development of research into microporous materials is shown in Figure 1.1.

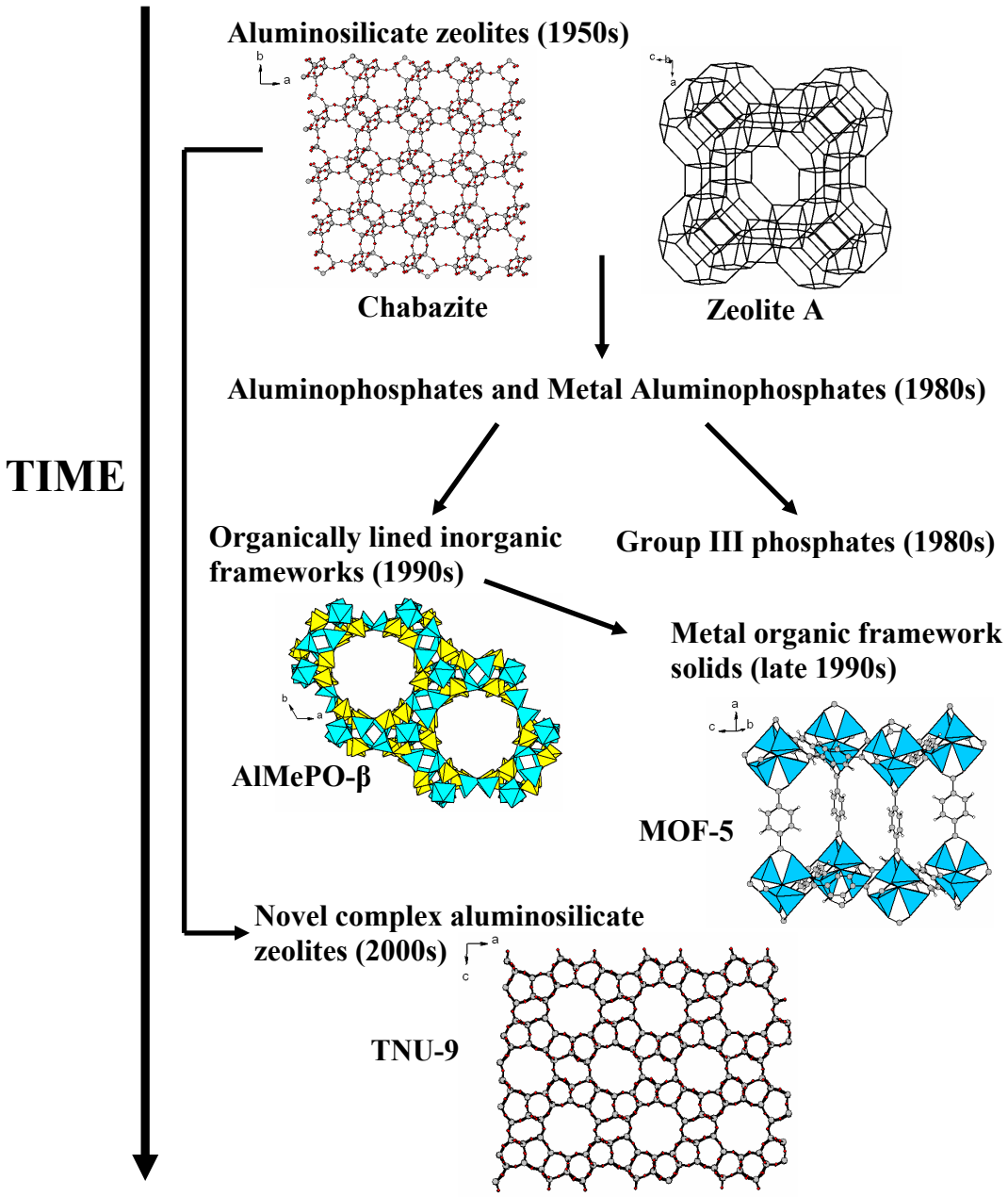

Figure 1.1 *– Timeline outlining development of research into microporous framework structures. References for example structures – Zeolite A – 8, Chabazite – 17, AlMePO-β – 18, MOF-5 – 19, TNU-9 – 20.*

1.2 Hydrothermal Synthesis

Zeolites are naturally formed in the presence of reasonably high temperatures (> 573 K) and pressures (> 300 MPa) found in the Earth's upper crust as a result of burial metamorphism. Therefore, early attempts to create synthetic zeolites were performed using similar conditions. It was not until the 1950s that zeolite chemistry became redirected towards the alternative milder hydrothermal preparation route proposed by Barrer and Milton.[8, 9, 21]

Hydrothermal synthesis is based on the principle that the precursors used in microporous framework formation are insoluble under ambient conditions, but are more soluble at elevated temperatures and pressures. Most microporous materials are synthesised using this route, commonly carried out in polytetrafluoroethylene (PTFE, Teflon^{TM}) lined acid digestion bombs under autogeneous pressure (usually between 333 K and 523 K).

Chemical behaviour inside an autoclave is an area of open framework synthesis which is very complex, and a complete understanding of the crystal growth in an autoclave would permit the rational design of novel open frameworks. The composition of the reaction variables, including time, temperature, template, concentration of reactants, pH and preparation method, can have major effects on the topology of the resulting framework. Temperature and time can be increased or decreased in order to maximise the efficiency of the reaction, but the composition of the gel is a more complex issue. The autoclave is usually a closed system, so the reaction variables directly affect one another and vary with the progress of the reaction.

1.3 MOF crystal growth and synthesis

In the synthesis of zeotypes, one of the major factors influencing the crystallisation is the presence of template molecules. These molecules can help control and direct the synthesis towards a specific structure over the course of the reaction, and can be removed by calcination from the pores. In contrast, the organic molecules in most porous MOFs are integral, coordinated parts of the framework structure, and the pores are filled by solvent molecules.

There are other factors that influence the crystal growth and synthesis of MOFs. The temperature of the hydrothermal reactions is important when considering the

dimensionality of the resulting structure.[22] When cobalt (II) hydroxide was reacted with succinic acid in a 1 : 1 molar ratio at temperatures between 333 and 523 K, five different phases were formed with a clear trend in connectivity.[23] The phases became denser and less hydrated as the temperature increased, resulting in more face sharing between the polyhedra. The reaction can be considered to be thermodynamically controlled, as the dimensionality changes with temperature.

The transition from a hydrated 1-D coordination polymer at the lowest temperature to an anhydrous 2-D hybrid metal oxide at the highest temperature illustrates the changes in dimensionality. This allows for a classification of hybrid solids in terms of the dimensionality of the inorganic connectivity (I^n) versus metal-organic-metal connectivity (O^n) as outlined in Table 1.1.

Table 1.1 *– Hybrid solids classified in terms of dimensionality of inorganic (I^n) and M-O-M (O^n) connectivity (adapted from reference 22).*

Inorganic connectivity I^n / **M-O-M connectivity O^n**	**0**	**1**	**2**	**3**
0	Molecular complexes	Hybrid inorg. Chains	Hybrid inorg. layers	3-D inorg. hybrids
1	Chain coordination polymers	Mixed inorg.-organic layers	Mixed inorg.-organic 3-D framework	-----
2	Layered coordination polymers	Mixed inorg.-organic 3-D framework	-----	-----
3	3-D coordination polymers	-----	-----	-----

The dimensionality and connectivity of MOF frameworks can also be influenced by the solvent used in the reaction gel, an example being the difference between MIL-47[24] and MIL-68.[25] Both these structures are built from the same infinite inorganic chains of vanadium octahedra coordinated by 1,4-benzenedicarboxlyate (terephthalate) linkers. The 3-D frameworks both have the same stoichiometry, but the solvents used are different (water for MIL-47, and N,N'-dimethylformamide (DMF) for MIL-68). This influences the connectivity of the chains, with MIL-47 adopting a structure related to the ReO_3 topology, and MIL-68 adopting a structure similar to the hexagonal bronze topology. No structural transition can take place between MIL-47 and MIL-68 without a reconstructive mechanism, indicating the strong influence of the solvent on the final structure.

The ultimate goal in the field of MOFs was to synthesise truly porous 3-D frameworks. Early attempts produced 2-D sheet structures, e.g. with copper[26] and nickel,[27] where the layers were held together by hydrogen bonds, resulting in poor thermal stability. As it became apparent that 3-D hybrid structures could be prepared, the concept of reticular synthesis became of value.

In zeotypes, the structures are built of primary building units (PBUs) which are TO_4 tetrahedra (where T is Al, Si, P etc). These TO_4 tetrahedra are the smallest subunits zeotypes can be constructed from, and they can be arranged geometrically into secondary building units (SBUs); these are the building blocks all known zeotypes can be theoretically assembled from.[28] If the SBU concept is applied to hybrid structures, it is possible to identify discrete metal-organic clusters forming *in-situ* during the crystallisation.[29] The clusters can be thought of as SBUs, and coordination of these to one another allows for the formation of the resulting geometries and structures. Judicious choice of precursors in the reactant gel can therefore allow specific SBUs to form, and for frameworks to be designed.

Looking at the example of MOF-5, SBUs are formed during the course of the reaction (Figure 1.2).[30] The Zn_4O SBU clusters in turn coordinate to one another via rigid terephthalate linkers, forming the MOF-5 framework.[19] The building of the SBUs into MOF-5 takes place following geometrical principles concerning periodic nets.[31] Starting from the ReO_3 topology, which is based on a six-connected net, the zinc clusters in MOF-5 can be thought of as being equivalent to corner sharing octahedra. Coordination of the SBUs with the terephthalate linkers expands the distances

between the ‘octahedra’, which creates free space within the framework and allows for retention of the six-connected net.

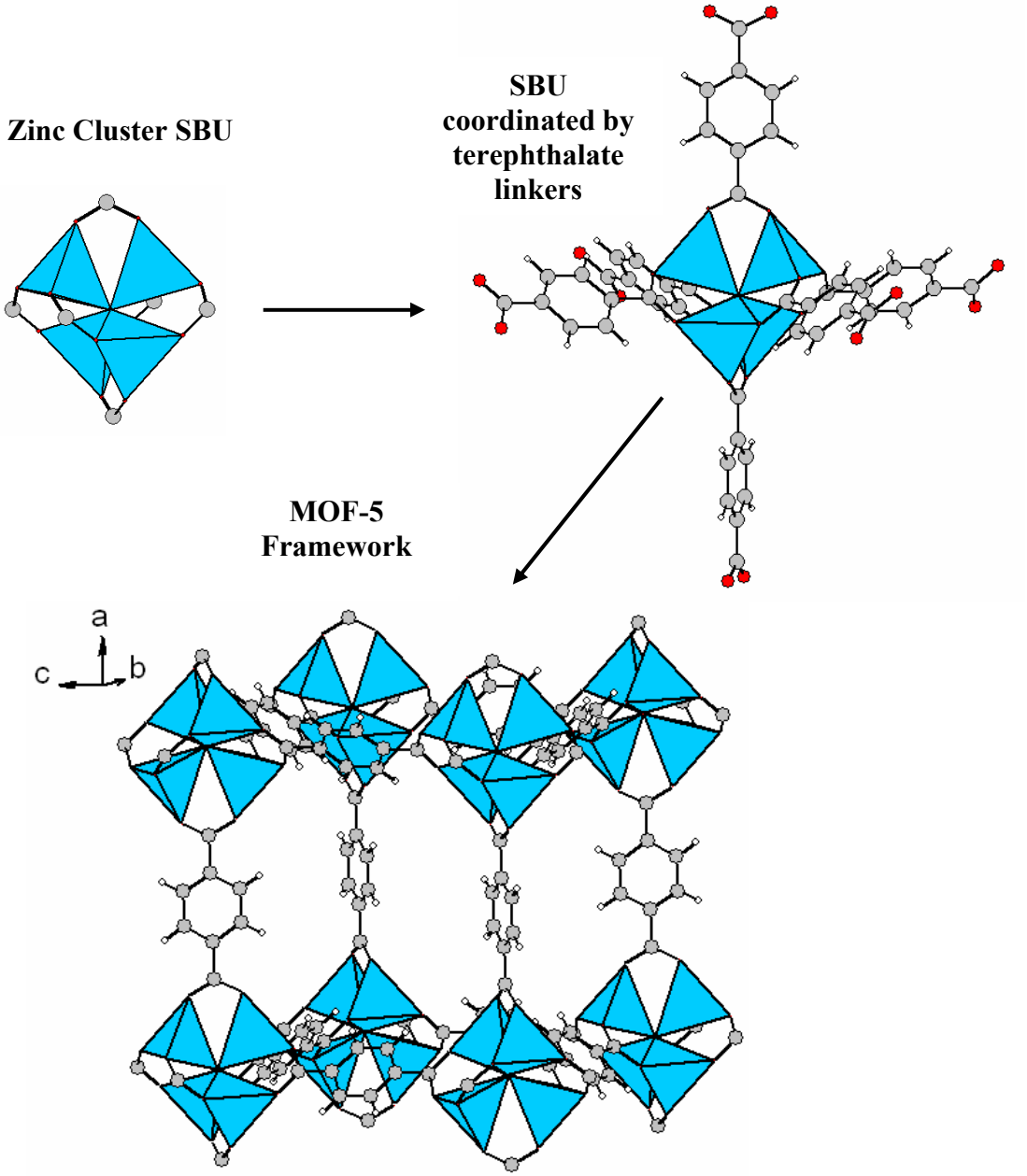

Figure 1.2 *– Scheme for coordination of structural units into MOF-5 framework. ZnO_4 tetrahedra in light blue, carbon atoms in grey and hydrogen atoms in white. Constructed using information from reference 30.*

The formation of SBUs and their subsequent coordination by linkers to form framework structures (such as for MOF-5 in Figure 1.2) is described as reticular synthesis. The use of longer dicarboxylate linkers allows for similar structures to MOF-5 to form with open voids that increase in a predictable manner (IRMOF-*n* series).[33] This means extended networks can be designed by starting with well-defined molecular building blocks which maintain structural integrity during the crystallisation process. Therefore, reticular synthesis can be described as the process of assembling rigid molecular building blocks into ordered structures held together by strong bonding. The application of the concept of reticular synthesis to MOFs has resulted in the discovery of many thermally stable and permanently porous materials, some of which are described in the next section.

1.4 Carboxylate Metal Organic Frameworks

Sustained and targeted research has been undertaken into MOF systems, resulting in the synthesis of several hundred porous structures.[1] Some of the most interesting frameworks have been synthesised in the metal carboxylate system, where di– and trivalent metals have been combined with di- and tricarboxylic acids, resulting in high symmetry structures. The M-O-C bonds are strong, giving the frameworks high thermal stabilities, while the carboxylate linkers are not prone to self condensation. A variety of metal environments have been reported, such as clusters of four zinc atoms in MOF-5 (Figure 1.2),[19] chains of vanadium atoms in MIL-47[24] and MIL-68[25] and clusters of three chromium atoms coordinating to the same μ_3 oxygen atom in MIL-100[34] and MIL-101.[35]

When Yaghi and co-workers reported the structure of MOF-5 in 1999 (Figure 1.2), it was the first 3-D metal organic framework structure reported to be stable to solvent removal, demonstrating permanent, reversible adsorption for nitrogen gas at standard conditions. The key to the 3-D pore topology and permanent porosity of MOF-5 are the strong metal-ligand bonds coupled to the relative rigidity of the terephthalate linkers. In practice, though, the hydrolytic stability of MOF-5 is a problem, as samples left in air over the course of time have reduced specific surface areas.[36]

As stated already, a whole family of related reticular MOF structures have been reported with the same basic structure as MOF-5, but using different dicarboxylate linkers (IRMOF-*n* series).[33] By using different dicarboxylic acid molecules (shown in

Figure 1.3) the topology and properties of the frameworks can be changed and modified in a predictable way, demonstrating the first real attempt to create porous hybrid solids by design using the reticular synthesis concept.

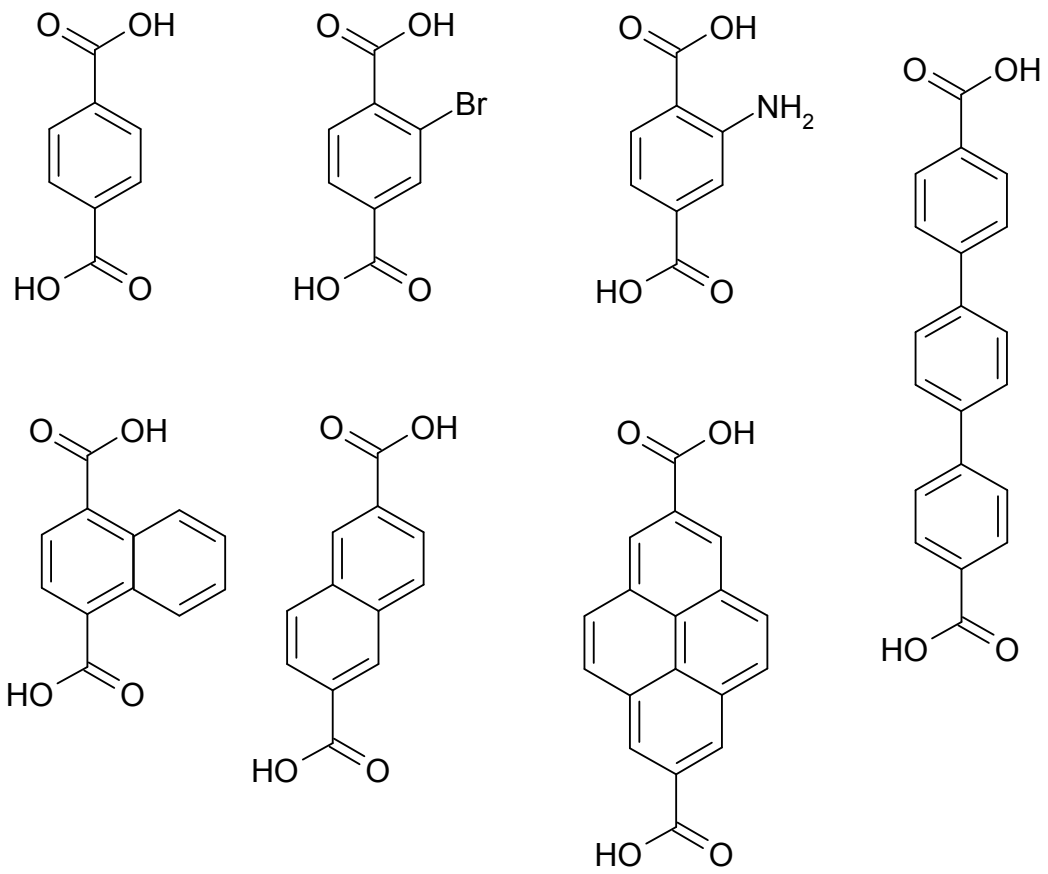

Figure 1.3 *– Examples of dicarboxylic acid linkers used in the IRMOF-n series of structures.*[33]

Around the same time MOF-5 was discovered, another interesting porous carboxylate MOF material was synthesised, termed HKUST-1 (Hong Kong University-1).[37] The structure was synthesised from copper nitrate and 1,3,5-benzenetricarboxylic acid (trimesic acid – Figure 1.4)), and contains dinuclear copper units with a short Cu-Cu distance of 2.63 Å. Viewed down the [100] direction, the structure contains 1-D square shaped channels *ca.* 10 Å in diameter. These 1-D channels are present in all three crystallographic directions, and the intersections result in large hexagonal shaped windows 10 Å in diameter (Figure 1.5).

Physically adsorbed water is present in the channels, and chemically adsorbed water is coordinated to the dinuclear copper species. The chemically adsorbed water can be

removed by thermal activation, resulting in empty coordination sites on the copper cations. These empty sites act as Lewis acids, resulting in favourable adsorption and catalytic properties.

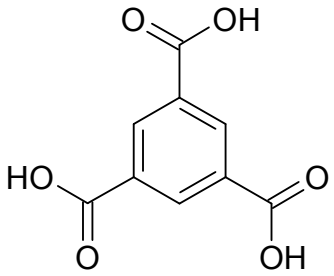

Figure 1.4 *– Trimesic acid (1.3,5-benzenetricarboxylic acid) linker used in synthesis of HKUST-1.*

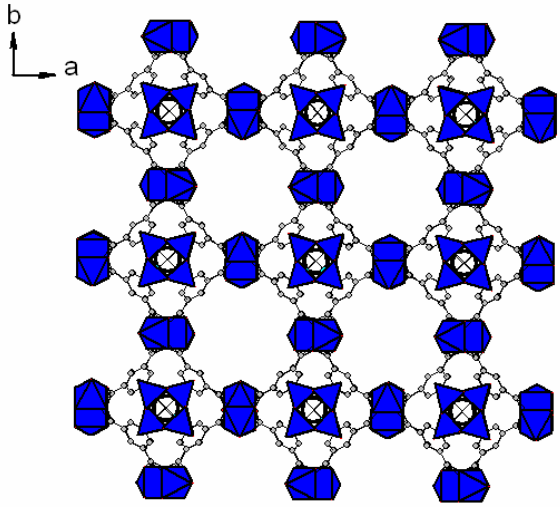

Figure 1.5 *– Representation of HKUST-1 looking down [100] direction at the 10 Å diameter square channels. Copper centred polyhedra in blue and carbon atoms in grey. Physically adsorbed water in the channels has been omitted for clarity.*[37]

The group of Férey in Versailles has produced an extensive series of carboxylate MOFs termed MIL-*n* (Materials of Institute Lavoisier-*n*). One of the most interesting structures synthesised is MIL-53, which incorporates terephthalate linkers and has Cr, Al, Ga and Fe versions.[38-43] Corner sharing metal octahedra are linked with terephthalate linkers containing delocalised π electrons to produce open frameworks.

As-synthesised MIL-53 has the chemical formula of $M^{III}(OH)[O_2CC_6H_4CO_2].[HO_2CC_6H_4CO_2H]_x.H_2O_y$, where x = ~ 0.75. The structure is built from infinite chains of metal octahedra linked together into diamond-shaped 1-D pores *ca.* 12 Å in diameter. These are filled with excess terephthalic acid molecules which can be removed by heating in air.

For Cr and Al this affords an open structure termed MIL-53ht, with pores *ca.* 13 Å in diameter, which exists only at high temperature.[38-40] On cooling in moist air water molecules coordinate in the pores, forming MIL-53lt. The reversible coordination of water molecules to the –OH groups results in rearrangement of the structure, and a reduction in the pore diameter to *ca.* 8 Å. The water can be removed above 333 K, restoring the MIL-53ht structure (Figure 1.6). In the Ga version of the dehydrated structure, the pores can be present in both open and closed forms depending on the temperature.[41] Above 493 K the pores are fully open, like the ht versions of Cr and Al MIL-53, and between 333 K and 493 K the pores are closed without any coordination of water. Below 333 K water coordinates, forming the MIL-53lt structure.

Dehydration of Fe MIL-53 does not result in any pore opening. At temperatures up to 413 K an intermediate form is produced with two types of closed pores, and above 413 K a closed pore structure forms where all the pores are the same.[42] As the temperature is increased the pores do not open, unlike the other MIL-53 structures, although on cooling in moist air water coordinates reversibly in the pores.[43] The remarkable flexibility displayed by Cr, Al and Ga MIL-53 is an interesting property which has been widely studied for gas adsorption.

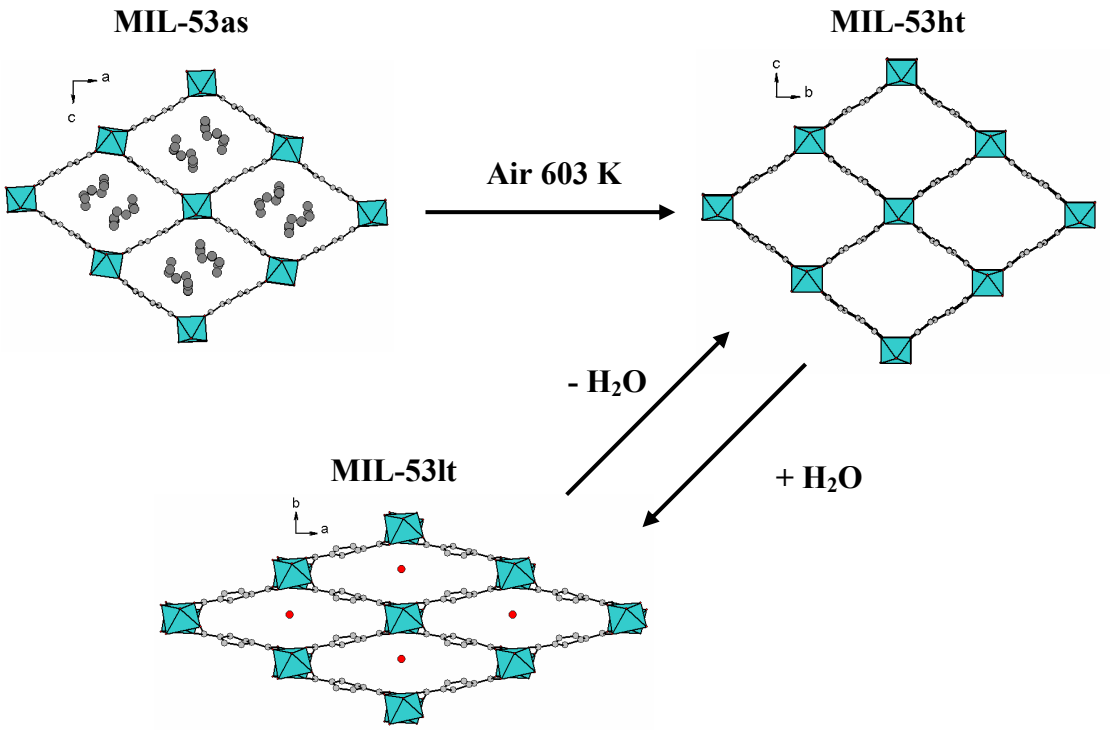

Figure 1.6 *– Illustration of structural rearrangements in Cr and Al MIL-53 viewed down 1-D channels following removal of excess terephthalic acid molecules and subsequent coordination of water.*[38-40] *Metal centred octahedra in blue and carbon atoms in grey. Oxygen atoms from adsorbed water in pores of MIL-53lt in red.*

MIL-47 is formed from infinite chains of vanadium octahedra, which are linked by terephthalate linkers into a similar structure to MIL-53.[24] The structure has large 1-D channels filled with excess terephthalic acid molecules which can be removed by heating in air at 573 K. Removal of the molecules from the pores results in the oxidation state of the vanadium changing from +3 to +4, giving a chemical formula of $V^{IV}O[O_2CC_6H_4CO_2]$. The empty pores are 11 × 10.5 Å in diameter, and they remain open on cooling to room temperature as they are hydrophobic in nature (no –OH groups present). The structure is shown below in Figure 1.7.

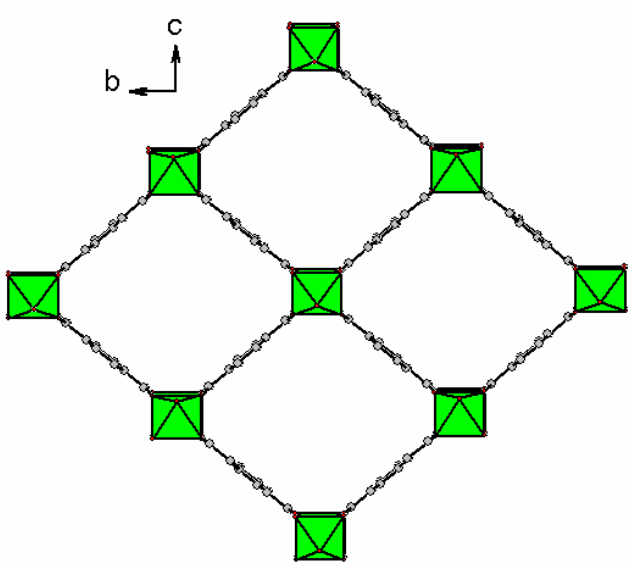

Figure 1.7 *– Structure of MIL-47, post heating at 573 K in air to remove terephthalic acid molecules from the pores, viewed in direction of 1D-channels.*[24] *Vanadium centred octahedra in green and carbon atoms in grey.*

As outlined previously, the structure of MIL-68 is related to MIL-47, as it is built from the same infinite chains of vanadium octahedra.[25] Crystallisation using DMF as the solvent leads to the terephthlate linkers coordinating to produce a structure with two distinct 1-D pore hierarchies. A smaller triangular shaped pore (8 Å in diameter) and a larger hexagonal pore (15 Å in diameter) are formed (Figure 1.8).

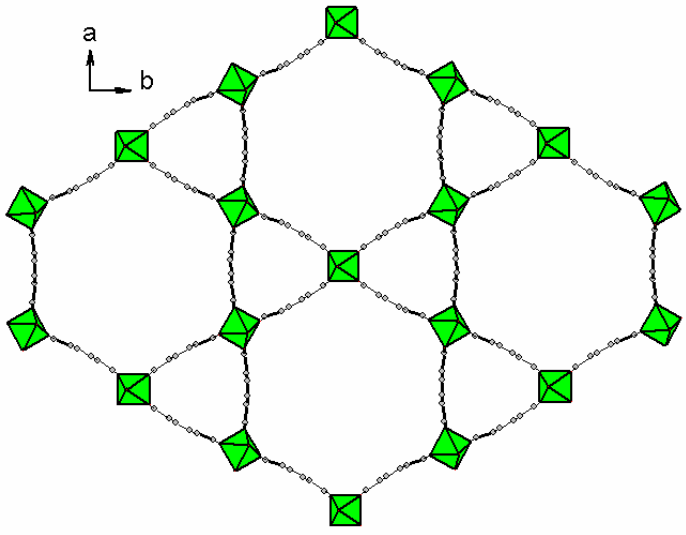

Figure 1.8 *– View of MIL-68 post removal of solvent molecules.*[25] *The two pore hierarchies are clearly observed. Colour scheme as Figure 1.7.*

Two of the most porous MOFs to have been synthesised so far are MIL-100[34] and MIL-101.[35] They are both very large pore structures, synthesised by reaction of either terephthalic acid or trimesic acid with chromium metal. The structure of MIL-100 was solved by a combination of computer modelling coupled to a targeted synthetic program.[34] The basic structural feature of MIL-100 and MIL-101, as mentioned before, is a chromium trimer where three chromium atoms are coordinated to the same μ_3 oxygen atom. Two out of the three Cr atoms in each trimer are coordinated to water molecules which can be removed, creating empty metal sites with Lewis acid properties (similar to the empty copper sites in HKUST-1). The third Cr atom is coordinated by an F^- ion.

The trimers assemble into a super tetrahedron building block via coordination with the carboxylate linkers (Figure 1.9), resulting in chemical compositions of $Cr_3F(H_2O)_3O[C_6H_3(CO_2)_3]_2.nH_2O$, n = ~ 28 for MIL-100 and $Cr_3F(H_2O)_2O[(O_2C)C_6H_4(CO_2)]_3.nH_2O$, n = ~ 25 for MIL-101. In MIL-100, the trimesate linkers are on the faces of the super tetrahedra, while in MIL-101 the terephthalate linkers are on the edges of the super tetrahedra. The super tetrahedra link through vertices forming a 3-D network of corner sharing polyhedra. The networks of MIL-100 and MIL-101 both have similarities to the zeolite topology MTN (Figure 1.10), the recognition of which greatly aided their structure solution.

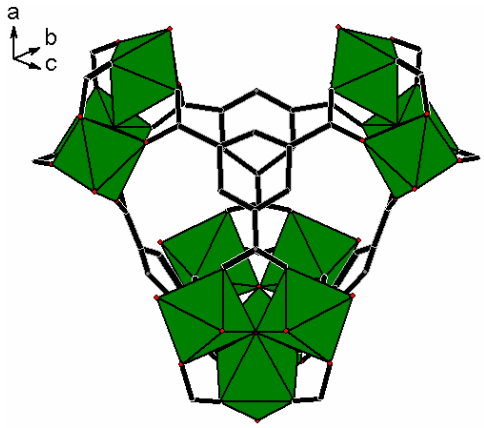

Figure 1.9 *– Super tetrahedron building block in MIL-100, composed of chromium trimers coordinated by trimesate linkers.[34] Chromium-centred octahedra in green.*

Within the super tetrahedra in MIL-100 there is a cage with an internal diameter of 6.6 Å, while the 3-D network delimits two distinct sizes of cages (Figure 1.11). One

cage forms as a pentagon dodecahedron with an internal diameter of *ca.* 25 Å, and pentagonal pore openings of 4.8 × 5.8 Å. The other cage forms as a polyhedron with 12 pentagonal and 4 hexagonal faces. The internal diameter is *ca.* 29 Å, and the large hexagonal pores are 8.6 $Å^2$.

In contrast, the super tetrahedra in MIL-101 have an internal diameter of 8.6 Å. The structure is similar to MIL-100, and the two different cages have internal diameters of 29 Å (with pentagonal windows 12 Å in diameter) and 34 Å (with hexagonal windows 14.5 Å × 16 Å) respectively. The cages in MIL-101 are filled with a large number of guest molecules, mainly excess terephthalic acid, which can be removed to activate the structure.

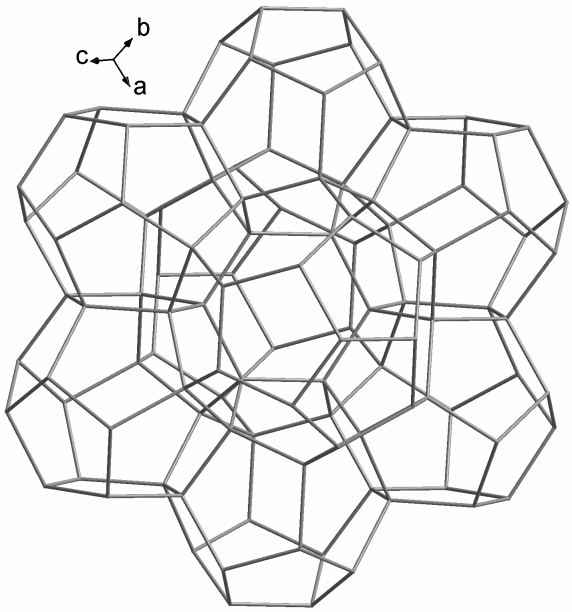

Figure 1.10 *– Structure of MIL-100 and MIL-101,*[34, 35] *represented with the centres of the super tetrahedra as the vertices and connections between the centres of the super tetrahedra as straight lines. Connectivity between the two different types of cages illustrated.*

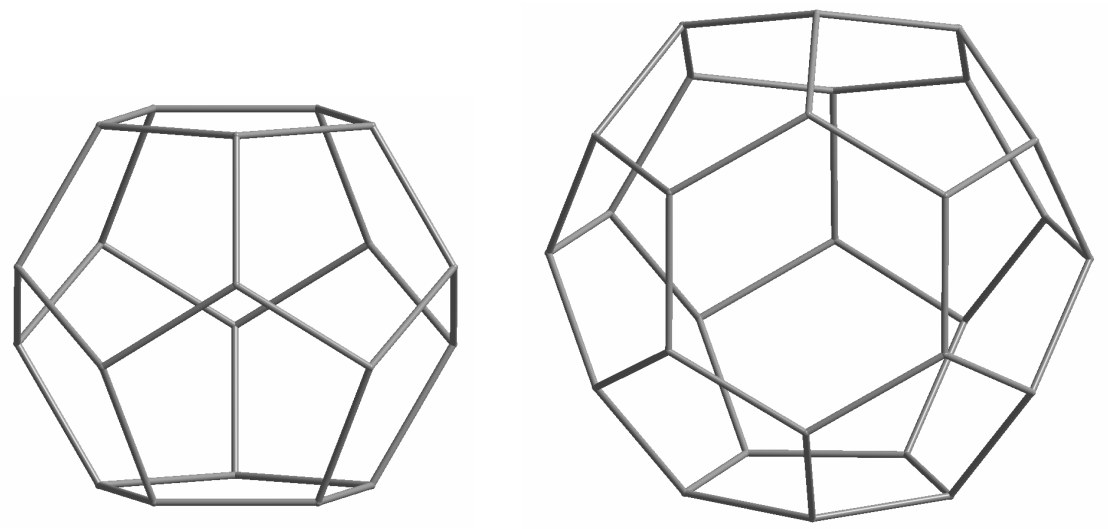

Figure 1.11 *– Cages in MIL-100 and MIL-101, represented as in Figure 1.10.*[34, 35] *Left - pentagon dodecahedron (Internal diameter: MIL-100 – 25 Å, MIL-101 – 29 Å); Right – polyhedron (Internal diameter: MIL-100 - 29 Å, MIL-101 - 34 Å).*

In inorganic chemistry, dimensions of pores as large as those in MIL-100 and MIL-101 are usually only observed in amorphous mesoporous solids (e.g. mesoporous silicas). MIL-100 and MIL-101 were the first examples of crystalline porous solids exhibiting mesoporous pore sizes, and the hierarchy of three distinct cage sizes within the frameworks, and the very large pore space meant possible applications in gas storage and separation were envisaged.

Another example of an interesting structural feature in a carboxylate MOF with empty metal sites on activation is the helical octahedral chain in CPO-27. CPO-27 has Co[44] and Ni[45] forms, and is isostructural with MOF-74[46] (synthesised using Zn). The linker is 2,5-dihydroxyterephthalic acid (Figure 1.12), and the framework has high symmetry (rhombohedral). It comprises of helical chains of metal octahedra along the direction of the *c*-axis linked together by the 2,5-dihydroxyterephthalate linkers, forming large *ca.* 10 Å diameter hexagonal 1-D channels (Figure 1.13).

Large amounts of water molecules are physically bound in the pores, along with chemically adsorbed water molecules coordinated to the metal sites (similar to HKUST-1, MIL-100 and MIL-101). On removal of the coordinated water molecules, as mentioned already, empty metal sites are formed. Like HKUST-1, MIL-100 and MIL-101, these sites act as Lewis acids, and studies into applications of CPO-27 will be discussed later on in this thesis.

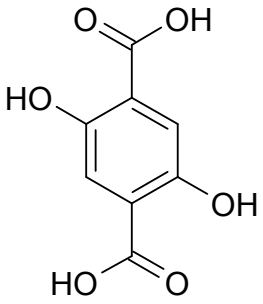

Figure 1.12 *– 2,5-dihydroxyterephthalic acid linker used in synthesis of Co and Ni CPO-27,*[44, 45] *and MOF-74.*[46]

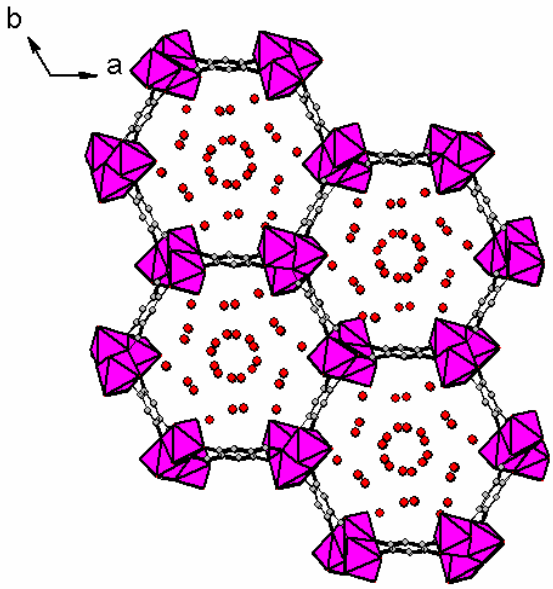

Figure 1.13 *– Structure of as-prepared Co CPO-27, looking down direction of large 10 Å hexagonal shaped channels.*[44] *Co centred octahedra in pink; carbon atoms in grey and oxygen atoms from physically adsorbed water in red.*

The examples outlined so far indicate a number of very different structural motifs to zeotypes form when using carboxylate linkers in MOFs. Several interesting frameworks can form, with large specific surface areas and high thermal stabilities, which could be useful for a number of possible applications. As well as carboxylates, many other types of organic molecules have also been used to create MOF frameworks, including bipyridyl,[47] imidazole (ZIF-*n* series)[48] and phosphonate[49] based ligands. This results in a vast catalogue of reported structures, which is increasing in number all the time.

1.5 Porous Phosphonate Frameworks

Porous metal phosphonates are rapidly gaining an important place amongst the various families of MOF materials.[50] There are a wide variety of phosphonate ligands that can be used, containing aliphatic or aromatic connectivity and functional groups such as amines, alcohols, sulphonates and carboxylates. Although relatively few phosphonic acid linkers are commercially available, many more can be synthesised using Mannich or Arbuzov type reactions (Scheme 1.1). Phosphonic acids have several applications, including as metal complexing agents and adsorbates at crystal surfaces,[51] so there is interest in the relevant synthetic methodology.

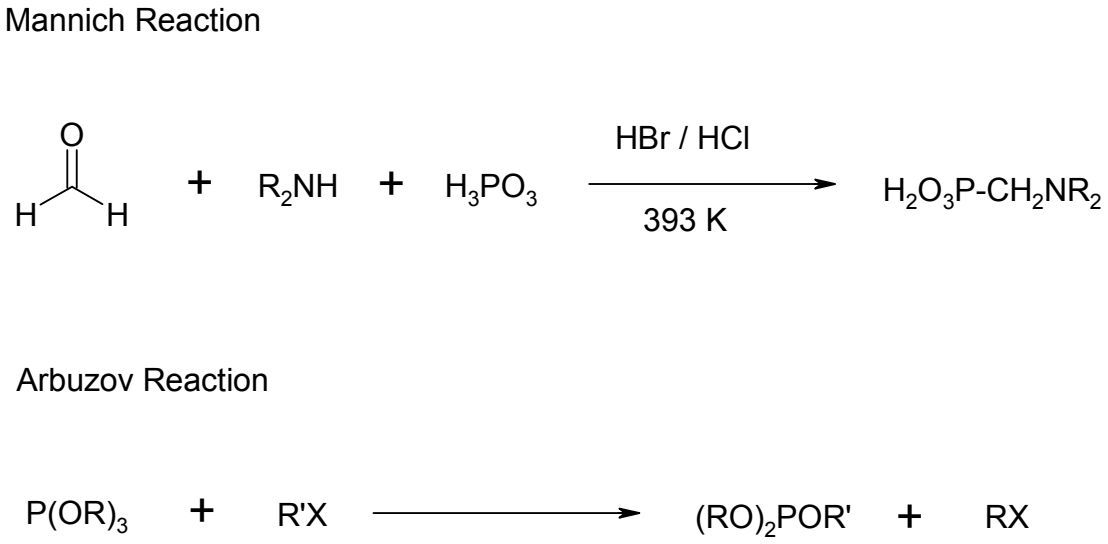

Scheme 1.1 *– Examples of basic reactions for the syntheses of phosphonic acids using the Mannich and Arbuzov type reactions.*

The phosphonate building block, R-PO_3, is analogous to the phosphite group H-PO_3 used previously in the synthesis of microporous materials.[52, 53] The phosphonate unit can be incorporated into frameworks as either the fully deprotonated or singly protonated form, and any number from one to four phosphonic acid groups can be present in the same ligand. If the ligand has other functional groups present, these can provide additional metal coordination sites, opening up many possibilities for the synthesis of novel materials and framework structures. Examples of some of the phosphonate ligands used are shown in Figure 1.14.

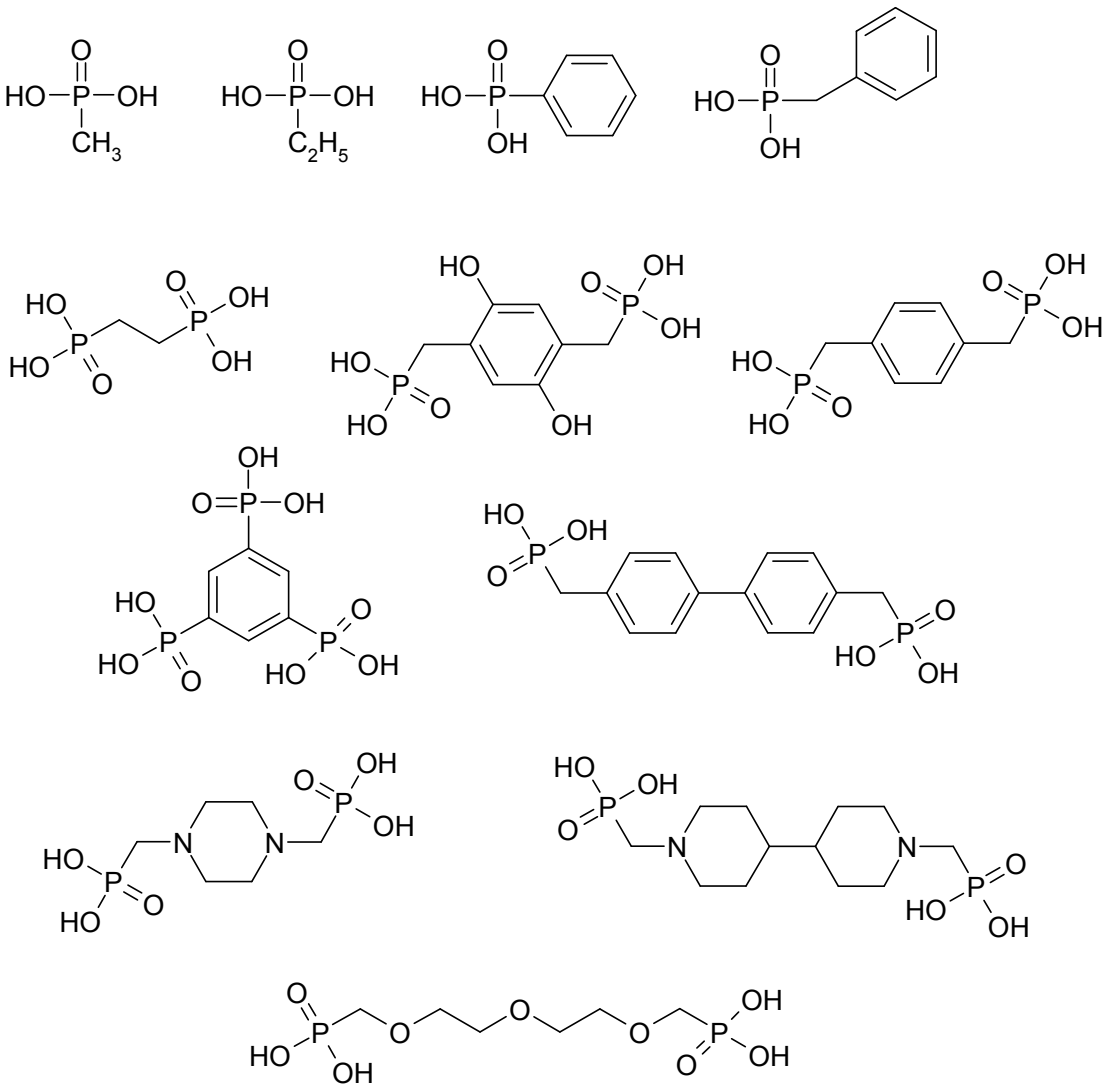

Figure 1.14 *– Examples of mono-, bis-, and tris-phosphonic acids used as linkers in open framework materials.*

Like carboxylic acids, phosphonic acids are not prone to self condensation. Also, the P-C bond is stable to high temperatures and phosphonates form strong P-O-M bonds with a variety of metals. They can bind through one, two or three of the oxygen atoms per phosphonate group, and this can result in phosphonate frameworks which are stable to high enough temperatures to be competitive with analogous metal carboxylate frameworks. These attractive features of metal phosphonates were recognised as long ago as 1976, although most materials prepared before the 1990s were non-porous layered solids.[50] In these structures, the inorganic metal phosphonate

and organic groups were spatially separated, and the solids themselves had intercalation but not adsorption properties.

The review of Maeda from 2004 outlines most of the open framework phosphonates known at that time.[54] Among the solids in the review, and in more recent examples, there is a lack of gas adsorption data. Several of the structures show reversible water loss and uptake, but few have been reported with adsorption properties for either small gas molecules (such as N_2) or large molecules. Some of the structures do not retain porosity on dehydration, due to the frameworks relaxing on loss of water and the pore(s) closing. Several crystalline phosphonate structures have been reported with permanent porosity and reversible water loss, split into organically lined 3-D inorganic frameworks and phosphonate metal organic frameworks.

In the organically-lined inorganic frameworks there are several examples of structures with permanent porosity, with one example discussed here. The synthesis and characterisation of the aluminium methyl phosphonates AlMePO-α and AlMePO-β (structural formula $Al_2(CH_3PO_3)_3$) in 1994 resulted in microporous materials with crystallographically well defined structures (Figure 1.15).[18, 55, 56] The polymorphs have similar structures, and contain aluminium in octahedral and tetrahedral coordination. The inorganic frameworks have hexagonal 1-D channels, lined with methyl groups, with free dimensions of about 6 Å. In the presence of high temperature and water vapour the β-polymorph is converted to the thermodynamically more stable α-form, in a topotactic manner.[57] If the structures are compared, the transformation takes place via coordinated movement of one of the crystallographically distinct aluminium cations. The β-polymorph has higher symmetry than the α-polymorph (space groups R3c and P31c respectively), and pores with a more oval cross section.

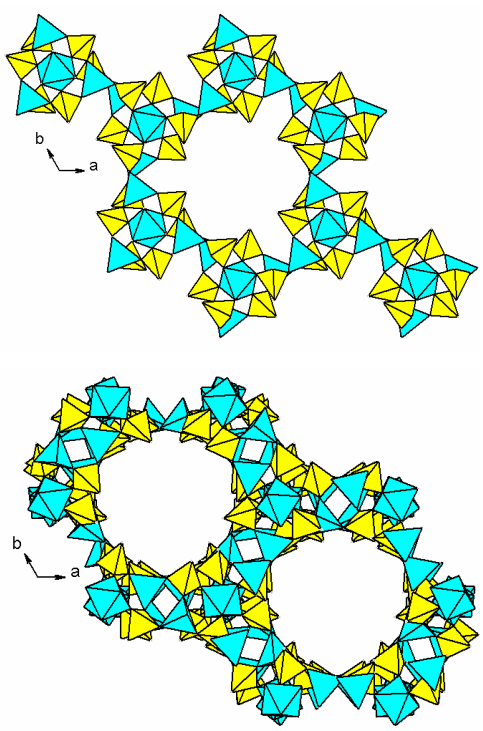

Figure 1.15 *– AlMePO polymorphs AlMePO-α (above) and AlMePO-β (below) viewed down the c-axis, with 6 Å diameter pores lined by methyl groups.* [18, 55, 56] *Al centred polyhedra in blue and phosphonate tetrahedra in yellow.*

The adsorption properties of the AlMePO polymorphs are dependent on the pore shape and internal surface chemistry.[58] Adsorption of water can only take place at high partial pressures, due to the hydrophobic nature of the internal surfaces.[59] Nitrogen is adsorbed by both structures, and the 77 K isotherm in AlMePO-α displays a step due to a packing change.[59, 60] The α-polymorph has been demonstrated to be a selective adsorbent in a separation with industrial interest. It adsorbs ethyl chloride preferentially in the presence of vinyl chloride, which is useful in the purification of vinyl chloride streams for production of poly vinyl chloride.[61]

A number of porous 3-D connected metal carboxylate and amine MOFs have been prepared, but only recently have attempts been made to generate analogues with di-, tri- or tetra-phosphonates. If the structures reported so far are grouped in terms of the ligand used, the most interesting are built using the bisphosphonate N,N'-piperazinebis(methylenephosphonic acid) shown in Figure 1.16 (termed here as L).

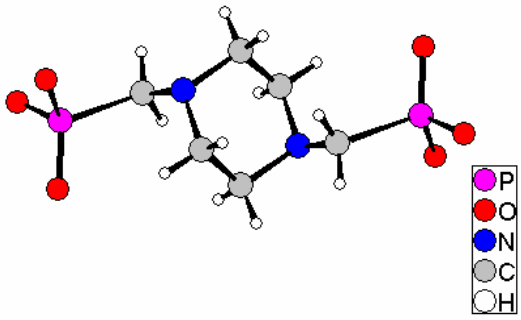

Figure 1.16 *– N,N'-piperazinebis(methylenephosphonate) ligand in a typical conformation.*[49]

The ligand is flexible, and can cross-link 1-D inorganic chains. It does this by coordinating via two or three of the oxygen atoms per phosphonate group, and also in some cases via the ring nitrogen, depending on the degree of protonation. The first solids synthesised with this ligand had the formula $MH_2L.xH_2O$ where M^{2+} = Mn, Co, Zn and Fe. In these structures, inorganic chains of tetrahedrally coordinated metal cations are linked by the bisphosphonate ligands (protonated on the nitrogen atoms) resulting in narrow 1-D channels containing water molecules (Figure 1.17).[62, 63]

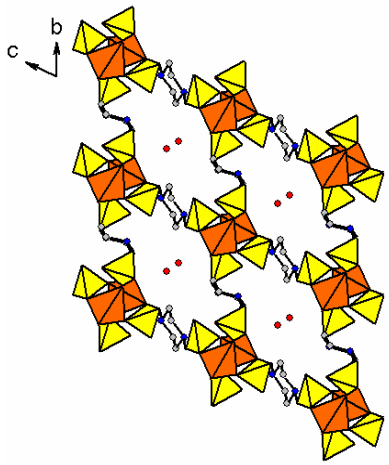

Figure 1.17 *– View down direction of pores in $ZnH_2L.xH_2O$ showing inorganic chains of zinc atoms connected via bisphosphonate linkers.*[63] *Zn centred tetrahedra in orange, phosphonate tetrahedra in yellow, carbon atoms in grey and nitrogen atoms in blue.*

The most interesting porous phosphonate MOFs prepared with this ligand are the STA-12 series.[49] The composition of the structures are $M_2L.nH_2O$, where n = 7-8 and M = Mn, Fe, Co and Ni (Figure 1.18). The framework structure, dehydration chemistry, adsorption properties and applications are explained in greater detail later on in this thesis.

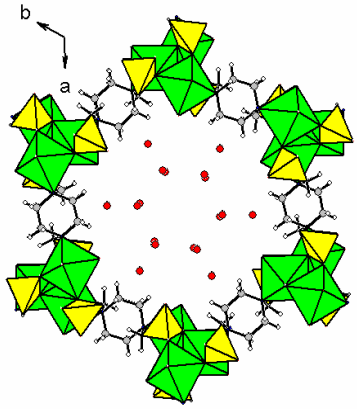

Figure 1.18 *– Ni STA-12 as-prepared projected down direction of one of the hexagonal 1-D -channels.[62] Ni centred octahedra in green, phosphonate tetrahedra in yellow, carbon atoms in grey and hydrogen atoms in white. Oxygen atoms of physisorbed water molecules in red.*

The ligand also forms MIL-91 with aluminium and titanium. The chemical formulae are $AlOH(H_2L).xH_2O$ and $TiO(H_2L).yH_2O$, where x = 3 and y = 4.5.[64] The inorganic part of the structure has 1-D chains, and the metals are in octahedral coordination. The chains are cross linked by bisphosphonate ligands, forming channels 3.5 × 4.5 Å which are large enough for small gas molecule adsorption (Figure 1.19).

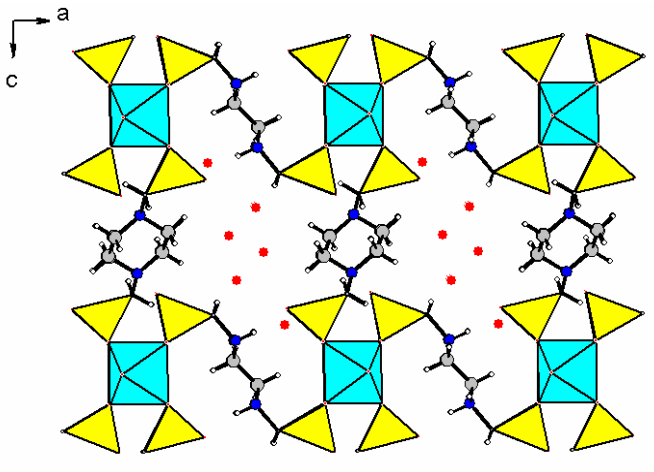

Figure 1.19 *– Projection down direction of small pores in $AlOH(H_2L).3H_2O$ (MIL-91).*[64] *Al centred octahedra in blue, phosphonate tetrahedra in yellow, carbon atoms in grey, nitrogen atoms in blue and hydrogen atoms in white.*

Similar MOF structures have also been reported using lanthanide metal cations and L. Inorganic chains of lanthanide cations are linked by the ligand, creating channels containing 10 - 15 wt% water. The water can be reversibly removed and adsorbed, but no permanent microporosity is observed.[65, 66] The structures are very flexible, and structural rearrangements take place on dehydration resulting in the pores closing to non-coordinating adsorbates (Figure 1.20).

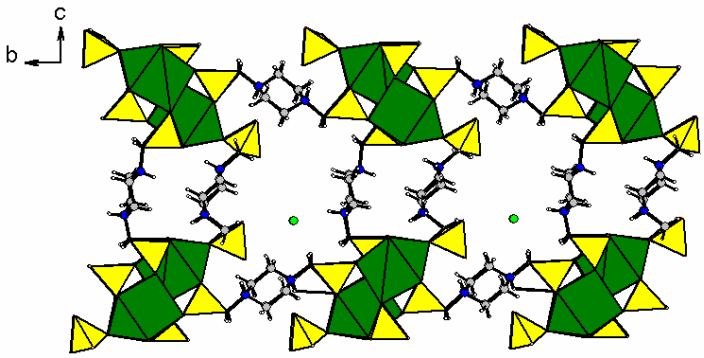

Figure 1.20 *– An open framework bisphosphonate (Ln) La-Eu (Ln_2LH_3Cl).*[65] *Water molecules are omitted from the channels. Ln centred polyhedra in dark green, phosphonate tetrahedra in yellow, carbon atoms in grey, nitrogen atoms in blue, hydrogen atoms in white and chlorine atoms (for charge balancing) in green.*

Other bisphosphonic acids that have been used to synthesise 3-D framework structures include methylene and xylenebisphosphonates, although very few of the structures have permanent porosity. Examples of non-porous framework solids include VSB-2, -3 and -4 nickel methylene bisphosphonates, MIL-22,[67] MIL-48[68] and structures in the reviews of Maeda[54] and Clearfield[69, 70] on open framework phosphonates. Some of the ligands used are complex, and result in remarkable structures outlined in the review of lanthanide phosphonates by Mao.[71]

Another example is the structure formed using the amine functionalised bisphosphonate ligand $HO_3PCH_2NH_2CH_2PO_3H$, $Co_3(O_3PCH_2NH_2CH_2PO_3)_2$.[72] The framework contains two crystallographically distinct Co atoms which form into chains running down the *c*-axis. The chains are cross-linked to one another by both the organic linkers and Co-O-P bridges, resulting in three different channel systems running in the direction of the *c*-axis. The channels are of irregular shapes with diameters of 3.2 Å, 3.4 × 4.6 Å and 3.4 Å respectively, and they are too small for gas molecule uptake (Figure 1.21).

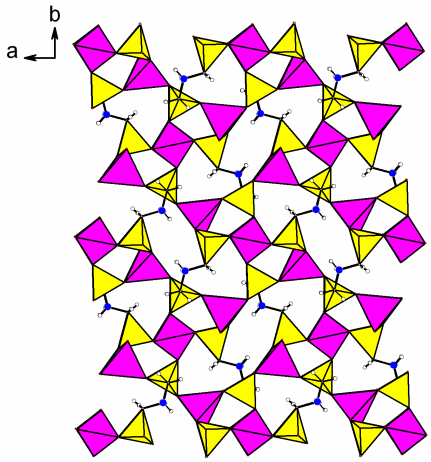

Figure 1.21 *– Structure of $Co_3(O_3PCH_2NH_2CH_2PO_3)_2$ viewed down the direction of the three types of small channels.[72] Co centred tetrahedra in pink, phosphonate tetrahedra in yellow, nitrogen atoms in blue and hydrogen atoms in white.*

Tri- and tetra-phosphonic acids have also been used as phosphonate MOF linkers. The adamantane ligand 1,3,5,7-tetrakis(4-phosphonatophenyl)adamantane forms an interpenetrated diamandoid lattice on reaction with copper.[73] The interpenetration forms micropores *ca.* 5 Å in diameter, which can be dehydrated, resulting in

permanent porosity for CO_2 (Figure 1.22). Distortion of the phosphonate oxygens of two ligands results in formation of Cu_3 trimers.

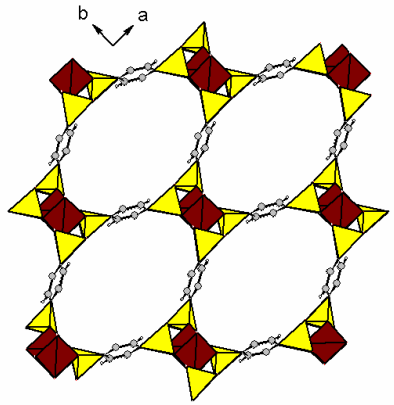

Figure 1.22 *– One of the two interpenetrated copper tetrakisphosphonate frameworks formed using an adamantane-based tetra phosphonic acid.*[73] *Cu centred polyhedra in brown, phosphonate tetrahedra in yellow, carbon atoms in grey and hydrogen atoms in white.*

Ligands that contain only one phosphonate functionality have also been studied. Several functional groups, including amines and carboxylates, have been used, resulting in complex structures with multiple functionalities. The phosphonate-organic structure $Pb(O_3PCH{=}CH_2)$ was synthesised from the reaction of lead (II) acetate and diethyl vinyl phosphonate.[74] The structure crystallises in the space group $R\bar{3}$ and the inorganic chains are linked together forming channels down the *c*-axis. Vinyl groups from the ligand point into the pore, and there is 5.4 Å between them across the channels (Figure 1.23).

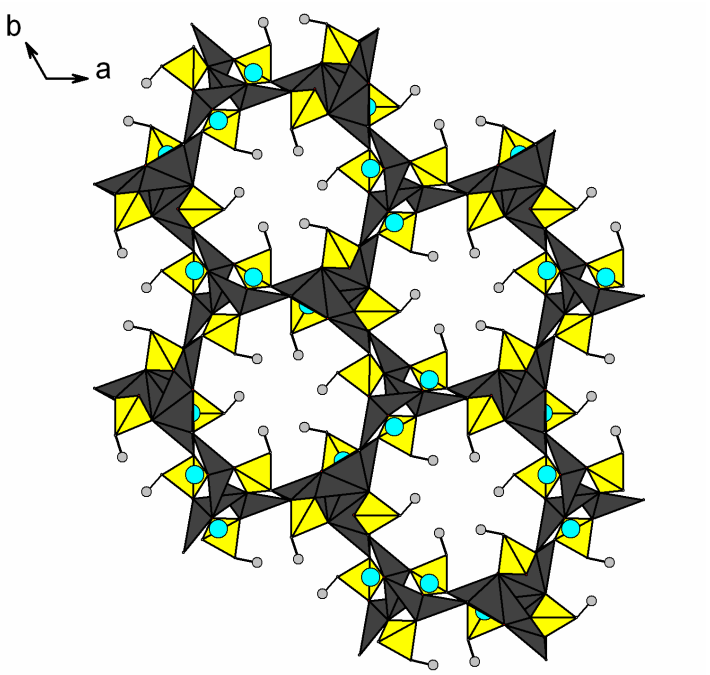

Figure 1.23 *- $Pb(O_3PCH{=}CH_2)$ looking down direction of c-axis.*[74] *Pb centred polyhedra in dark grey, phosphonate tetrahedra in yellow, Pb atoms lining the channels in light blue and carbon atoms in grey.*

Using aminomethylphosphonic acid (ampa) as the linker, several different structures are formed with various metals.[75] With mercury, one ampa molecule bridges two Hg^{2+} centres. One of the centres coordinates to the amine group in the linker, while the other coordinates to the phosphonate oxygen atoms. The structure is stable up to 423 K and forms a 3-D framework with pores 5 × 9 Å (Figure 1.24).

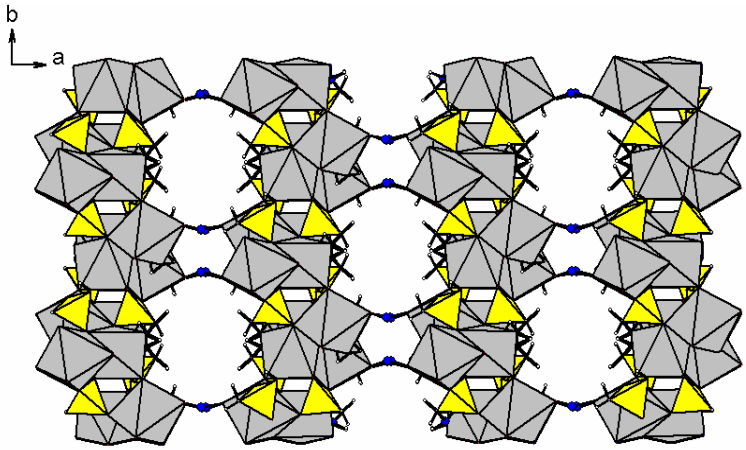

Figure 1.24 *– Representation of Hg^{2+} aminomethylphosphonate looking down the direction of the oval shaped channels.[75] Hg centred octahedra in grey, phosphonate tetrahedra in yellow, nitrogen atoms in blue and hydrogen atoms in white.*

Another example is a recent study using 4-phosphono-benzoic acid with zinc in solvothermal reaction conditions, producing six structure types.[76] Using DMF and 1,3-butanediol as the solvents in the reaction gel produced two related 3-D connected frameworks. Coordination of the zinc cations with the PO_3 groups in the linkers results in double-crankshaft chains, allowing the structures to form zeolite-type topologies. A topology similar to GIS – type zeolites is formed with DMF as the solvent (producing pores 6 × 9 Å in diameter), while a topology similar to the MER, GIS and PHI types of zeolites is formed with 1,3-butanediol. The pores are 7 × 8 Å in diameter, but there is also significant amounts of 1,3-butanediol coordinated within the pores (Figure 1.25). The results from this study indicate zeolite type topologies can form with phosphonate frameworks, meaning comparisons can be made between phosphonate MOFs and fully inorganic frameworks.

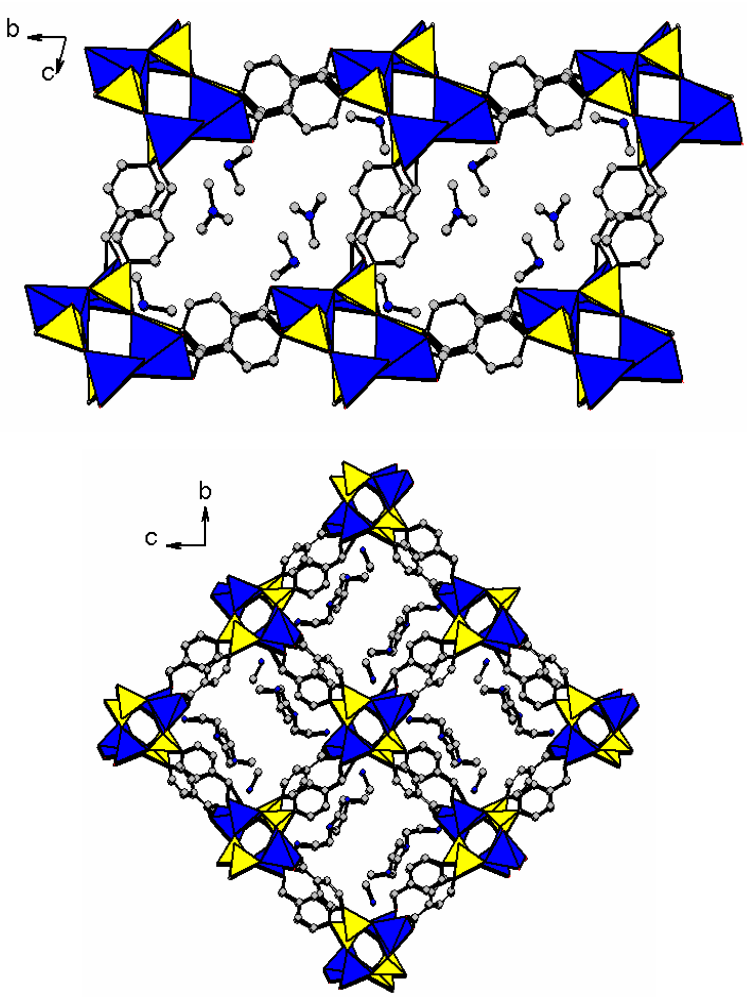

Figure 1.25 *– Two different structures formed by reaction of Zn with 4-phosphono-benzoic acid in solvothermal systems. Solvents used: (Top) DMF; (Bottom) 1,3-butanediol. Guest molecules present in pores.*[76] *Zn centred tetrahedra in blue, phosphonate tetrahedra in yellow, carbon atoms in grey and nitrogen atoms in blue.*

The structures outlined above indicate the complexity phosphonate frameworks can possess, along with the many types of ligands that can be used. When these structures can be engineered to give single phases by modifying conditions within the syntheses the possibilities are almost limitless, as outlined in the recent review by Shimizu *et al*.[77] Several stable porous phosphonate structures have been discovered, and there is the potential for a great many more to be synthesised for potential applications.

1.6 Gas adsorption in microporous materials

Gas adsorption and storage in microporous materials is an important technology,[78] with applications and potential applications ranging from energy and the environment to biology and medicine.[79] Highly porous materials, such as zeolites, carbon materials, polymers and metal-organic frameworks (MOFs), offer a wide variety of chemical compositions and structures suitable for adsorption and storage of many different gases, including hydrogen, methane and carbon dioxide. There are large challenges associated with designing materials to have sufficient adsorption capacity and, if needed, controllable delivery rates, suitable lifetimes and recharging characteristics. The different chemistry of the gases of interest means the properties of the porous materials have to be matched to the required application.

There are several advantages of storing gases in microporous materials. The main one is more gas can be adsorbed at high pressure in a solid than can be stored at high pressure in a tank of the same volume, resulting in an increased storage density. There is also an increase in the safety, and small amounts of gas can be handled more easily when stored in a small amount of solid.

The large number of possible organic linkers, combined with the almost infinite ways in which they can connect metal ions and metal ion clusters, means MOFs have potential uses in many gas storage applications.[80] The internal surface areas for the most porous MOFs[81] exceed 5000 $m^2 g^{-1}$, which is much higher than zeolites (typical surface areas of several hundred $m^2 g^{-1}$). Examples of recent studies of gas adsorption on MOFs include a study by Yaghi *et al*. into the uptake of harmful gases such as sulphur dioxide, benzene and carbon monoxide using members of the IRMOF-*n* series of solids,[82] and another study by Calero *et. al*.[83] into the adsorption and separation of natural gas mixtures using the IRMOF-1 and HKUST-1 structures. This indicates MOFs could be of use in helping to remove, store and separate environmentally harmful gases. More information on the background to the use of MOFs in gas adsorption is outlined in Chapter 5 of this thesis.

1.7 Catalysis using microporous materials

Microporous materials are widely used in catalysis, with zeotypes being important for several industrial processes in the petro- and agrochemical fields.[84, 85] The regular and well defined pore structures allow molecules of appropriate sizes and shapes to enter the frameworks, so shape and size selectivity can be imparted onto the reactions (Figure 1.26). The pore geometries mean only selected shapes and sizes of molecules can enter the structures, and diffusion limiting steps mean only products of specific shapes and sizes can exit. Within the pores transition states form at active sites, and space restrictions can result in a favouring for some reaction mechanisms.[86–88]

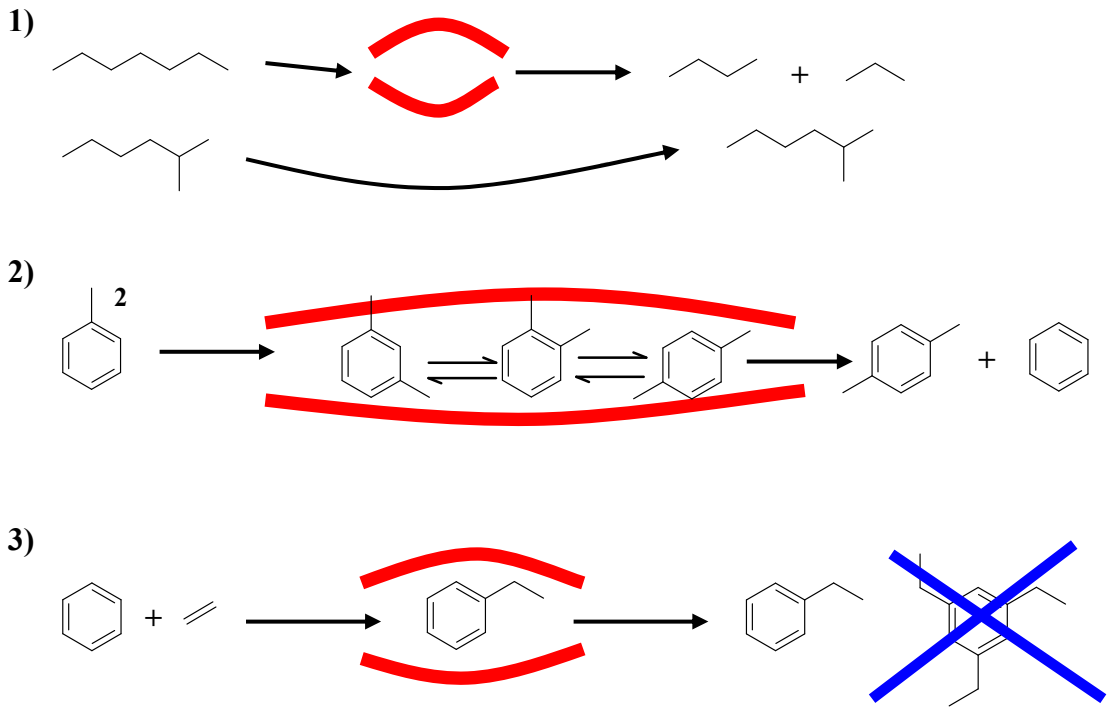

Figure 1.26 *– Examples of shape and size selectivity – 1) Reactants, 2) Products and 3) Transition State (adapted from reference 88).*

There are also other advantages of zeotypes in catalysis. These include good thermal and hydrothermal stability, allowing gas phase reactants at high pressure and temperatures to be used, and relatively high measured acidity, with both Lewis and Brønsted types present.[89]

There are many different types of reactions catalysed using zeotypes, including fluidised bed catalytic cracking of long chain hydrocarbons for petrochemical uses[89]

and conversion of methanol to olefins producing gasoline range hydrocarbons, with zeotypes acting as acid catalysts.[90-92] Zeotypes can also be used as catalysts in decomposition of NO, with Cu-containing ZSM-5 and SAPO-34 particularly active, with potential applications in deNO_x processes.[93, 94] Also incorporation of transition metal species such as Co, Mn and Fe into framework positions in MAPO structures can introduce redox properties to the materials.[95] Coupled to ion exchange of transition metals into the pores offers great opportunities in catalysis.

1.8 Microporous hybrid solids as catalysts

Microporous metal organic framework solids (MOFs) with coordinatively unsaturated (CUS) metal sites have potential as catalysts for environmentally-benign liquid phase reactions. Compared to zeolites, most MOFs do not have high thermal or hydrothermal stability, although the resulting pore sizes and architectures are often very different. Structures similar to complexes used in homogeneous catalysis can also be present in the frameworks, allowing for known reactions to be undertaken.[96]
Fujita *et al.* reported in 1994 a two-dimensional square network synthesised from Cd^{2+} and 4, 4'-bipyridine.[97] The structure was built from two-dimensional sheets held together *ca.* 6 Å apart via weak interactions with bridging *o*-dibromobenzene molecules. The material catalyses the cyanosilylation of aldehydes[97] (Scheme 1.2) and imines,[98] and the reactions were demonstrated to be fully heterogeneous, with no observed conversion in the reaction mixture after removal of the solid

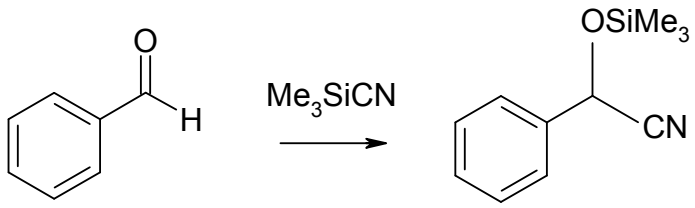

Scheme 1.2 *– Cyanosilylation of benzaldehyde catalysed by Cd(II) 4,4'-bipyridine structure - 313 K, 24 hours. 77% conversion, Turn Over Number (TON) = 0.136, Turn Over Frequency (TOF) = 5.67 × 10^{-3} h^{-1}.*

Aoyama *et al.* reported the formation of a porous organic network synthesised from anthracenebisresorcinol[99] with immobilised zirconium atoms in the pores.[100] The Zr atoms interacted with the organic network, forming stable complexes, and the resulting material functioned as a catalyst for the enantiomeric Diels-Alder reaction of acrolein and cyclohexadiene (Scheme 1.3), going to completion in 3 hours at 298 K (half life at 3 mol% loading, τ = 140 h). This was significantly faster than with the organic network alone, and there was no evidence for leaching of Zr into the reaction mixture. As the Zr complexes were only present in the cavities, this indicated the reaction was taking place inside the pores.

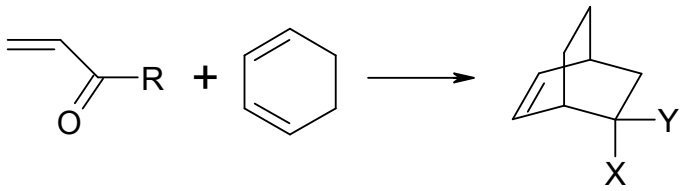

Scheme 1.3 *- Acrolein – cyclohexandiene Diels – Alder reaction. Products:* ***endo*** *– X = COR, Y = H,* ***exo*** *– X = H, Y = COR. Ratio endo : exo = 95:5.*

A feature of MOFs is the possibility of incorporating chiral linkers directly into the frameworks. In 2000, Seo *et al.* reported the synthesis of the chiral MOF POST-1.[101] The structure was synthesised from the reaction of the chiral linker shown in Figure 1.27 and Zn^{2+}. Three zinc ions were bonded to six organic linkers, forming trinuclear units joined together into 2-D sheets stacked on top of one another via van der Waals interactions. This created large, chiral 1-D pores down the *c*-axis, with similar shapes to equilateral triangles with sides *ca.* 13.4 Å. Depending on the organic building block used the channels can have either D- or L- configuration.

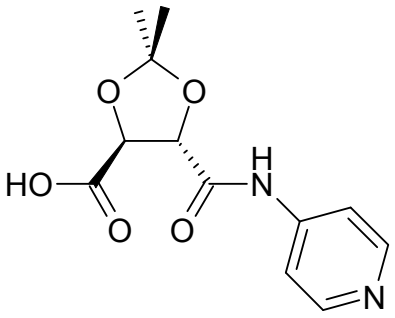

Figure 1.27 *– Organic building block used for POST-1 – shown here is the D-version.*

The transesterification reaction in Scheme 1.4 was investigated, and after 55 hours of stirring at 300 K using an excess of POST-1 there was 77% conversion to the ethyl acetate product. The reaction of the same precursor with racemic alcohols found an 8% enantiomeric excess (ee) of the R or S products after the same length of time, depending on whether the D- or L- type of POST-1 was used. This is a low ee value, but demonstrates the potential for chiral hybrid frameworks to be used as enantioselective catalysts.

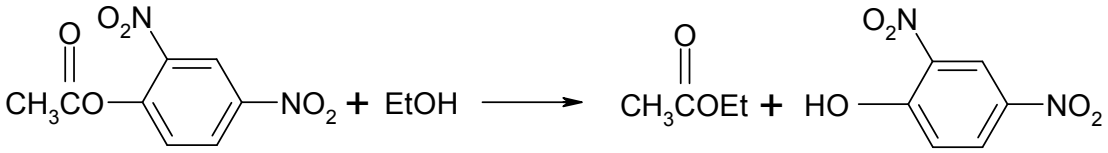

Scheme 1.4 *– Transesterification reaction - conditions – 300 K for 55 hours in CCl_4.*

Mori *et al.* in 2004 reported the formation of a series of MOFs containing Rh^{2+} centres formed using fumaric acid, terephthalic acid or a porphyrin-based ligand.[102] Rhodium is an extensively characterised metal for hydrogenation reactions, and it activates, dissociates and transfers hydrogen atoms. Various reactions were reported, including hydrogen exchange using propane as the substrate and hydrogenation using ethylene as the substrate. In the latter reaction, the Rh^{2+}-porphyrin ligand structure was shown to be stable in a closed gas circulation system at 200 K, while the product stream was composed of 100% ethane after 5 hours (TOF = 2.13×10^{-2} h^{-1}). This

indicated it is possible to design MOF structures with active sites similar to known solid catalysts.

HKUST-1 has been investigated in several studies involving catalytic reactions.[103, 104] Activated HKUST-1 has CUS Cu^{2+} sites which can act as Lewis Acids. It adsorbs molecules strongly, and both these features can be exploited in catalysis. Both liquid phase cyanosilylation[103] and rearrangement of terpene derivatives[104] have been investigated. In the cyanosilylation of benzaldehyde at 313 K (Scheme 1.2),[103] after 72 hours there was 88.5% selectivity to the product with 57% conversion of the benzaldehyde. Low polarity solvents were found to be beneficial as HKUST-1 has low solubility in them, and they do not compete for adsorption onto the Lewis acid sites. However, some solvents, e.g. dichloromethane, caused the framework of the structure to break down in the presence of benzaldehyde. This indicated the HKUST-1 structure appears to have a limited compatibility with some organic solvents and substrates.

In the isomerisation of α-pinene oxide to campholenic aldehyde,[104] which is an important fragrance molecule (Scheme 1.5), the reaction can only produce a high yield if a Lewis acid is used. The selectivity to the product is usually over 85% in the presence of Lewis acids, while in the presence of Brønsted acids it is much lower (around 55%). As a result, the product selectivity gives a measure of the types of acidity present. The reported selectivity was above 80% when using HKUST-1 as the catalyst, indicating mainly Lewis acidity is present. The product selectivity is not dependent on the post synthesis activation methods used, and dichloromethane was found to be the best solvent for the reaction.

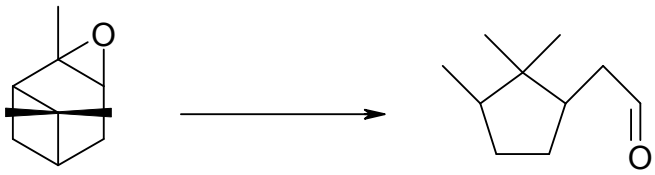

Scheme 1.5 *– Isomerisation reaction of α-pinene oxide to campholenic aldehyde. Reaction conditions – 0.1 g HKUST-1, 0.1 g α-pinene oxide and 5 ml solvent mixed at 298 K for 72 hours.*

Some members of the MOF-*n* series have been investigated for catalytic activity for the *tert*-butylation of both toluene and biphenyl.[105] IRMOF-1 and IRMOF-8 have been used, and the results indicated a high selectivity to *para*-substituted products, revealing outstanding shape selectivity for large polyaromatics. The MOF-*n* structures were shown to have similar kinetics to other well known alkylation catalysts, and were active in the first few minutes of the reaction. Also, no major structural modifications were needed for the structures to be active in the reactions.

Enantioselective epoxidation is important in several oxidation reactions, and a study using an interpenetrated Zn-Mn MOF (Figure 1.28), with a Mn salen entity within the framework, reported enantiomeric excesses comparable with free molecular catalysts.[106] The catalytic activity towards asymmetric epoxidation was examined using 2,2-dimethyl-2*H*-chromene as the substrate and 2-(*tert*-butylsulphonyl)iodosylbenzene as the oxidant (Scheme 1.8). The reactivity was constant over the course of the reaction, and the ee was 82%. The ee value was lower than observed for Mn salen molecular catalysts, due to the presence of pyridine groups binding to Zn atoms causing electron withdrawal from the Mn salen unit.

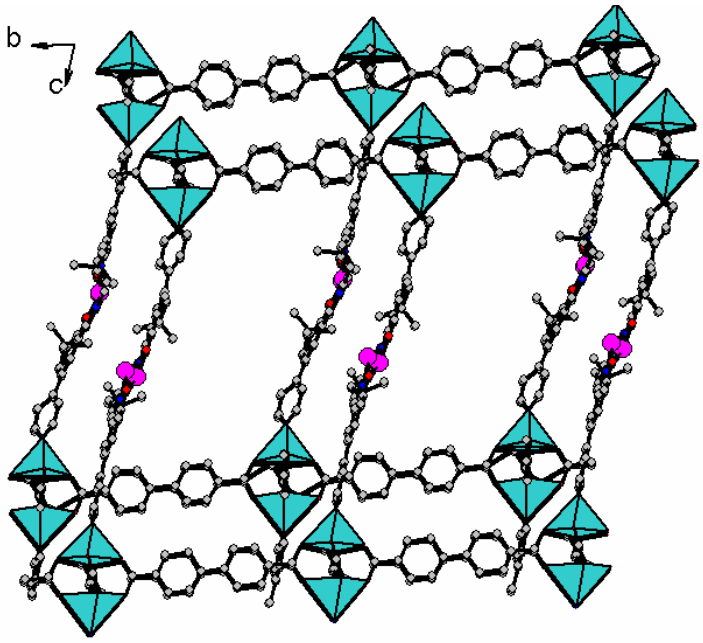

Figure 1.28 *– Zn-Mn interpenetrated MOF, with Mn salen linkers bridging Zn cations.[106] Zn centred polyhedra in light blue, carbon atoms in grey, oxygen atoms in red and Mn cations in pink.*

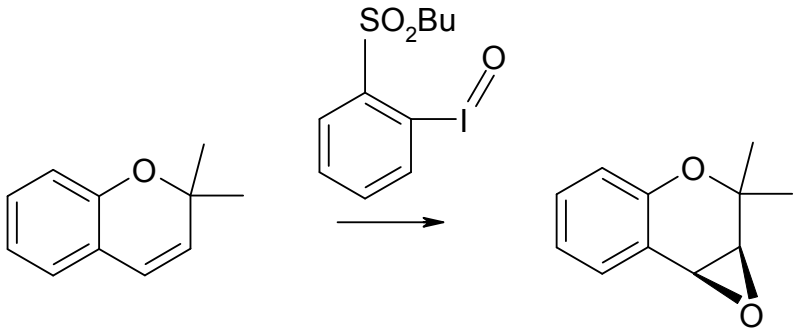

Scheme 1.8 *– Asymmetric epoxidation reaction. Reaction ratio - substrate : oxidant : catalyst = 4000 : 2000 : 1. Reaction conditions – 298 K for 3.4 hours. 71% yield, TON = 1430.*

Another study into oxidation catalysis was reported by Maksimchuk *et al.* in 2008.[107] Keggin heteropolyanions (POMs) based on Ti^{4+} and Co^{2+} were substituted into MIL-101. The POMs interacted strongly with the MOF support, and were used to oxidise alkene substrates. In the oxidation of cyclohexene with H_2O_2 (Scheme 1.9), the conversion of the substrate was increased by a factor of 5 when Ti-POM was immobilised on MIL-101 compared to the unmodified framework. The selectivity to the products changed, with an increase in the amount of cyclohexane-1,2-diol produced with Ti-POM immobilisation. The POMs were stable and did not leach into the reaction mixture.

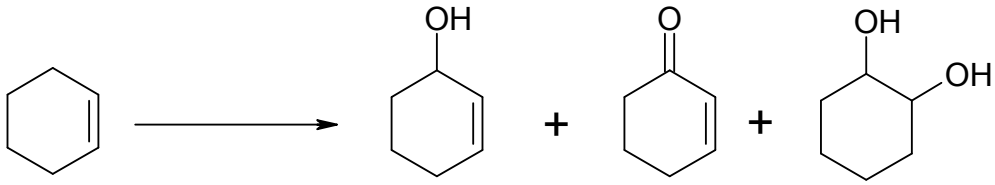

Scheme 1.9 *– Oxidation of cyclohexene reaction. Reaction ratios – substrate : oxidant : catalyst = 1000 : 2000 : 4.5 (Ti-POM). Reaction conditions – 303 K, 6 hours. TOF = 92* h^{-1}.

The studies outlined so far have involved using MOFs as acid or oxidation catalysts. Modification of the MIL-101 structure can allow for basic activity.[108] Refluxing activated MIL-101 in toluene with ethylene diamine resulted in coordination of diamine molecules to the CUS Cr sites. Modified MIL-101 was active for the Knoevenagel condensation of benzaldehyde and ethyl cyanoacetate (Scheme 1.10). The conversion of the reactants to the ethyl *trans*-α-cyanocinnamate product was 97%, with product selectivity >99%. The major difference to unmodified MIL-101 was the 3 × greater conversion of the reactants to the product.

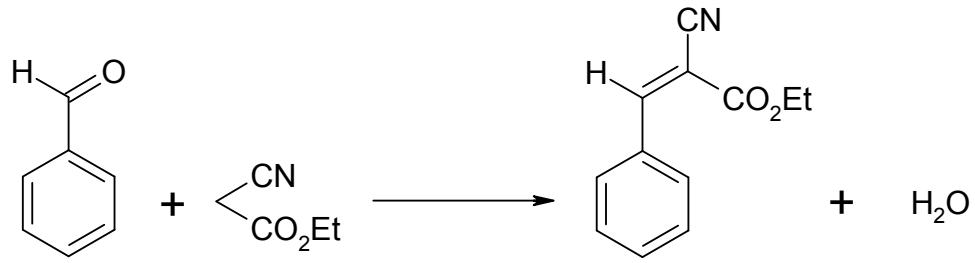

Scheme 1.10 *– Knoevenagel condensation reaction of benzaldehyde and ethyl cyanoacetate. Reaction ratios – benzaldehyde : ethyl cyanoacetate = 1 : 1. Reaction conditions – 353 K for 19 hours, reactants dispersed in 25 ml cyclohexene with 20 mg catalyst. TOF = 328* h^{-1}.

Another approach is to incorporate basic functionalities into the linkers. An example was the interpenetrated structure formed from Cd^{2+} and the amide 4-btpa (1,3,5-benzene tricarboxylic acid tris[*N*-(4-pyridyl)amide).[109] The amide groups are located on the surfaces of the pores and can interact with guest species. Using the structure as a catalyst in the same Knoevenagel reaction as in Scheme 1.10 resulted in 98% conversion of the reactants to the cinnamate product (TON = 41.41, TOF = 3.45 h^{-1}), almost 5 × more than using just the amide ligand as a catalyst. The 98% conversion was reached after 2.5 hours, indicating the basic properties of this structure were greater than ethylene diamine modified MIL-101. This is mainly due to greater accessibility of the basic interaction sites compared to modified MIL-101.

1.9 Aims of thesis

The aims of the work contained in this thesis are as follows:

1) Investigate the synthesis of the bisphosphonate framework STA-12 (and related phases), and synthesise various large pore carboxylates for comparative purposes.
2) Characterise synthesised structures using X-ray diffraction and a range of chemical analyses.
3) Investigate dehydration properties of STA-12 using X-ray diffraction, thermal analysis, UV-visible spectroscopy and Infra-red spectroscopy.
4) Characterise adsorption and chemisorption properties of STA-12 for a range of fuel related gases and probe molecules, using adsorption calorimetry and infra-red spectroscopy.
5) Test activity of STA-12 in two different catalytic reactions (selective oxidation and Knoevenagel condensation), and compare to large pore carboxylates.

1.10 References

1) S. Kaskel, *Handbook of Porous Solids*, *Wiley*, *New York*, 2002, **Vol. 2**

2) A. K. Cheetham, G. Férey and T. Loiseau, *Angew. Chem. Int. Ed.*, 1999, **38,** 3268

3) M. E. Davis, *Nature*, 2002, **417**, 813

4) A. F. Cronstedt, *Kongl. Svenska Vetenskaps Akademiens.*, 1756, **17**, 20

5) C. R. Hebd and H. d. S. C. Deville, *Seances Acad. Sci.*, 1862, **54**, 324

6) J. W. McBain, *Rutledge*, *London*, 1932, **ch. 5**

7) www.dow.com/uss/index.htm

8) R. M. Barrer, *J. Chem. Soc.*, 1948, 2158

9) D. W. Breck, W. G. Eversole, R. M. Milton, T. B. Reed and T. L. Thomas, *J. Am. Chem. Soc.*, 1956, **78**, 5968

10) S. T. Wilson, B. M. Lok, C. A. Messina, T. R. Cannan and E. M. Flanigen, *J. Am. Chem. Soc.*, 1982, **104**, 1146

11) www.iza-online.org

12) R. M. de Vos and H. Verweij, *Science*, 1998, **279**, 1710

13) G. Férey, M. Latroche, C. Serre, F. Millange, T. Loiseau and A. Percheron-Guegan, *Chem. Commun.*, 2005, 2976

14) N. Rosi, J. Eckert, M. Eddaoudi, D. T. Vodak, J. Kim, M. O'Keefe and O. M. Yaghi, *Science*, 2003, **300**, 1127

15) G. Férey, *Chem. Soc. Rev.*, 2008, **37**, 191

16) M. J. Rosseinsky, *Micropor. Mesopor. Mater.*, 2004, **73**, 15

17) L. S. Dent and J. V. Smith, *Nature*, 1958, **181**, 1794

18) K. Maeda, J. Akimoto, Y. Kiyozumi and F. Mizukami, *Angew. Chem. Int. Ed.*, 1995, **34**, 1199

19) H. Li, M. Eddaoudi, M. O'Keefe and O. M. Yaghi, *Nature*, 1999, **402**, 276

20) S. B. Hong, H-K. Min, C-H. Shin, P. A. Cox, S. J. Warrender and P. A. Wright, *J. Am. Chem. Soc.*, 2007, **129**, 10870

21) R. M. Barrer, L. Hinds and E. A. White, *J. Am. Chem. Soc.*, 1952, 1561

22) A. K. Cheetham, C. N. R. Rao and R. K. Feller, *Chem. Commun.*, 2006, 4780

23) P. M. Forster, A. R. Burbank, C. Livage, G. Férey and A. K. Cheetham, *Chem. Commun.*, 2004, 368

24) K. Barthelet, J. Marrot, D. Riou and G. Férey, *Angew. Chem. Int. Ed.*, 2006, **41**, 281

25) K. Barthelet, J. Marrot, G. Férey and D. Riou, *Chem. Commun.*, 2004, 520

26) W. Mori and S. Takamizawa, *J. Solid State Chem.*, 2000, **152**, 120

27) S. Feng and R. Xu, *Acc. Chem. Res.*, 2001, **34**, 239

28) C. Baerlocher, W. M. Mier and D. H. Olsen, *Atlas of Zeolite Framework Types*, *Elsevier*, *Amsterdam*, 2001, **5th Edition**

29) M. Eddaoudi, D. B. Moler, H. Li, B. Chen, T. Reinke, M. O'Keefe and O. M. Yaghi, *Acc. Chem. Res.*, 2001, **34**, 319

30) M. E. Braun, C. D. Steffek, J. Kim, P. G. Rasmussen and O. M. Yaghi, *Chem. Commun.*, 2001, 2532

31) M. O'Keefe, M. Eddaoudi, H. Li, T. Reinke and O. M. Yaghi, *J. Solid State Chem.*, 2000, **152**, 3

32) O. M. Yaghi, M. O'Keefe, N. W. Ockwig, H. K. Chae, M. Eddaoudi and J. Kim, *Nature*, 2003, **423**, 705

33) M. Eddaoudi, J. Kim, N. Rosi, D. Vodak, J. Wachter, M. O'Keefe and O. M. Yaghi, *Science*, 2002, **295**, 469

34) G. Férey, C. Serre, C. Mellot-Draznieks, F. Millange, S. Surble, J. Dutour and I. Margiolaki, *Angew. Chem. Int. Ed.*, 2004, **43**, 6296

35) G. Férey, C. Mellot-Draznieks, C. Serre, F. Millange, J. Dutour, S. Surble and I. Margiolaki, *Science*, 2005, **309**, 2040

36) J. G. Vitillo, L. Regli, S. Chavan, G. Ricchiardi, G. Spoto, P. D. C. Dietzel, S. Bordiga and A. Zecchina, *J. Am. Chem. Soc.*, 2008, **130**, 8386

37) S. S. Y. Chui, S. M. F. Lo, J. P. H. Charmant, A. G. Orpen and I. D. Williams, *Science*, 1999, **283**, 1148

38) F. Millange, C. Serre and G. Férey, *Chem. Commun.*, 2002, 822

39) C. Serre, F. Millange, C. Thouvenot, M. Noguès, G. Marsolier, D. Louër and G. Férey, *J. Am. Chem. Soc.*, 2002, **124**, 13519

40) T. Loiseau, C. Serre, C. Hugenard, G. Fink, F. Taulelle, M. Henry, T. Bataille and G. Férey, *Chem. Eur. J.*, 2004, **10**, 1373

41) G. Férey, F. Millange, M. Morcrette, C. Serre, M-L. Doublet, J-M. Grenèche and J-M. Tarascon, *Angew. Chem. Int. Ed.*, 2007, **46**, 3259

42) M. Vougo-Zanda, J. Huang, E. Anokhina, X. Wang and A. J. Jacobson, *Inorg. Chem.*, 2008, **47**, 11535

43) C. Volkringer, T. Loiseau, N. Guillou, G. Férey, E. Elkaïm and A. Vimont, *Dalton. Trans.*, 2009, 2241

44) P. D. C. Dietzel, Y. Morita, R. Blom and H. Fjellvåg, *Angew. Chem. Int. Ed.*, 2005, **44**, 6354

45) P. D. C. Dietzel, B. Panella, M. Hirscher, R. Blom and H. Fjellvåg, *Chem. Commun.*, 2006, 959

46) N. L. Rosi, J. Kim, M. Eddaoudi, B. Chen, M. O'Keefe and O. M. Yaghi, *J. Am. Chem. Soc.*, 2005, **127**, 1504

47) E. Biemmi, T. Bein and N. Stock, *Solid State Sciences*, 2006, **8**, 363

48) K. S. Park, Z. Ni, A. P. Cote, J. Y. Choi, R. Huang, F. J. Uribe-Romo, H. K. Chae, M. O'Keefe and O. M. Yaghi, *PNAS*, 2006, **103**, 10186

49) J. A. Groves, S. R. Miller, S. J. Warrender, C. Mellot-Draznieks, P. Lightfoot and P. A. Wright, *Chem. Commun.*, 2006, 3305

50) S. R. Miller and P. A. Wright, eds. C. M. Lukehart and R. A. Scott, *Nanomaterials: Inorganic and Bioinorganic Perspectives*, *Wiley*, *UK*, 2008

51) D. Bosbach, P. V. Coveney, J. L. W. Griffin, A. Putnis, P. Risthaus, S. Stackhouse and A. Whiting, *J. Chem. Soc.*, *Perkin Trans. 2*, 2002, 1238

52) Y. Yang, Y. Zhao, J. Yu, Y. Zhou, N. Pang, H. Su and S. Pang, *Z. Anorg. Allg. Chem.*, 2008, **634**, 1780

53) S. Mandal and S. Natarajan, *Inorg. Chem*, 2008, **47**, 5305

54) K Maeda, *Micropor. Mesopor. Mater.*, 2004, **73**, 47

55) K. Maeda, Y. Kiyozumi and F. Mizukami, *Angew. Chem. Int. Ed.*, 1994, **33**, 2335

56) K. Maeda, J. Akimoto, Y. Kiyozumi and F. Mizukami, *J. Chem. Soc.*, *Chem. Commun.*, 1995, 1033

57) V. J. Carter, P. A. Wright, J. D. Gale, R. E. Morris, E. Sastre and J. PerezPariente, *J. Mater. Chem.*, 1997, **7**, 2287

58) V. J. Carter, J. P. Kujanpää, F. G. Riddell, P. A. Wright, J. F. C. Turner, C. R. A. Catlow and K. S. Knight, *Chem. Phys. Letts.*, 1999, **12**, 505

59) K. Maeda, Y. Kiyozumi and F. Mizukami, *J. Phys. Chem. B*, 1997, **101**, 4402

60) C. Schumacher, J. Gonzalez, P. A. Wright and N. A. Seaton, *Phys. Chem. Chem. Phys.*, 2005, **7**, 2351

61) C. Herdes, A. Valente, Z. Lin, J. Rocha, J. A. P. Coutinho, F. Medina and L. F. Vega, *Langmuir*, 2007, **23**, 7299

62) R. LaDuca, D. Rose, J. R. D. DeBord, R. C. Haushalter, C. J. O'Connor and J. Zubieta, *J. Solid State Chem.*, 1996, **123**, 408

63) J. A. Groves, P. A. Wright and P. Lightfoot, *J. Chem. Soc., Dalton Trans.,* 2005, 2007

64) C. Serre, J. A. Groves, P. Lightfoot, A. M. Z. Slawin, P.A. Wright, N. Stock, T. Bein, M. Haiuas, F. Taulelle and G. Férey, *Chem. Mater.*, 2006, **18**, 1451

65) J. A. Groves, P. A. Wright and P. Lightfoot, *Inorg. Chem.*, 2005, **44**, 1736

66) J. A. Groves, N. F. Stephens, P. A. Wright and P. Lightfoot, *Solid State Sciences*, 2006, **8**, 397

67) C. Serre and G. Férey, *Inorg. Chem.*, 1999, **38**, 5370

68) K. Barthelet, C. Merlier, C. Serre, M. Riou-Cavellec, D. Riou and G. Férey, *J. Mater. Chem.*, 2002, **12**, 1132

69) A. Clearfield, *Curr. Opin. Solid State Mater. Sci.*, 1996, **1**, 268

70) A. Clearfield, *Curr. Opin. Solid State Mater. Sci.*, 2002, **6**, 495

71) J. G. Mao, *Coord. Chem. Rev.*, 2007, **251**, 1493

72) A. Turner, P-A. Jaffrès, E. J. MacLean, D. Villemin, V. McKee and G. B. Hix, *Dalton Trans.*, 2003, 1314

73) J. M. Taylor, A. H. Mahmoudkhani and G. K. H. Shimizu, *Angew. Chem. Int. Ed.*, 2007, **46**, 795

74) G. B. Hix, A. Turner, L. Vahter and B. M. Kariuki, *Micropor. Mesopor. Mater.*, 2007, **99**, 62

75) C. R. Samanamu, E. N. Zamora, J-L. Montchamp and A. F. Richards, *J. Solid State Chem.*, 2008, **181**, 1462

76) Z. Chen, Y. Zhou, L. Weng and D. Zhao, *Cryst. Growth Des.*, 2008, **8**, 4045

77) G. K. H. Shimizu, R. Vaihyanathan and J. M. Taylor, *Chem. Soc. Rev.*, 2009, **38**, 1430

78) P. L. Llewellyn and G. Maurin, *C. R. Chemie*, 2005, **8**, 283

79) R. E. Morris and P. S. Wheatley, *Angew. Chem. Int. Ed.*, 2008, **47**, 4966

80) U. Müller, M. Schubert, F. Teich, H. Puetter, K. Schierle-Arndt and J. Pastre, *J. Mater. Chem.*, 2006, **16**, 626

81) G. Férey, C. Mellot-Draznieks, C. Serre, F. Millange, J. Dutour, S. Surble and I. Margiolaki, *Science*, 2005, **309**, 2040

82) D. Britt, D. Tranchemontagne and O. M. Yaghi, *Proc. Acad. Sci. USA*, 2008, **105**, 11623

83) A. Martin-Calvo, E. Garcia-Perez, J. Manuel Castillo and S. Calero, *Phys. Chem. Chem. Phys.*, 2008, **10**, 7085

84) J. M. Thomas and W. J. Thomas, *Principles and Practice of Heterogeneous Catalysis*, *VCH*, *Cambridge*, 1997

85) J. Weitkamp, *Solid State Ionics*, 2000, **131**, 175

86) C. R. Marcilly, *Topics in Catal.*, 2000, **13**, 357

87) M. Schenk, B. Smit, T. J. H. Vlugt and T. L. M. Maesen, *Angew. Chem. Int. Ed.*, 2001, **40**, 736

88) T. F. Dengen, *J. Catal.*, 2003, **216**, 32

89) M. Stöcker, *Micropor. Mesopor. Mater.*, 2005, **82**, 257

90) J. M. Thomas, *Angew. Chem. Int. Ed.*, 1994, **33**, 913

91) L. K. Carlson, P. K. Isbester and E. J. Munson, *Solid State Mag. Reson.*, 2000, **16**, 93

92) I. L. Franklin, A. M. Beale and G. Sankar, *Catal. Today*, 2003, **81**, 623

93) A. Frache, B. Palella, M. Cadoni, R. Pirone, P. Ciambelli, H. O. Pastore and L. Marchese, *Catal. Today*, 2002, **75**, 359

94) A. Frache, B. Palella, M. Cadoni, R. Pirone, H. O. Pastore and L. Marchese, *Top. Catal.*, 2003, **22**, 53

95) U. Lohse, R. Bertram, K. Jamcke, I. Kurzawski and B. Parlitz, *J. Chem. Soc. Faraday Trans.*, 1995, **91**, 1163

96) P. M. Forster and A. K. Cheetham, *Top. Catal.*, 2003, **24**, 79

97) M. Fijita, Y. J. Kwon, S. Washizu and K. Ogura, *J. Am. Chem. Soc.*, 1994, **116**, 1151

98) O. Ohmori and M. Fujita, *Chem. Commun.*, 2004, 1586

99) K. Endo, T. Koike, T. Sawaki, O. Hayashida, H. Masuda and Y. Aoyama, *J. Am. Chem. Soc.*, 1997, **119**, 4117

100) T. Sawaki and Y. Aoyama, *J. Am. Chem. Soc.*, 1999, **121**, 4793

101) J. S. Seo, D. Whang, H. Lee, S. I. Jun, J. Oh, Y. J. Jeon and K. Kim, *Nature*, 2000, **404**, 982

102) W. Mori, S. Takamizawa, C. N. Kato, T. Ohmura and T. Sato, *Micropor. Mesopor. Mater.*, 2004, **73**, 31

103) K. Schlichte, T. Kratzke and S. Kaskel, *Micropor. Mesopor. Mater.*, 2004, **73**, 81

104) L. Alaerts, E. Séguin, H. Poelman. F. Thibault-Starzyk, P. A. Jacobs and D. E. De Vos, *Chem. Eur. J.*, 2006, **12**, 7353

105) U. Ravon, M. E. Domine, C. Gaudillère, A. Desmartin-Chomel and D. Farrusseng, *New J. Chem.*, 2008, **32**, 937

106) S. Cho, B. Ma, S. T. Nguyen, J. T. Hupp and T. E. Albrecht-Schmitt, *Chem. Commun.*, 2006, 2563

107) N. V. Maksimchuk, M. N. Timofeeva, M. S. Melgunov, A. N. Shmakov, Y. A. Chesalov, D. N. Dybtsev, V. P. Fedin and O. A. Kholdeeva, *J. Catal.*, 2008, **257**, 315

108) Y. K. Hwang, D. Hong, J. Chang, S. H. Jung, Y. Seo, J. Kim, A. Vimont, M. Daturi, C. Serre and G. Férey, *Angew. Chem. Int. Ed.*, 2008, **120**, 4212

109) S. Hasegawa, S. Horike, R. Matsuda, S. Furukawa, K. Mochizuki, Y. Kinoshita and S. Kitagawa, *J. Am. Chem. Soc.*, 2007, **129**, 2607

Chapter 2: Characterisation Techniques

2.1 Introduction

The main aim of this work is to investigate the chemistry and possible applications of large pore metal phosphonates and related framework structures. To accomplish this, samples were synthesised via hydrothermal routes, characterised, and tested for potential applications in adsorption and catalysis. X-ray diffraction, gas and vapour adsorption, solid state Infra-red (IR) and UV-visible spectroscopy, scanning electron microscopy (SEM), energy dispersive X-ray (EDX) spectroscopy and thermal gravimetric (TGA) and elemental analysis have all been used to characterise the samples. The background to these techniques is outlined in this chapter.

2.2 Basic Crystallography[1-3]

2.2.1 Crystals

The structures of crystalline materials are arrangements of atoms possessing translational symmetry, described in terms of a lattice which is an infinite periodic array of points in identical environments (lattice points). The crystal structure can be described in terms of arrangements of atoms at these lattice points. The unit cell is the smallest repeating unit of a crystal and is a parallel-sided, 3-D box which when repeated in 3-D using translation alone describes a crystalline solid. The unit cell is defined by six parameters, three lengths (a, b, c) and three angles (α, β, γ) that define the angles between the lengths. Depending on the arrangement of the lattice points in the unit cell, different Bravais lattice types result (Figure 2.1).

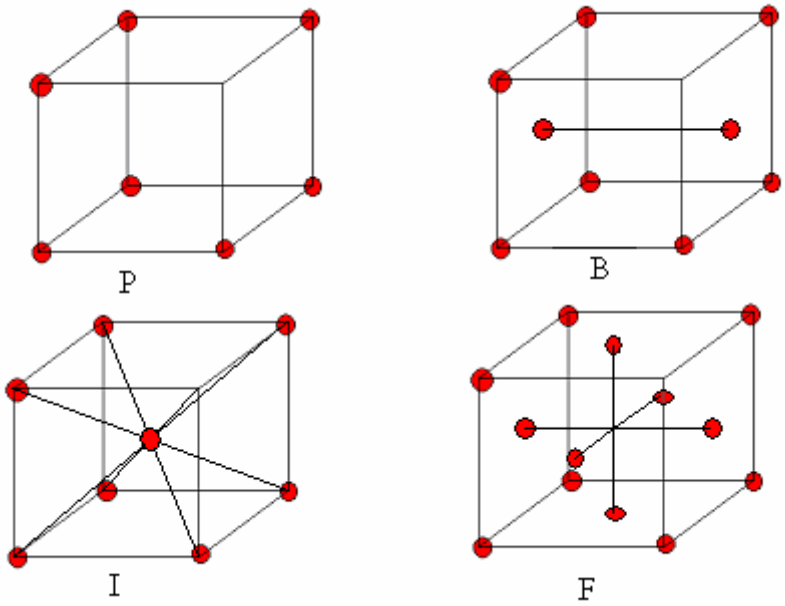

Figure 2.1 *- Possible lattice point positions. 'P' is representative of a primitive unit cell, 'B' shows a lattice point centred on the (010) plane, or B-plane, 'I' is a body centred unit cell and 'F' has a lattice point on all the face centres.*

2.2.2 Seven Crystal Systems

All crystals can be described in terms of seven types of distinct subunits, associated with the seven crystal systems (described in Table 2.1).

Table 2.1 *- Seven crystal systems.*

Crystal system	**Lengths**	**Angles**	**Defining symmetry**
Triclinic	$a \neq b \neq c$	$\alpha \neq \beta \neq \gamma$	None
Monoclinic	$a \neq b \neq c$	$\alpha = \beta = 90°$ $\gamma \geq 90°$	Twofold axis or mirror plane or inverse twofold axis
Orthorhombic	$a \neq b \neq c$	$\alpha = \beta = \gamma = 90°$	Three orthogonal twofold or inverse twofold axis
Tetragonal	$a = b \neq c$	$\alpha = \beta = \gamma = 90°$	One fourfold or inverse fourfold axis
Trigonal	$a = b = c$	$\alpha = \beta = \gamma \leq 120°$	One threefold or inverse threefold axis
Hexagonal	$a = b \neq c$	$\alpha = \beta = 90°$ $\gamma = 120°$	One sixfold or inverse sixfold axis
Cubic	$a = b = c$	$\alpha = \beta = \gamma = 90°$	Four threefold axes

The seven crystal systems described in Table 2.1 can be classified further depending on the symmetry elements present. There are 32 ways rotation axes, mirror planes, centres of symmetry and rotary inversion axes can be used to describe the 7 crystal systems, with these described as point groups. There are also 14 distinct space lattices (Bravais lattices), formed by combinations of the crystal systems and the lattice type. Combining all the possible symmetry elements produces 230 space groups, which are the 230 ways objects can be arranged in space. Table 2.2 lists the Bravais lattices, and the space group symmetry elements and symbols. Space group symbols contain information on the lattice type and the relationship of symmetry elements to the principle axes of the cell. For example, *Pnma* is an orthorhombic space group describing a primitive unit cell with an *n*-glide perpendicular to the *a*-axis, a mirror plane perpendicular to the *b*-axis, and an *a*-glide perpendicular to the *c*-axis.

Table 2.2 *– Bravais Lattices and Symmetry Elements (inversion sign often written above number in space group notation).*

Bravais Lattice	**Crystal System**
P	Triclinic, Monoclinic, Orthorhombic, Tetragonal, Trigonal, Hexagonal, Cubic
C	Monoclinic, Orthorhombic
I	Orthorhombic, Tetragonal, Cubic
F	Orthorhombic, Cubic
Symmetry Element	**Symbol**
Centre of inversion	-1
Mirror plane	m(≡ -2)
Glide plane	a, b, c, n, d
Rotation axis	2, 3, 4, 6
Screw axis	2_1, 3_1, 3_2, 4_1, 4_2, 4_3, 6_1, 6_2, 6_3, 6_4, 6_5
Inversion axis	-3, -4, -6

The 32 point groups are derived without using translational symmetry. Combinations of rotations and parallel translations produce screw axes, designated by integers n and m, where n = 1, 2, 3, 4 or 6 and m < n. For example, 4_1 is a fourfold screw axis with a translation between equivalent points 1/4 of a unit cell translation. Combining mirror planes and translations produces a glide plane. Glide planes can be described with reference to the vectors *a*, *b*, and *c* defining the unit cell edges. For example, an *a*-glide perpendicular to the *b*-axis results in reflection through the plane and translation by 1/2*a*.

Therefore, a space group is described by a capital letter identifying the lattice type (P, C, F, I) followed by the point group symbols. The convention is rotation and reflection symmetry is followed by screw axes and glide planes. The effects of symmetry on a unit cell can be referenced to a point *x*, *y*, *z* in space, and the elements of symmetry for a specific space group act upon this point.

2.2.3 Miller Indices[1 - 3]

Miller indices define sets of planes within a crystal. They are quoted as three numbers in parentheses (*hkl*), where *a/h*, *b/k* and *c/l* giving the intercept of the plane with the three unit cell edges *a*, *b* and *c*. For example, the (111) plane intercepts the *a*, *b* and *c*-axes at the unit cell length, so the indices (111) represent a set of parallel planes intersecting the axes at points separated by *a*, *b* and *c*.

2.3 X-ray Diffraction[1]

X-ray diffraction (XRD) is a powerful technique in the analysis of crystalline structures, as it can be used for the routine identification of phases and in-depth structure analysis and solution. Diffraction takes place if the radiation wavelength is the same magnitude as the object separation, and X-ray radiation is well suited to investigating the arrangements of atoms in materials as the wavelength (~ 1 Å) and inter-atomic distances are on a similar scale.

2.3.1 X-Rays

X-rays are generated in a lab setting by accelerating electrons, emitted from an electrically heated tungsten cathode, through 10 to 30 keV, towards a metal target (such as Fe, Mo, Co, Cr and Cu). The impact produces two types of X-rays:

1) As the electrons hit the metal target they slow down, or stop. When this happens they lose energy – most of the energy is converted to heat but some is emitted as a broad spectrum of wavelengths (white radiation), including X-rays.

2) The electrons from the source have enough energy to ionise electrons in the metal target, creating vacancies in lower orbitals. The vacancies are filled by electrons from outer shells dropping down, obeying the Aufbau principle. Energy is released in the form of X-rays, and as the transitions are quantised specific energy values are associated with each transition. They are also subject to the condition $\Delta l = \pm 1$, e.g. p $\rightarrow$ s or d.

In the case of the second type of X-ray mentioned above, the wavelength is dependent on the energy gap between the electron shells and the identity of the metal element. X-rays generated this way have wavelengths characteristic of the metal target. For example, in the case of Cu a vacancy in the 1s orbital (K) can be filled by electrons from either the 2p (L) or 3p (M) orbitals (Figure 2.2):

$2p \rightarrow 1s$ transition K_α, $\lambda = 1.5418$ Å (L – K transition)

$3p \rightarrow 1s$ transition K_β, $\lambda = 1.3922$ Å (M – K transition)

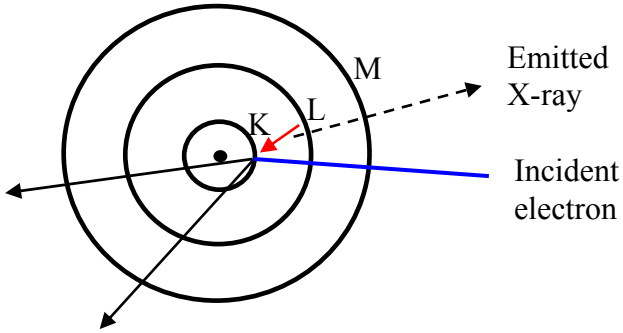

Figure 2.2 *- Schematic illustration of the generation of a K_α X-ray. Red arrow indicates movement of electrons, which generates the emitted X-ray.*

The K_α wavelength is more intense than the K_β wavelength, as the $2p \rightarrow 1s$ transition occurs more frequently than the $3p \rightarrow 1s$ transition. The K_α transition occurs as a doublet of $K_{\alpha1}$ and $K_{\alpha2}$, the subdivision due to the total angular spin momentum quantum number j. Two possible spin states exist for the 2p electrons ($2p_{1/2}$ and $2p_{3/2}$), so the transitions take place with a small difference in energy, which results in slightly different wavelengths. The K_α transitions are sufficiently different to allow one to be selected for use in diffraction experiments, and the X-rays produced by the K_α and K_β transitions form sharp peaks at well defined wavelengths superimposed on the background white radiation.

In some transition metal elements, such as Mn, Fe and Co, the electrons in the d-orbitals have similar ground state energies to the electrons in the s and p-orbitals. Low energy secondary X-rays can be produced via ionisation of d-orbital electrons by Cu K_α X-rays, which have wavelengths near the absorption edge energy. The secondary X-rays can have similar wavelengths to the K_α transitions, and this fluorescence can be exploited to identify elements present in a material. On the other hand, the

secondary X-rays can interfere in techniques which rely on the collection of monochromatic X-ray radiation, e.g. X-ray diffraction.

2.3.2 Diffraction of X-rays by crystals[3]

Bragg's law is a mathematical construct describing the interference pattern generated by X-rays interfering constructively after scattering by a crystal, although it does not reflect what is actually going on. According to the mathematical construct (Figure 2.3), when an X-ray beam enters a crystal, the angle between the incident beam, I, and the lattice planes in the crystal is termed theta, θ. X-rays which reach lower lattice levels of a crystal structure travel a greater distance (shown as AB + BA in Figure 2.3), known as the path difference. From trigonometry, the path difference can be written as 2 *d* sin θ, and for total constructive interference to happen it has to be an integer multiple of the wavelength of the X-ray beam

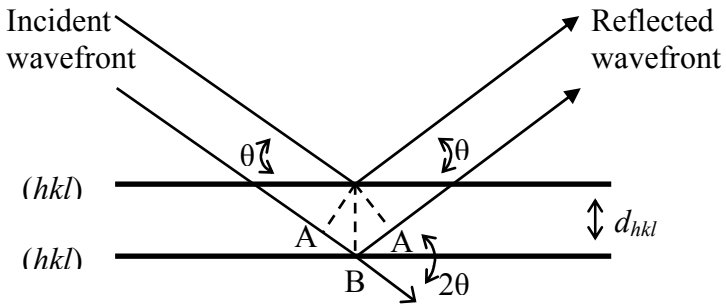

$$AB = d \sin \theta$$

$$\text{Total path difference} = 2AB = 2d \sin \theta$$

$$\text{For constructive interference } 2AB = n\lambda = 2d \sin \theta$$

Figure 2.3 *- Derivation of Bragg's Law from consideration of two parallel 'reflecting' X-ray beams.*

Bragg's Law can therefore be written as in Equation 2.1:

$$n\lambda = 2d \sin \theta$$

Equation 2.1 *– Bragg's Law.*

The intensity of reflection varies, and gets weaker as sin θ/λ increases (higher scattering angles). At low scattering angles, the X-rays produced are more likely to be of a similar phase to the non-scattered X-ray beam. At higher scattering angles, interaction of the X-ray beam with electrons at opposing sides of the atom can result in the generated X-rays having a path difference, principally due to the size of the atom. Therefore, greater destructive interference takes place, resulting in a decrease in the intensity of the X-rays at higher scattering angles.

2.3.3 X-ray powder diffraction[3]

All of the samples analysed in this thesis are polycrystalline powders – i.e. made up of many tiny crystallites too small to be analysed by single crystal methods. A small amount of powder placed in an X-ray beam contains many crystallites at a random orientation to the beam. Therefore, for a set of (*hkl*) planes a diffraction beam exists in all possible orientations. This produces a cone around the direct beam, the surface of which is formed by the accumulation of all of the diffracted beams for a set of planes. The diffraction maxima are spread into concentric rings on the surface of the cone.

In a typical X-ray powder diffractometer, the diffracted X-rays are recorded by a detector scanning through an arc from $2\theta = 1 - 3^{\circ}$ up to 90° (Figure 2.4). The ring base of each diffraction cone is traversed once, and is recorded as a peak in the diffractogram (Figure 2.5). The height (intensity) of the peak reflects the intensity (brightness) of the ring that would be observed if photographic film had been used for the data collection. Therefore, powder X-ray diffractograms represent 3-D information on a 2-D scale and information can be lost due to summing of intensities and peak overlap.

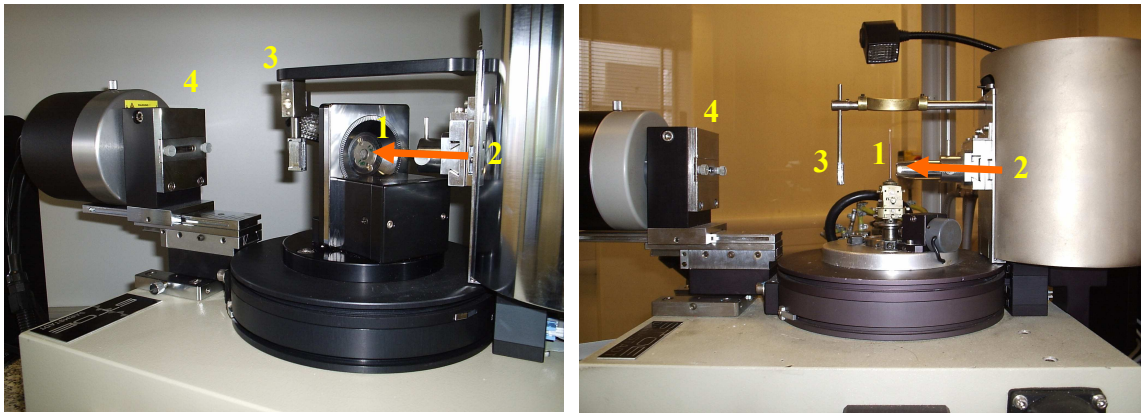

(a) (b)

Figure 2.4 *- Two of the X-ray powder diffractometer setups used in this work: (a) for thin film discs, and (b) for glass capillaries. (1 – sample holder, 2 – X-ray source, 3 – beam stop, 4 – detector. Orange arrow indicates direction of X-ray beam).*

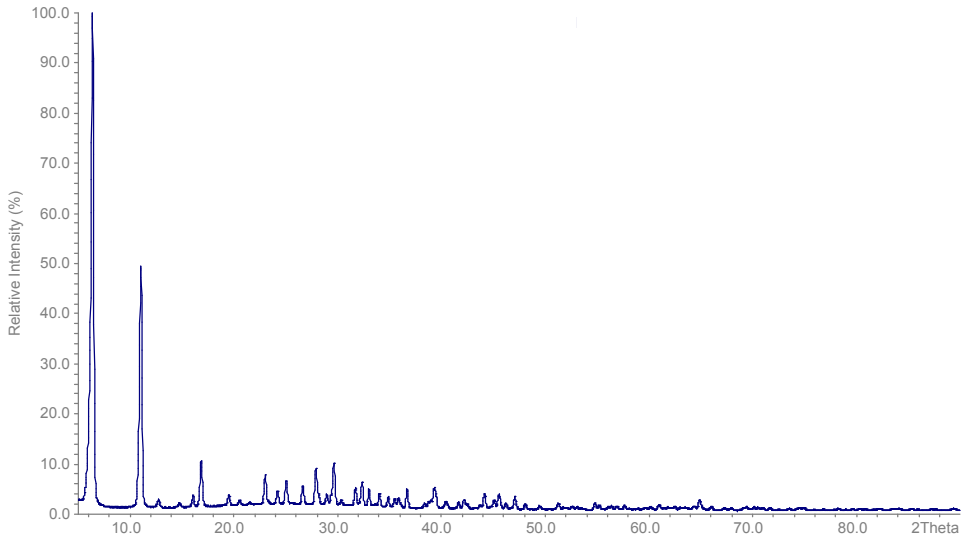

Figure 2.5 *– X-ray powder diffractogram of Ni STA-12 in a glass capillary (Cu K_α radiation).*

2.3.4 Structure solution using X-ray powder diffraction[1]

Computer programs, such as DICVOL91[4], are used to index the positions of the peaks, providing information on the crystal system and unit cell parameters. An inspection of the indexing identifies likely space groups from systematic absences, and this information is input into computer program suites, such as EXPO2004,[5]

which use statistical *ab initio* methods to produce model crystal structures (known as direct methods).

The unit cell parameters of the model structures are refined mathematically (Rietveld refinement) against the measured data, using program suites such as GSAS.[6] Using the model structure, the intensity, y_{io}, observed at a certain 2θ angle in the powder X-ray pattern can be compared with the calculated intensity, y_{ic}, from the model. The difference between the observed and calculated intensities can be refined using a least squares process, where the standard deviations due to the peak profiles and the background taken into account. Several parameters can be adjusted by refinement, including the unit cell, atomic coordinates and thermal oscillations of the atoms.

In Rietveld refinement, an accurate model for the reflection profile function ($G(\Delta\theta_{ik})$ is very important. The shape of a powder diffraction peak depends on a number of parameters, including the radiation source, the wavelength distribution in the X-ray beam and the detector system. Several functions can be used to describe the peak shape, including Gaussian, Lorentzian and pseudo-Voigt, and a combination of the functions describes all the peaks in the powder pattern. The background is usually due to diffuse and incoherent scattering and electronic noise from the detector system. The variation of the background with 2θ angle is defined by refinement of the coefficients of a power series.

For a refinement to be undertaken the parameters due to the peak profile, background, unit cell, atomic coordinates and thermal oscillations of the atoms are input into GSAS,[6] along with a standard instrument profile curve. The differences between the measured powder diffraction pattern and the calculated pattern from the model structure are minimised by refining all of the parameters. The atomic coordinates are refined by allowing the *x*, *y*, *z* positions to move, often with restraints to ensure chemically reasonable distances and angles.

The agreement between the observed and calculated patterns is estimated by several indicators, especially R_p and R_{wp} (expressed as percentages). R_p is a measure of the exact fit of the profile of the calculated powder pattern to the measured powder pattern, while R_{wp} measures the difference in the profiles, weighted according to standard deviations of the calculated error. The model structure sometimes does not include all of the electron density measured by the diffraction experiment, and the missing electron density can be found using Fourier mapping. The highest intensity peaks produced in the Fourier map can be added as atomic positions in the model

structure and refined, allowing for the difference in the profiles to be minimised further.

In the work undertaken in this thesis, the data from the STA-12 structures synthesised with Mn, Co and Fe were refined against the published model for Ni STA-12. The unit cell, background and peak profiles were the only parameters that were refined, and the atomic coordinates were not allowed to move. The results of the refinements could then allow for comparisons to indicate if STA-12 had been successfully synthesised for Co, Fe and Mn, and also how the unit cell parameters changed (lengths *a*, *b*, *c* and unit cell volume). An example of a final Refinement plot is shown in Figure 2.6.

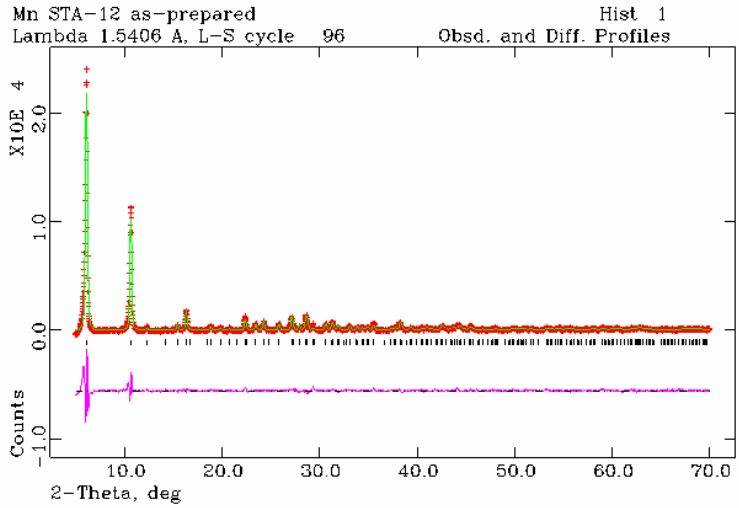

Figure 2.6 *– Rietveld refinement of Mn STA-12 using model for Ni STA-12(Cu K_α radiation) – red: measured pattern, green: calculated pattern, purple: difference between measured and calculated patterns (R_{wp} = 11.25 %).*

2.3.5 Phase identification using X-ray powder diffraction

In this work, X-ray powder diffraction has been used in two ways to help identify phases via comparison to previously published crystal structures. The STA-12 data was refined against the unit cell parameters for Ni STA-12, using the GSAS program suite (as described above).[6] The other way that phases have been identified has been by direct comparison to theoretical patterns produced by Stöe X-ray diffraction software,[7]or Diamond 3 crystal visualisation software.[8] The unit cell parameters,

space group and *x*, *y*, *z* atomic positions of the published structure are input into the programs, and the generated powder diffractogram peak positions are compared to the measured data (Figure 2.7).

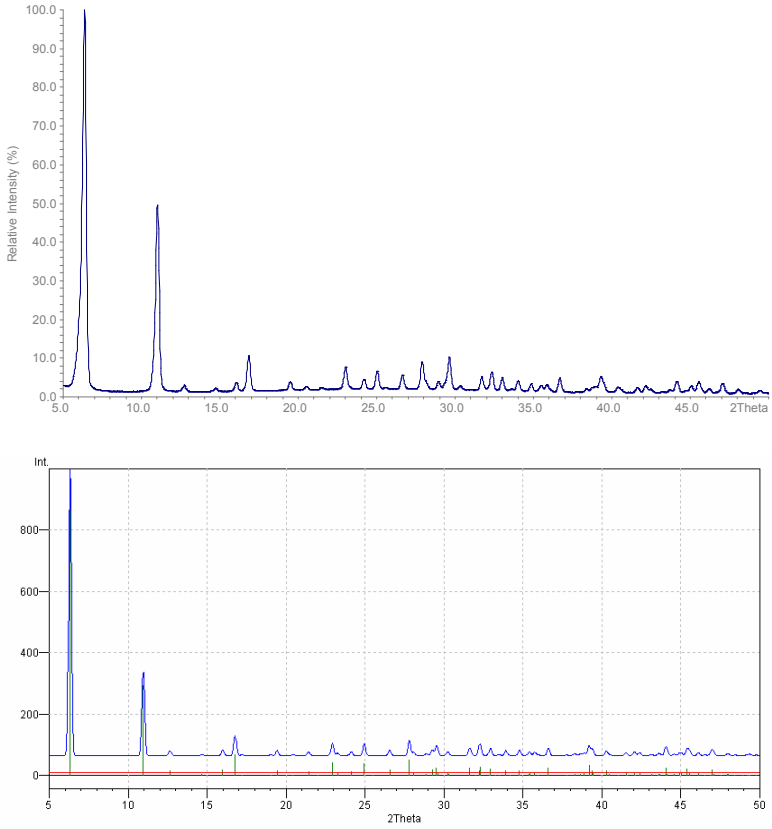

***Figure 2.7** – Comparison between measured powder diffraction pattern for Ni STA-12 (top) and theoretical powder diffraction pattern for Ni STA-12 generated by Diamond 3 software [8] (bottom) over 5 – 50° 2θ range.*

Both Fe and Co are transition metals that suffer from significant amounts of fluorescence when Cu is used as the X-ray target (mentioned in Section 2.3.2). This causes a high background intensity and poor peak resolution in the powder diffractograms. Therefore, for Fe and Co STA-12, Fe K_α radiation has been employed instead of Cu K_α radiation. The wavelength of Fe K_α X-rays are 1.9361 Å, compared to 1.5406 Å for Cu K_α X-rays. The longer wavelength means the large numbers of secondary X-rays generated near the absorption edge when Cu K_α is used are not produced. Therefore, the background intensity is lower and the signal-to-noise ratio is improved.

2.4 Gas and Vapour Adsorption[9]

2.4.1 Introduction

The measurement of the adsorption (and desorption) of gases and vapours is widely used to determine the surface area, pore volume and pore size distribution of porous solids.[10] The use of selected molecules can also provide information on the pore connectivity and surface chemistry. Adsorption is performed at a constant temperature while the pressure is varied, and there are two different ways in which the gas or vapour adsorption can be measured:

1) Volumetrically – the amount of adsorption is inferred from pressure measurements made before and after the measurement.

2) Gravimetrically – the sample is weighed as the pressure of the adsorbate is increased. The increase in the weight of the sample is correlated to the uptake.

The uptake of gas can be expressed as an equivalent volume at standard pressure, as a true volume or mass, or as moles per gram. This is plotted against the equilibrium pressure (p/p_o) at a constant temperature, and the plot is an isotherm of the adsorbate uptake. The work of Brunauer *et al.* resulted in a classification scheme for isotherms, with the identification of five basic types (Figure 2.8).[11]

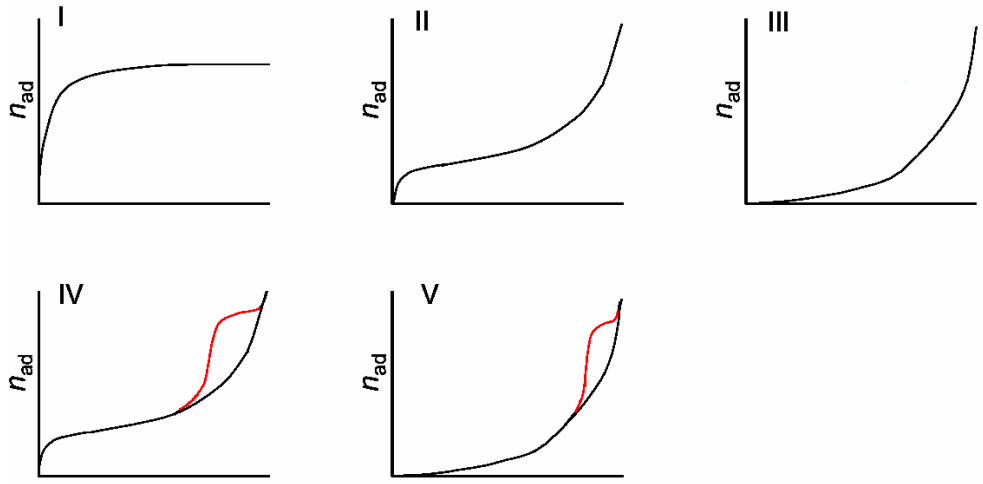

Figure 2.8 *– The Brunauer classification of the five types of adsorption isotherms.*[11] *Red lines indicate desorption hysteresis loops for Types IV and V.*

Type I, or Langmuir, isotherms, are typical of microporous solids, and are characterised by a rapid rise in the volume adsorbed at low pressures, corresponding to monolayer adsorption. This is followed by a plateau governed by the total pore volume, interpreted as filling of the micropores. Any gradual increase in adsorption at high partial pressures can be attributed to multilayer coverage of the external surfaces (Figure 2.9).

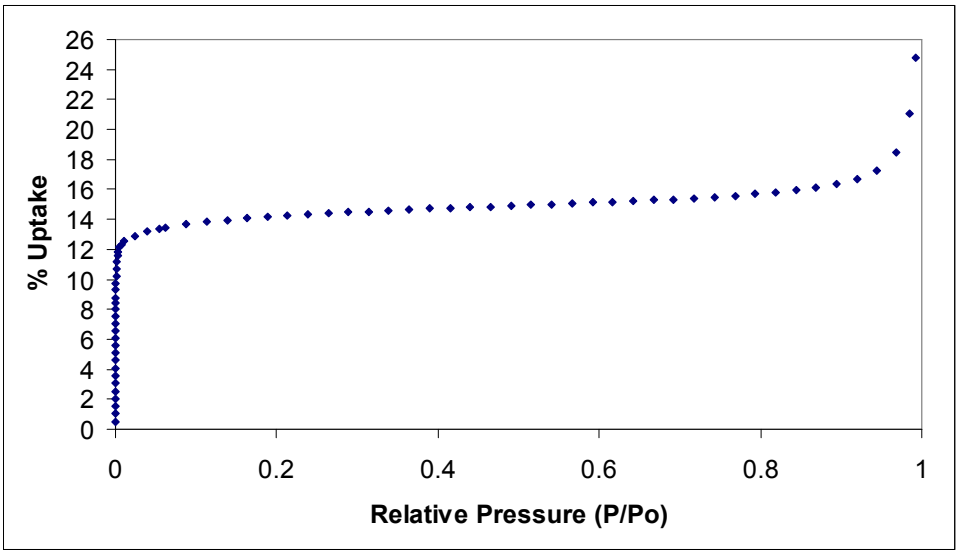

Figure 2.9 *– Experimental N_2 adsorption isotherm at 77K for microporous Ni STA-12 – note classic Type I isotherm shape, and increased uptake at higher pressures due to multilayer coverage of external surfaces of particles. Measured volumetrically.*

Type II and III isotherms are characteristic of multilayer adsorption onto open surfaces. In the case of Type II isotherms there is more affinity for the surface, resulting in Type I behaviour at lower pressures. In Type III isotherms, there is a greater affinity for adsorbate interactions, and uptake is not observed until higher pressure.

Type IV and V isotherms are characteristic of porous systems demonstrating both multilayer adsorption and capillary condensation, resulting in a steep adsorption slope at high pressures. Mesoporous solids, which are outside the scope of this work, normally exhibit Type IV isotherms. The initial monolayer coverage is built on at higher pressures, as the pore system is of sufficient diameter that multilayer adsorption happens before capillary condensation.

2.4.2 Determination of specific surface area and porosity

One of the most common methods used for obtaining specific surface areas of samples from N_2 adsorption data is the Brunauer-Emmet-Teller (BET) equation.[9] The equation is applicable to multilayer adsorption in Type II isotherms, and in the lower pressure regions of Type IV isotherms. The BET theory models an even monolayer on the adsorbent surface, and subsequent formation of multilayers onto the initially formed monolayer.[12] There are several assumptions in BET theory which can result in movement away from ideal Langmuir adsorption for microporous materials, such as the heats of formation for the multilayers are the same, and that there are no lateral interactions between the adsorbed species. Therefore, BET theory is not generally believed to be a good model for adsorption on microporous materials.

The pore volume is a measure of the free space in the crystalline framework seen by the adsorbate, and is taken to be a better estimation for the porosity of microporous materials. The pore volumes in $cm^{-3}g^{-1}$ can be calculated, using the BJH method,[9] from the quantity adsorbed. In order to obtain as accurate results as possible a gas with as small a quadrupole as possible is used.

2.4.3 Differential heats of adsorption – microcalorimetry[9, 13]

The adsorption of molecules onto a solid surface is an exothermic process. The magnitude and variation, as a function of adsorbate coverage, of the heat evolved can reveal information about the type of bonding between the adsorbate and the surface. It can also indicate if there are any lateral interactions between the adsorbed species. Heats of adsorption are determined using calorimetric methods, involving determining the heat evolved when a known amount of adsorbate is adsorbed (usually by measuring the temperature rise in the solid). The heat of adsorption at a constant volume can be expressed as in Equation 2.2.

$$q_i = (Q_i/n)_v$$

Equation 2.2 *– Heat of adsorption – Q_i = heat evolved, n = number of moles of adsorbate adsorbed.*

If this process is repeated as the amount of adsorbate is varied, a graph can be plotted of Q_i versus n at a constant temperature and volume. The gradient (Equation 2.3) of the plot is the differential heat of adsorption, which measures the variation in the heat of adsorption with the amount of adsorbed species.

$$q_D = (\delta Q_i/\delta n)_{V,\,T}$$

Equation 2.3 *– Calculation of differential heats of adsorption.*

Gas adsorption microcalorimetry at 77 K can be used to characterise adsorption sites, and in conjunction with model adsorbents (such as zeolites) can be used to study the mechanisms and phenomena taking place during adsorption. At ambient temperatures, microcalorimetry can be directly related to the adsorption behaviour taking place in applications such as gas storage and separation. In this work, it has been used to characterise the low temperature adsorption of H_2 and CO, and ambient temperature adsorption of CO_2 and CH_4 onto STA-12 (see Chapter 5).

2.5 Solid State Infra-red (IR) spectroscopy

2.5.1 Vibrating diatomic molecules[14]

When two atoms combine to form a covalent diatomic molecule there is a balancing of forces. The two atoms settle at a mean internuclear distance so the forces are just balanced and the energy of the whole system is at a minimum. If the atoms are moved closer together the repulsive forces increase rapidly, and attempting to move the atoms further apart is resisted by the attractive force.

Changes in the vibrational quantum number give rise to a spectrum if the vibration interacts with radiation. For example, for Infra-red spectroscopy the requirement is that a change in the dipole moment of the molecule must occur for a spectrum to be produced. This means gas phase Infra-red spectra will only be observed with heteronuclear diatomic molecules, as homonuclear diatomic molecules have no change of dipole moment on vibration. This is not true if a homonuclear diatomic molecule is adsorbed on a surface. Interaction with a surface can result in polarisation and a dipole being induced, and vibrations becoming Infra-red active.

Real diatomic molecules do not obey the laws of simple harmonic motion described by Hooke's law, as when the bond is stretched there is a point where it breaks and dissociates. For small compressions and extensions the bond is perfectly elastic, but for larger amplitudes (greater than 10% of the bond length) a more complicated behaviour takes place, known as anharmonic motion (Figure 2.10).

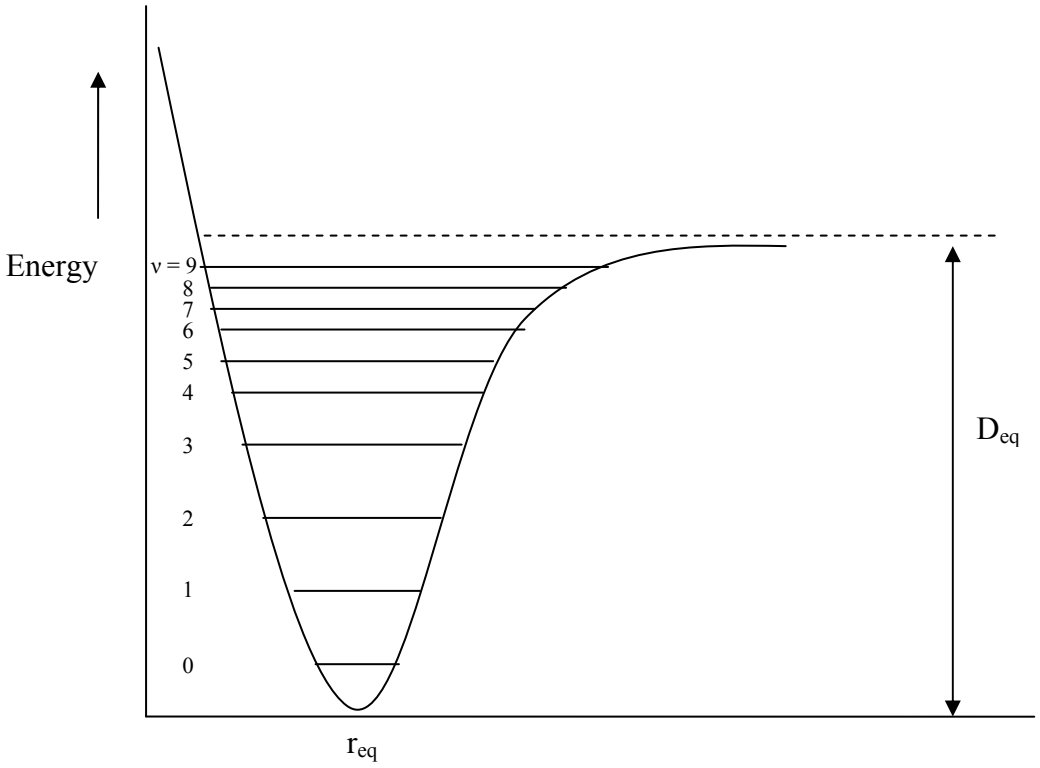

Figure 2.10 *– The Morse curve – the energy of a diatomic molecule undergoing anharmonic extensions and compressions. Lowest energy level, υ = 0, has some energy.* D_{eq} *is the bond dissociation energy and* r_{eq} *is the zero energy state.*

The selection rules for the anharmonic oscillator, $\Delta\upsilon = \pm 1, \pm 2, \pm 3 \ldots$, result in decreasing differences between the energy levels. The jumps between energy levels are of rapidly reducing probability, and normally only the lines where $\Delta\upsilon = \pm 1, \pm 2, \pm 3$, at the most, have observable intensity. The spacing between the vibrational levels is of the order of 10^3 cm^{-1}, and the population of the $\upsilon = 1$ state is only 1 % of the ground state population at room temperature. Therefore, transitions originating at $\upsilon = 1$ can be discounted, and only transitions from $\upsilon = 0 \rightarrow \upsilon = 1$ (very large intensity), $\upsilon = 0 \rightarrow \upsilon = 2$ (small intensity) and $\upsilon = 0 \rightarrow \upsilon = 3$ (negligible intensity) need to be considered. The $\upsilon = 0 \rightarrow \upsilon = 1$ transition is known as the fundamental absorption,

while the $\upsilon = 0 \rightarrow \upsilon = 2$ and $\upsilon = 0 \rightarrow \upsilon = 3$ transitions are the first and second overtones respectively. In this work only the fundamental absorptions are analysed for the probe molecules used.

2.5.2 Vibrations of polyatomic molecules[14]

In a molecule containing N atoms, the positions of the atoms are constrained by specifying three coordinates, for example *x*, *y* and *z*. The total number of coordinate values is 3N, meaning the molecule has 3N degrees of freedom. When the 3N coordinates are fixed, the bond angles and distances are fixed as well and no other specifications are needed.

The molecule is free to move in space without changing shape. This translational movement uses three of the 3N degrees of freedom, leaving 3N - 3. The rotation of a non-linear molecule can also be resolved into three perpendicular axes, requiring three degrees of freedom. Therefore, the molecule is left with 3N - 6 degrees of rotational freedom. The molecules also have internal vibrations, so a non-linear N-atomic molecule will have 3N - 6 fundamental vibrations. If the molecule is linear there is no rotation about the bond axis, so only two degrees of rotational freedom are required. Therefore, there are 3N – 5 fundamental vibrations present in a linear polyatomic molecule.

As a linear N-atomic molecule has N - 1 bonds between the atoms, N - 1 of the vibrations are bond-stretching motions, while the other 2N - 5 (non-linear) or 2N – 4 (linear) vibrations are bending motions. In a diatomic molecule N = 2, the linear degrees of freedom present are 3N - 5 = 1 and only one fundamental vibration is present. Water is a non-linear triatomic molecule, and Figure 2.11 shows the structure and the 3N - 6 allowed vibrational modes with arrows indicating the motion during half of the vibration.

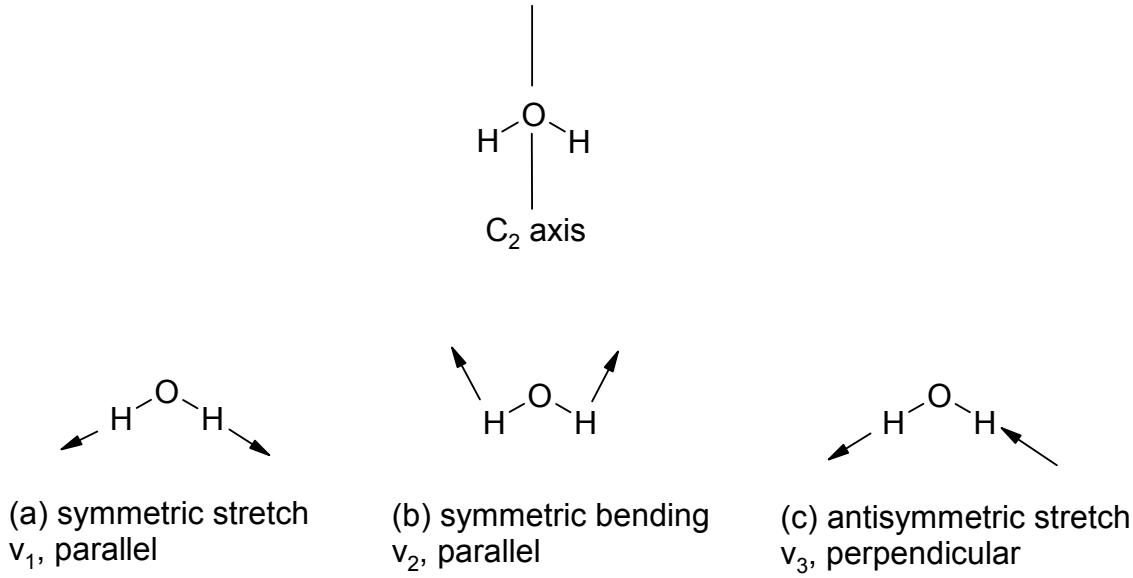

Figure 2.11 *– Structure and symmetry of H_2O, with the three allowed vibrational modes outlined.*

In order for the vibrational modes to be Infra-red active there has to be a dipole change, which must take place along the line of a symmetry axis (parallel, or $\parallel$) or at right angles to the line (perpendicular, or $\perp$). The allowed vibrations are labelled υ_1, υ_2 and υ_3, and this convention is used to label vibrations in decreasing frequency within their symmetry type. The symmetric vibrations of H_2O are labelled υ_1 for the highest fully symmetric frequency (3650 cm^{-1}) and υ_2 for the next highest (1590 cm^{-1}); the antisymmetric vibration is labelled υ_3 (3750 cm^{-1}). The bending vibrations are also termed as δ modes.

In this work, the Infra-red spectra of several different small polyatomic molecules (H_2, CO, CO_2, CH_3CN, CH_3OH and H_2O) adsorbed onto the STA-12 framework have been analysed. Each of these molecules has several possible vibrations under the selection rules that can result in dipole changes, and the vibrations and the associated frequencies are outlined in Table 2.3.

Table 2.3 *– Fundamental vibrations and resulting Infra-red frequencies for small polyatomic molecules. Vibrations outlined by asterisks (*) are IR inactive in the absence of a dipole (which can be induced by adsorption onto a surface).*

Molecule	ν_1	ν_2	ν_3
H_2	4060 cm^{-1} (not IR active)*	-	-
CO	2140 cm^{-1}	-	-
H_2O	3650 cm^{-1} ($\parallel$)	1590 cm^{-1} ($\parallel$, δ mode)	3750 cm^{-1} ($\perp$)
CO_2	1330 cm^{-1} ($\parallel$, not IR active)*	667 cm^{-1} ($\perp$, δ mode)	2349 cm^{-1}($\parallel$)

CH_3CN and CH_3OH both obey the 3N-6 selection rule. Therefore, there are 12 vibrational degrees of freedom present in each molecule, making the IR spectra quite complicated. Looking at the adsorption of these molecules onto a surface, only some of the fundamental vibrations are important. For CH_3CN this is the vibration of C≡N (2260 cm^{-1}), while for CH_3OH both the vibrations (3600 - 3200 cm^{-1} and 2800 - 2400 cm^{-1}, depending on the amount of hydrogen-bonding present) and bending (1600 cm^{-1}) of O-H, and the vibrations of C-H (3200 - 2800 cm^{-1}) are important.

2.5.3 Combinations of vibrations in polyatomic molecules

In polyatomic molecules, some of the vibrational states can have similar frequencies. If the vibrations are related by symmetry, peaks in IR spectra can split due to accidental degeneracy.[15-17] This effect is known as Fermi resonance, and can introduce complexity into an Infra-red spectra. As stated in Section 2.5.2, the spectrum of CH_3CN is complex, and it can be difficult to assign vibrations to bands in the ν(C≡N) wavenumber range. Use of the deuterated form of acetonitrile, CD_3CN, reduces the complexity by removing the Fermi resonance effects from interaction of

ν(C≡N) with ν(C-C) and δ(C-H), making it easier to assign vibrations due to ν(C≡N) in spectra of adsorbed molecules.[15]

These effects can also be seen in the spectra produced by polyatomic molecules with significant hydrogen bonding present.[15, 17] In the case of water, the interaction with adsorption sites can produce an interesting effect explained by Evans.[18] When a large amount of water is present, hydrogen bonding can result in a sharp fundamental vibrational frequency resonating with an overtone frequency (example in Figure 2.12). As the overtone has a low intensity compared to the fundamental, Fermi resonance interaction results in a minimum forming at the frequency of the fundamental vibration. The intensity of this missing band is redistributed on both sides of the minimum, creating two equally spaced maxima that are the same intensity as one another. This is observed at medium coverage of water on Ni STA-12, with the appearance of bands at 3100 cm^{-1} and 3400 cm^{-1} resulting from the interaction of two δ(OH) modes, due to the formation of a hydrogen bonded network of water (see Chapter 4).

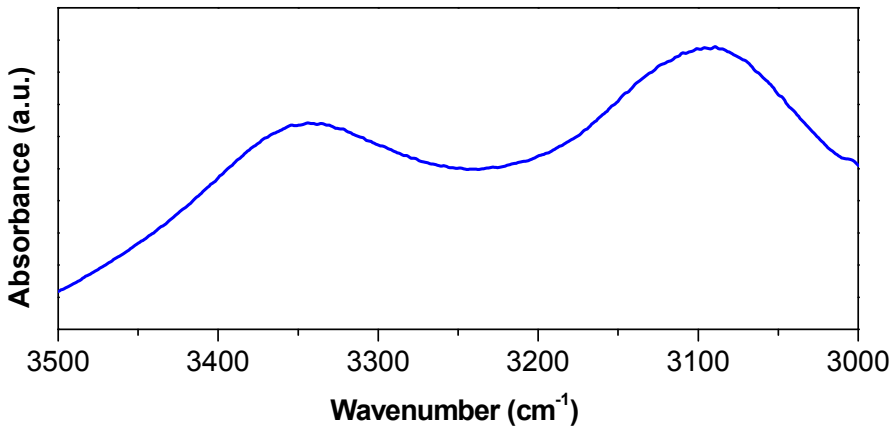

Figure 2.12 *– 3500 – 3000 cm^{-1} region of Infra-red spectrum of medium coverage of water on Ni STA-12. Identical intensity bands at 3100 and 3400 cm^{-1} due to Evans window formation from Fermi resonance of δ(OH) modes,.*

2.5.4 Solid State Fourier Transform Infra-red Spectroscopy

Infra-red spectroscopy of adsorbed molecules is widely used in the characterisation of active sites on the surfaces of heterogeneous catalysts.[19] The Infra-red spectra of adsorbed molecules are different from those produced for free molecules.[20] Adsorbed molecules cannot rotate, meaning only vibrational states can be present. This reduces the complexity of the spectra, and means no rotational overtones are present. The adsorption of molecules can also result in dipoles being induced in homonuclear diatomic molecules due to polarisation. This means these molecules, such as H_2, become IR active, and information can be obtained about their interaction with adsorption sites.

Many of the probe molecules used for Infra-red spectroscopy interact strongly with the adsorption sites, resulting in significant changes to the sites.[19] This can result in the production of complex spectra which are hard to interpret and understand. In reality, an ideal probe molecule for adsorption should be characterised by as low as possible adsorption enthalpy (ΔH). The equilibrium between molecules in the gas phase and in the adsorbed state is driven by the Gibbs free energy ($\Delta G = \Delta H - T\Delta S$), and adsorbed states require a decrease in the entropy of the system relative to the gas phase. For a significant fraction of the molecules to be present in the adsorbed state, the entropy has to be minimised by low enough temperatures. To observe an adsorption process characterised by an adsorption enthalpy ΔH, the experiment(s) have to be performed at a temperature T, so $T\Delta S$ is as small as possible.

Some of the probe molecules need temperatures in the range of liquid helium (especially H_2) in order for the entropic term to be small enough. For a long time, though, the lowest temperature at which adsorption IR experiments could be performed was limited to 77 K (temperature of liquid nitrogen). This was due to an incompatibility between the high temperatures needed to activate the samples and the materials needed to produce very low temperatures down to that of liquid helium. This has been solved in experimental setups where the activation and cryogenic experiments are contained within the equipment. The sample is moved, using a magnetic manipulator, from an activation oven to an IR cell modified *adhoc* to allow for dosing of controlled amounts of gas at temperatures down to 20 K. A more detailed description of this experimental setup is contained elsewhere.[21]

As mentioned previously, in this work the Infra-red spectra of several different small polyatomic molecules adsorbed onto the STA-12 framework have been analysed. H_2 (Figure 2.13) and CO were adsorbed using the cryogenic temperature experimental setup, while CO_2, CH_3CN, CH_3OH and H_2O were adsorbed at ambient temperature. This allows for an in depth characterisation of the dehydration of STA-12 (Chapter 4), and the adsorption sites present in STA-12 at both low and ambient temperatures (Chapter 5).

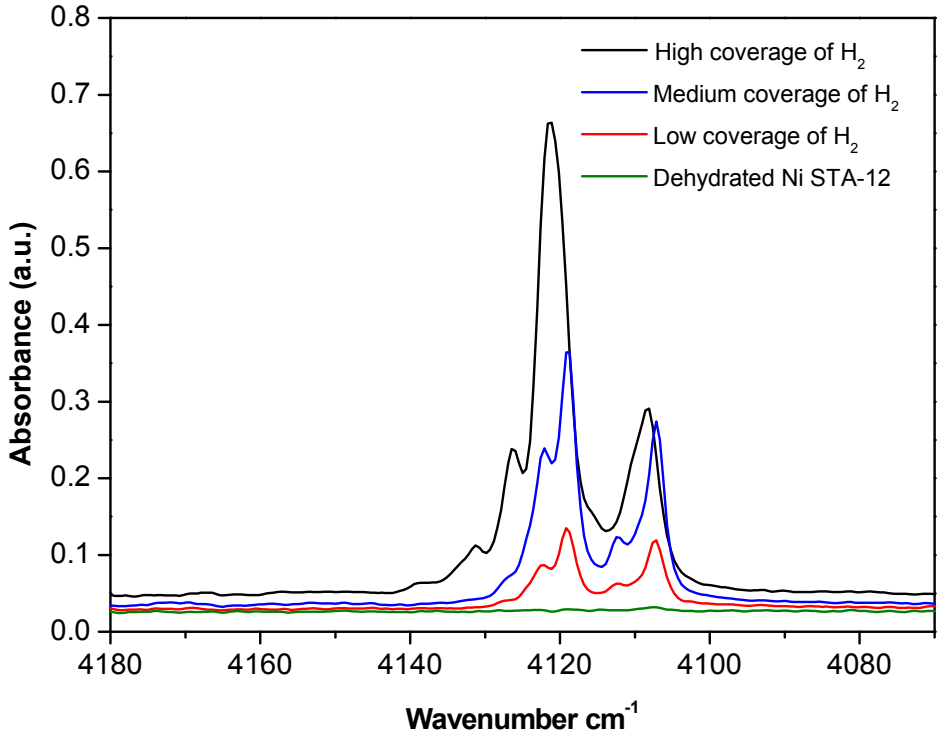

Figure 2.13 *– Hydrogen adsorption Infra-red spectra at 15 K on Ni STA-12. Note the presence of peaks, which is due to induced dipoles making H_2 IR active. In depth explanation of spectra in Chapter 5.*

2.6 Solid State UV-Visible (UV-vis) Spectroscopy

2.6.1 Background to UV-vis[22, 23]

The phosphonate frameworks synthesised in this work incorporate transition metals, and exhibit vivid colours (see Chapter 4). The observed colours can be misleading for a number of reasons, for example due to particle size. Therefore, UV-vis spectroscopy

has been employed to help characterise the colours and give insights into the coordination environments surrounding the metal cations.

The transitions of electrons between the outermost energy levels of an atom have energy changes in the range of $10^4 – 10^5$ cm^{-1} (or $10^2 – 10^3$ kJ mol^{-1}). The ranges of energies are associated with the near IR, visible and UV areas of the electromagnetic spectrum. Several types of energy transition can take place, the most important for transition metal complexes being:

1) Transition of an electron from a lower to a higher localised orbital on the same atom. Examples include *d-d* and *f-f* transitions in transition metals. These are often formally spin not allowed, and are associated with weak colours.

2) Transition of an electron from a localised orbital on one atom to a higher energy localised orbital on an adjacent atom, known as *charge transfer*. These transitions are normally spin allowed, and are associated with intense adsorption bands and strong colours.

A typical reflectance UV-vis spectrum for Ni STA-12 is shown in Figure 2.14, and two principal features can be noted. Above 35000 cm^{-1} there is a very intense adsorption, known as the adsorption edge. This can take place due to charge transfer transitions, and can place a high frequency limit on the spectral range. The other feature of the spectrum is the presence of broad bands at lower wavenumber, associated with *d-d* transitions.

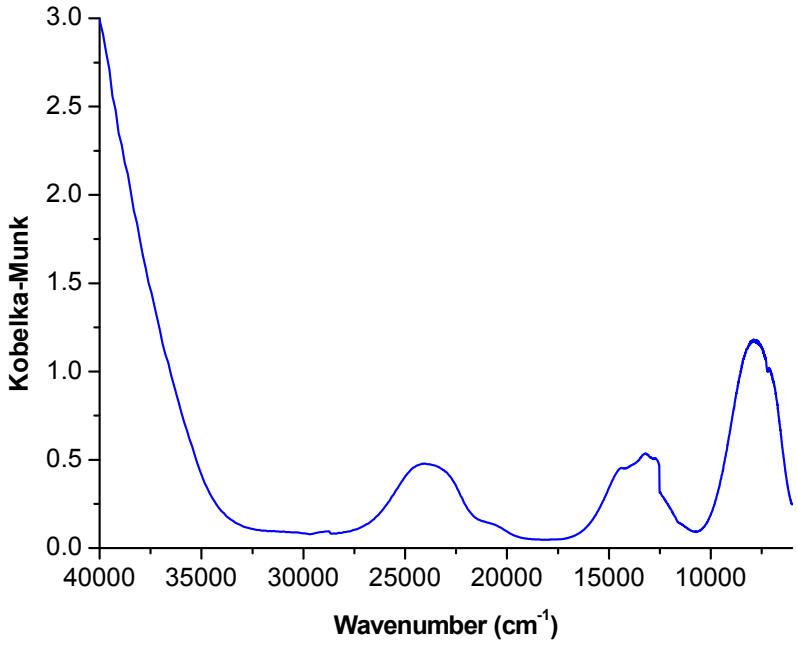

Figure 2.14 *– Diffuse Reflectance UV-vis-NIR spectrum of Ni STA-12. Collected using a Varian Carey 5 spectrophotometer with a reflectance sphere.*

2.6.2 Analysis using UV-vis spectroscopy

One of the main uses of UV-vis spectroscopy is for analysis of the coordination sphere of atoms. Using the example of hydrated Ni STA-12, Ni^{2+} is present in the framework. The electron configuration is d^8, and this can be written as $t_{2g}^6 e_g^2$ (high spin ground state).[25] Electronic transitions in the *d*-orbitals when Ni^{2+} is in O_h coordination can be predicted using crystal field theory. For the hexaquo complex, three bands at 8600 cm^{-1} ($^3A_{2g}$ (F) → $^3T_{2g}$ (F)), 13500 cm^{-1} ($^3A_{2g}$ (F) → $^3T_{1g}$ (F)) and 25300 cm^{-1} ($^3A_{2g}$ (F) → $^3T_{1g}$ (P)) are present. Comparison of the values to the spectrum in Figure 2.14 indicates a reasonable match, with slight shifts in the band positions. It can therefore be concluded that Ni^{2+} is in octahedral coordination in hydrated Ni STA-12.

Analysis of the area beyond the adsorption edge in Figure 2.14 indicates the extinction coefficient of the transition is high due to charge transfer. From crystal field considerations, the transition will be due to electrons moving from atoms in the ligand to the Ni^{2+}. Therefore, the strong intensity can be related to the organic in the framework (Chapter 4).

2.7 Scanning Electron Microscopy (SEM) and Energy Dispersive X-ray Spectroscopy (EDX)[25]

Scanning Electron Microscopy (SEM) has been used in this thesis to investigate powder samples. A fine beam of electrons is scanned across the surface of a sample allowing an image to be created by analysis of secondary and backscattered electrons. Electrons can act as waves, with a wavelength (λ = 0.00251 nm) which is much shorter than visible light (λ = ~ 500 nm). This allows imaging on a very small scale; with a magnification of up to several thousand (Figure 2.15). SEM can be used to obtain information on sample morphology, surface profiles and micro structural arrangements. The electron beam does not pass through the sample, and information is obtained on the surface and the first few layers.

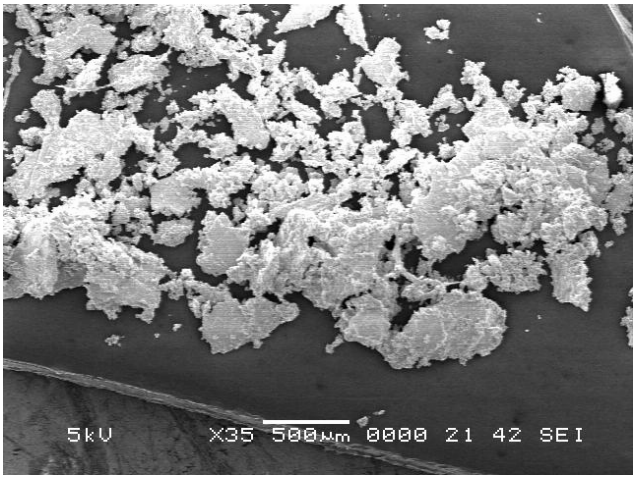

Figure 2.15 *– Scanning Electron Microscope image of a polycrystalline powder of Ni STA-12.*

The electron beam can also stimulate the emission of X-rays via a similar process as described in Figure 2.2. As the energy transitions are quantised, the X-rays produced have characteristic wavelengths dependent on the elements present in the sample. This means the spectrum of the emitted X-rays can be analysed to ascertain which elements are present.

EDX can be used to provide the local inorganic chemical compositions across a sample, with standards of known composition used to calibrate the relative amounts of each element present. Elemental ratios can be calculated from the results, and

insights gained into if doping of elements into structures has been successful (Chapter 3). An example of an EDX spectrum of Cr MIL-53 is shown in Figure 2.16. The spectrum indicates the elements present, and plots the output as intensity versus the energy of the pulses in keV. The results are converted using computer manipulation into a series of atomic and weight percents.

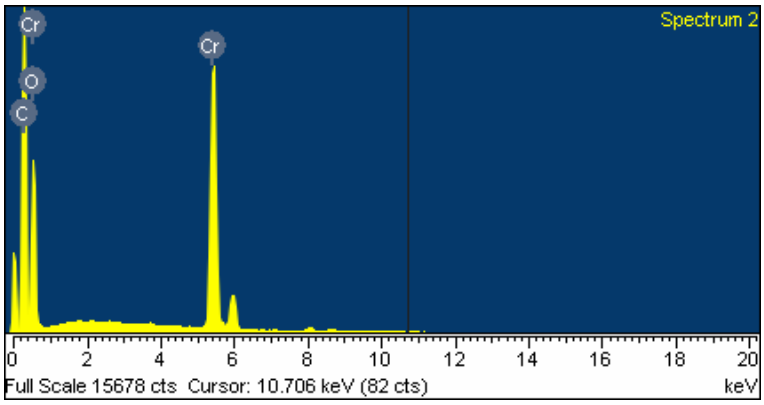

Figure 2.16 *– Example of a typical EDX spectrum for Cr MIL-53.*

2.8 Thermogravimetric Analysis[26]

Thermogravimetric Analysis (TGA) is used to analyse weight loss from samples, with the method involving the weight of the sample being monitored as the temperature increases under a controlled atmosphere of flowing gas. In this work, the weight loss from the synthesised MOF frameworks can be interpreted as the loss of water, solvents or occluded ligand(s) from the pores, and the profile of the thermogram has been used to calculate the amounts present in the as-synthesised structures. An example of the TGA analysis of MIL-100 is shown in Figure 2.17.

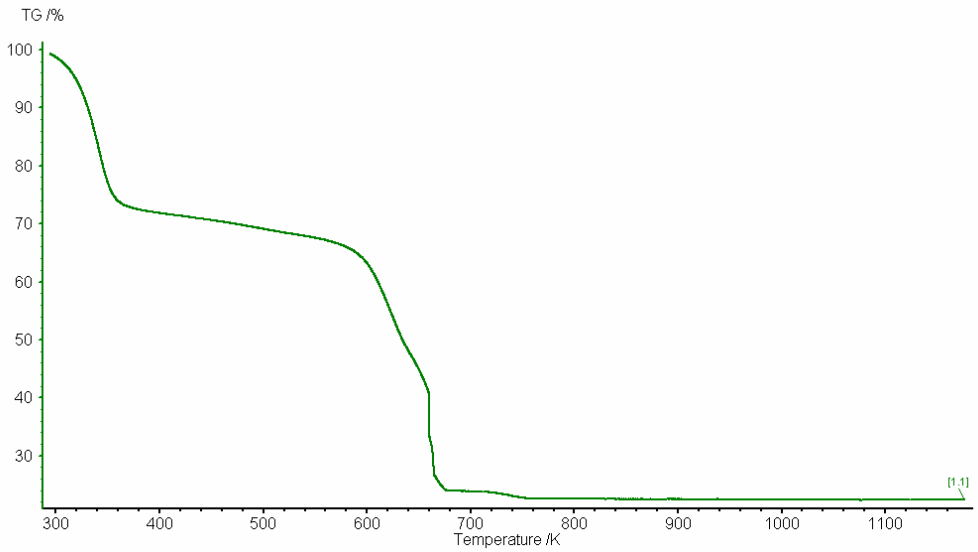

Figure 2.17 *- Thermogravimetric analysis of MIL-100 measured at 5K/min in air. The weight loss below 400 K is due to water from Cr metal sites, and the weight loss above 600 K is due to breakdown of the organic ligand.*

2.9 Organic Elemental Microanalysis

Elemental microanalysis is used to identify organic species present in samples, with percentages of carbon, hydrogen and nitrogen measured (errors ± 1 %). The results can indicate whether an organic ligand is present as part of a MOF structure, and in what ratio with the metal species.

2.10 References

1) C. Giacovazzo, H. L. Monacco, D. Viterloo, F. Scordari, G. Lulli, G. Zanotti and M. Catti, *Fundamentals of Crystallography*, *Oxford University Press,* 1992

2) C. Hammond, *The Basics of Crystallography and Diffraction*, *Oxford University Press*, 2006, **2nd ed.**

3) V. K. Pecharsky and P. Y. Zavalij, *Fundamentals of Powder Diffraction and Structural Characterisation of Materials*, *Springer*, 2005

4) A. Boultif and D. Louer, *J. Appl. Crystallogr.*, 1991, **24**, 987

5) A. Altomare, R. Caliandro, M. Camalli, C. Cuocci, C. Giacovazzo, A. Grazia, G. Moliterni and R. Rizzi, *J. Appl. Crystallogr.*, 2004, **37**, 1025

6) Bruker AXS ltd, TOPAS V3.0: General Profile and Structure Analysis Software for Powder Diffraction Data. 2004

7) WINXPOW, Stöe

8) Diamond 3 Crystal and Molecular Structure Visualisation, Crystal Impact

9) G. Attard and C. Barnes, *Surfaces*, *Oxford University Chemistry Primer 59*, *Oxford University Press*, 1998

10) K. Sing, *Colloids and Surfaces A*, 2001, **187 – 188**, 3

11) S. Braunauer, L. S. Deming, W. E. Deming and E. Teller, *J. Am. Chem. Soc.*, 1940, **62**, 1723

12) S. Braunauer, P. H. Emmett and E. Teller, *J. Am. Chem. Soc.*, 1938, **60**, 309

13) P. L. Llewellyn and G. Maurin, *C. R. Chemie*, 2005, **8**, 283

14) C. N. Banwell, *Fundamentals of Molecular Spectroscopy*, *McGraw-Hill Book Company*, 1972, 65

15) A. Zecchina, F. Geobaldo, G. Spoto, S. Bordiga, G. Ricchiardi, R. Buzzoni and G. Petrini, *J. Phys. Chem.*, 1996, **100**, 16584

16) A. Zecchina, G. Spoto and S. Bordiga, *Phys. Chem. Chem. Phys.*, 2005, **7**, 1627

17) D. A. Othen and O. Knop, *Can. J. Chem.*, 1975, **53**, 3837

18) J. C. Evans, *Spectrochim. Acta*, 1960, **16**, 994

19) G. Spoto, S. Bordiga, A. Zecchina, D. Cocina, E. N. Gribov, L. Regli, E. Groppo and C. Lamberti, *Catal. Today*, 2006, **113**, 65

20) E. Garrone and C. O. Arean, *Chem. Soc. Rev.*, 2005, **34**, 846

21) G. Spoto, E. N. Gribov, G. Ricchiardi, A. Damin, D. Scarano, S. Bordiga, C. Lamberti and A. Zecchina, *Prog. Surf. Sci.*, 2004, **76**, 71

22) A. K. Brisdon, *Inorganic Spectroscopic Methods*, *Oxford Chemistry Primer 62*, *Oxford University Press*, 2005

23) A. R. West, *Basic Solid State Chemistry*, *Wiley*, 1999, **2nd ed.**

24) T. M. Dunn, D. S. McClure and R. G. Pearson, *Some aspects of Crystal Field Theory*, *Harper*, 1965

25) P. J. Goodhew and F. J. Humphreys, *Electromicroscopy and Analysis*, *Taylor and Francis*, 1988, **2nd ed.**

26) F. W. Fifield and D. Kealey, *Principles and Practice of Analytical Chemistry*, *Blackie and Academic Professional*, 1990, **3rd ed.**

Chapter 3: Synthesis of MOFs

3.1 Introduction

In Chapter 1 an introduction to metal organic frameworks was presented, with emphasis on phosphonate materials. The syntheses undertaken for the structures studied in this thesis are outlined in this chapter. Both phosphonate and carboxylate MOFs have been synthesised and characterised, and they will be compared in possible applications later on in this thesis (Chapters 5 and 6).

3.2 Experimental and Characterisation Techniques

The reactions to synthesise MOFs were carried out via hydrothermal crystallisation from aqueous gels in 25ml Parr type Teflon lined steel autoclaves. Gels were prepared by mixing the starting materials before subsequent heating. After removal from the oven the products were filtered, washed with distilled water and dried at 323 K.

The samples were routinely examined by X-ray powder diffraction, using Stöe STAD i/p diffractometers operating using either monochromatic Cu $K_{\alpha 1}$ radiation (λ=1.5406 Å) or monochromatic Fe $K_{\alpha 1}$ radiation (λ=1.9361 Å). Rietveld refinement of STA-12 materials was undertaken with the GSAS program suite[1] using the cell parameters and atomic coordinates for as-prepared Ni STA-12 as the starting point.[2] The contents of carbon, hydrogen and nitrogen in the samples were measured by a Carlo Erba elemental analyser. The inorganic compositions (Metals, P and O) were examined semi-quantitatively by EDX using a JEOL-5600 SEM with an Oxford INCA Energy 200 EDX system. The EDX results were calibrated using known standards for each element.

Thermogravimetric analysis was conducted using a Netzsch TG209 thermogravimetric analyser. About 5 mg of sample was loaded into an alumina crucible and data collected from room temperature to 1173 K at a heating rate of 5 K min^{-1} in flowing air. The empty crucible was subjected to the same heating cycle, and the background trace was subtracted to give the final, corrected, data.

Nitrogen gas adsorption at 77 K was performed on about 50 mg of samples heated under vacuum. Isotherms were measured volumetrically using a Micromeritics ASAP 2020 surface area and pore analyser.

3.3 Synthesis of phosphonate ligands

The phosphonate ligands used in this thesis were synthesised using a modified Mannich reaction, outlined by Irani *et al.* in 1966.[3] The letter **R** represents the connection to the rest of the ligand molecule, which in this case is a piperazine ring (with or without methyl group functionalities). The reaction proceeds on both of the nitrogen atoms in the piperazine ring producing a N,N'-piperazinebis(methylenephosphonic acid) as shown below in Schemes 3.1 and 3.2.

$$\mathbf{R}_2\text{-NH} + CH_2O + HP(O)(OH)_2 \rightarrow \mathbf{R}_2\text{N-}CH_2\text{-}P(O)(OH)_2 + H_2$$

Scheme 3.1 *– Modified Mannich reaction.*

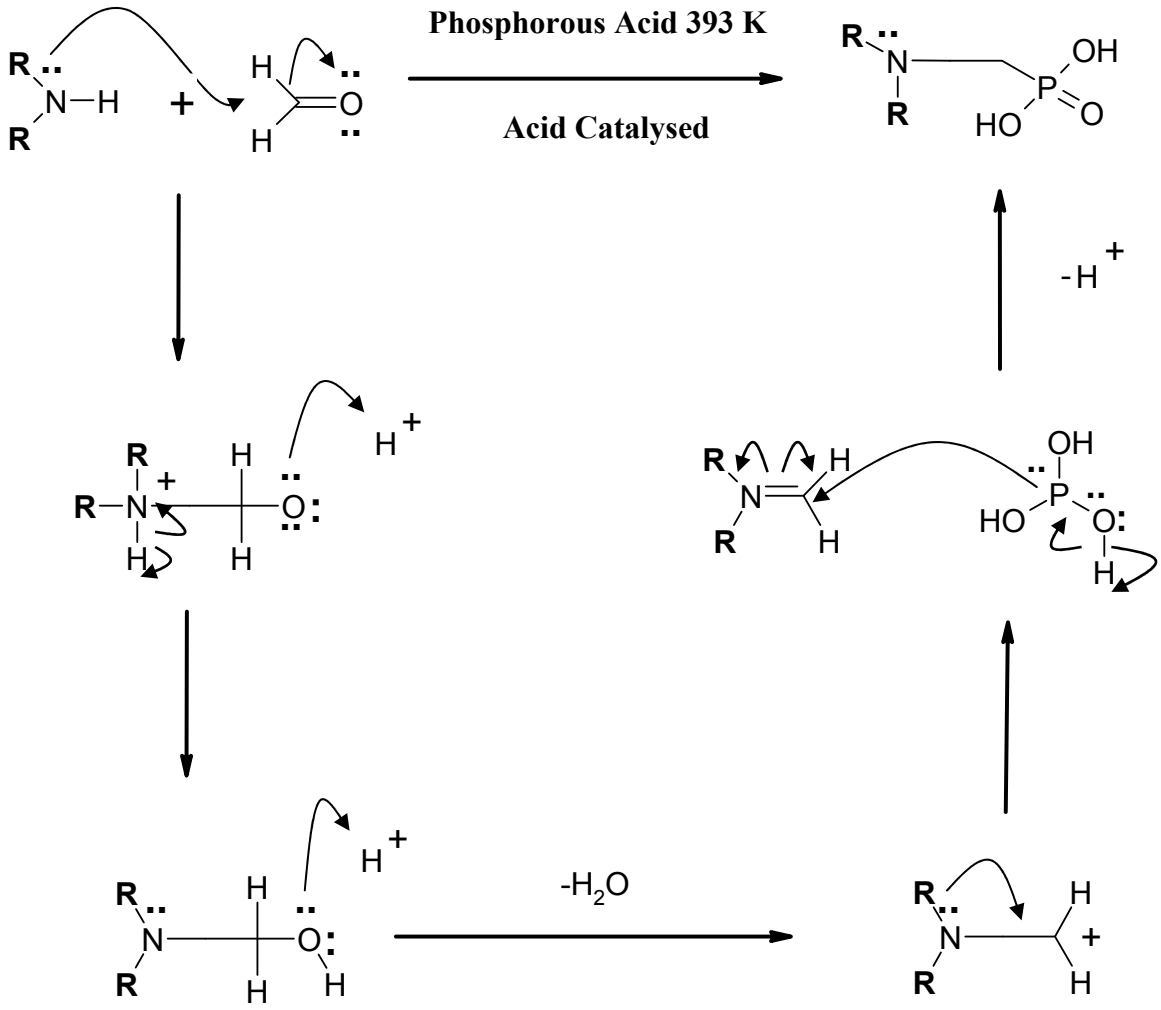

Scheme 3.2 *– Modified Mannich reaction mechanism, showing electron movements.*

The ligand molecules N,N'-piperazinebis(methylene phosphonic acid), and the racemic 2-methyl and 2,5-dimethyl derivatives were synthesised using this reaction. Respectively they are termed H_4L, H_4L-Me and H_4L 2,5-diMe (structures shown below in Figure 3.1).

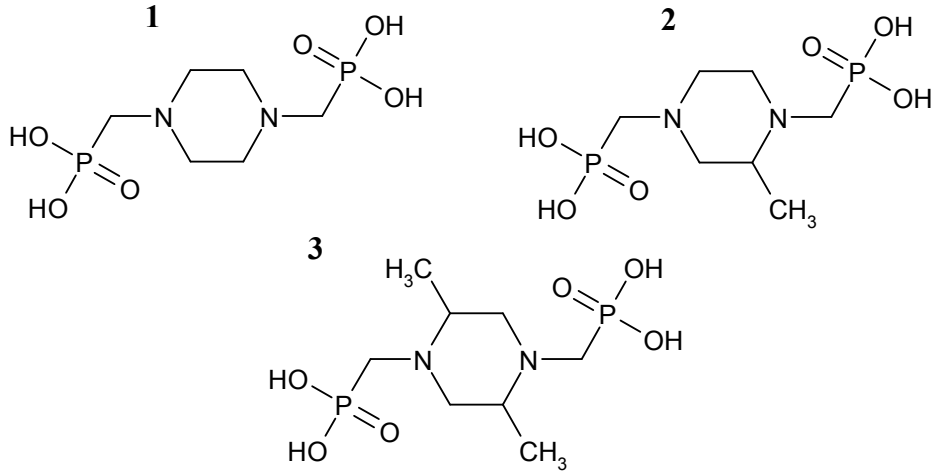

Figure 3.1 *- Phosphonate ligands - 1) N,N'-piperazinebis(methylenephosphonic acid) (H_4L); 2) racemic 2-methyl derivative (H_4L-Me); 3) racemic 2,5-dimethyl derivative (H_4L 2,5-diMe).*

The products from the general procedure for synthesising the ligands[2] were found to have evidence for incomplete reaction of the starting products.[4] The product impurity was believed to be a mono-methylenephosphonic acid version of the desired product, and to prevent this the quantities of formaldehyde and phosphorous acid were increased by 20% and the reaction refluxed for 12 hours (instead of 8 hours). The revised experimental procedure was as follows:

A solution of piperazine, 2-methyl piperazine or 2,5-dimethyl piperazine (0.09 moles), phosphorous acid (19.25 g, 0.234 moles) and HBr (18 %, 100 ml) was stirred and formaldehyde solution (38.5 ml, 35 wt% in water) added drop-wise over 30 minutes. The mixture was refluxed for 12 hours at 393 K, allowed to cool to room temperature and placed in the fridge overnight to ensure complete precipitation. The product was filtered, washed with cold water (3 x 30 ml), and dried thoroughly overnight at 423 K. The white powder product was characterised by ^{1}H and ^{31}P NMR and chemical analysis (CHN).

In the synthesis of the 2-methyl ligand the general experimental procedure was slightly modified. The H_4L and H_4L 2,5-diMe ligands precipitate easily out of solution as the

reaction proceeds, but the same is not true for the H_4L ligand. After refluxing for the full 12 hours the product remains in solution. The most effective procedure for isolating the product was to remove most of the solvent by rotary evaporation until the solution turned viscous and a deep yellow in colour. Then 100 ml of a cold ethanol/water mix (9:1 ratio) was added, resulting in precipitation of the product. The solution was left until all traces of yellow HBr residue had re-dissolved, and the product was filtered as outlined above.

3.3.1 Product Characterisation

N,N'-piperazinebis(methylene phosphonic acid):

^{1}H NMR (300 MHz, D_2O) δ = 3.4 (4H, d, J = 13Hz, C$\underline{H}_2$-PO_3H_2), 3.6 (8H, m, 4×(N-C$\underline{H}_2$)).

^{31}P NMR (300 MHz, D_2O) δ = 7.08 (2P, t, J = 27.42Hz, CH_2-$\underline{P}O_3H_2$).

Chemical analysis; weight%; calculated: C, 21.1%; H, 4.7%; N, 8.2%; measured: C, 22.16%; H, 5.58%; N, 8.71%.

Yield = 27.43 g, 96%.

N,N'-2-methyl-piperazinebis(methylene phosphonic acid):

^{1}H NMR (500 MHz, D_2O) δ = 1.46 (3H, d, J = 7.24 Hz, (N-C(C$\underline{H}_3$)H-CH_2), 3.34 (1H, t, J =14.50 Hz, (P-C$\underline{H}_2$-N-$(CH_2)_2$), 3.38 (2H, d, J = 14.43 Hz (N-C$\underline{H}_2$-PO_3H_2), 3.54 (1H, t, J =14.45 Hz, (P-C$\underline{H}_2$-N-$(CH_2)_2$)), 3.40 (1H,d, J =16.9 Hz, N-C$\underline{H}_2$-$CHCH_3$-N), 3.93 (1H,d, J =17.01 Hz, N-C$\underline{H}_2$-$CHCH_3$-N), 3.93 (1H,d, J =16.9 Hz, N-CH_2-C$\underline{H}CH_3$-N) 3.54, 3.73, 3.98 and 4.11 4x(1H,d, J =16.8 Hz, N-C$\underline{H}_2$-CH_2-N). Values from ^{1}H-^{13}C HSQC. ^{31}P NMR (300 MHz, D_2O) δ = 7.125, (1P, t, J = 32.81 Hz, CH_2-$\underline{P}O_3H_2$), 7.53, (1P, t, J = 33.0 Hz, CH_2-$\underline{P}O_3H_2$).

Chemical analysis; weight%; calculated: C, 23.7%; H, 5.12%; N, 7.89%; measured: C, 22.74%; H, 5.87%; N, 7.26%.

Yield = 24.63 g, 95%.

N,N'-2,5-dimethyl-piperazinebis(methylene phosphonic acid):

^{1}H NMR (300 MHz, D_2O) δ = 1.46 (6H, d, J = 7.30 Hz, 2x(N-C(C$\underline{H}_3$)H-CH_2)), 3.6 (10H, m, 2x(N-C$\underline{H}_2$-C(CH_3)$\underline{H}$-N), 2x(N-C$\underline{H}_2$-PO_3H_2))

^{31}P NMR (300 MHz, D_2O) δ = 7.08 (2P, t, J = 27.52Hz, CH_2-$\underline{P}O_3H_2$)

Chemical analysis; weight%; calculated: C, 26.1%; H, 5.4%; N, 7.6%; measured: C, 23.36%; H, 5.79%; N, 6.38%. Slightly lower than expected %C and %N coupled to higher than expected %H indicates presence of water in the sample.

Yield = 28.78g, 92%.

3.4 Synthesis of bisphosphonates

The synthesised bisphosphonate ligands were reacted hydrothermally with various metal sources, referencing a previously published procedure.[2] The variables of the reactions are outlined in Table 3.1.

Table 3.1 *– Reaction conditions used for preparation of phosphonate structures. All metal sources are divalent acetates. Initial pH of reaction gels for metals other than Ni altered with KOH (1 × 10^{-3} mol cm^{-3} in H_2O). pH measured using indicator paper.*

Metal	Ligand	Ratio in gel (M:L:H_2O)	pH	T (K)	Time (Hours)	Product Colour	Structure
Ni	H_4L	2 : 1 : 900	5	493	72	Green	**1**
Ni	H_4L-Me	2 : 1 : 900	5	493	72	Green	**1**
Ni	H_4L 2,5-diMe	2 : 1 : 900	5	493	72	Green	**2**
Co	H_4L	2 : 1 : 900	5	463	120	Blue	**3**
Co	H_4L	2 : 1 : 900	7	463	120	Pink	**1**
Co	H_4L-Me	2 : 1 : 900	7	463	120	Purple	**1**
Co	H_4L 2,5-diMe	2 : 1 : 900	7	463	120	Purple	**-**
Mg	H_4L	2 : 1 : 900	7	493	96	White	**4**
Fe	H_4L	2 : 1 : 900	5	463	120	Brown	**1**
Mn	H_4L	2 : 1 : 900	6	463	96	Cream	**1**

As indicated in Table 3.1, four structures form using different metals and bisphosphonate ligands, while keeping the metal : ligand : H_2O molar ratio constant. The most dominant structure is **1,** formed for all of the metals apart from Mg, and with the ligands H_4L and H_4L-Me. This is STA-12, and a description of it and structures **2** - **4** is given in the rest of the chapter.

3.5 Structure 1 – STA-12

3.5.1 Characterisation

As shown in Table 3.1, STA-12 was synthesised using four different metal acetate sources and the ligands H_4L and H_4L-Me. The experimentally produced powder diffraction patterns are shown in Figures 3.2 and 3.3. The crystal structure of Ni STA-12 was solved and refined from a combination of powder diffraction and computer modelling, as it has the best resolved powder diffraction pattern and is the most crystalline version of the structure.[2, 5]

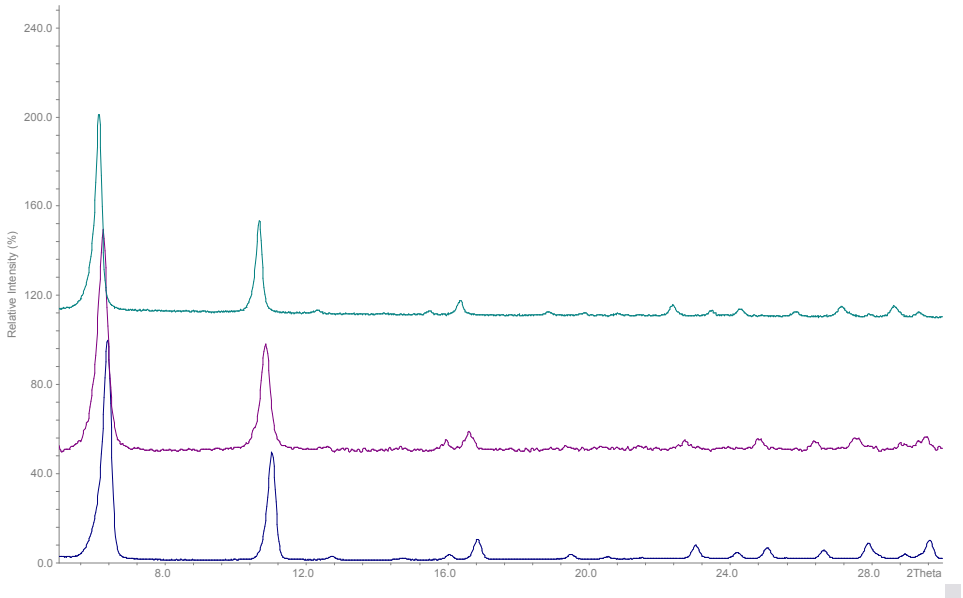

Figure 3.2 *– Laboratory powder X-ray diffraction patterns of (bottom) Ni STA-12, (middle) Ni Me STA-12 and (top) Mn STA-12 (Cu K_α radiation).*

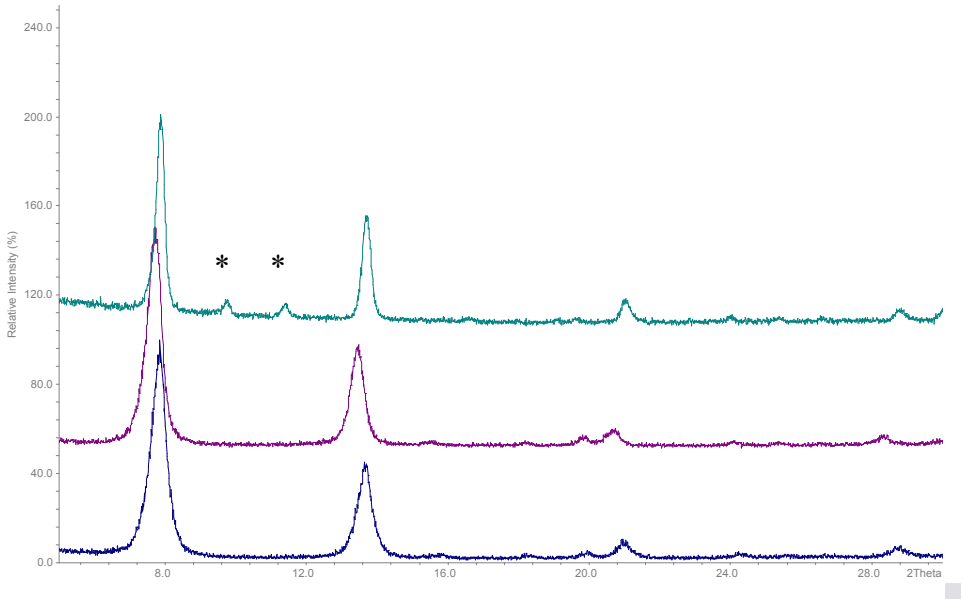

Figure 3.3 *– Laboratory powder X-ray diffraction patterns of (bottom) Co STA-12, (middle) Co Me STA-12 and (top) Fe STA-12 (Fe K_α radiation). Asterisks indicate peaks from impurity phase, which is Fe version of the structure reported by Zubieta et al. ($FeH_2L.H_2O$).*[6]

The X-ray powder diffraction patterns indicate STA-12 can be successfully synthesised from Mn^{2+}, Fe^{2+}, Co^{2+} and Ni^{2+} cation sources with a rhombohedral structure. EDX analysis of the inorganic content shows the metal : phosphorus ratio is 1 : 1 for all of the samples. As the H_4L and H_4L-Me ligands both contain two phosphorus atoms, this indicates the metal to ligand ratio is 2 : 1, suggesting the chemical formula is $M_2L.xH_2O$.

Table 3.2 *– Elemental analysis (CHN) of the organic content in the STA-12 structures. Expected values for Ni STA-12 in brackets.*[2] *Error in values - ± 1 %.*

Metal	Ligand	%C	%H	%N
Ni	H_4L	(13.87)	(5.16)	(5.39)
Ni	H_4L	13.77	4.87	5.39
Ni	H_4L-Me	14.99	3.56	5.67
Co	H_4L	14.18	4.63	5.02
Co	H_4L-Me	16.12	4.16	4.99
Fe	H_4L	13.80	3.99	4.98
Mn	H_4L	13.45	4.87	5.27

Elemental analysis of the organic content of the STA-12 samples (Table 3.2) indicates a reasonable comparison to the calculated values for Ni STA-12. The amount of carbon present is increased when the H_4L-Me ligand is used, due to the presence of methyl groups on the ligands. The results also indicate the metal : ligand ratio is 2 : 1 for all of the structures, confirming the EDX analysis. Thermal analysis and nitrogen adsorption experiments have also been undertaken on the STA-12 structures. This work is outlined and discussed in Chapter 4.

3.5.2 Structure solution of Ni STA-12 (structural analysis by Stuart Miller)[5]

The structure of Ni STA-12 was originally solved using X-ray data collected from a lab diffractometer, coupled to computer simulation.[2] During the course of this work, a sample of Ni STA-12 was analysed in a sealed 0.7 mm quartz capillary using high resolution X-ray diffraction at station ID-31 at the European Synchrotron Radiation Facility (λ = 0.8002 Å, 2θ range = 2 – 38°).[5, 7] Pattern indexing was carried out within the EXPO2004 suite using TREOR.[8] Rietveld refinement of the structural model was undertaken using the GSAS program suite,[1] and the crystallographic parameters from the high resolution structure solution of Ni STA-12 are outlined in Table 3.3 (atomic coordinates outlined in Appendix 1).

Table 3.3 *– Crystallographic parameters for high resolution structure solution of as-prepared Ni STA-12.*[5]

Formula	$Ni_2(H_2O)_2L.6H_2O$
Unit Cell Composition	$Ni_{18}P_{18}O_{126}N_{18}C_{54}H_{216}$
Formula Weight (Unit Cell)	4748.3
Calculated density (g cm^{-3})	1.832
Space Group	R-3
a (Å)	27.8342(1)
b (Å)	27.8342(1)
c (Å)	6.2421(3)
α (°)	90
β (°)	90
γ (°)	120
V (Å^3)	4188.12
Diffractometer	ESRF (ID-31)
Temperature (K)	100
Wavelength (Å)	0.8002
R_{wp}	0.0596
R_p	0.0411

3.5.3 Description of high resolution structure of Ni STA-12[5]

The framework structure of Ni STA-12 is shown below in Figure 3.4. The framework has large hexagonal pores with a free diameter, after taking into account the van der Waals radii of hydrogen, of *ca.* 10 Å. The pores themselves contain physically adsorbed water.

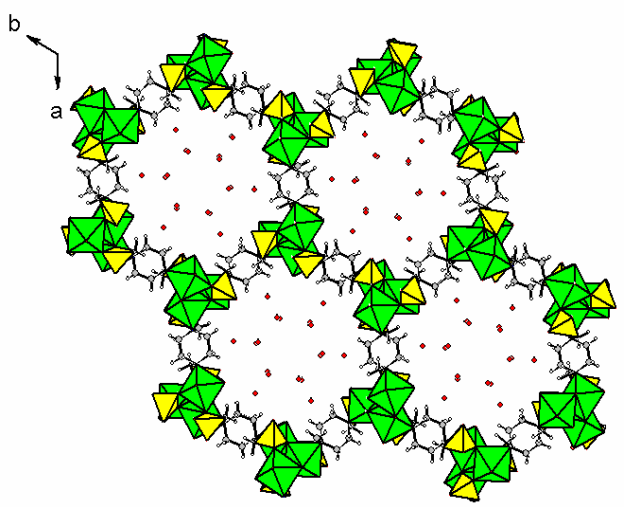

Figure 3.4 *– Framework structure of Ni STA-12 viewed down the c-axis. Ni centred octahedra in green, phosphonate tetrahedra in yellow, carbon atoms in grey and hydrogen atoms in white. Oxygen atoms of physisorbed water molecules in red.*

The framework is composed of helical chains of edge-sharing NiO_5N octahedra. Each NiO_5N octahedron is composed of a nickel coordinated by four oxygen atoms belonging to two phosphonate tetrahedra, an oxygen atom from a coordinating water molecule and a nitrogen atom from the piperazine ring of a ligand. The piperazine ring sits on a centre of symmetry, and each inorganic chain is linked to three others by the ligands. Therefore, each individual bisphosphonate ligand coordinates via four oxygen atoms and the two nitrogen atoms to two inorganic helical chains. This results in phosphonate oxygens projecting into the pore space.

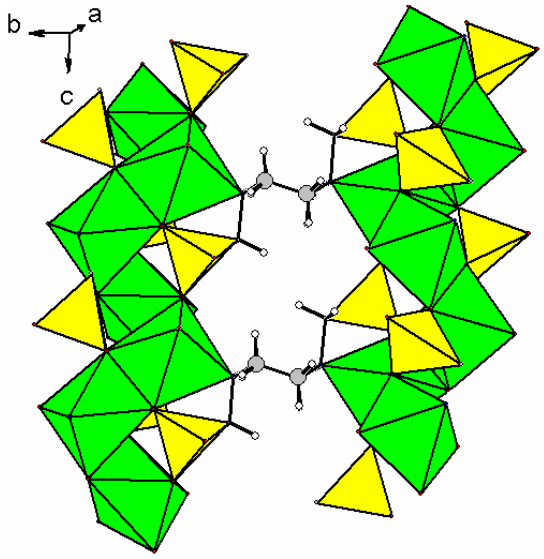

Figure 3.5 *– Close up view of two inorganic chains in Ni STA-12 connected by bis(phosphonate) linkers, with piperazine rings in chair conformation (colour scheme as Figure 3.4).*

The physically adsorbed water molecules in the pores could be located very accurately as the collection temperature was low (100 K) and the data was of a high resolution.[5] A hydrogen-bonded array of physisorbed water molecules was determined, which is hydrogen-bonded to the phosphonate oxygen atoms projecting into the pores and the oxygen atoms of the coordinated water molecules on the nickel cations.

The oxygen atoms of the physisorbed water are tetrahedrally coordinated to other oxygen atoms in the hydrogen-bonding scheme (Figure 3.5), and the structure is similar to hexagonal ice.[9] In hexagonal ice all the hydrogen bonds are directly between adjacent layers. In Ni STA-12, one out of every two of the links between the layers of water oxygen atoms occurs through two hydrogen bonds via an intermediate oxygen atom of a physisorbed water molecule. The columnar array is commensurate with the framework, and it is able to make hydrogen bonds with it.

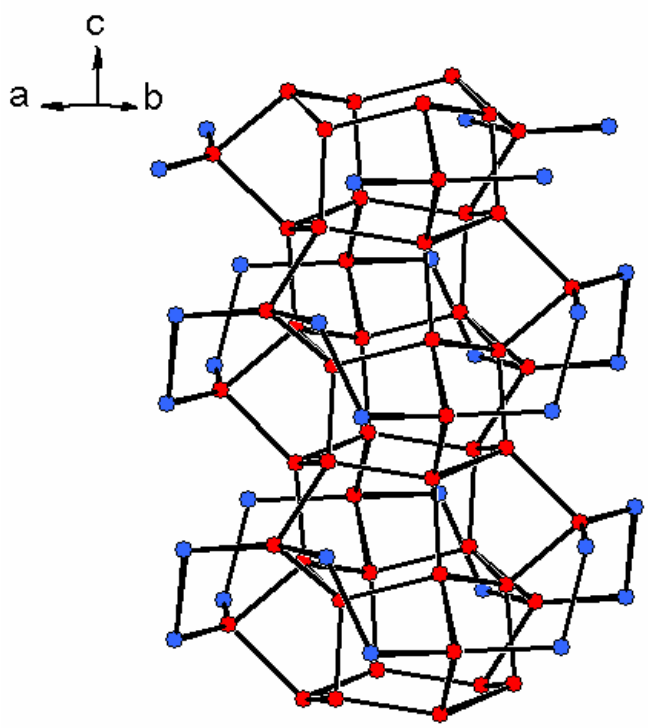

Figure 3.5 *– Hydrogen-bonded array of physisorbed water molecules within a pore of Ni STA-12, measured at 100K. Red spheres represent oxygen atoms of physisorbed water molecules in the channels and blue spheres represent oxygen atoms bound to nickel and phosphorus atoms that are part of the Ni STA-12 framework.*

3.5.4 Structural studies of other STA-12 structures

3.5.4.1 H_4L ligand

Table 3.4 outlines the crystallographic parameters from Rietveld refinements of Mn, Co and Fe STA-12 compared to the published parameters for Ni STA-12 measured at room temperature on a lab diffractometer.[2] Figures 3.6, 3.7 and 3.8 show the final Rietveld plots for, respectively, Mn, Co and Fe STA-12. They indicate the correct phases are forming for these metals (more information on parameters and goodness of fit for Rietveld refinements in Appendices 2 and 5).

Table 3.4 - *Crystallographic parameters for STA-12 structures formed using the H_4L ligand, compared to Ni STA-12[2] ($M_2(H_2O)_2L.5.4H_2O$).*

Metal	Mn	Fe	Co	Ni[2]
Space Group	R-3	R-3	R-3	R-3
a (Å)	28.534(4)	27.986(4)	28.0243(33)	27.9486(4)
b (Å)	28.534(4)	27.986(4)	28.0243(33)	27.9486(4)
c (Å)	6.4222(11)	6.3976(14)	6.2734(8)	6.2302(1)
α (°)	90	90	90	90
β (°)	90	90	90	90
γ (°)	120	120	120	120
V (Å^3)	4528.3(12)	4339.5(15)	4266.8(9)	4214.6(1)
Diffractometer	Lab (STOE)	Lab (STOE)	Lab (STOE)	Lab (STOE)
T (K)	298	298	298	298
λ (Å)	1.5406 (Cu K_α)	1.9361 (Fe K_α)	1.9361 (Fe K_α)	1.5406 (Cu K_α)
R_{wp}	0.1125	0.1183	0.1386	0.061

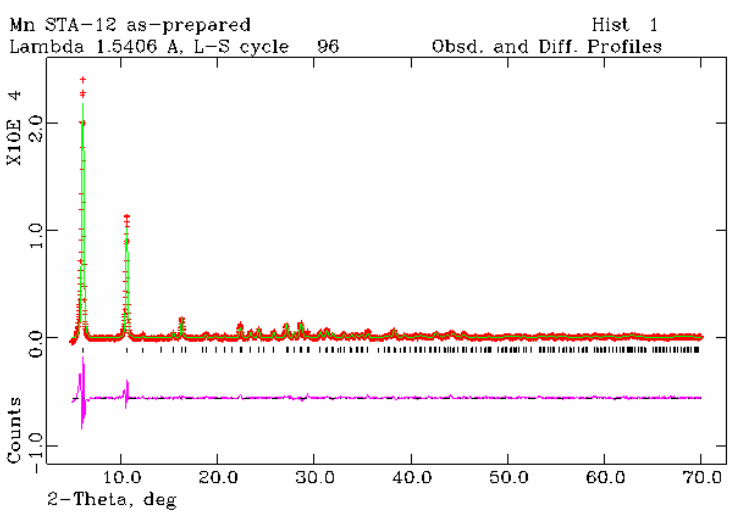

Figure 3.6 *- Rietveld refinement of Mn STA-12 (Cu K_α radiation) – red: measured pattern, green: calculated pattern, purple: difference between measured and calculated patterns.*

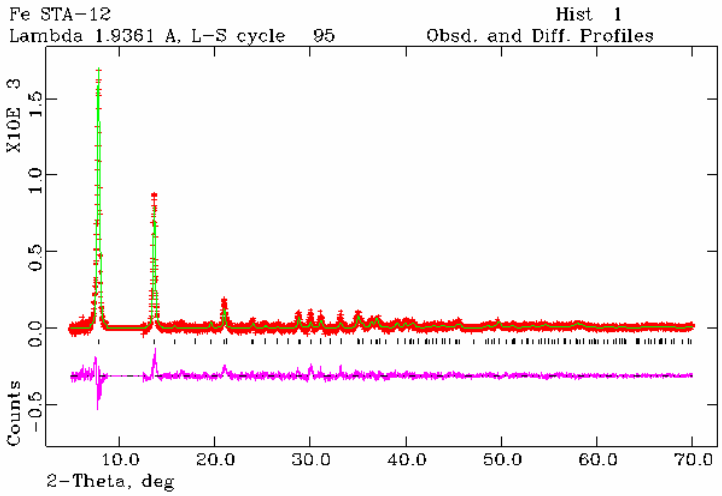

Figure 3.7 *- Rietveld refinement of Fe STA-12 (Fe K_α radiation). Colour scheme as Figure 3.6. Impurity peaks discounted from refinement.*

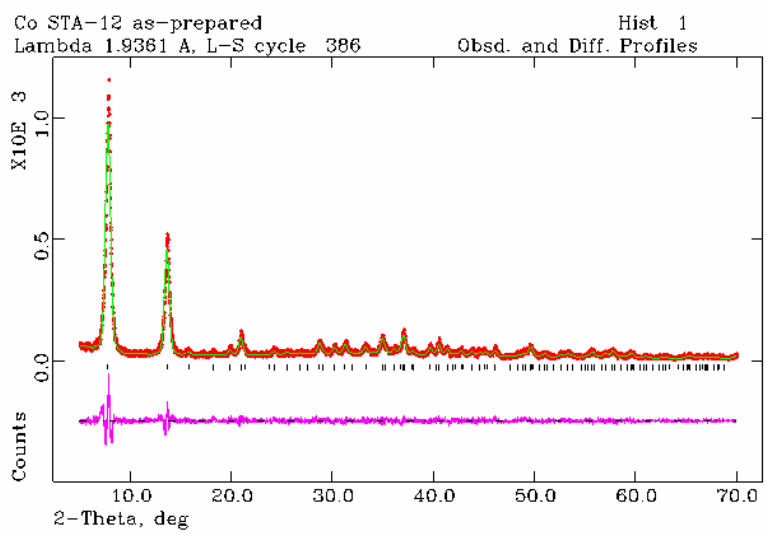

Figure 3.8 *- Rietveld refinement of Co STA-12 (Fe K_α radiation). Colour scheme as Figure 3.6.*

Structural analysis indicates X-ray data from Co, Fe and Mn STA-12 (Figures 3.6, 3.7 and 3.8) fit well to the model for Ni STA-12. The unit cell parameters for each of the structures are different, as are the unit cell volumes. Comparison to the ionic radii (6 coordinate, high spin, 2+ charge) for the metals can help to show if any trends are present (Table 3.5).

Table 3.5 *– Comparison of ionic radii of Mn^{2+}, Fe^{2+}, Co^{2+} and Ni^{2+} with the a and c cell parameters and the unit cell volumes of the STA-12 structures.*

Metal	**Ionic radii[10] (pm)**	***a* cell parameter (Å)**	***c* cell parameter (Å)**	**Volume (Å^3)**
Mn	83	28.534(4)	6.4222(11)	4528.3(12)
Fe	78	27.986(4)	6.3976(14)	4339.5(15)
Co	74.5	28.0243(33)	6.2734(8)	4266.8(9)
Ni	69	27.9486(4)	6.2302(1)	4214.6(1)

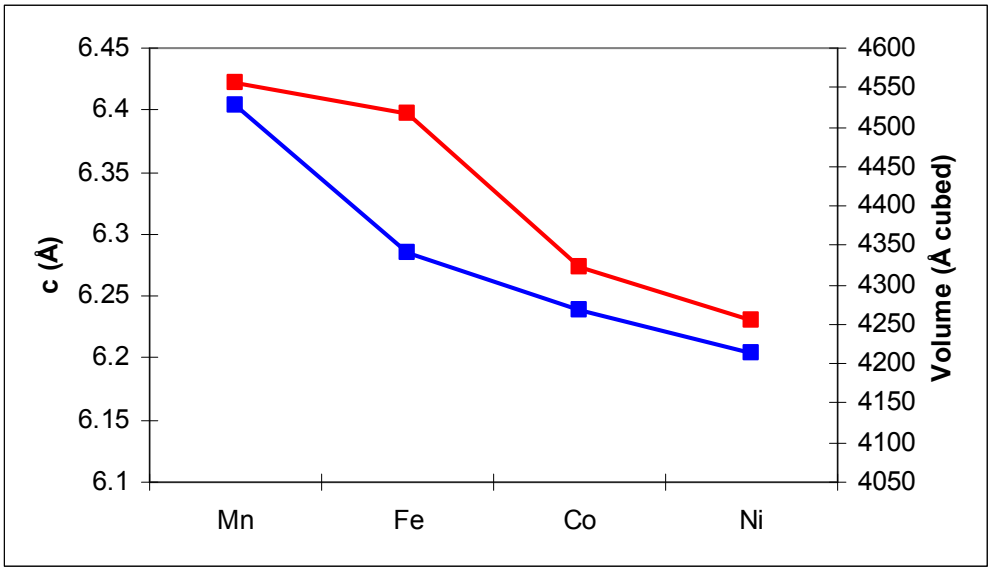

Figure 3.9 *– Comparison of changes in the length of c (red line) and the unit cell volume (blue line) with the reduction in the size of the metal ionic radii in STA-12.*

As the ionic radii decrease in size from Mn^{2+} to Ni^{2+}, there is a decrease in the *c* cell parameter (from 6.4222(11) Å in Mn STA-12 to 6.2302(1) Å in Ni STA-12) and the unit cell volume (from 4528.3(12) $Å^3$ in Mn STA-12 to 4214.6(1) $Å^3$ in Ni STA-12). The trend is shown visually in Figure 3.9. The decrease in the ionic radii has a marked effect on the *c* cell parameter, as this is the measure of the distance along the helical inorganic chains. As the radii decrease in size, this distance becomes smaller and the length of the helical chains is subsequently reduced.

The effective nuclear charge increases from Mn^{2+} to Ni^{2+} resulting in the ligand field increasing, and the coordination sphere of the metals decreasing. The phosphonate ligands will coordinate closer to the metal, with this reflected in the decrease in the unit cell volumes. High spin Mn^{2+}, which has a d-electron configuration of d^5, has a spherical charge distribution where all of the d-orbitals are filled with unpaired electrons. This could help to explain why the cell volume difference between Mn and Fe STA-12 (188.8 $Å^3$) is much larger than the cell volume difference between Fe and Co (72.7 $Å^3$), and Co and Ni STA-12 (52.2 $Å^3$).

3.5.4.2 H_4L-Me ligand

Table 3.5 outlines the crystallographic parameters from Rietveld refinements of Co and Ni Me STA-12 compared to the parameters for Co and Ni STA-12.[2] Figures 3.10 and 3.11 show the final Rietveld plots for, respectively, Co and Ni Me STA-12. They indicate the correct phases are forming for these metals (more information on parameters and goodness of fit for Rietveld refinements in Appendices 2 and 5).

.

Table 3.6 *- Crystallographic parameters for STA-12 structures formed using the H_4L-Me ligand (Ni Me STA-12 and Co Me STA-12), compared to Ni STA-12[2] and Co STA-12.*

Metal and Ligand	Co H_4L	Co H_4L-Me	Ni H_4L[2]	Ni H_4L-Me
Space Group	R-3	R-3	R-3	R-3
a (Å)	28.0243(33)	28.5268(35)	27.9486(4)	27.9789(28)
b (Å)	28.0243(33)	28.5268(35)	27.9486(4)	27.9789(28)
c (Å)	6.2734(8)	6.2984(9)	6.2302(1)	6.2391(6)
α (°)	90	90	90	90
β (°)	90	90	90	90
γ (°)	120	120	120	120
V ($Å^3$)	4266.8(9)	4394.4(12)	4214.6(1)	4230(8)
Diffractometer	Lab (STOE)	Lab (STOE)	Lab (STOE)	Lab (STOE)
T (K)	298	298	298	298
λ (Å)	1.9361 (Fe K_α)	1.9361 (Fe K_α)	1.5406 (Cu K_α)	1.5406 (Cu K_α)
R_{wp}	0.1386	0.1472	0.061	0.1221

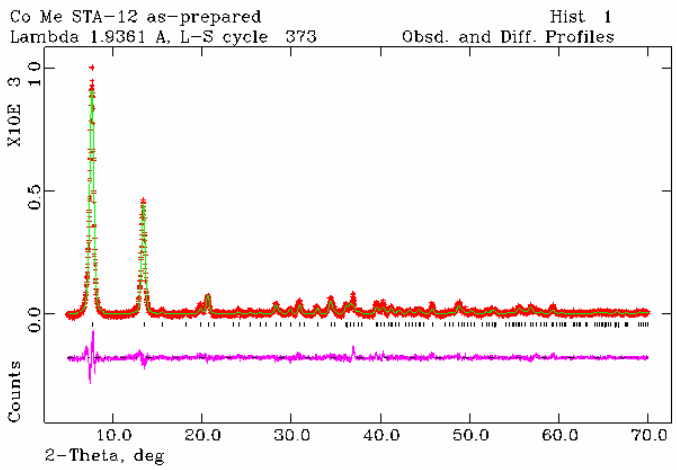

Figure 3.10 *- Rietveld refinement of Co Me STA-12 (Fe K_α radiation). Colour scheme as Figure 3.6.*

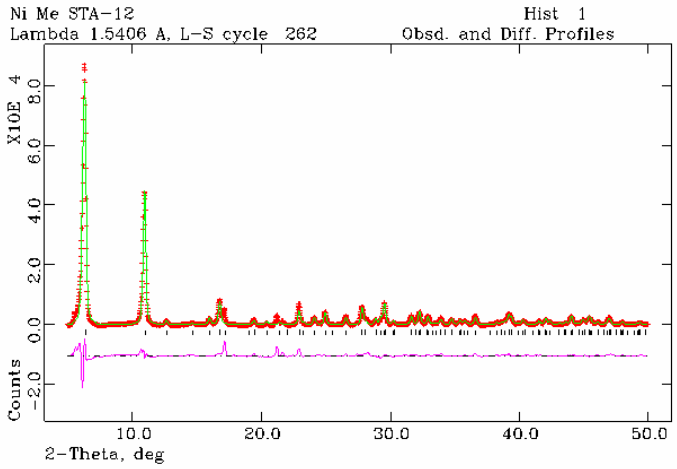

Figure 3.11 *- Rietveld refinement of Ni Me STA-12 (Cu K_α radiation). Colour scheme as Figure 3.6.*

The diffraction data indicates the STA-12 structures synthesised using the H_4L-Me ligand are not as crystalline as the comparable structures synthesised with the H_4L ligand, as the peaks in the diffraction patterns are broader (Figures 3.10 and 3.11). This is likely to be due to the fact the methyl groups are randomly ordered over the four carbon atoms on the piperazine rings of the ligands. The structural study indicates the *a* cell parameter in Co Me STA-12 increases by ~ 0.5 Å, and the unit cell volume increases by ~ 128 $Å^3$, when compared to Co STA-12 (Table 3.6). The increases can be explained as due to more

atoms being present in the unit cell, and there being just enough room in the structure for the methyl groups on the ligand. This results in an increase in the unit cell volume, and an increase in the *a* cell parameter (which is the measure of the distance between the inorganic chains in the structure) due to a slight rearrangement of the atoms.

The data from the structural study of Ni Me STA-12 (Table 3.6) indicates the *a* cell parameter and the unit cell volume are similar in magnitude to Ni STA-12, with the differences considered to be within error. This behaviour is different to that observed for Co Me STA-12, and indicates less strain is present. Ni^{2+} has a d-electron configuration of d^8, compared to d^7 for Co^{2+}, and this could account for the different behaviour of Co and Ni Me STA-12. The ligand field strength and ionic radii (Table 3.5) are different for the two metals, meaning the extra atoms present on the ligand do not result in any rearrangements of the structure in Ni Me STA-12. The methyl groups are likely to have different orientations on the ring than those in Co Me STA-12, meaning the unit cell volume does not increase and the distance between the inorganic chains does not change (*a* cell parameter).

3.6 Structure 2 – Ni + H_4L 2,5-diMe

The reaction of Ni (II) acetate with the H_4L 2,5-diMe ligand forms a powder with a similar green colour to Ni STA-12 and Ni Me STA-12. The unit cell was indexed using Stöe software as hexagonal, with $a = b = 18.165$ Å, $c = 6.274$ Å, $\alpha = \beta = 90°$, $\gamma = 120°$. These parameters are similar to the cell of the Ni phosphate VSB-5 reported by Guillou *et al.*,[11] which has hexagonal 1-D pores *ca.* 10 Å in diameter (Figure 3.12).

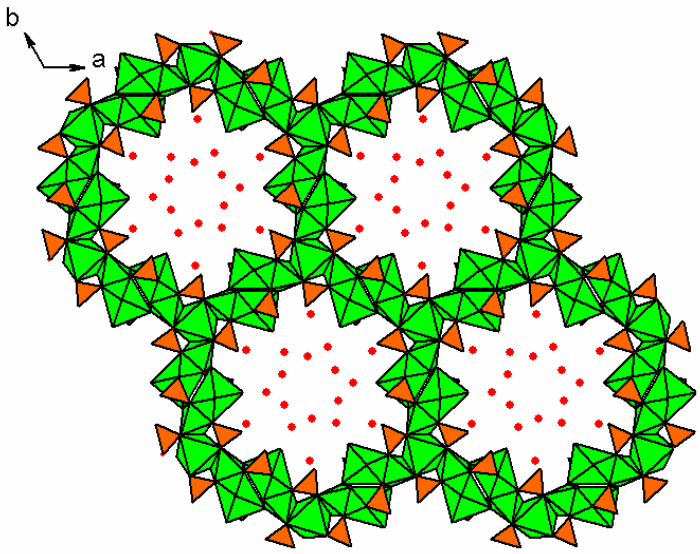

Figure 3.12 *– Structure of the Ni phosphate VSB-5 viewed down the 1-D channels running along the c-axis.*[11] *NiO_6 octahedra in green and PO_4 tetrahedra in orange. Oxygen atoms of physisorbed water molecules in red.*

Analysis of the organic content of the structure (Table 3.7) indicates there is no carbon or nitrogen present, and EDX analysis shows the Ni : P ratio is 3 : 2. Therefore, it seems the H_4L 2,5-diMe ligand is breaking down during hydrothermal treatment of the gel under these reaction conditions. Direct comparison of a theoretical X-ray powder diffraction pattern for Ni VSB-5 (generated from the Diamond 3 program) with the Ni H_4L 2,5-diMe structure (Figure 3.13) shows there is a close correlation in the peak 2θ positions, indicating Ni VSB-5 is forming during the reaction.

Table 3.7 *- Elemental analysis (CHN) of the organic content in the Ni H_4L 2,5-diMe structure. Error in values - ± 1 %.*

Metal	Ligand	%C	%H	%N
Ni	H_4L 2,5-diMe	-	3.25	-

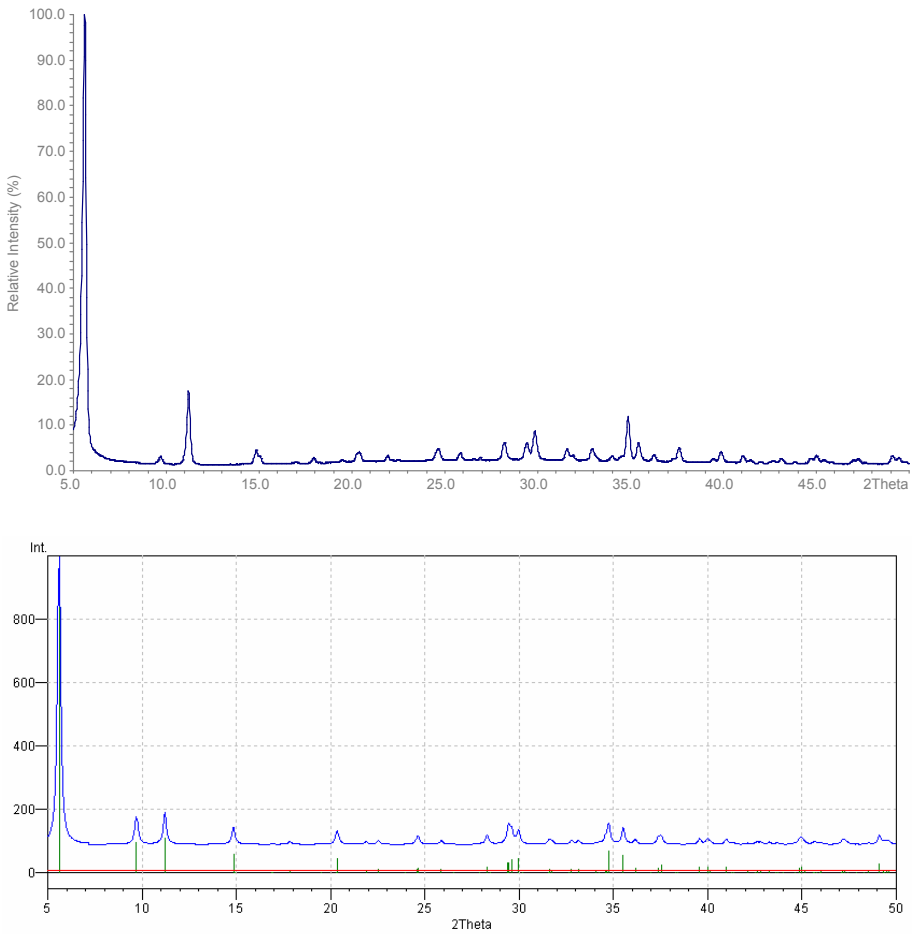

Figure 3.13 *- X-ray powder diffraction patterns of (top) Ni + H_4L 2,5-diMe and (bottom) Ni VSB-5 theoretical pattern generated from Diamond 3 program (Cu K_α radiation).*

3.7 Structure 3 – $CoH_2L.H_2O$

Reaction of Co acetate with the H_4L ligand at low pH (~ 5) results in the formation of small, blue, plate-like crystals. Blue is a colour associated with Co in tetrahedral coordination, and EDX analysis indicates the ratio of metal : ligand is 1 : 1. The elemental analysis results (Table 3.8) are similar to those expected for the Co phase synthesised by Zubieta *et al.*,[6] where Co^{2+} is tetrahedrally coordinated (Co analogue of $ZnH_2L.H_2O$ structure shown in Figure 1.17 in Chapter 1). This indicates the pH does not seem to be high enough to fully deprotonate the ligand during the synthesis.

Table 3.8 *- Elemental analysis (CHN) of the organic content in $CoH_2L.H_2O$. Error in values - ± 1 %.*

	Metal	Ligand	%C	%H	%N
Theoretical	Co	H_4L	20.72	4.78	7.73
Actual	Co	H_4L	20.47	4.00	7.73

Comparison of the X-ray powder diffraction pattern of $CoH_2L.H_2O$ with a theoretical pattern of the Co^{2+} phase synthesised by Zubieta *et al.*[6] generated by the Diamond 3 program (Figure 3.14) indicates the 2θ peak positions are closely matched. No nitrogen gas is adsorbed, although water can be reversibly removed.

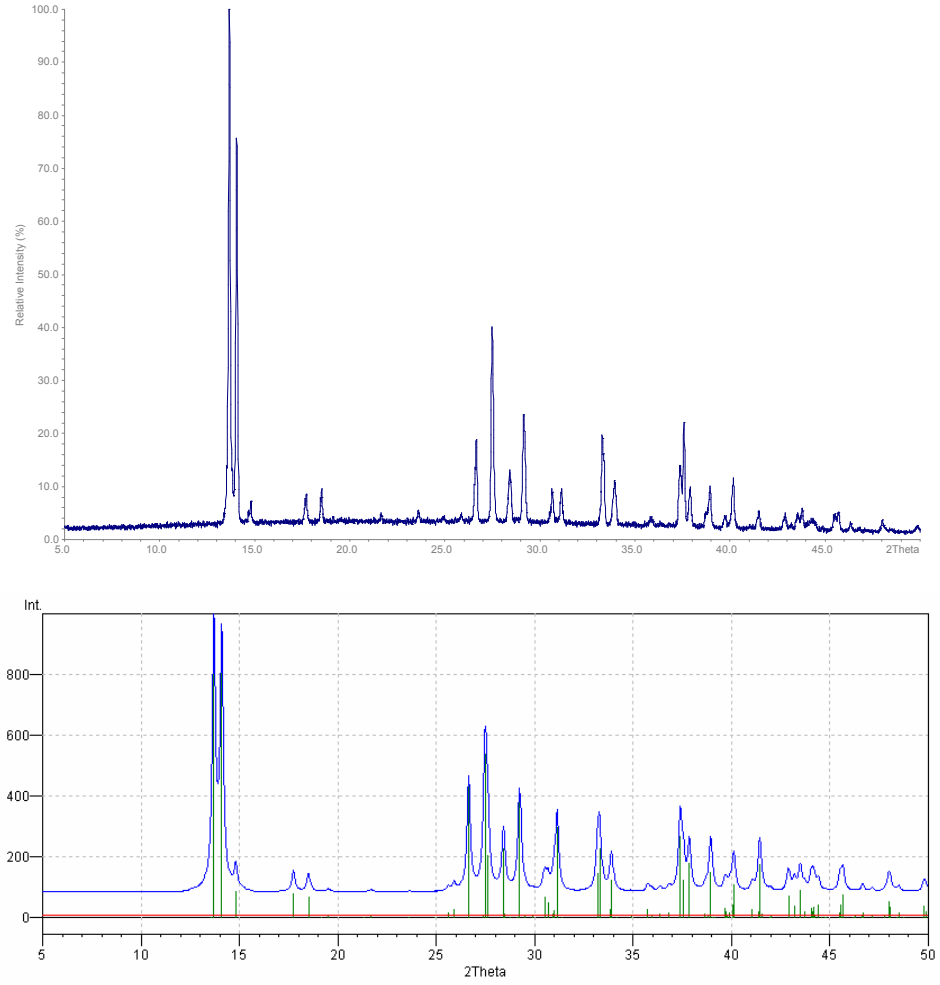

Figure 3.14 *- X-ray powder diffraction patterns of (top) $CoH_2L.H_2O$ and (bottom) Co Zubieta[6] theoretical pattern generated from Diamond 3 program (Fe K_α radiation).*

3.8 Structure 4 – Mg H_2L

Reaction of Mg with the H_4L ligand in the ratio 2 : 1 produces a white powder. The X-ray powder diffraction pattern indicates a novel structure is synthesised and indexing of the unit cell using Stöe software shows it has monoclinic symmetry (Figure 3.15).

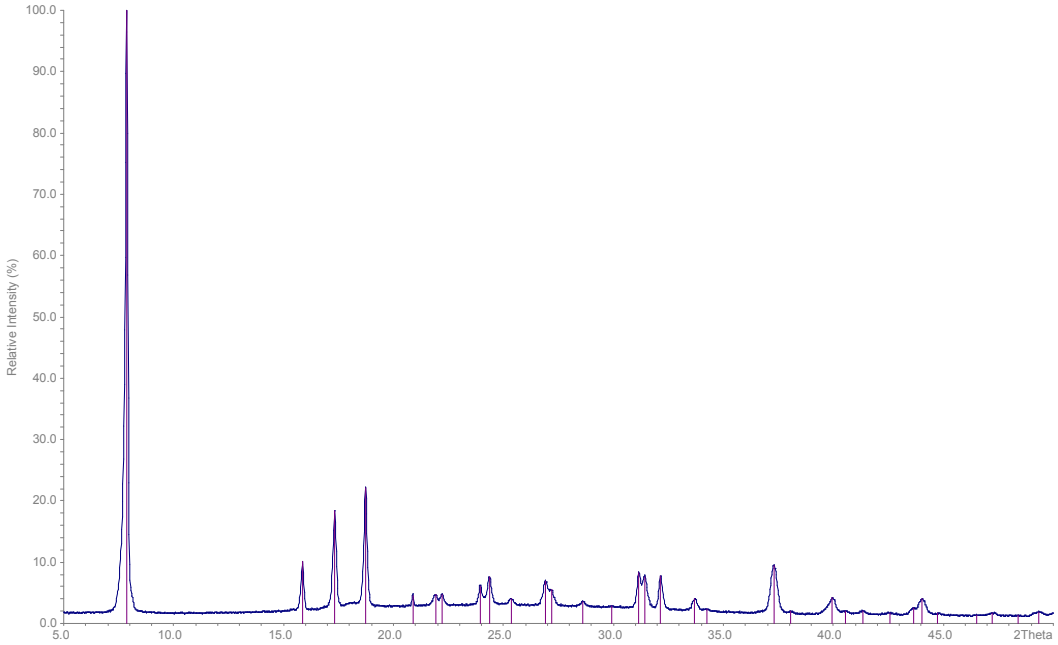

Figure 3.15 *- X-ray powder diffraction pattern of Mg H_2L (monoclinic cell, a = 24.547(13) Å, b = 5.739(2) Å, c = 12.995(1) Å; α = 90°, β = 120.821(4)°, γ = 90°) (Cu K_α radiation).*

Table 3.9 *- Elemental analysis (CHN) of organic content in Mg H_2L. Error in values - ± 1 %.*

Metal	Ligand	%C	%H	%N
Mg	H_4L	20.80	4.43	7.45

Analysis of the organic content indicates the ligand is intact, and the ratio of the metal : ligand is 2 : 1 (Table 3.9). EDX analysis confirms this, as the ratio of Mg : P is 1 : 1. When the structure undergoes thermal treatment, there is a fully reversible weight loss of

10 % which can be attributed to water between 453 and 473 K (Figure 3.16). Above 650 K a gradual weight loss is observed due to breakdown of the ligand. At 1000 K there is an increase in the weight of the sample, attributed to the formation of Mg pyrophosphate ($Mg_2P_2O_7$) by incorporation of oxygen from the flowing air in the experiment.

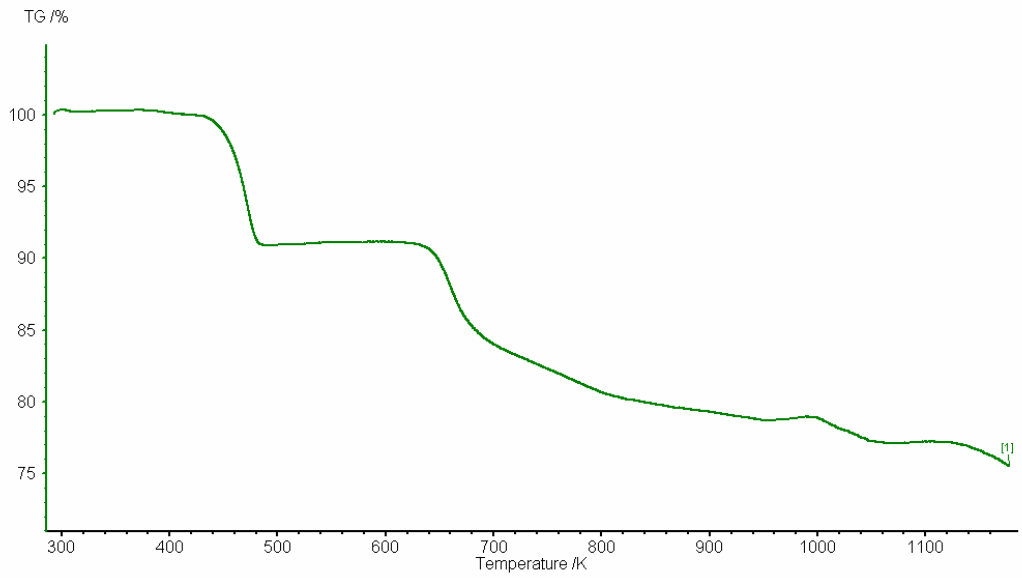

Figure 3.16 *– Thermal analysis of Mg H_4L at 5K/min in air.*

The structure does not adsorb nitrogen when dehydrated, and the X-ray powder pattern after dehydration at 473 K indicates there are changes. This means the structure is distorting on water loss, and it is noticeable that this distortion is not fully reversed upon exposure to moist air (Figure 3.17).

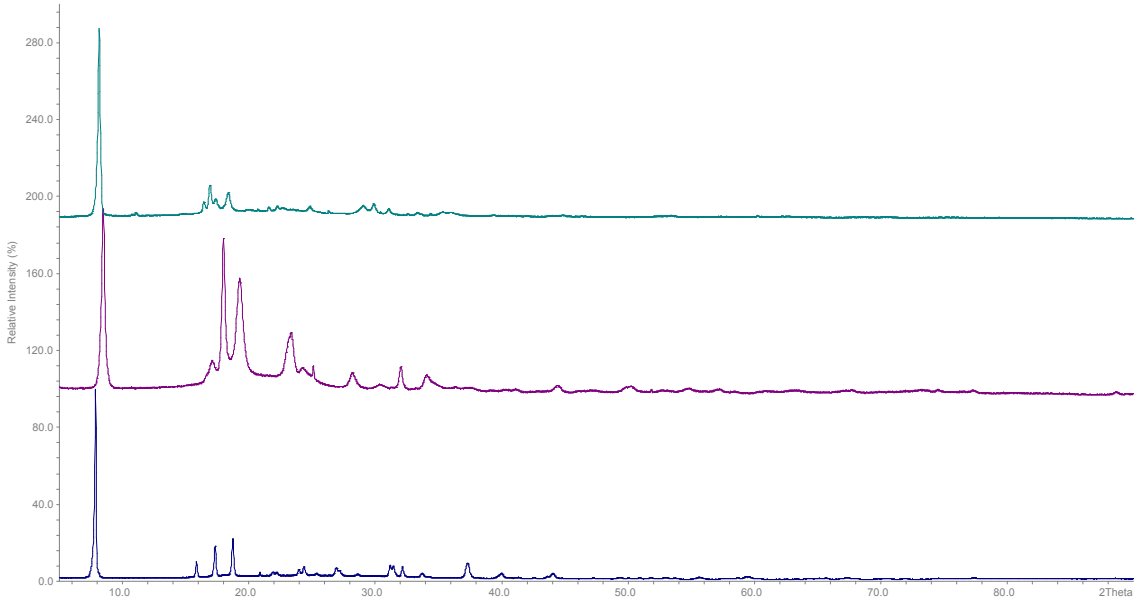

Figure 3.17 *- Laboratory powder X-ray diffractograms of Mg H_2L (bottom to top) as-prepared, evacuated 473 K, rehydrated (Cu K_α radiation).*

3.9 Synthesis of mixed metal STA-12 samples

As STA-12 can be synthesised using Mn, Fe, Co and Ni a study was undertaken to see if more than one metal could be included simultaneously into the structure. A known amount of Ni^{2+} was replaced by another divalent metal in the reaction gel, with the ratios and metals used outlined in Table 3.10 below. All the hydrothermal crystallisations were undertaken at 493 K for 72 hours with no changes to the initial pH.

Table 3.10 *– Hydrothermal reaction ratios for Ni mixed metal STA-12 (imp. = impurity).*

Metal 1	Metal 2	Ratio in gel (M_1:M_2:L:H_2O)	Product Colour	Structure
Ni	Mg	1.6 :0.4 :1 :900	Green	STA-12
Ni	Mn	1.6 :0.4 :1 :900	Green	STA-12
Ni	Fe	1.6 :0.4 :1 :900	Yellow	STA-12
Ni	Co	1.6 :0.4 :1 :900	Grey	STA-12
Ni	Zn	1.6 :0.4 :1 :900	Green	STA-12 + imp.

The results of the reactions indicate changing the reaction gels by replacing some of the Ni^{2+} with other divalent metals allows for mixed metal STA-12 samples to be synthesised. The X-ray powder diffraction patterns (Figure 3.18) shows the structure is STA-12 for Mg, Mn, Fe and Co materials, with an impurity phase present for Zn.

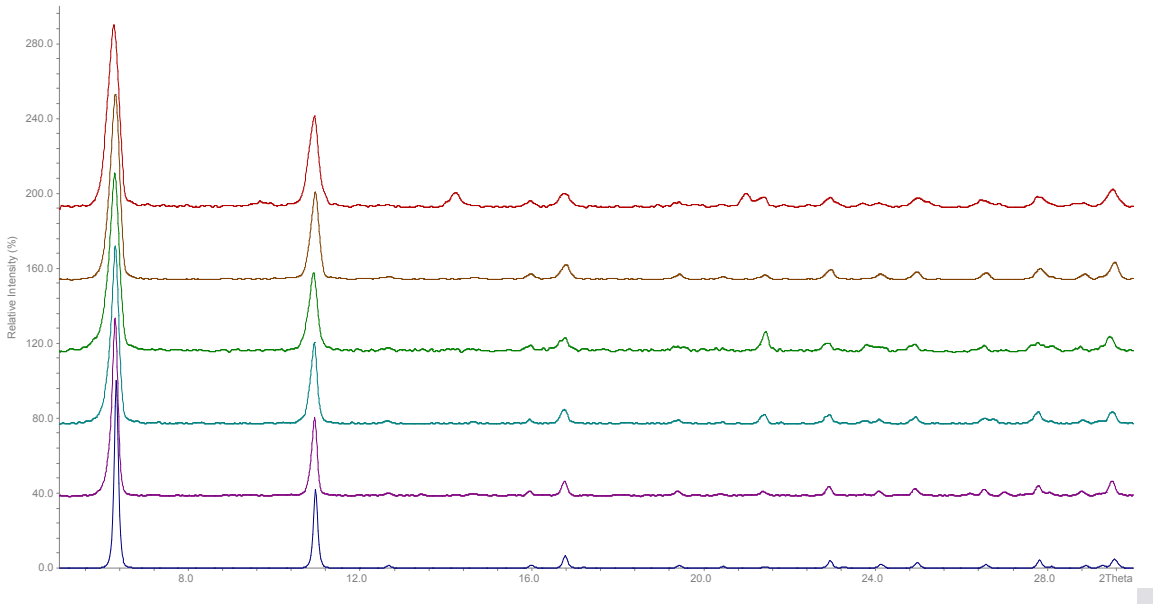

Figure 3.18 *- X-ray powder diffraction patterns of (top) to (bottom) Ni STA-12 + 20% Zn, Ni STA-12 + 20% Mg, Ni STA-12 + 20% Mn, Ni STA-12 + 20% Fe and Ni STA-12 + 20% Co. Compared to Ni STA-12 theoretical pattern generated by Stöe software (Cu K_α radiation).*

When 20% of the Ni is replaced in the gel by Zn the impurity phase present is the $ZnH_2L.H_2O$ phase discovered by Groves *et. al*.[12] The peaks at 2θ values of 10º, 14º and 23° match up well to the phase which is the Zn analogue of the $CoH_2L.H_2O$ structure (Section 3.7, structure shown in Figure 1.17 in Chapter 1).[6] For the structures where Mg, Mn, Fe and Co are replacing Ni^{2+} in the reaction gel, EDX has been used to indicate if the divalent metals are replacing Ni (Table 3.11).

Table 3.11 *– EDX results for mixed metal STA-12 samples averaged over 10 point analyses. Calibrated to known standards for each element.*

Structure	Ni / P	Doping Metal / P
Ni STA-12	1	**-**
Ni STA-12 + 20% Co	0.772	0.199
Ni STA-12 + 20% Fe	0.826	0.185
Ni STA-12 + 20% Mn	0.767	0.166
Ni STA-12 + 20% Mg	0.831	0.181

If 20% of the Ni is successfully being replaced in the framework by another divalent metal, the EDX analysis should indicate the ratio of doping metal/P is equal to 0.2. The results indicate that of all the metals, Co is the nearest the expected result. For Fe, Mn and Mg the ratio of doping metal/P is lower than expected, especially for Mn. The colours of the samples are homogeneous, so the lower than expected values are probably a result of different kinetics of reaction for the various metals. Elemental mapping analysis indicates the doped metals are spread evenly throughout the structure, meaning Ni^{2+} is being replaced in a random fashion by the other divalent metals.

As the replacement of Ni^{2+} by other divalent metals is successful, there may be effects on the thermal properties of STA-12 (Figure 3.19). The thermal properties are fairly similar, with comparable weight loses due to water (298 – 473 K region). The plateau after water has been removed is increased to a higher temperature when Co^{2+} and Mg^{2+} are doped, and reduced to a lower temperature when Fe^{2+} is doped.

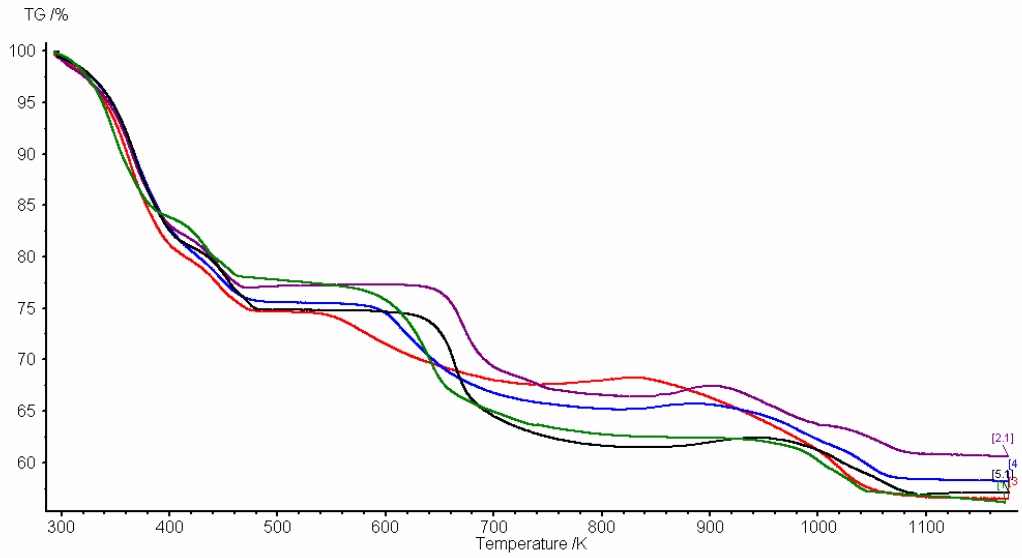

Figure 3.19 *– Thermal analysis of mixed metal STA-12. Ni STA-12 - Green; Ni STA-12 + 20% Co – Purple; Ni STA-12 + 20% Fe - Red, Ni STA-12 + 20% Mn - Blue and Ni STA-12 + 20% Mg - Black.*

Nitrogen adsorption experiments on the mixed metal STA-12 structures (Figure 3.20) indicate they are porous with reasonable uptakes when compared to Ni STA-12. In depth analysis of the thermal properties of STA-12 are discussed in Chapter 4, while in Chapter 6 the effect of replacing Ni^{2+} with known amounts of other divalent metals will be investigated in catalytic test reactions.

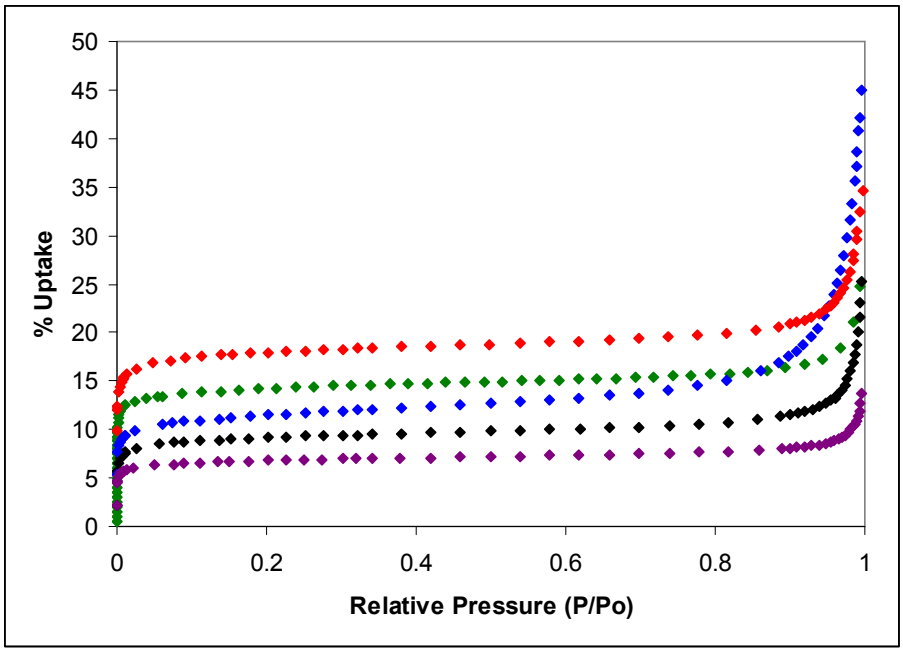

Figure 3.20 *– Nitrogen adsorption data at 77 K for mixed metal STA-12 samples. Colour coding for samples same as Figure 3.19.*

3.10 Synthesis of CPO-27

Ni and Co CPO-27 (structure described in Figure 1.13 in Chapter 1) were prepared to provide comparison with STA-12. They were originally synthesised by Dietzel *et. al.* from Ni (II) and Co (II) acetate and 2,5-dihydroxyterephthalic acid in a water/tetrahydrofuran mixed system.[13, 14] The reaction conditions used are outlined in Table 3.12, and the X-ray powder diffraction patterns (Figure 3.21) indicate the syntheses have been successful.

Table 3.12 *– Reaction conditions for synthesis of CPO-27. Metal acetate precursors dissolved in 10 ml H_2O and 2,5-dihydroxyterephthalic acid linkers dissolved in 10 ml THF before combination into gel.*

Metal	Ratio in gel (Metal:Ligand)	T (K)	Time (Hours)	Structure
Ni	2 : 1	373	72	Ni CPO-27
Co	2 : 1	373	72	Co CPO-27

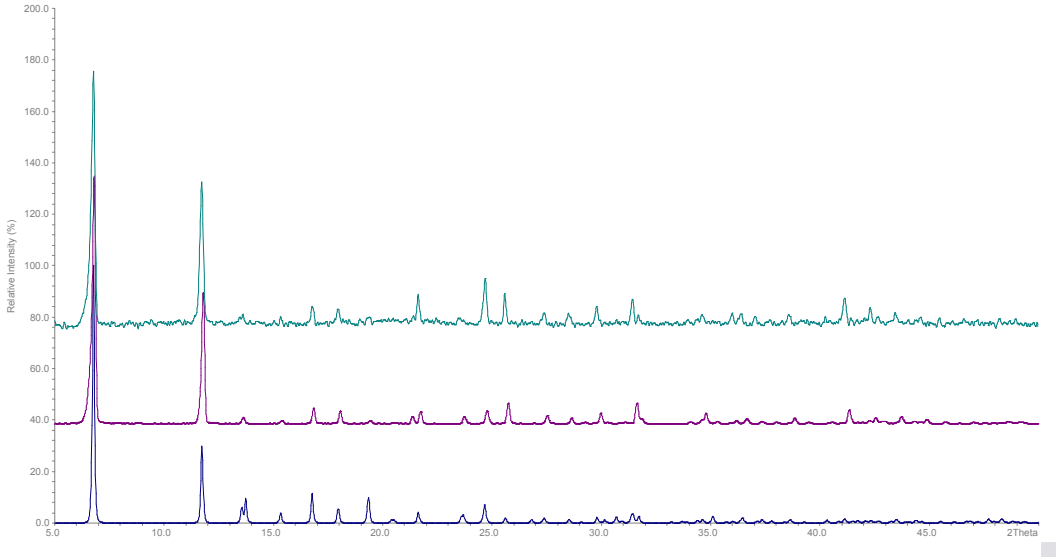

Figure 3.21 *- X-ray powder diffraction patterns of (top) Co CPO-27 and (middle) Ni CPO-27. Compared to (bottom) Co CPO-27 theoretical pattern generated by Stöe software (Cu K_α radiation).*

3.11 Synthesis of MIL structures

Several carboxylate MOFs (from the MIL-*n* series) were synthesised to compare to STA-12. As outlined in Chapter 1, a variety of reaction conditions and design methodologies have produced some interesting large and very large pore 3-D MOF structures.

3.11.1 Synthesis of MIL-47

The reaction of 1,4-benzenedicarboxylic acid (terephthalic acid) and vanadium (III) chloride hydrothermally in the ratio 1 : 0.25 : 100 produces the MIL-47 structure,[15] described in Chapter 1 (Figure 1.7). The as-prepared structure crystallises with linker molecules in the pores, removed by heating at 573 K in air to render it permanently porous. The powder X-ray diffraction patterns of the as-prepared and heated versions, compared to theoretical patterns, are outlined in Figures 3.22 and 3.23. The comparisons indicate MIL-47 has been successfully synthesised.

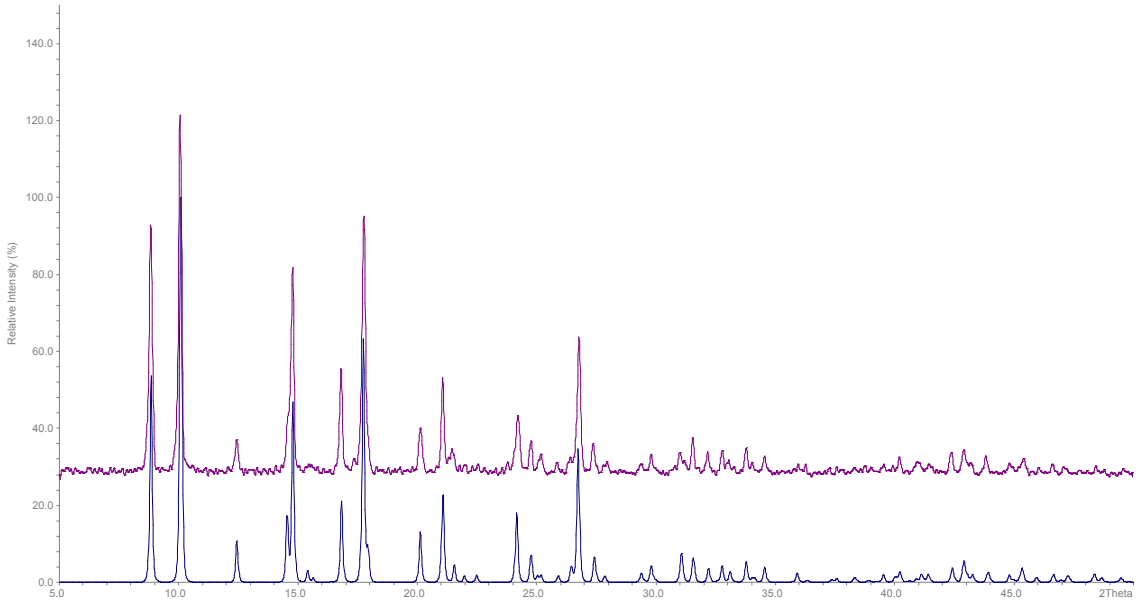

Figure 3.22 *- X-ray powder diffraction pattern of (top) as-prepared MIL-47. Compared to MIL-47as theoretical pattern generated by Stöe software (Cu K_α radiation).*

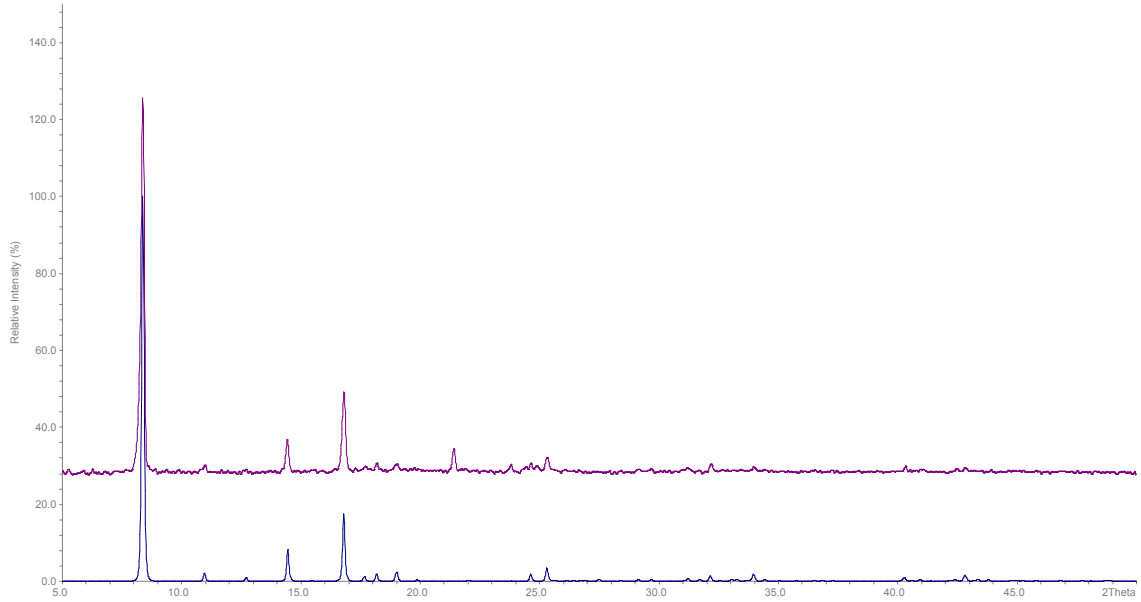

Figure 3.23 *- X-ray powder diffraction pattern of (top) MIL-47 heated at 573 K. Compared to MIL-47 theoretical pattern generated by Stöe software (Cu K_α radiation).*

3.11.2 Synthesis of MIL-53

MIL-53 was synthesised by reaction of chromium (III) and aluminium (III) nitrate with terephthalic acid.[16, 17] The structure has been previously described in Chapter 1 (Figure 1.6), and the reaction conditions used to synthesise Cr and Al MIL-53 are outlined in Table 3.13. The resulting X-ray powder diffraction patterns of the as-prepared structures, compared to theoretical patterns, are outlined in Figure 3.24.

Table 3.13 *– Reaction conditions for synthesis of Cr (+ HF in reaction to help dissolution of Cr nitrate) and Al MIL-53.*

Metal	Ratio in gel (Metal:Ligand:H_2O)	T (K)	Time (Hours)	Structure
Cr	1 : 1 : 280	493	72	Cr MIL-53
Al	1 : 0.5 : 80	493	72	Al MIL-53

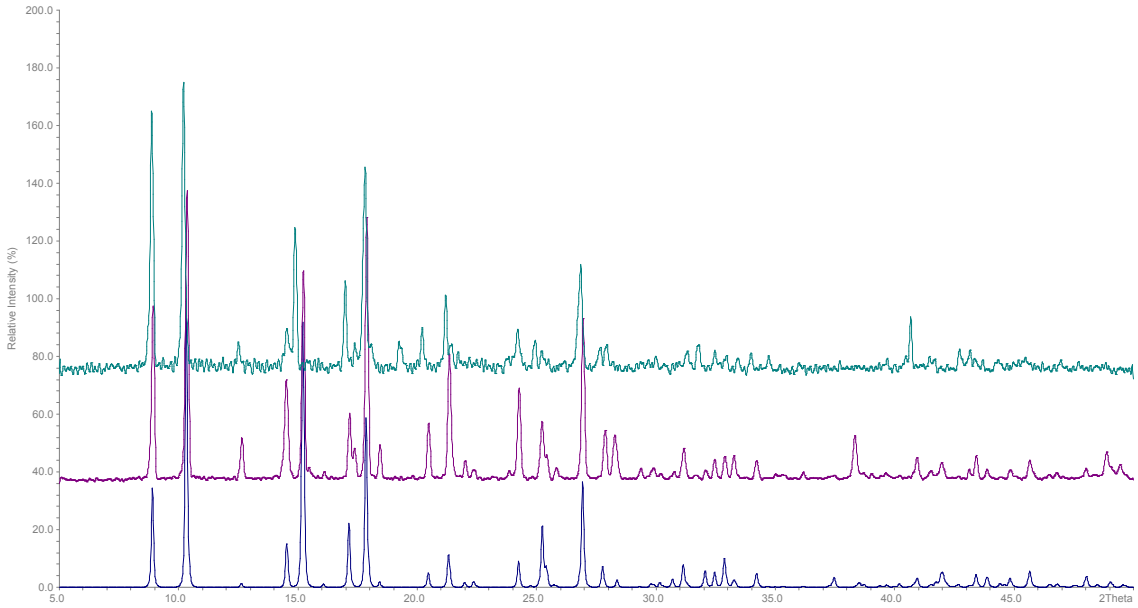

Figure 3.24 *- X-ray powder diffraction patterns of (top) as-prepared Cr MIL-53 and (middle) as-prepared Al MIL-53. Compared to (bottom) Al MIL-53as theoretical pattern generated by Stöe software (Cu K_α radiation).*

The X-ray powder diffraction patterns (Figure 3.24) indicate both the Al and Cr versions of MIL-53 have been successfully synthesised. Heating at 603 K removes the excess terephthalic acid molecules from the pores, forming the open pore ht version of the structure. On cooling to room temperature the pores take up water, forming the small pore lt version (explained in Figure 1.6 in Chapter 1).

3.11.3 Synthesis of MIL-68

The reaction of vanadium (IV) sulphate and terephthalic acid using N,N'-dimethylformamide (DMF) as the solvent in the ratio 1 : 2 : 117 produces the MIL-68 structure (described in Figure 1.8 in Chapter 1).[18] Using similar reaction conditions to MIL-47 produces MIL-68 as small, yellow, acicular crystals. The resulting X-ray powder diffraction pattern, compared to a theoretical pattern, is shown in Figure 3.25.

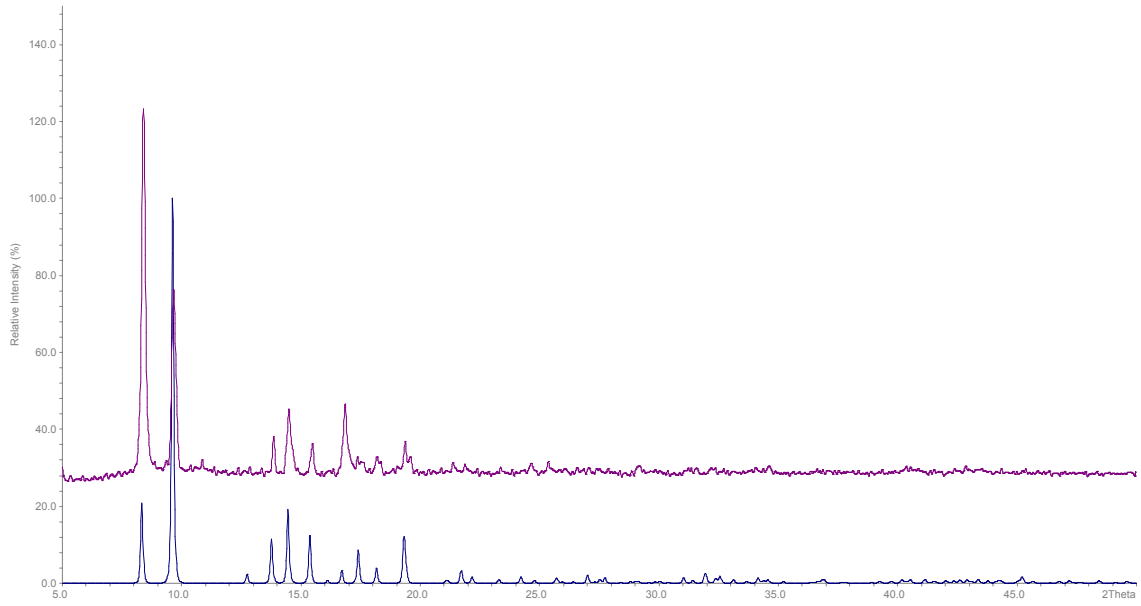

Figure 3.25 *- X-ray powder diffraction pattern of MIL-68 as-prepared compared to MIL-68as theoretical pattern generated by Stöe software (Cu K_α radiation).*

The pores of the MIL-68 structure are filled with disordered water and DMF molecules which are removed by heating in air at 523 K. The amount of these molecules present varies, affecting the peak intensities in the X-ray diffraction pattern compared to the idealised model (which has no guest molecules in the pores – Figure 3.25). Therefore, the X-ray diffraction patterns indicate MIL-68 is successfully synthesised as the peak positions match up well.

3.11.4 Synthesis of MIL-100

As described in Chapter 1, MIL-100 is a very large pore MOF with mesoporous sized cages (Figures 1.9, 1.10 and 1.11). It is formed by the hydrothermal reaction of chromium metal and trimesic acid in the presence of HF in the ratio (Metal : Ligand : HF : H_2O) 1 : 0.67 : 2 : 265.[19] Water molecules are bound to the chromium metal sites, and can be removed, leaving coordinatively unsaturated sites which act as Lewis acids. Coupled to the very large pore sizes, this creates some interesting properties, and the resulting nitrogen adsorption isotherm is shown in Figure 3.26.

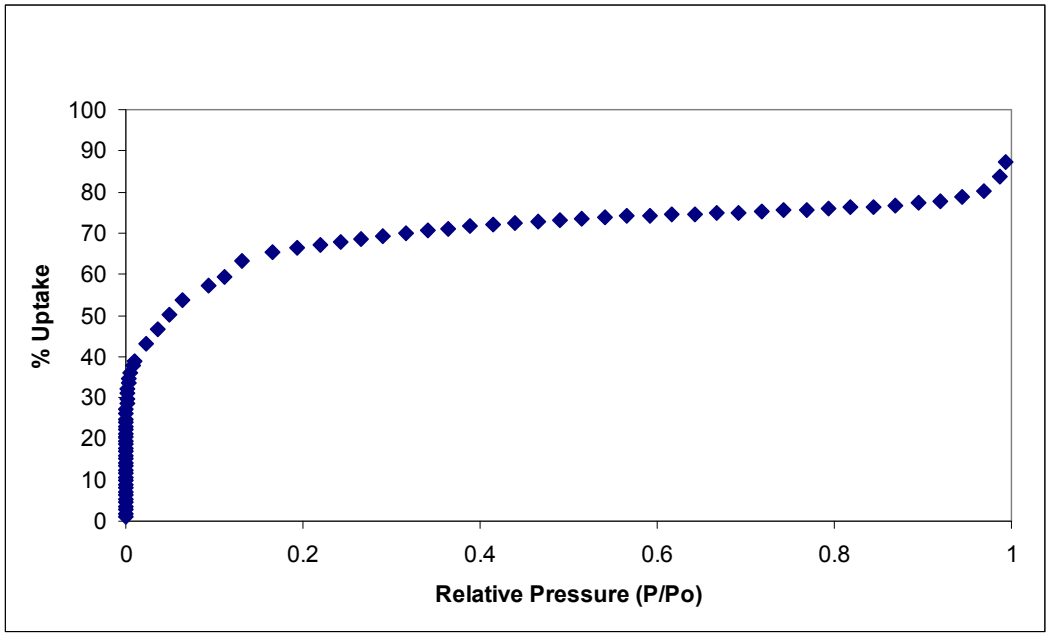

Figure 3.26 *– Nitrogen adsorption data at 77 K for MIL-100.*

Nitrogen adsorption indicates there is an uptake at $p/p_o = 0.4$ of *ca.* 70 wt%. The shape of the isotherm is somewhere between Type I and Type IV, reflecting the hierarchy of large micropores and mesoporous cages present in the structure. It is also a similar shape to that reported by Ferey *et. al.*,[19] where the reported uptake of 625 $cm^3\ g^{-1}$ at $p/p_o = 0.4$ corresponds to *ca.* 75 wt%. This is only slightly higher than that measured for the sample in Figure 3.26, suggesting MIL-100 has been successfully synthesised.

3.12 Conclusions about MOF syntheses

The bisphosphonate ligand N,N'-piperazinebis(methylenephosphonic acid) and the related derivatives with one and two methyl groups on the piperazine ring can be synthesised using a modified acid-catalysed Mannich reaction, and subsequently characterised by elemental analysis and NMR. Using these ligands in hydrothermal reactions with different metal sources produces four different structures when the metal : ligand ratio in the gel is 2 : 1. The structures synthesised are STA-12 (Mn, Fe, Co and Ni versions), Ni VSB-5, $CoH_2L.H_2O$ and Mg H_2L.

STA-12 can be synthesised using both the H_4L and H_4L-Me ligands, and the version formed using Ni and the H_4L ligand is the most crystalline with the best resolved X-ray powder diffraction pattern. The structure has been solved from both lab and synchrotron data, with the main features being helical chains of NiO_5N octahedra joined by ligands into 10 Å diameter hexagonal shaped pores containing significant amounts of water which orders at low temperature (100 K). Structural studies of the various STA-12 structures indicate the unit cell *c* parameters and volumes decrease in line with the decrease in the ionic radii of M^{2+}; the Co, Fe and Mn structures are less crystalline than the Ni structure; and using the H_4L-Me ligand reduces the crystallinity, and increases the unit cell volume due to more atoms being present.

Mixed metal samples of STA-12 can be formed based on Ni STA-12. A known amount of the Ni in the reaction gel (20 mol %) can be replaced with the same amount of Mg, Mn, Fe or Co. EDX analysis confirms more than one metal is present and the dopant metal is homogenously spread, while X-ray analysis shows STA-12 is formed. The samples are porous and potentially have interesting chemical properties that could be exploited for use in applications.

Reaction of the H_4L 2,5-diMe ligand with Ni, using the same reaction conditions as Ni STA-12, results in breakdown of the linker and formation of VSB-5, which is a fully inorganic Ni phosphate. This indicates an analogous MOF structure to Ni STA-12 cannot be formed, and the H_4L 2,5-diMe ligand is unstable under the reaction conditions.

$CoH_2L.H_2O$ is formed when the starting pH of the gel for Co STA-12 is 5 instead of 7, indicating there is a strong pH dependency in this reaction. The low pH means the H_4L ligand is not fully deprotonated during the course of the hydrothermal reaction, resulting in the formation of the previously reported blue coloured phase $CoH_2L.H_2O$. The Co^{2+} cations are tetrahedrally coordinated by only the phosphonate oxygens of the ligand, due to the nitrogen atoms being protonated. The structure has small pores which do not adsorb nitrogen and contain reversibly removable physically adsorbed water.

The hydrothermal reaction of Mg with H_4L results in the formation of a novel phase. The ratio of the metal : linker is the same as in STA-12, while elemental analysis indicates the ligand molecules are intact. The X-ray pattern can be indexed as monoclinic, and on dehydration it changes indicating there is some structural distortion. A weight loss of

10% due to water takes place between the relatively high temperatures of 453 and 473 K. This indicates water is strongly bound, although no nitrogen is adsorbed possibly due to the presence of small pores or structural distortions.

Several large pore carboxylate MOF structures (Ni and Co CPO-27, MIL-47, Al and Cr MIL-53, MIL-68 and MIL-100) have been synthesised to compare to STA-12. X-ray powder diffraction patterns, compared to theoretical computer generated patterns, indicate the structures have been successfully synthesised. They can then be used in investigations of the adsorption and catalytic properties of STA-12.

3.13 References

1) A. C. Larson and R. B. von Dreele, *Generalised crystal structure analysis system*, Los Alamos National Laboratory, USA, 1998

2) J. A. Groves, S. R. Miller, S. J. Warrender, C. Mellot-Draznieks, P. Lightfoot and P. A. Wright, *Chem. Commun.*, 2006, 3305

3) K. Moedritzer and R. R. Irani, *J. Org. Chem.*, 1966, **31**, 1603

4) J. P. Mowat, Honours Project "Synthesis and Characterisation of Novel Microporous Bisphosphonates", *University of St Andrews*, *St Andrews*, 2007

5) S. R. Miller, G. M. Pearce, P. A. Wright, F. Bonino, S. Chavan, S. Bordiga, I. Margiolaki, N. Guillou, G. Férey, S. Bourelly and P. L. Llewellyn, *J. Am. Chem. Soc.*, 2008, **130**, 15967

6) R. LaDuca, D. Rose, J. R. D. Debord, R. C. Haushalter, C. J. O'Connor and J. Zubieta, *J. Solid State Chem.*, 1996, **123**, 408

7) A. N. Fitch, *J. Res. NIST*, 2004, **109**, 133

8) A. Altomare, R. Caliandro, M. Camalli, C. Cuocci, C. Giacovazzo, A. Grazia, G. Moliterni and R. Rizzi, *J. Appl. Crystallogr.*, 2004, **37**, 1025

9) C. Janiak and T. G. Scharmann, *J. Am. Chem. Soc.*, 2002, **124**, 14010

10) R. D. Shannon, *Acta. Cryst. A*, 1976, **32**, 751

11) N. Guillou, Q. Gao, P. M. Forster, J-S. Chang, M. Nogués, S-E. Park, G. Férey and A. K. Cheetham, *Angew. Chem. Int. Ed.*, 2001, **40**, 2831

12) J. A. Groves, P. A. Wright and P. Lightfoot, *J. Chem. Soc.*, *Dalton Trans.*, 2005, 2007

13) P. D. C. Dietzel, Y. Morita, R. Blom and H. Fjellvåg, *Angew. Chem. Int. Ed.*, 2005, **44**, 6354

14) P. D. C. Dietzel, B. Panella, M. Hirscher, R. Blom and H. Fjellvåg, *Chem. Commun.*, 2006, 959

15) K. Barthelet, J. Marrot, D. Riou and G. Férey, *Angew. Chem. Int. Ed.*, 2006, **41**, 281

16) C. Serre, F. Millange, C. Thouvenot, M. Nogués, G. Marsolier, D. Louër and G. Férey, *J. Am. Chem. Soc*, 2002, **124**, 13519

17) T. Loiseau, C. Serre, C. Huguenard, G. Fink, F. Taulelle, M. Henry, T. Bataille and G. Férey, *Chem. Eur. J.*, 2004, **10**, 1373

18) K. Barthelet, J. Marrot, G. Férey and D. Riou, *Chem. Commun.*, 2004, 520

19) G. Férey, C. Serre, C. Mellot-Draznieks, F. Millange, S. Surblé, J. Dutour and I. Margiolaki, *Angew. Chem. Int. Ed.*, 2004, **43**, 6296

Chapter 4: STA-12 - Dehydration Studies

4.1 Introduction

As shown in Chapter 3 the structure of STA-12 contains a large amount of water, both physically adsorbed in the pores and coordinated directly to the metal cations. A study of the dehydration mechanisms is therefore required for an understanding of structural changes taking place during thermal activation to give a porous solid. Thermal activation is used later on in this work (Chapters 5 and 6) during studies of the adsorption and catalysis properties, so it is important the structures present during these processes are described and fully characterised.

4.2 Experimental and Characterisation Techniques

Powder samples were dehydrated by attaching a filled quartz capillary to a glass line. The samples were thermally treated over the course of several hours and sealed under vacuum (pressures of 1×10^{-3} Torr). The resulting powder samples were routinely examined by X-ray powder diffraction in a similar way to that outlined in Chapter 3. Structural refinement and analysis of the unit cell parameters was undertaken with the GSAS program suite[1] using the cell parameters and atomic coordinates for as-prepared Ni STA-12 as the starting point.[2] The structure of dehydrated Mn STA-12 was solved by restraining bonds and angles to chemically sound values and allowing atoms to move.
Diffuse reflectance-UV-Vis-near IR measurements were performed (in Turin) using a Varian Carey 5 spectrophotometer with a reflectance sphere. The powder samples were

pressed into pellets and thermally treated under vacuum at 423K in a quartz glass cell, which was then mounted onto the spectrophotometer.

Infra-red spectroscopic measurements were performed (in Turin) under controlled atmospheres using environmental cells which allow thermal treatment under vacuum, dosing of H_2O vapour and *in situ* spectra collection. FTIR spectra were collected in transmission mode on thin films deposited on a silicon wafer, at a resolution of 2 cm^{-1} using a Bruker IFS 66 FTIR spectrometer.

Thermogravimetric analysis and N_2 adsorption measurements were carried out as outlined in Chapter 3, with some additional N_2 adsorption measurements being carried out gravimetrically, using a Hiden IGA (Intelligent Gravimetric Analyser).

4.3 Dehydration of Ni STA-12[3]

Thermogravimetric analysis of Ni STA-12 shows water loss in three steps (Figure 4.1). 18 wt% is lost below 373 K, which is equivalent to three water molecules per Ni, and this weight loss is interpreted as due to physically adsorbed water. 7 wt% is lost between 373 and 423 K in two steps, interpreted as due to chemically adsorbed water and the loss of one water molecule per Ni. The approximate ratio of the weight loss is 2 : 1, which represents the loss of two thirds and then one third of the water chemically bound to the Ni^{2+} cations. The total water loss is 25 wt%, corresponding to a chemical formula of $Ni_2(H_2O)_2L.5.4H_2O$. The curve has a plateau in the 423 – 593 K range before a progressive weight loss due to structure decomposition. This plateau indicates once Ni STA-12 is dehydrated the structure suffers no more weight loss until 593 K, and the upper temperature for the plateau is similar to that observed for Ni CPO-27 (573 K).[4] At 1000 K the weight loss trace for Ni STA-12 has a slight weight rise, which can be attributed to the formation of Ni pyrophosphate ($Ni_2P_2O_7$) via incorporation of oxygen from the flowing air in the experiment.

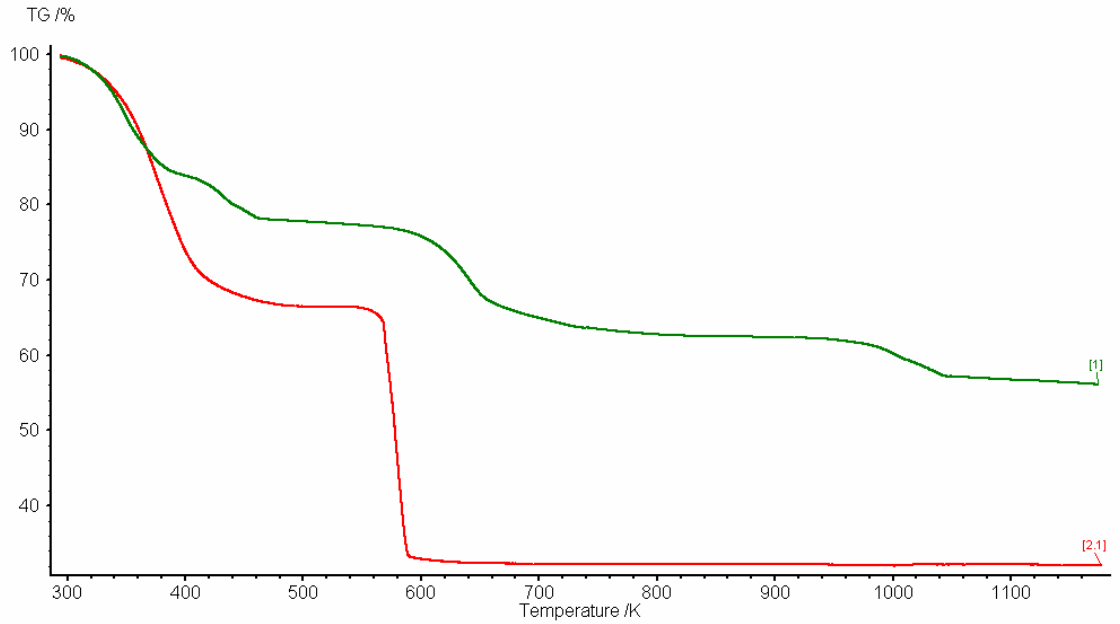

Figure 4.1 *– Thermogravimetric analysis of (green) Ni STA-12 and (red) Ni CPO-27 measured at 5K/min in air.*

Laboratory powder diffraction data indicates the rhombohedral symmetry of the as-prepared material is retained on evacuation at 323 K. It is lost on evacuation at 373 K where an intermediate, further dehydrated structure appears (Figure 4.2), accompanied by a colour change from green to brown/yellow (Figure 4.3). Evacuation at temperatures ≥ 423 K results in the formation of a fully dehydrated structure. The dehydrations are fully reversible, with restoration of the as-prepared structure and symmetry.

Figure 4.2 *– Laboratory powder X-ray diffractograms of Ni STA-12 (bottom to top) as-prepared, evacuated 323 K, 373 K, 423 K, re-hydrated (Cu K_α radiation).*

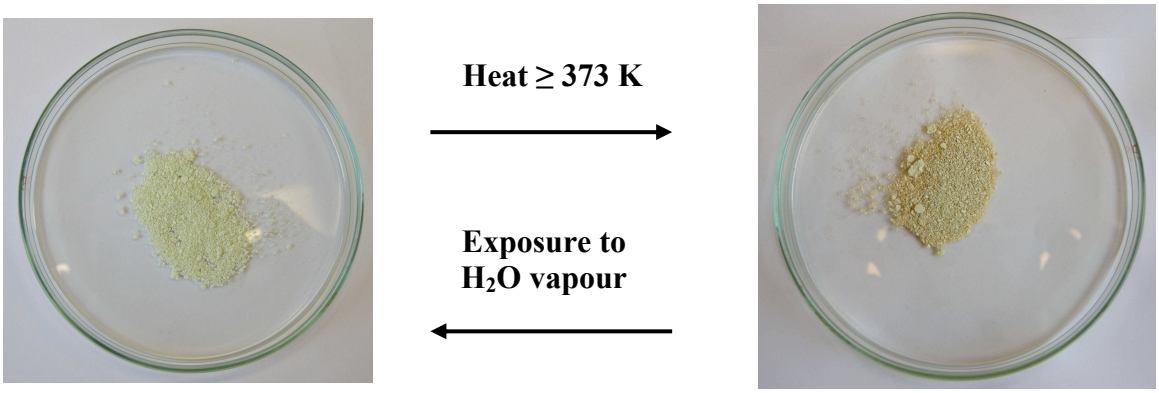

Figure 4.3 *– Illustration of colour change taking place in Ni STA-12 on dehydration. (Left) Light green as-prepared; (Right) Brown-yellow dehydrated.*

4.3.1 Nitrogen adsorption - Ni STA-12

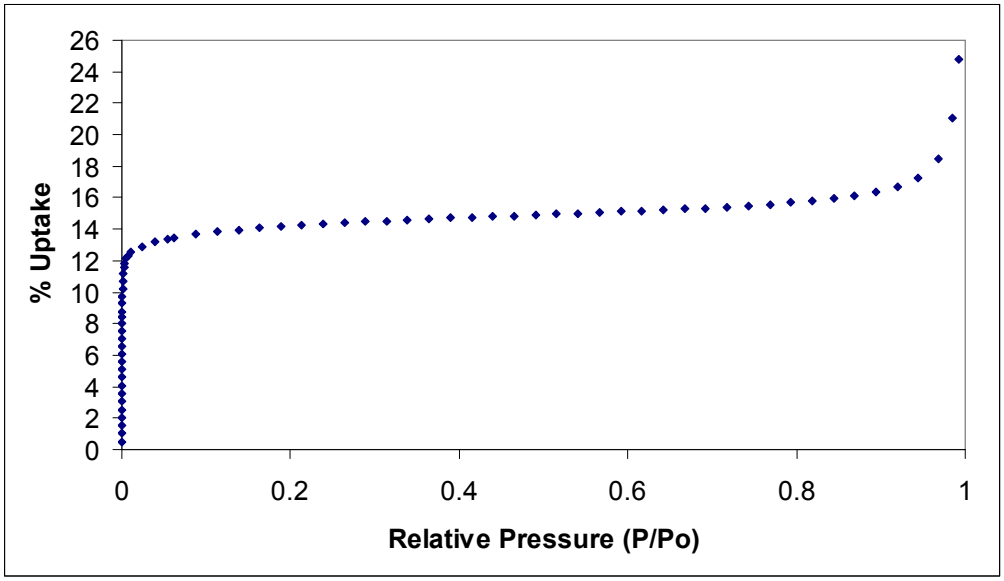

Figure 4.4 *- N_2 adsorption isotherm at 77 K for Ni STA-12. Measured volumetrically.*

The fully reversible nitrogen adsorption isotherm for fully dehydrated Ni STA-12 (Figure 4.4) has a Type I shape until higher p/p_o values, where a secondary uptake is noticeable which can be related to uptake between the particles in the sample. At a value of p/p_o = 0.4, Ni STA-12 has an uptake of 14 wt%, indicating the dehydrated structure has a porosity of 113 cm^3g^{-1}.

4.3.2 Structure solution of dehydrated forms of Ni STA-12 (work undertaken by Stuart Miller)[3]

As the X-ray diffraction patterns of Ni STA-12 are observed to change on dehydration, it was possible to solve the structures of the various phases using synchrotron data in a similar way to the as-prepared structure (Chapter 3).[5] Pattern indexing for the structure evacuated at 323 K was carried out within the EXPO2004 suite using TREOR.[6] For the structure evacuated at 423 K (fully dehydrated) the cell was indexed using the TOPAS suite [7, 8] and structural refinement was undertaken using the GSAS program suite.[1]

The sample evacuated at 373 K was found to be unstable in the synchrotron beam, and lab data was discovered to not be of a high enough resolution (Figure 4.3) to allow for structure solution. The cell was indexed as triclinic, using DICVOL91,[9] and crystallographic data for the three dehydrated forms of Ni STA-12[3] are outlined in Table 4.1 (atomic coordinates for structures dehydrated at 323 K and 423 K are outlined in Appendices 3 and 4).

Table 4.1 *– Crystallographic parameters for dehydrated forms of Ni STA-12.*[3]

Dehydration T (K)	323	373	423
Formula	$Ni_2(H_2O)_2L$	$Ni_2(H_2O)_{0.667}L$	Ni_2L
Unit Cell Composition	$Ni_{18}P_{18}O_{72}N_{18}C_{54}H_{108}$	$Ni_6P_6O_{20}N_6C_{18}H_{40}$	$Ni_6P_6O_{18}N_6C_{18}H_{36}$
Formula Weight (Unit Cell)	3775.5	1198.5	1162.5
Calculate density (g cm^{-3})	1.506	1.432	1.473
Space Group	R-3	P-1	P-1
a (Å)	27.9144(1)	6.1288(7)	6.03475(5)
b (Å)	27.9144(1)	15.3497(19)	14.9156(2)
c (Å)	6.1655(2)	16.6292(21)	16.1572(7)
α (°)	90	114.608(7)	112.5721(7)
β (°)	90	98.449(14)	95.7025(11)
γ (°)	120	94.740(32)	96.4950(11)
V ($Å^3$)	4160.58(2)	1388.8(2)	1318(3)
Diffractometer	ESRF (ID31)	Lab (STOE)	ESRF (ID31)
Temperature (K)	100	298	100
Wavelength (Å)	0.8002	1.5406	0.8002
R_{wp}	0.0782	-	0.0694
R_p	0.0547	-	0.0512

4.3.3 Description of dehydrated Ni STA-12 structures[3]

From a combination of the high resolution structural determination of as-prepared Ni STA-12 (Chapter 3) and the TGA analysis, the first weight loss is associated with removal of all of the physisorbed water from the pores. The second and third weight losses are therefore attributed to removal of water bound to the Ni^{2+} cations.

Evacuation at 323 K removes the physisorbed water and rhombohedral symmetry is retained similar to the as-prepared structure. The as-prepared and evacuated at 323 K structures are essentially the same, the main difference being the presence or absence of physisorbed water in the pores (Figure 4.5).

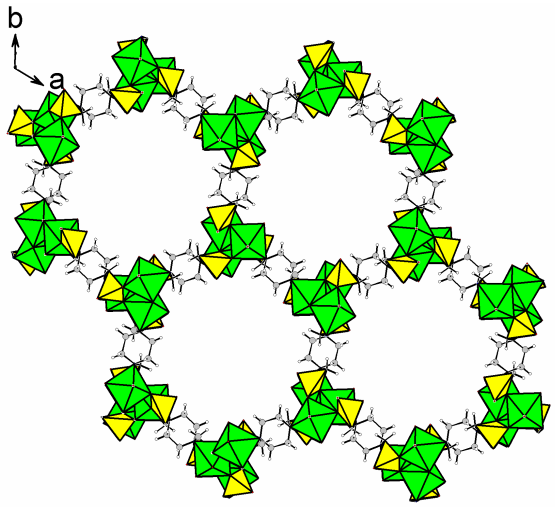

Figure 4.5 *– Framework structure of Ni STA-12 evacuated at 323K (viewed down c-axis). Ni centred octahedra in green, phosphonate in tetrahedra yellow, carbon atoms in grey and hydrogen atoms in white.*

As observed in Figure 4.3, when Ni STA-12 is evacuated at 373 K the colour changes from light green to brown/yellow. This suggests the local symmetry surrounding the Ni^{2+} cations changes with dehydration, and this can be followed by UV-visible spectroscopy (Figure 4.6). As-prepared Ni STA-12 is characterized by an intense band at 37000 cm^{-1}, associated with the organic linker, and a series of bands in the metal *d-d* transition region.

These comprise bands at 23800, 14300 and 7800 cm^{-1}, with a further band at 5200 cm^{-1}. For Ni^{2+} in O_h symmetry only three weak bands in the *d-d* transition region (Chapter 2) would be expected (23800 cm^{-1} - $^3A_{2g}$ (F) → $^3T_{1g}$ (P), 14300 cm^{-1} - $^3A_{2g}$ (F) → $^3T_{1g}$ (F) and 7800 cm^{-1} - ^3A_2g (F) → $^3T_{2g}$ (F)),[10] so the appearance of a fourth band in the near Infra-red region (5200 cm^{-1}) is the result of nitrogen being inside the first coordination sphere of Ni^{2+}. When nitrogen is coordinated to Ni^{2+}, the point group changes from O_h to C_{4v}, resulting in spin orbital splitting and an extra electron transition.

Thermal treatment under vacuum at 423 K causes major changes in the spectrum, especially in the *d-d* region. There are now bands at 23300, 19300, 12350, 9170, 5550 and 5100 cm^{-1}, while the organic linker contribution has a small red shift. The number of bands suggest the NiO_4N polyhedra in fully dehydrated Ni STA-12 are five-coordinate, and are intermediate between tetragonal pyramids and trigonal bipyramids.[11] Therefore, removing the water coordinated directly to the Ni^{2+} cations results in a large modification of the electronic structure. These changes are fully reversible, as seen from the X-ray data.

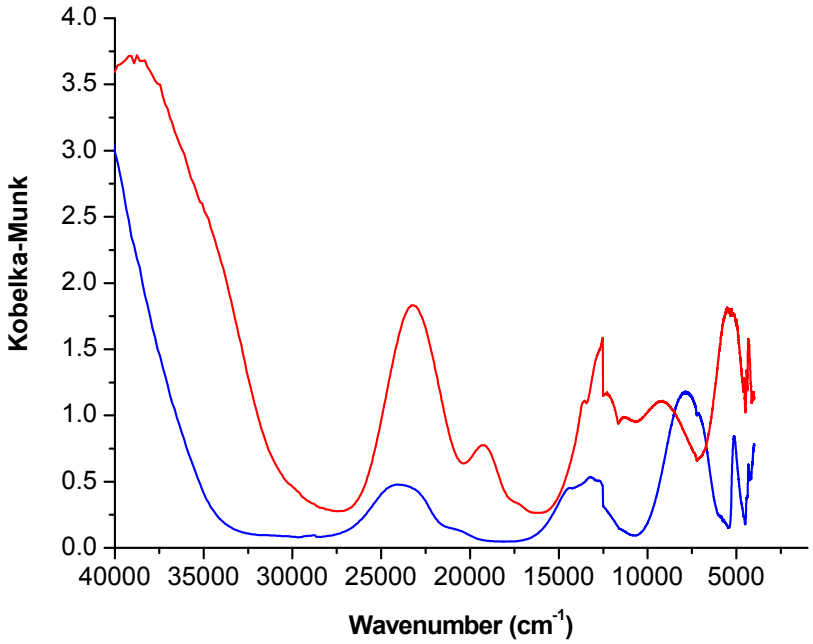

Figure 4.6 *– Diffuse Reflectance UV-vis-NIR of Ni STA-12. (Blue) as-prepared; (Red) evacuated 423 K.*

Using the information from X-ray diffraction and UV-visible spectroscopy, the structural modifications taking place when Ni STA-12 is completely dehydrated can be understood (Figure 4.7). The framework is based on helical chains of nickel-centred polyhedra linked by bisphosphonate ligands, and the methylenephosphonate groups are in axial positions to the piperazine rings (which adopt chair configurations like the as-prepared structure). The structure has large pores running down the channel axis, and the channels are elliptical in cross section. The free dimensions of the pores, taking into account the van der Waals radii of hydrogen, are 8 Å × 9 Å rather than *ca.* 10 Å in the as-prepared structure.

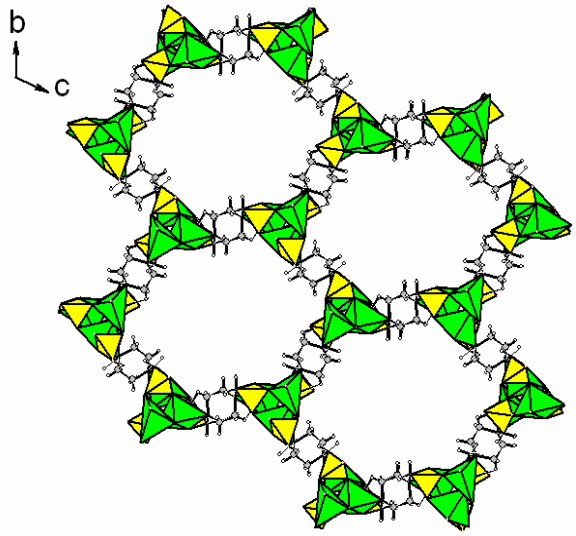

Figure 4.7 *– Framework structure of fully dehydrated Ni STA-12 viewed down the channel axis. Ni centred polyhedra in green, phosphonate tetrahedra in yellow, carbon atoms in grey and hydrogen atoms in white.*

The removal of the coordinated water results in formation of three crystallographically distinct nickel cations. The nickel cations are still coordinated by one ligand nitrogen, but are now coordinated by only four oxygen atoms, all from phosphonate groups. As a result, the nickel cations are five-coordinate (as observed by UV-vis-NIR - Figure 4.6).
The spiral inorganic chains are shown in Figure 4.8 compared to the as-prepared structure. The NiO_4N polyhedra are both corner and edge-sharing. $Ni(1)O_4N$ and

$Ni(2)O_4N$ share an edge, $Ni(1)O_4N$ and $Ni(3)O_4N$ share a corner and all the PO_3C tetrahedra are corner-sharing as in the as-prepared structure. There are also three crystallographically distinct phosphorus atom positions, with two out of the three phosphonate groups ($P(1)O_3C$ and $P(2)O_3C$) changing coordination so all three oxygen atoms are bound to nickel cations. The third phosphonate group ($P(3)O_3C$) remains in its original position with a P-O bond pointing into the pore (which might be P=O).

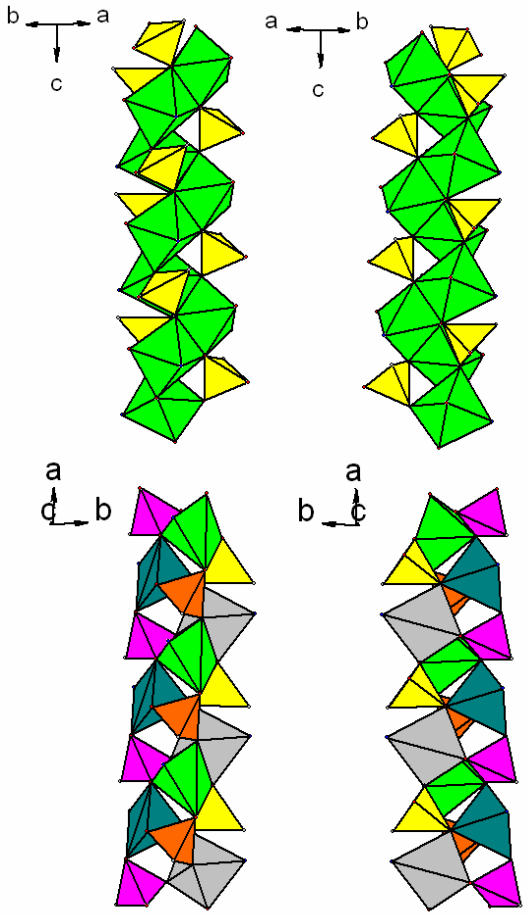

Figure 4.8 *– Two different views of the inorganic chain in as-prepared (top) and fully dehydrated (bottom) Ni STA-12. As-prepared – NiO_4N polyhedra in green, PO_3C tetrahedra in yellow; Dehydrated - crystallographically distinct NiO_4N and PO_3C polyhedra in different colours, Ni(1) green; Ni(2) grey; Ni(3) dark blue-green; P(1) orange; P(2) purple; P(3) yellow.*

The structural reorganisation to transform Ni STA-12 from the hydrated to the dehydrated form is illustrated in Figure 4.9. The rearrangement proceeds via the loss of

coordinated water molecules from the nickel cations. There is then rotation of two out of every three of the phosphonate groups ($P(1)O_3C$ and $P(2)O_3C$) to allow full coordination with nickel cations, while the third phosphonate group ($P(3)O_3C$) does not change coordination.

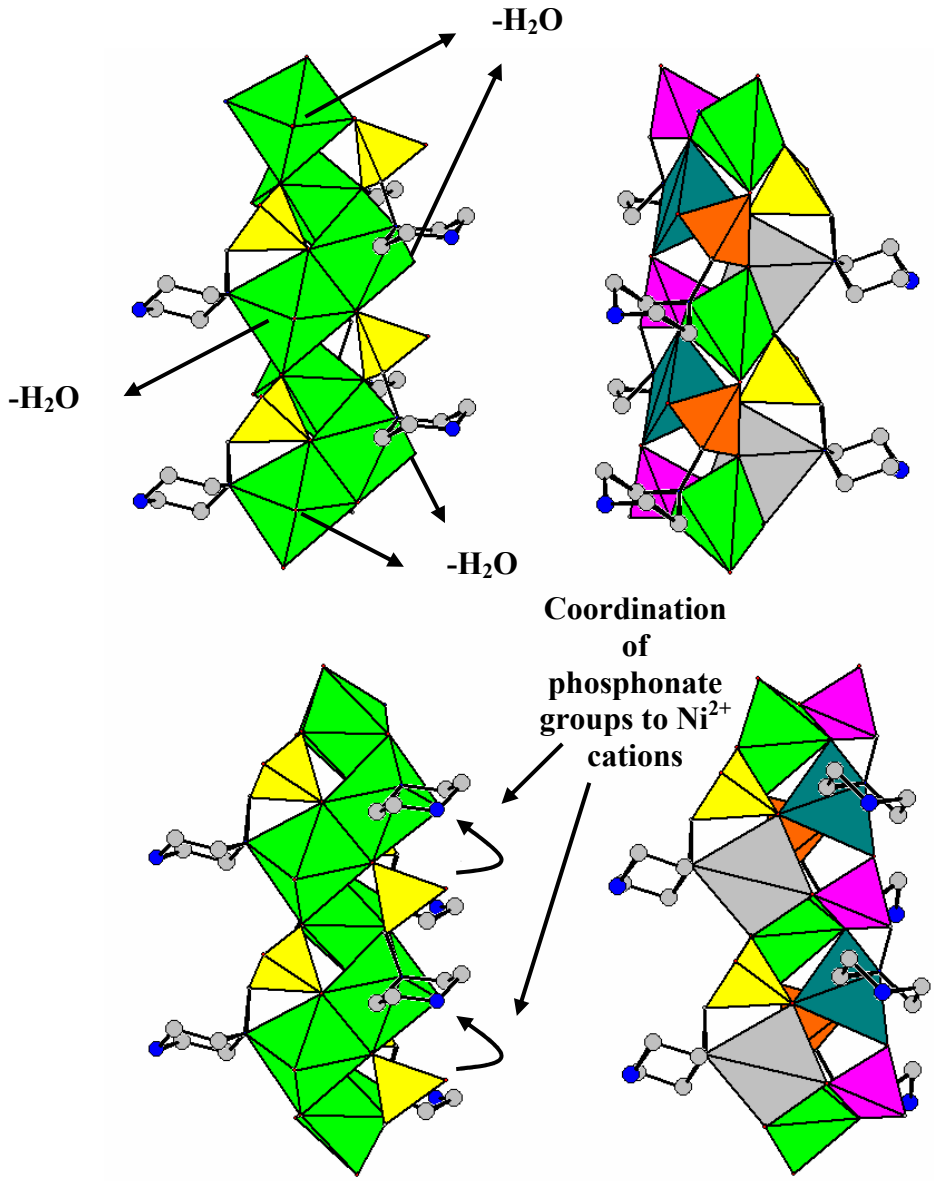

Figure 4.9 *– Two comparisons of inorganic chains and coordinated piperazine rings for (left) as-prepared and (right) fully dehydrated Ni STA-12, showing with arrows the rearrangements giving rise to the structural changes occurring on loss of water molecules coordinated to the nickel cations. Colour scheme as Figure 4.8.*

4.3.4 Infra-red study of dehydration mechanism for Ni STA-12 (in collaboration with Prof S. Bordiga at University of Turin, Italy)

4.3.4.1 Description of spectra produced[3]

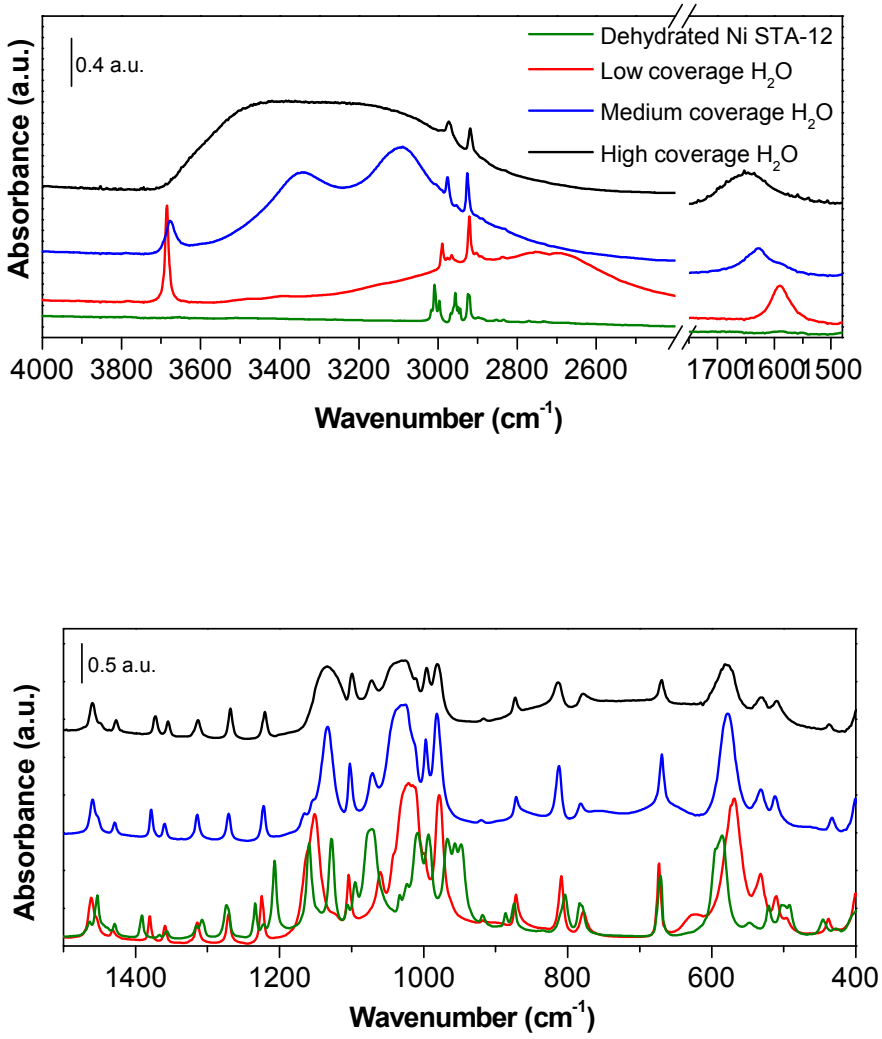

Figure 4.10 *– Effect of dehydration/hydration on IR spectra of Ni STA-12. (Top) OH stretching and bending region; (Bottom) framework bending region.*

In order to allow for greater clarity in Figure 4.10, the data has been offset along the vertical scale, with the coverage of H_2O increasing from the bottom to the top. The IR spectrum of the as-prepared sample (black line in Figure 4.10) in the high frequency region (3800 – 1500 cm^{-1}) has bands from hydrogen-bonded water adsorbed onto the framework. Two broad bands are observed at 3300 cm^{-1} and 1630 cm^{-1}, from stretching ν(OH) and bending δ(OH). The sharp bands at 2920 cm^{-1} and 2990 cm^{-1} are from symmetrically distinct C-H vibrations. In the low frequency region (1500 – 400 cm^{-1}) the spectrum has several framework resonances, assigned as vibrations of CH_2 groups (1460 cm^{-1} and 1373 cm^{-1}); vibrations from combinations of ν(C-C), ν(C-N) and ν(P-O) (1160 cm^{-1} – 950 cm^{-1}); and bending of PO_3C (580 cm^{-1}, 530 cm^{-1} and 508 cm^{-1}).[12-15]

Dehydration at 423 K results in large changes in the IR spectrum (green spectrum in Figure 4.10). In the high frequency region the features from water disappear, and the C-H vibrations are more complex, with splitting of peaks as a result of the reduction in symmetry from rhombohedral to triclinic. The framework region also changes, with the bands better resolved and some slight shifting in peak positions. A narrow band at 1207 cm^{-1} appears, suggesting P=O groups are formed (from the $P(3)O_3C$ tetrahedra).[12-15]

H_2O was dosed stepwise onto the sample. At low H_2O coverage (red spectrum) in Figure 4.10) there is the appearance of a sharp band at 3685 cm^{-1} indicating isolated -OH groups are forming. The broad bands at 2700 cm^{-1} and 1590 cm^{-1} are due to stretching and bending of -OH groups in a system with strong hydrogen bonds.[16, 17] The C-H region starts to be dominated by two bands as the symmetry increases to rhombohedral. There is also a reduction in the intensity of the band at 1207 cm^{-1}, indicating P=O is reacting with water.

There are also changes in the ν(P-O) region with the bands at 1126 cm^{-1}, 1072 cm^{-1} and 959 cm^{-1} decreasing in intensity, and the bands at 1150 cm^{-1}, 1026 cm^{-1} and 977 cm^{-1} increasing in intensity. This can be explained as the result of distortion of the PO_3C tetrahedra as they move into positions similar to the as-prepared structure. There is also a broad band at 496 cm^{-1} associated with bending of an Ni-OH species.

At intermediate H_2O coverage (blue spectrum in Figure 4.10) the changes in the IR spectra occur in the high frequency region. The band at 3685 cm^{-1} decreases in intensity as the free –OH groups form hydrogen bonds with incoming water. The band for

hydrogen bonded –OH groups at 2700 cm^{-1} decreases in intensity, and the spectrum has new maxima at 3100 cm^{-1} and 3400 cm^{-1}. These maxima can be explained as the formation of an Evans window (Chapter 2) at 3200 cm^{-1} due to Fermi Resonance of 2δ(OH) in hydrogen bonded water.[16, 17]

When large amounts of adsorbed water are present (black spectrum at top of graphs in Figure 4.10) the band due to free –OH groups is completely removed, and a broad absorption centred at 3300 cm^{-1} forms. The IR spectrum obtained after equilibrium with H_2O vapour is the same as the spectrum collected on the as-prepared solid. This means the reversibility of the dehydration/hydration process, seen from the colour changes and X-ray data, is confirmed.

4.3.4.2 Interpretation of dehydration/hydration mechanism from Infra-red spectra

The IR spectrum for low coverage of H_2O, combined with knowledge about the fully and partially hydrated structures, indicates water adsorption generates two types of hydroxyl groups, of which one is strongly hydrogen bonded. Two possible configurations are a free Ni-OH group and a hydrogen-bonded POH-ONi or vice versa, suggested below in Scheme 4.1. The free -OH groups have no acidic character, so they are likely to be Ni-OH groups, meaning the situation on the left in Scheme 4.1 is more likely.

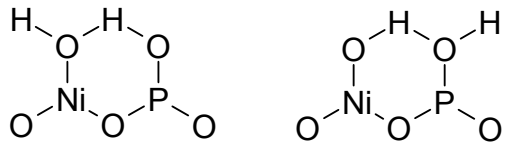

Scheme 4.1 *– Two possible cyclic species formed by adsorption of first water molecules.*

Further hydration results in the fully coordinated phosphonate groups reacting so one P-O bond in every PO_3C is pointing into the pores. As discussed before, the mechanism (Figure 4.9) involves coordination of a water molecule at a nickel cation site, displacing

the phosphonate oxygen from the nickel. There is then rotation of the phosphonate group so one of the P-O bonds is pointing into the pore space.

4.4 Dehydration of Ni Me STA-12

Thermogravimetric analysis of Ni Me STA-12 (Figure 4.11) shows water loss in two steps, with 15 wt% lost below 393 K and 9 wt% lost between 393 and 493 K. The second weight loss, which is due to chemisorbed water, occurs in a single broad event. The curve has a plateau in the 493 – 600 K temperature range before structural decomposition. The TGA analysis indicates Ni Me STA-12 has a thermal stability, total water loss and final water loss temperature similar to Ni STA-12. At 1000 K the weight loss indicates there is a slight weight rise, attributed to the formation of Ni pyrophosphate ($Ni_2P_2O_7$) via incorporation of oxygen from the flowing air in the experiment.

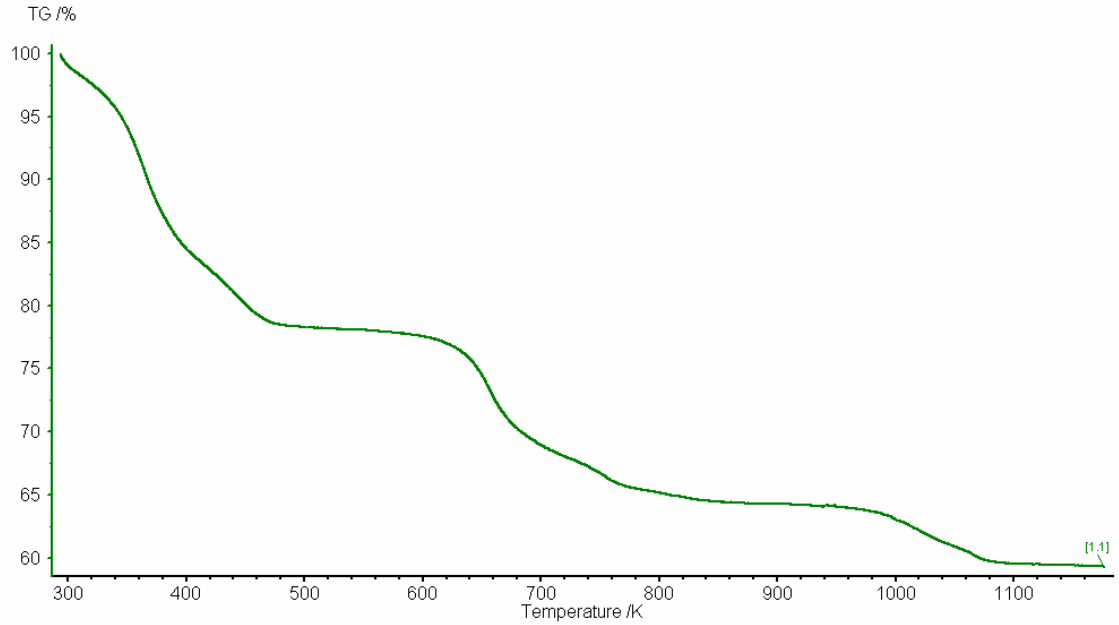

Figure 4.11 *- Thermogravimetric analysis of Ni Me STA-12 measured at 5K/min in air*

Laboratory powder diffraction data (Figure 4.12) indicates the rhombohedral symmetry of Ni Me STA-12 is retained with evacuation up to 423 K, although the crystallinity is reduced (increase in peak width). The cell parameters from Rietveld refinement are

outlined in Table 4.2 compared to Ni Me STA-12 (from Table 3.6 in Chapter 3), and the final Rietveld plot is shown in Figure 4.13 (more information on parameters and goodness of fit for Rietveld refinement in Appendix 5). The data shows the *a* cell parameter increases slightly by 0.3 Å, the *c* cell parameter reduces slightly by 0.12 Å and the unit cell volume stays the same after water loss. This indicates there appears to be some strain building up in the structure as dehydration takes place. The dehydration is accompanied by a similar colour change to Ni STA-12, and is also fully reversible with restoration of the original structure and crystallinity.

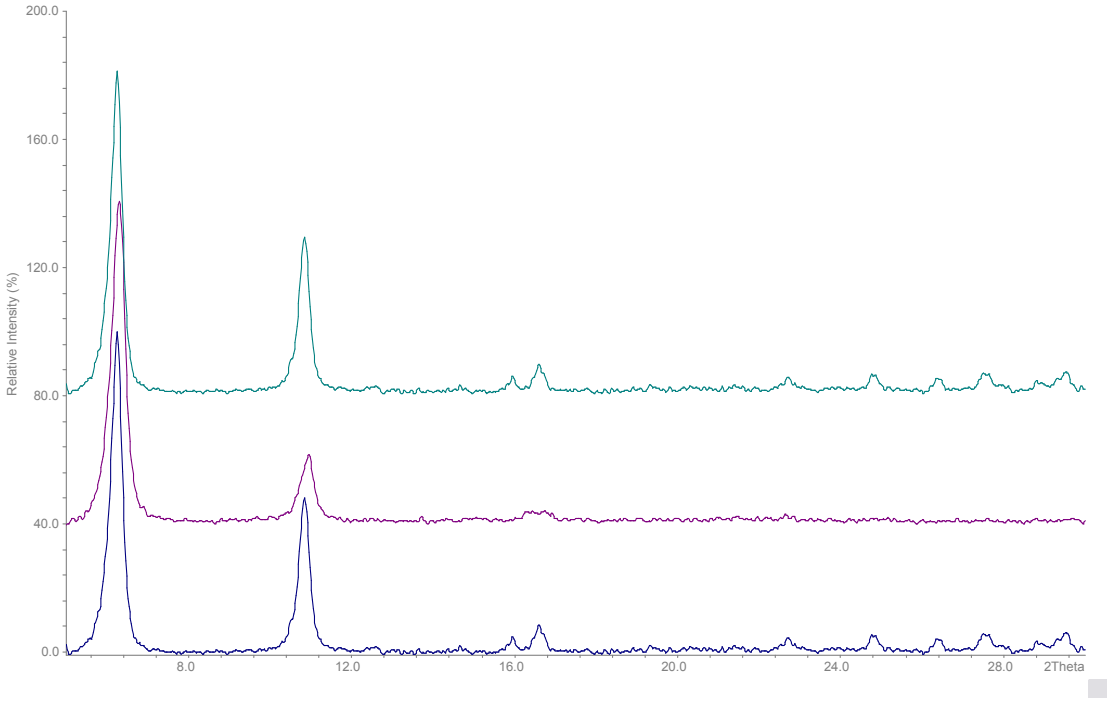

Figure 4.12 *– Laboratory powder X-ray diffractograms of Ni Me STA-12 (bottom to top) as-prepared, evacuated 423 K, re-hydrated (Cu K_α radiation).*

Table 4.2 *– Comparison of cell parameters of as-prepared and dehydrated Ni Me STA-12.*

Formula	$Ni_2(H_2O)_2$L-Me.5.4H_2O	Ni_2L-Me
Space Group	R-3	R-3
a (Å)	27.9789(28)	28.250(25)
b (Å)	27.9789(28)	28.250(25)
c (Å)	6.2391(6)	6.119(13)
α (°)	90	90
β (°)	90	90
γ (°)	120	120
V (Å^3)	4230(8)	4229(11)
Diffractometer	Lab (STOE)	Lab (STOE)
Temperature (K)	298	298
Wavelength (Å)	1.5406 (Cu K_α)	1.5406 (Cu K_α)
R_{wp}	0.1221	0.1244

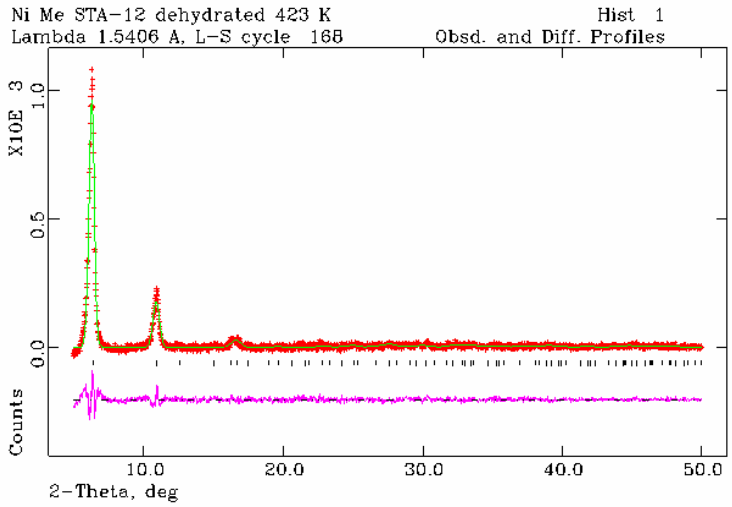

Figure 4.13 *- Rietveld refinement of dehydrated Ni Me STA-12 (Cu K_α radiation) – red: measured pattern, green: calculated pattern, purple: difference between measured and calculated patterns.*

4.4.1 Nitrogen adsorption - Ni Me STA-12

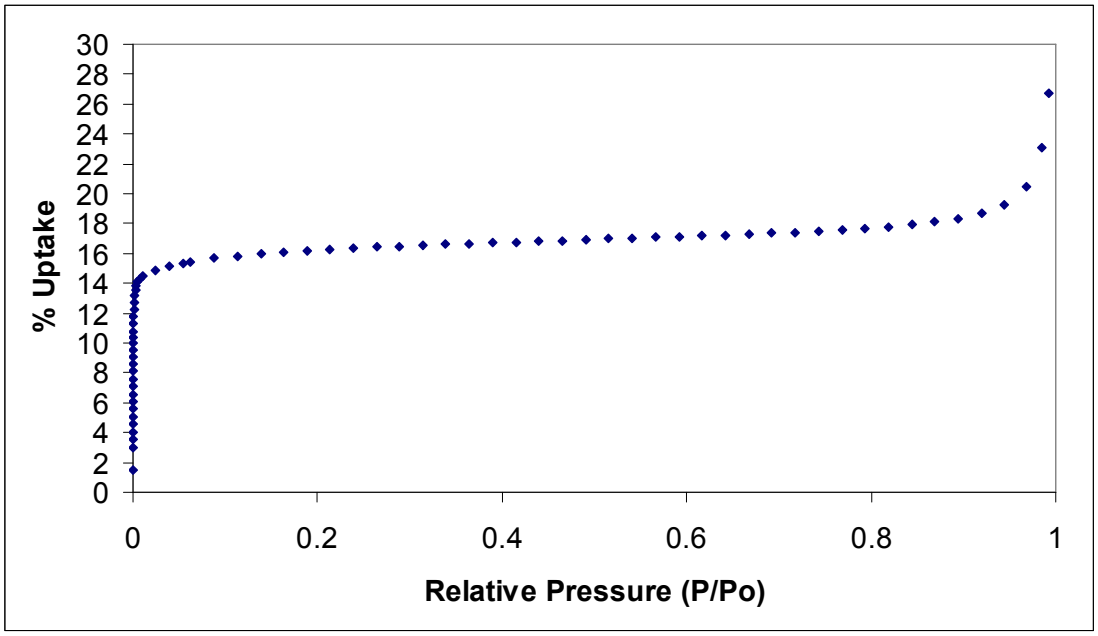

Figure 4.14 *- N_2 adsorption isotherm at 77 K for Ni Me STA-12. Measured volumetrically.*

The nitrogen adsorption isotherm for Ni Me STA-12 dehydrated at 423 K is fully reversible (Figure 4.14). It has a Type I shape up until higher p/p_o values, where there is a secondary uptake similar to that observed for Ni STA-12. At $p/p_o = 0.4$, Ni Me STA-12 has an uptake of 16 wt%, translating to a porosity of 130 cm^3g^{-1}, which is slightly higher than Ni STA-12.

4.5 Comparison of dehydration behaviour of Ni STA-12 and Ni Me STA-12

The structural data from dehydration of Ni STA-12 is helpful for understanding the dehydration behaviour of Ni Me STA-12. When prepared with the H_4L-Me ligand the STA-12 structure does not distort from rhombohedral to triclinic symmetry on dehydration (Figure 4.12). While there is enough space for the methyl groups in equatorial positions on the piperazine rings in the fully hydrated structure, the methyl

groups would have unreasonably close distances to the nearest framework atom in a hypothetical dehydrated Ni Me STA-12 (with the same triclinic symmetry framework as fully dehydrated Ni STA-12).

The distances between equatorial H atoms and framework atoms in fully dehydrated Ni STA-12 are, at 2.5 Å, only just large enough to accommodate the H and framework atom van der Waals radii (Figure 4.15). If methyl groups were present on the ligand, there would not be enough room, so the structure retains rhombohedral symmetry after dehydration. This helps to explain the higher adsorption uptake for N_2, as the 'propping' open of the pores by the methyl groups allows for higher porosity.

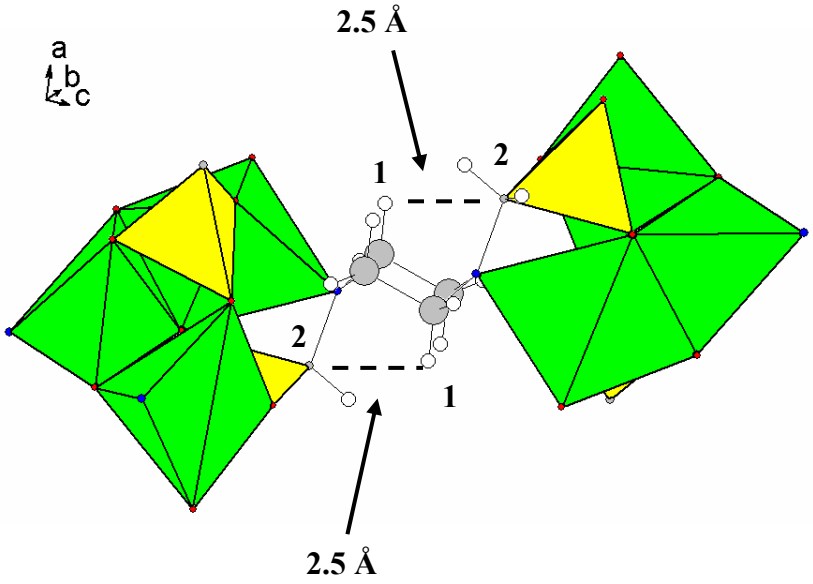

Figure 4.15 *– View of one ligand connecting two inorganic chains in fully dehydrated Ni STA-12. Distance between equatorial hydrogen (1) and nearest framework atom (2) outlined by dashed lines (colour scheme as Figure 4.7).*

Replacing half of the H_4L ligand in the reaction gel with the H_4L-Me ligand produces the Ni STA-12 structure with a lower crystallinity. On dehydration there is no change from rhombohedral symmetry, although the peaks become significantly broader, indicating strain is present in the crystalline lattice (Figure 4.16). Reducing the number of methyl groups present by a half therefore prevents structural distortion from taking place. Enough of the equatorial positions on the piperazine rings must be taken up by methyl

groups, meaning there are still steric grounds to prevent the structural rearrangement from taking place.

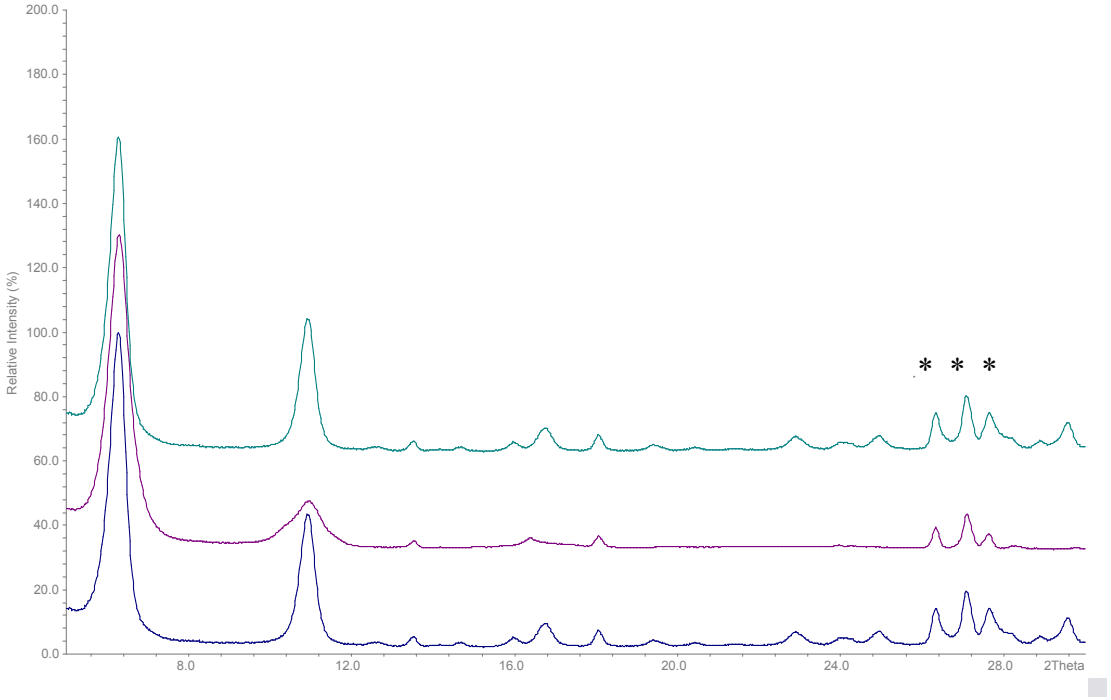

Figure 4.16 *- Laboratory powder X-ray diffractograms of Ni 50% L: 50% L-Me STA-12 (bottom to top) as-prepared, evacuated 423 K, re-hydrated (Cu K_α radiation). Asterisks indicate impurity phase.*

4.6 Dehydration of Co STA-12

Looking at the thermogravimetric analysis of Co STA-12 (Figure 4.17) there is water loss in two steps, with 14 wt% lost below 373 K and 11 wt% lost between 373 K and 423 K. The total weight loss for water is the same as for Ni STA-12, but the second weight loss attributed to chemisorbed water is not composed of two separate steps. The curve has a plateau in the 423 – 603 K range, indicating Co STA-12 has no weight loss after removal of water at a higher temperature than Ni STA-12. The temperature is also higher than that seen for Co CPO-27 (573 K compared to 603 K).[18] Above 603 K Co STA-12 decomposes, and at 920 K the weight loss trace indicates there is a slight weight rise,

which can be attributed to the formation of Co pyrophosphate ($Co_2P_2O_7$) via incorporation of oxygen from the flowing air in the experiment.

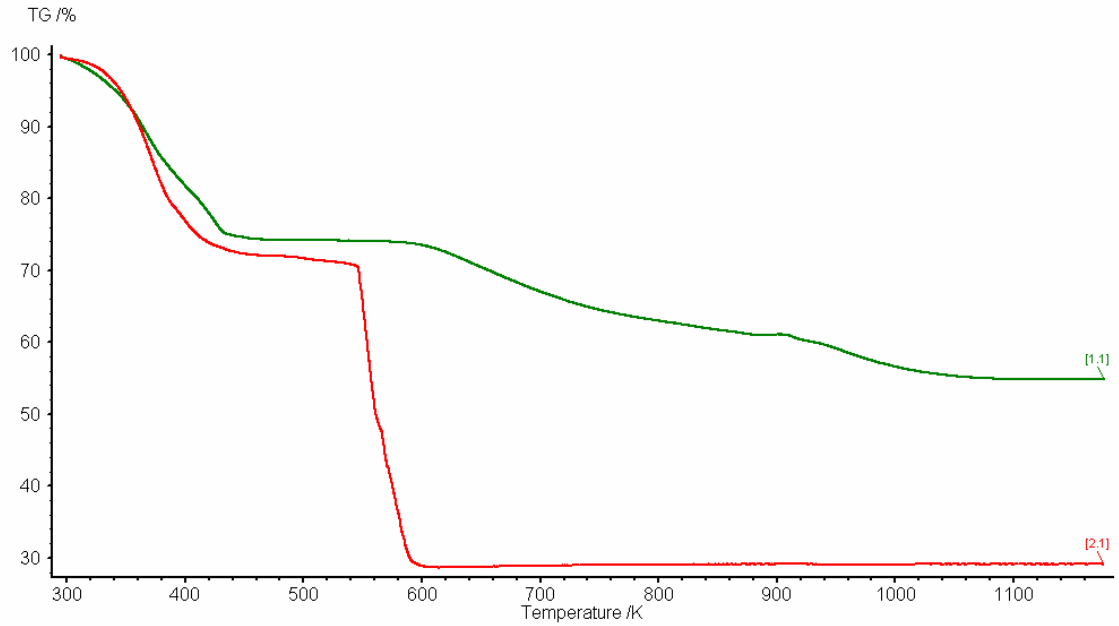

Figure 4.17 *- Thermogravimetric analysis of (green) Co STA-12 and (red) Co CPO-27 measured at 5K/min in air.*

Evacuation of Co STA-12 at 323 K results in a colour change from pink to dark blue (Figure 4.18). Laboratory powder diffraction data indicates rhombohedral symmetry is lost, with a splitting of the first peak. This evolves over higher temperatures of evacuation, until at 473 K this has split into three separate peaks (Figure 4.19). Using the structure for fully dehydrated Ni STA-12 as a starting point,[3] and keeping the atomic coordinates fixed, the cell was refined and indexed as triclinic with similar unit cell parameters and unit cell volume to fully dehydrated Ni STA-12 (Table 4.3). The final Rietveld plot is shown in Figure 4.20 (more information on parameters and goodness of fit for Rietveld refinement in Appendices 4 and 5), and it indicates the structural distortions taking place in Co STA-12 as water is removed must be similar to those happening during dehydration of Ni STA-12. The evacuations are fully reversible, with the restoration of the original structure and symmetry.

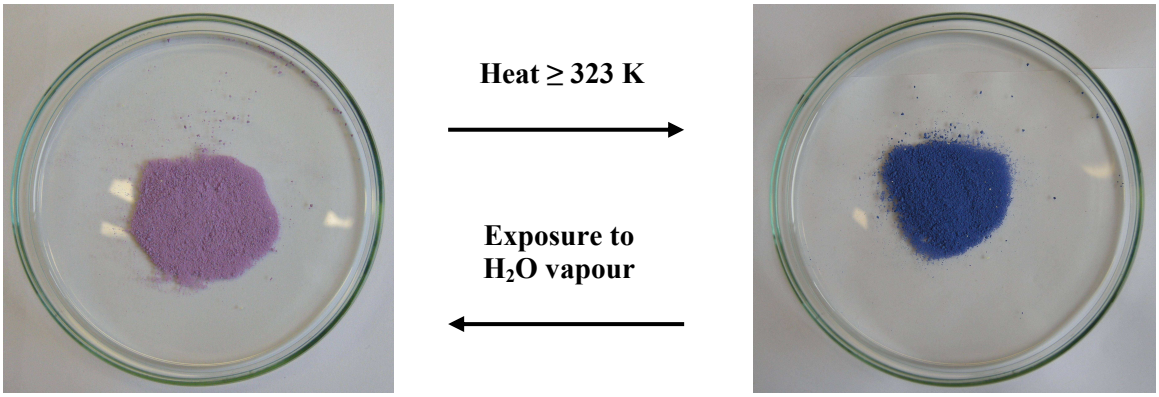

Figure 4.18 *- Illustration of colour change taking place in Co STA-12 on dehydration. (Left) Pink as-prepared; (Right) Dark blue dehydrated.*

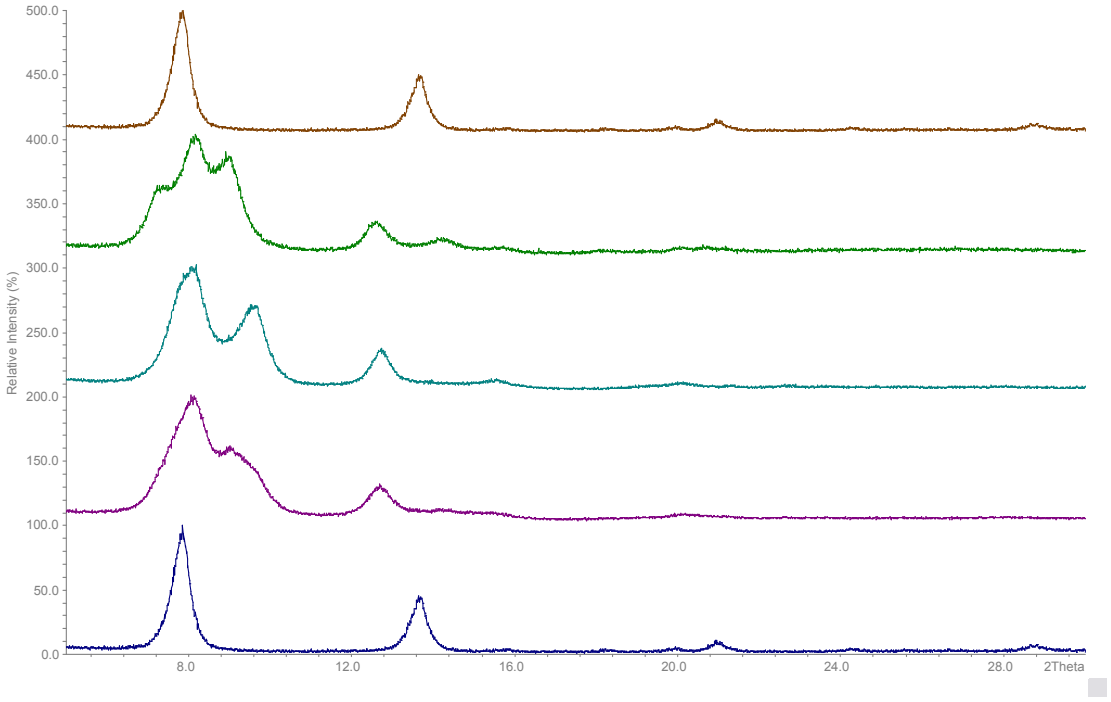

Figure 4.19 *– Laboratory powder X-ray diffractograms of Co STA-12 (bottom to top) as-prepared, evacuated 323 K, 373 K, 473 K, rehydrated (Fe K_α radiation).*

Table 4.3 *- Comparison of cell parameters for fully dehydrated Ni STA-12*[3] *and dehydrated Co STA-12.*

Formula	Ni_2L	Co_2L
Space Group	P-1	P-1
a (Å)	6.03475(5)	5.933(26)
b (Å)	14.9156(2)	14.73(4)
c (Å)	16.1572(7)	16.293(25)
α (°)	112.5721(7)	108.89(15)
β (°)	95.7025(11)	93.0(7)
γ (°)	96.4950(11)	97.5(10)
V (Å^3)	1318(3)	1329(7)
Diffractometer	ESRF (ID31)	Lab (STOE)
Temperature (K)	100	298
Wavelength (Å)	0.8002	1.9361 (Fe K_α)
R_{wp}	0.0694	0.1199

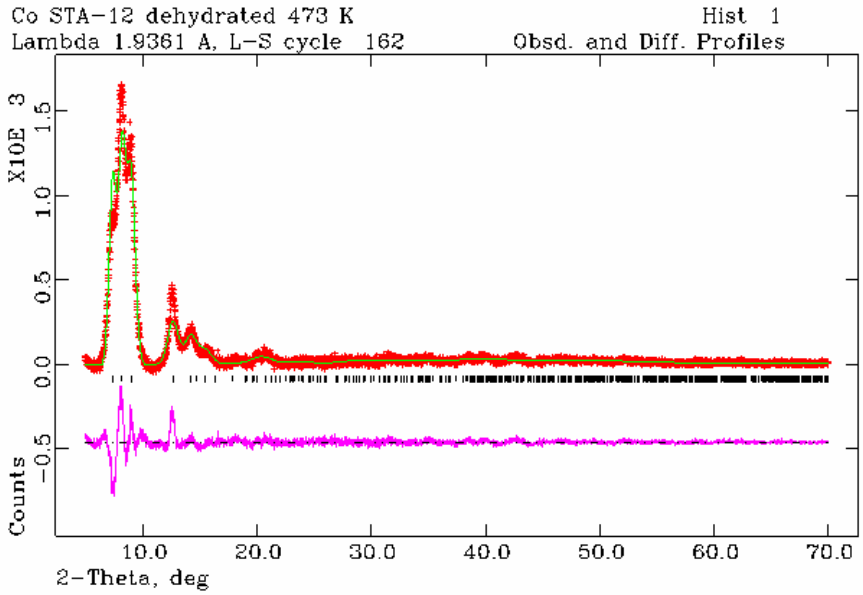

Figure 4.20 *- Rietveld refinement of dehydrated Co STA-12, keeping atomic coordinates the same as dehydrated Ni STA-12*[3] *(Fe K_α radiation). Colour scheme as Figure 4.13.*

4.6.1 Nitrogen adsorption – Co STA-12

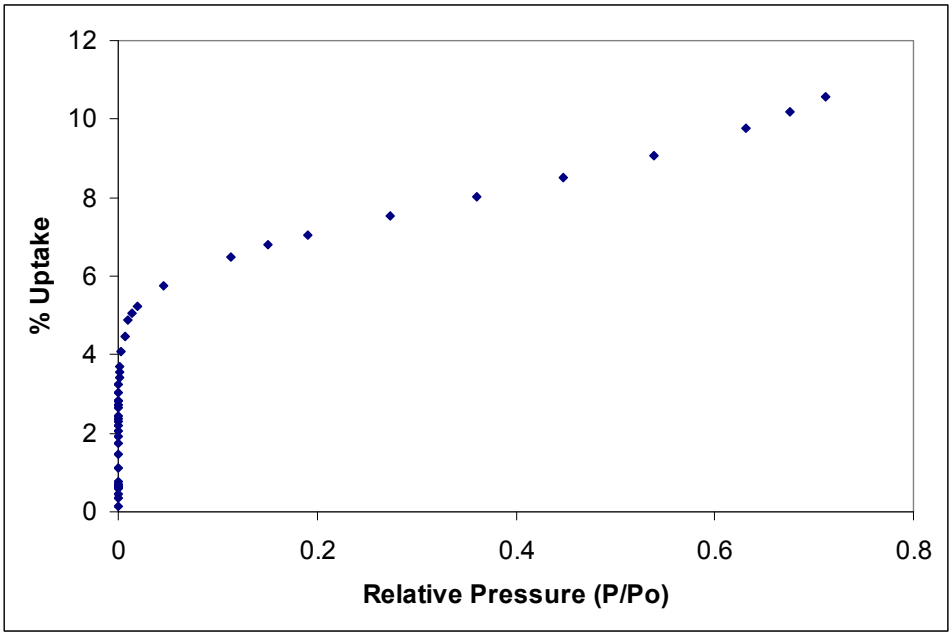

Figure 4.21 - *N_2 adsorption isotherm at 77 K for Co STA-12. Measured gravimetrically.*

The nitrogen isotherm does not take on the classic Type I profile for microporous materials, and has features similar to a Type II isotherm (Figure 4.21). This suggests the particle size is very small, resulting in adsorption on the particle surfaces. Another possibility is the framework is flexible, allowing more N_2 uptake as the pressure increases. At $p/p_o = 0.4$ the uptake is 8 wt%, equivalent to a porosity of 65 cm^3g^{-1}. The uptake for N_2 and the pore volume are much lower than for Ni STA-12 (8 wt% and 65 cm^3g^{-1}, compared to 14 wt% and 113 cm^3g^{-1}), possibly due to Co STA-12 not being as crystalline as Ni STA-12.

4.6.2 UV-vis-NIR study of Co STA-12 dehydration (in collaboration with Prof S. Bordiga at University of Turin, Italy)

The peak profiles, background and unit cell parameters for Co STA-12 were refined against the model for fully dehydrated Ni STA-12, but the positions of the atoms could not be determined. The blue colour after dehydration suggested the Co^{2+} could be four-coordinate after water loss, although there is no five-coordinate model structure.

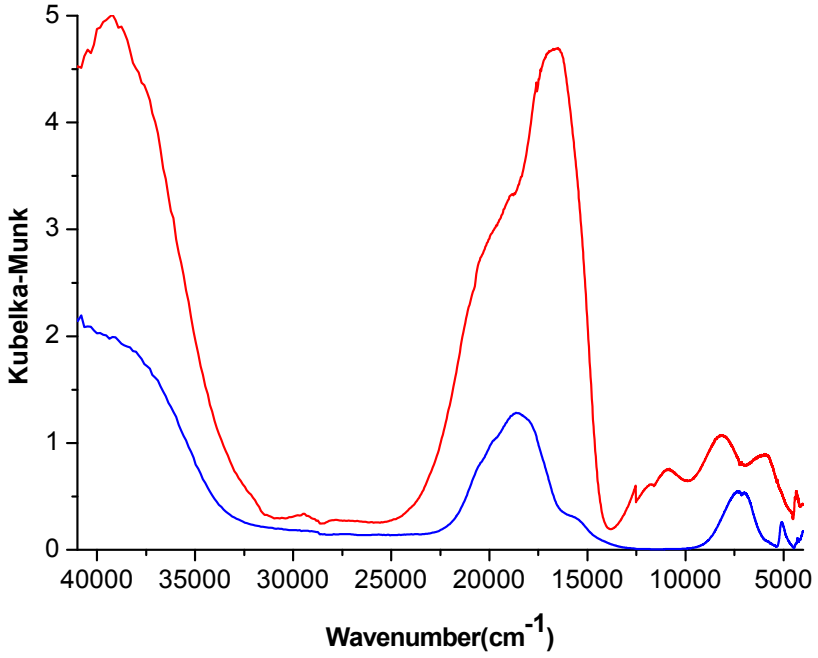

Figure 4.22 *- Diffuse Reflectance UV-vis-NIR of Co STA-12. (Blue) as-prepared; (Red) evacuated 423 K.*

The UV-visible spectrum of Co STA-12 (Figure 4.22) has an intense band at 37000 cm^{-1} associated with a charge transfer between Co^{2+} and the ligand. There is also a series of bands in the *d-d* region, comprising peaks at 18700 cm^{-1}, 16200 cm^{-1}, 7200 cm^{-1} and 5000 cm^{-1}. With Co^{2+} in O_h symmetry only three weak bands due to spin-allowed *d-d* transitions would be expected (18700 cm^{-1} – $^4T_{1g}$ (F) → $^4T_{1g}$ (P), 16200 cm^{-1} – $^4T_{1g}$ (F) → $^4A_{2g}$ (F) and 7200 cm^{-1} – $^4T_{1g}$ (F) → $^4T_{2g}$ (F)),[19] so the appearance of a third band in the near Infra-red region (5000 cm^{-1}) can be explained as due to the presence of nitrogen

inside the first coordination sphere of Co^{2+}. When nitrogen is coordinated to Co^{2+}, the point group changes from O_h to C_{4v}, resulting in spin orbital splitting (see Ni STA-12). Dehydration at 423 K results in major changes in the spectrum, especially in the *d-d* transition region. The band due to the organic linker shows a small red shift, and there are new bands at 18800, 16750, 10900, 8200 and 6000 cm^{-1}. This suggests the Co^{2+} cations are reducing in coordination with loss of water.

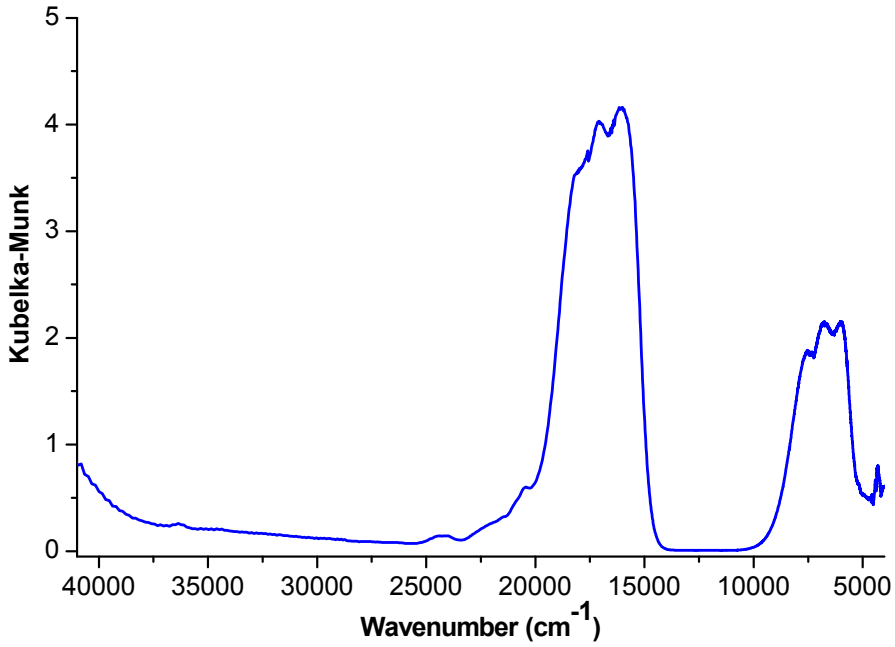

Figure 4.23 *- Diffuse Reflectance UV-vis-NIR of $CoH_2L.H_2O$.*

The UV-visible spectrum of $CoH_2L.H_2O$ (Chapter 3, Section 3.7) has two main bands, split into triplets at 18000, 17000, 16000 cm^{-1}, and 7500, 6800 and 6050 cm^{-1}. For Co^{2+} in T_d coordination two transitions are expected (17000 cm^{-1} – $^4A_2$ (F) → $^4T_1$ (P) and 6800 cm^{-1} – $^4A_2$ (F) → $^4T_1$ (F)), and the triplets are explained as due to spin orbital splitting of the $^4T_1$ (F) and $^4T_1$ (P) orbitals. Comparison of the spectrum to that measured for dehydrated Co STA-12 (Figure 4.22) indicates there are no matching band positions. This means after water loss, Co^{2+} cations are not tetrahedrally coordinated, and this evidence, coupled to the comparison of the unit cell with that of dehydrated Ni STA-12, indicates the Co^{2+} cations must be five-coordinate.

4.6.3 Infra-red study of dehydration mechanism for Co STA-12 (in collaboration with Prof S. Bordiga at University of Turin, Italy)

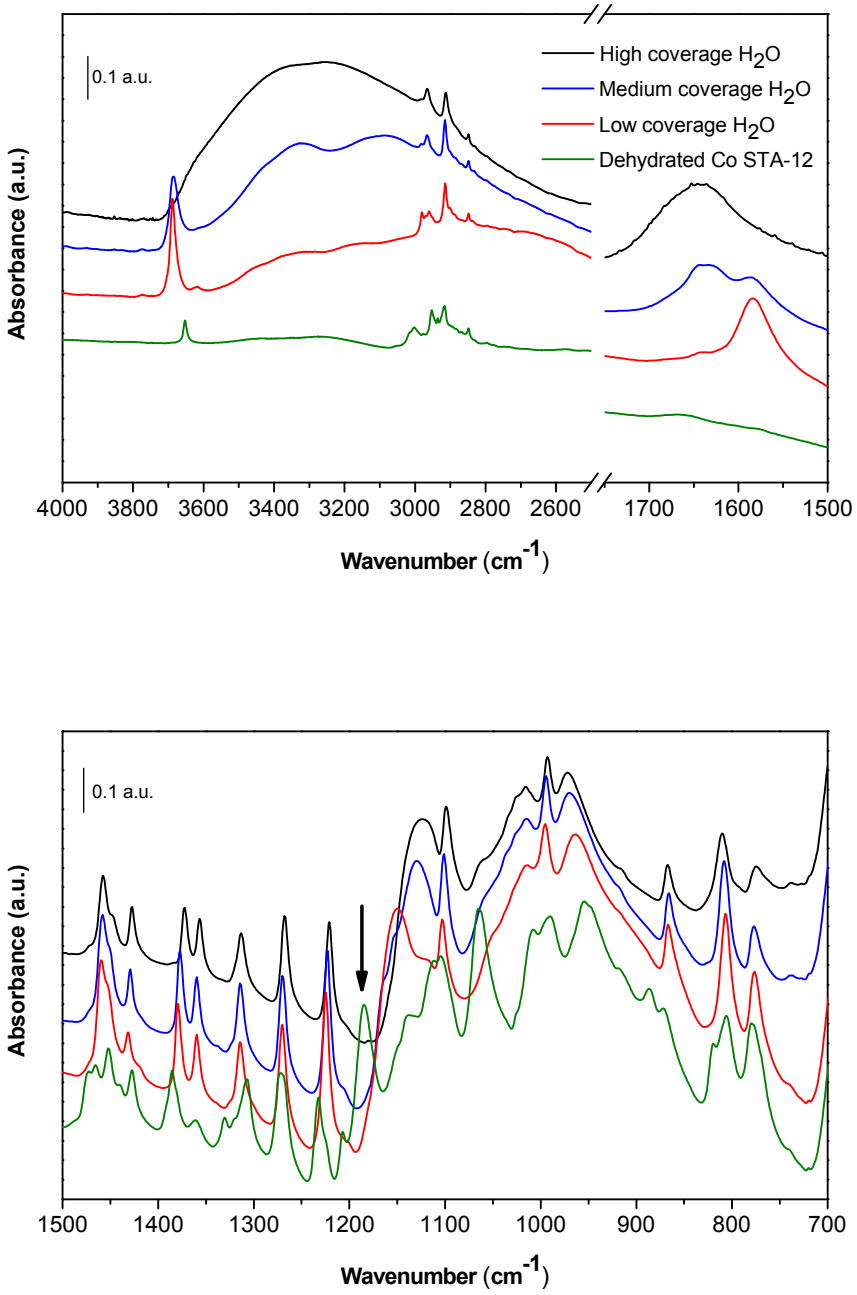

Figure 4.24 *– Effect of dehydration/hydration on IR spectra of Co STA-12. (Top) OH stretching and bending region; (Bottom) framework bending region.*

The effect of dehydration under high vacuum (< 1×10^{-3} Torr) at 298 K, and subsequent rehydration, is followed by Infra-red spectroscopy (Figure 4.24). In order to allow for greater clarity in Figure 4.24, the data has been offset along the vertical scale, with the coverage of H_2O increasing from the bottom to the top. The spectral changes for Co STA-12 are similar to those of Ni STA-12, with the main differences being a change in the position of the band attributed to P=O in the dehydrated solid (at 1185 cm^{-1} instead of 1207 cm^{-1} – outlined by arrow) and the presence of a small peak at 3650 cm^{-1} after removal of water. This indicates there are some residual –OH groups present in the structure, even after dehydration. This evolves into a peak at 3685 cm^{-1} on adsorption of water, attributed to free –OH groups (as seen for Ni STA-12).

All of the water can be removed from the structure under vacuum at 298 K, indicating the strength of interactions between water and Co STA-12 are lower than in Ni STA-12. As seen already in the X-ray study, the distortions in the structure come about at the relatively low temperature of 323 K, accompanied by a colour change, which supports there being weaker interactions with water.

Therefore, all the evidence from X-ray structural work, UV-visible spectroscopy and IR studies of the dehydration and rehydration indicates Co STA-12 undergoes a similar mechanism to Ni STA-12 for water loss and subsequent structural distortion. There appears to be residual –OH groups after dehydration, probably due to structural defects in dehydrated Co STA-12, and as a result of the lower crystallinity of Co STA-12 compared to Ni STA-12 the structure cannot be solved or characterised to quite the same level of detail as is possible for Ni STA-12.

4.7 Dehydration of Co Me STA-12

Thermogravimetric analysis of Co Me STA-12 (Figure 4.25) indicates water is lost in one step, with 24 wt% lost below 403 K. The total weight loss is the same as for Co STA-12, and the curve has a plateau in the 403 – 573 K range, meaning Co Me STA-12 is not as thermally stable as Co STA-12. Above 573 K the structure decomposes, and at 940 K the weight loss trace show a slight weight rise, attributed to formation of Co pyrophosphate ($Co_2P_2O_7$) via incorporation of oxygen from the flowing air in the experiment.

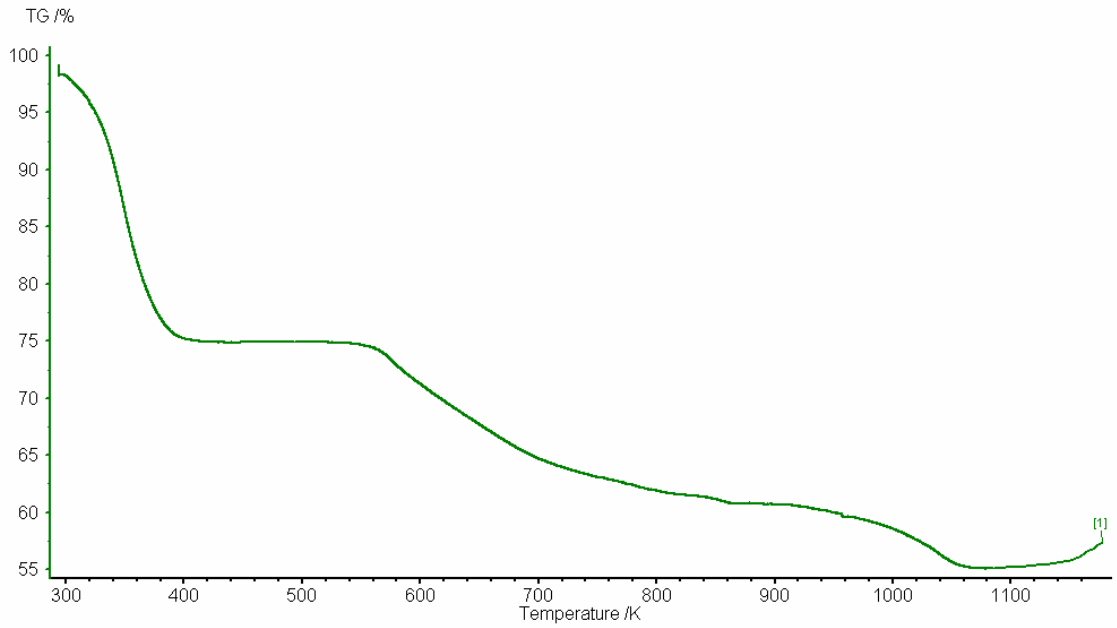

Figure 4.25 *- Thermogravimetric analysis of Co Me STA-12 measured at 5K/min in air.*

Evacuation of Co Me STA-12 at 323 K results in a similar colour change to that seen for Co STA-12. Laboratory powder diffraction data indicates rhombohedral symmetry is retained on evacuation up to 423 K (Figure 4.26), with a slight loss of crystallinity (increase in peak width), a slight increase in the cell volume (66 $Å^3$) and a slight increase in the *a* cell parameter (0.29 Å) compared to as-prepared Co Me STA-12 (Table 4.4), which is similar behaviour to that seen for Ni Me STA-12. Therefore, the behaviour with water loss can be understood by referencing Figure 4.15. The final Rietveld plot is shown in Figure 4.27 (more information on parameters and goodness of fit for Rietveld refinement in Appendix 5), and the dehydrations are fully reversible with restoration of the original structure and crystallinity.

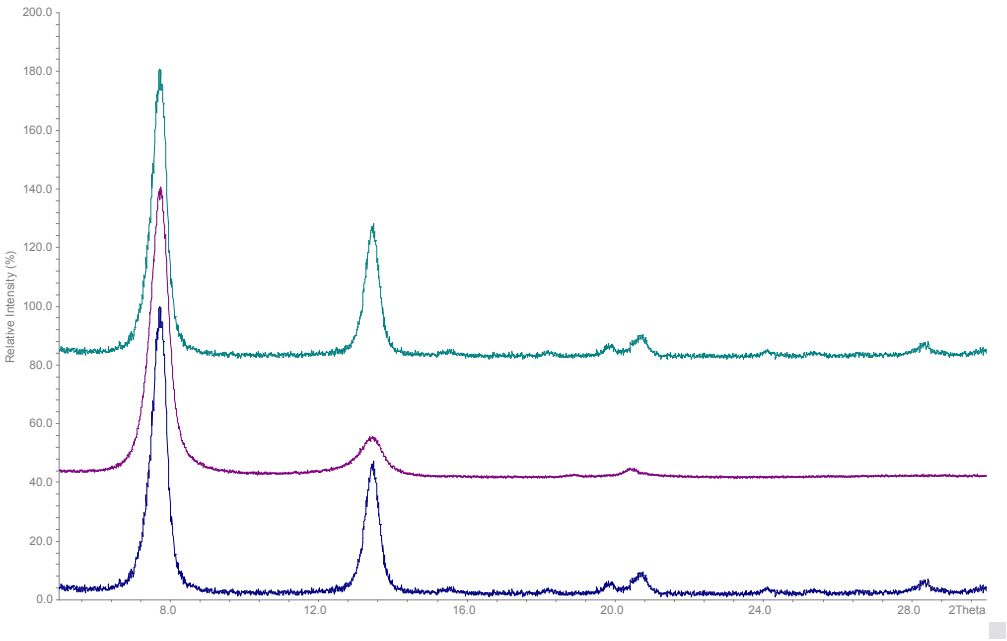

Figure 4.26 *– Laboratory powder X-ray diffractograms of Co Me STA-12 (bottom to top) as-prepared, evacuated 423 K, rehydrated (Fe K_α radiation).*

Table 4.4 - *Comparison of cell parameters of as-prepared and dehydrated Co Me STA-12.*

Formula	$Co_2(H_2O)_2L$-Me.5.4H_2O	Co_2L-Me
Space Group	R-3	R-3
a (Å)	28.5268(35)	28.816(18)
b (Å)	28.5268(35)	28.816(18)
c (Å)	6.2984(9)	6.204(13)
α (º)	90	90
β (º)	90	90
γ (º)	120	120
V (Å^3)	4394.4(12)	4461(11)
Diffractometer	Lab (STOE)	Lab (STOE)
Temperature (K)	298	298
Wavelength (Å)	1.9361 (Fe K_α)	1.9361 (Fe K_α)
R_{wp}	0.1472	0.1251

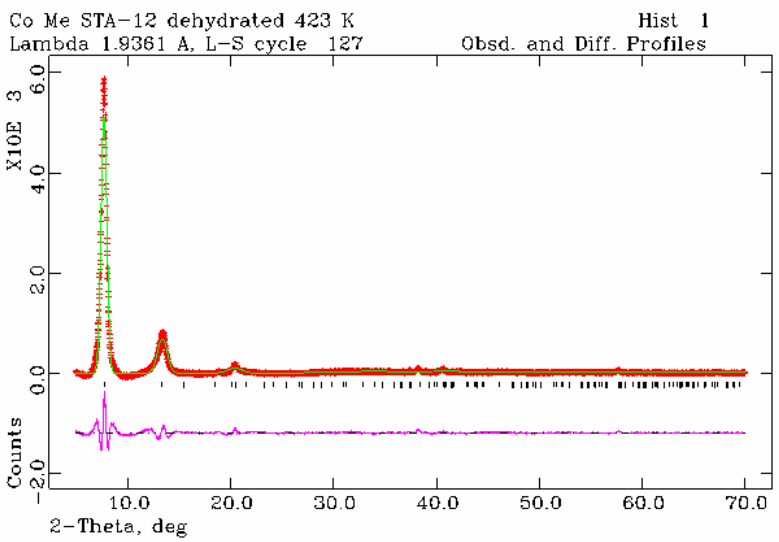

Figure 4.27 *- Rietveld refinement of dehydrated Co Me STA-12 (Fe K_α radiation). Colour scheme as Figure 4.13.*

4.7.1 Nitrogen adsorption – Co Me STA-12

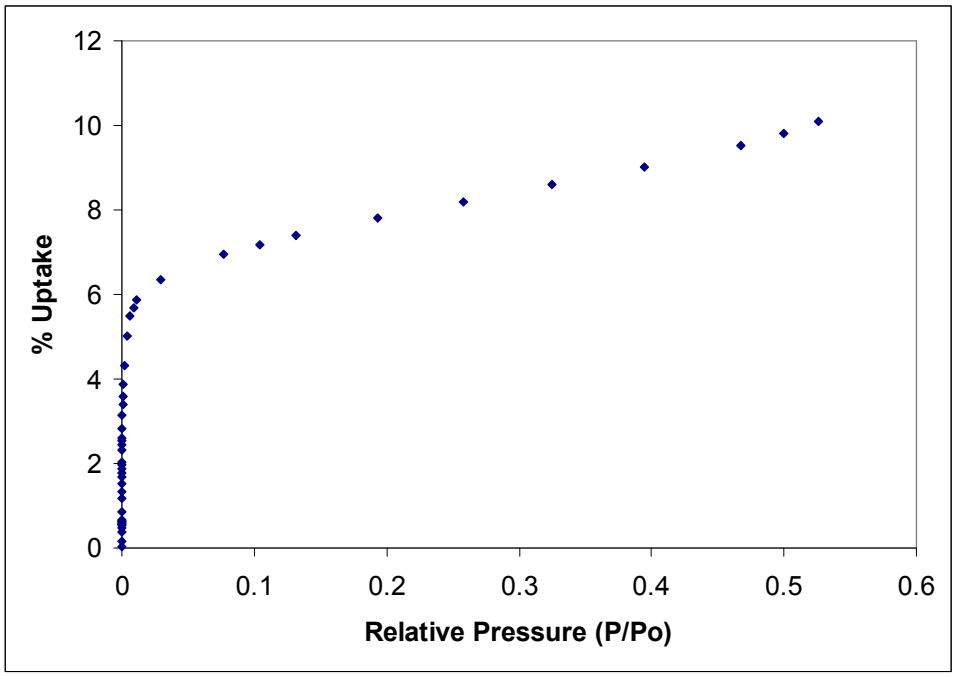

Figure 4.28 *- N_2 adsorption isotherm at 77 K for Co Me STA-12. Measured gravimetrically.*

Like Co STA-12, the nitrogen isotherm for Co Me STA-12 does not take on the typical Type I profile for microporous materials, and has some features similar to a Type II isotherm (Figure 4.28). There is an initial fast uptake to 6 wt% at low values of p/p_o, equivalent to a porosity of 49 $cm^{-3}g^{-1}$, then a gradual slower uptake to 11 wt% as p/p_o increases. At $p/p_o = 0.4$ the uptake is 8.5 wt%, equivalent to a porosity of 69 cm^3g^{-1}. Co Me STA-12 has a slightly higher uptake and porosity than Co STA-12 (8.5 wt% and 69 cm^3g^{-1} compared to 8 wt% and 65 cm^3g^{-1}), mirroring what happens with Ni STA-12 and Ni Me STA-12.

4.8 Dehydration of Mn STA-12

Thermal analysis of Mn STA-12 shows water is lost in two steps (Figure 4.29), with 14 wt% lost below 360 K and 15 wt% lost between 360 K and 395 K. The total weight loss is the same as that measured for Ni and Co STA-12. The curve has a plateau in the 395 - 560 K range, indicating Mn STA-12 is not as thermally stable after water loss than Ni or Co STA-12. Above 560 K the structure decomposes, and at 830 K the weight loss trace show a slight weight rise, attributed to formation of Mn pyrophosphate ($Mn_2P_2O_7$) via incorporation of oxygen from the flowing air in the experiment.

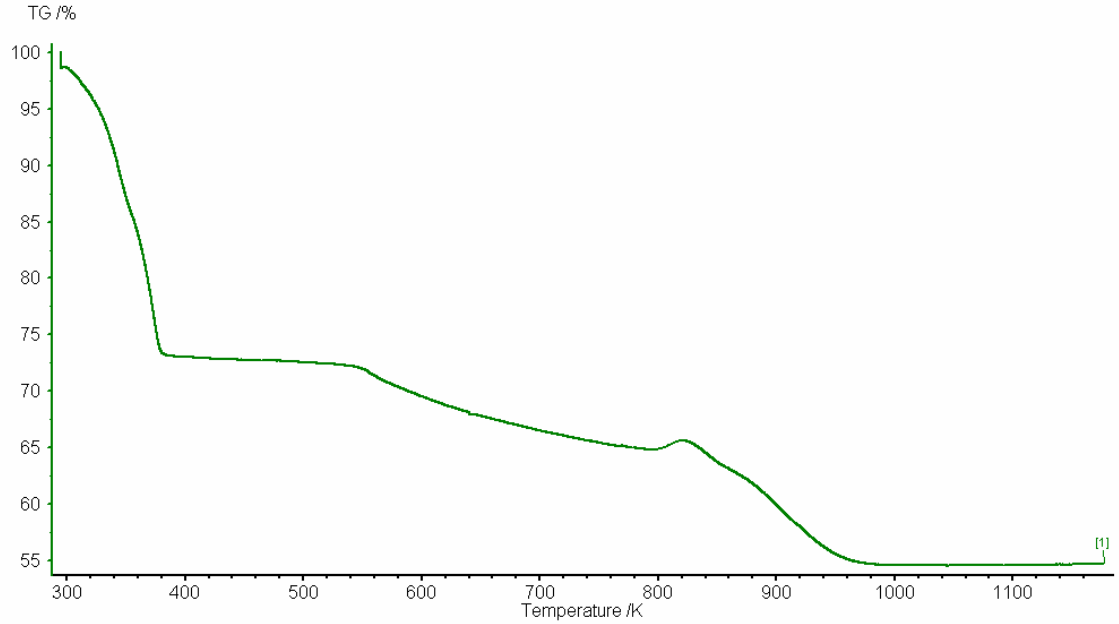

Figure 4.29 *- Thermogravimetric analysis of Mn STA-12 measured at 5K/min in air.*

No colour change is observed on dehydration of Mn STA-12, with the structure remaining a cream colour. Laboratory powder diffraction data indicates rhombohedral symmetry is retained on evacuation at 423 K (Figure 4.30), with the peaks shifting to higher 2θ values compared to the as-prepared structure. The dehydrated structure does not adsorb any nitrogen gas at 77 K, while the dehydrations are fully reversible restoring the original structure.

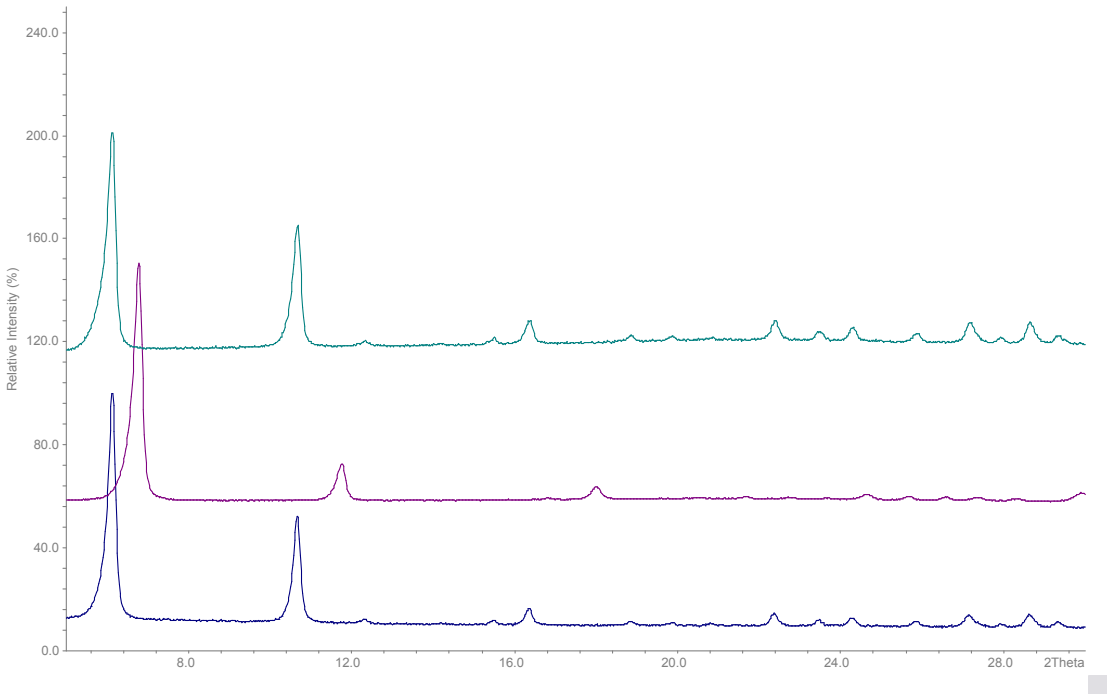

Figure 4.30 *– Laboratory powder X-ray diffractograms of Mn STA-12 (bottom to top) as-prepared, evacuated 423 K, rehydrated (Cu K_α radiation).*

4.8.1 Structural study of dehydrated Mn STA-12 and description of structure

The structure of dehydrated Mn STA-12 was solved using the data from as-prepared Ni STA-12[2] as a starting point, with chemically reasonable constraints placed on bond lengths and inter-atomic distances. The atoms positions were allowed to refine within the restraints, and the atomic coordinates and cif file are presented in Appendix 6. Table 4.5 outlines the crystallographic parameters of dehydrated Mn STA-12 compared to the as-prepared structure. The main differences on dehydration are the 2.42 Å reduction in the *a* cell parameter, the 0.46 Å reduction in the *c* cell parameter and the ~ 1000 $Å^3$ reduction in the unit cell volume. The final Rietveld plot is shown in Figure 4.31.

Table 4.5 - *Comparison of cell parameters of as-prepared and dehydrated Mn STA-12.*

Formula	$Mn_2(H_2O)_2L.5.4H_2O$	Mn_2L
Space Group	R-3	R-3
a (Å)	28.534(4)	26.111(4)
b (Å)	28.534(4)	26.111(4)
c (Å)	6.4222(11)	5.9609(18)
α (°)	90	90
β (°)	90	90
γ (°)	120	120
V($Å^3$)	4528.3(12)	3519.5(13)
Diffractometer	Lab (STOE)	Lab (STOE)
Temperature (K)	298	298
Wavelength (Å)	1.5406 (Cu K_α)	1.5406 (Cu K_α)
R_{wp}	0.1125	0.1029

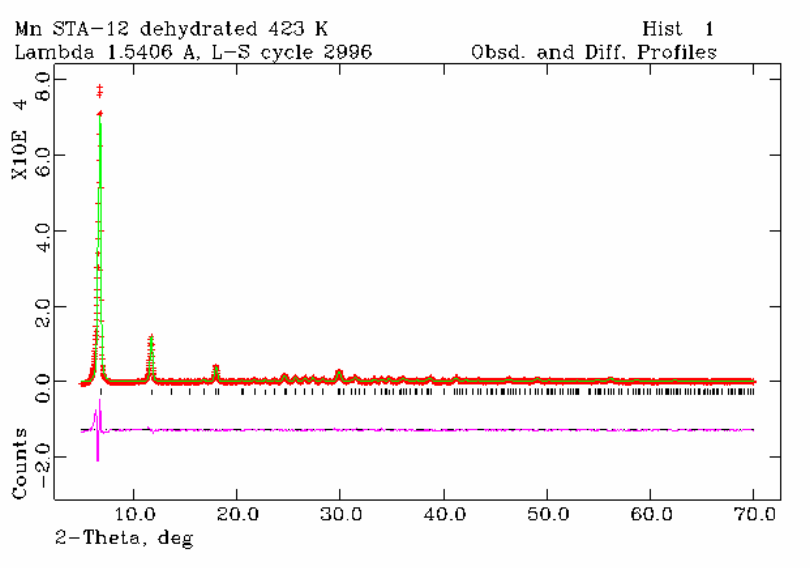

Figure 4.31 - *Rietveld refinement of dehydrated Mn STA-12 (Cu K_α radiation). Colour scheme as Figure 4.13. (R_{wp} = 0.1029, R_p = 0.0585).*

The structure of dehydrated Mn STA-12 has large *ca.* 9.5 Å diameter hexagonal shaped pores running down the direction of the *c*-axis, while the Mn centred polyhedra are distorted trigonal bipyramids. The linking of the inorganic chains by the ligands is similar to that seen in the as-prepared and dehydrated Ni STA-12 structures (Figure 4.32).

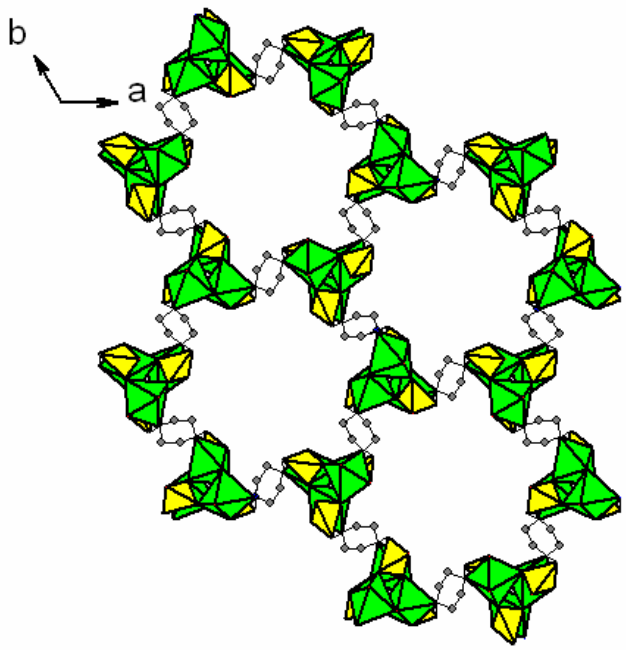

Figure 4.32 *– Framework structure of Mn STA-12 evacuated at 423 K (viewed down c-axis). Mn centred octahedra in green, phosphonate tetrahedra in yellow and carbon atoms in grey.*

The torsion angles in the piperazine rings change as water is lost from the structure. This results in the rings and phosphonate groups rotating, the distances between the inorganic chains decreasing, and retention of the rhombohedral symmetry. This helps to explain the 2.42 Å reduction in the *a* cell parameter compared to the as-prepared structure, and indicates the ligand is reasonably flexible (as discussed in Chapter 1, Section 1.5).

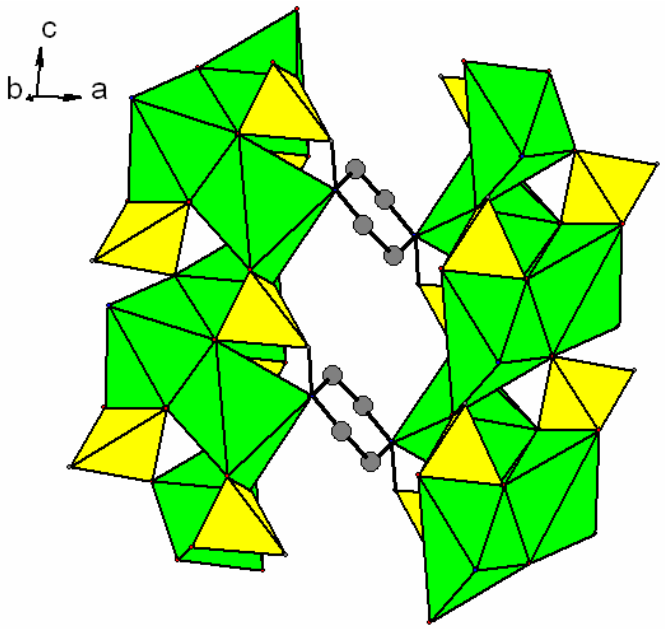

Figure 4.33 *- Close up view of two inorganic chains in dehydrated Mn STA-12 connected by bis(phosphonate) linkers, with piperazine rings in distorted chair conformation. Colour scheme as Figure 4.32.*

The rhombohedral symmetry is not lost when water is removed, as Mn^{2+} has a larger ionic radius than Co^{2+} and Ni^{2+} (Table 3.5 in Chapter 3) which results in different dehydration behaviour. It was unexpected that the structure did not adsorb nitrogen gas. The results of the structural study indicate the reason is not crystallographic in nature, as open pores 9.5 Å in diameter are present, along with accessible adsorption sites. A study into dehydration of Mg CPO-27 by Dietzel *et. al*[20] indicated an amorphous surface layer formed as dehydration proceeded, resulting in not all of the water being removed from the pores and lower than expected N_2 adsorption. It appears something similar is happening to Mn STA-12 on dehydration, although from TGA data all the water is being removed. The formation of an amorphous surface layer would help to explain the lack of nitrogen adsorption, and highly polar water molecules can reverse the change, restoring the original structure.

4.8.2 Infra-red study of dehydration mechanism for Mn STA-12 (in collaboration with Prof S. Bordiga at University of Turin, Italy)

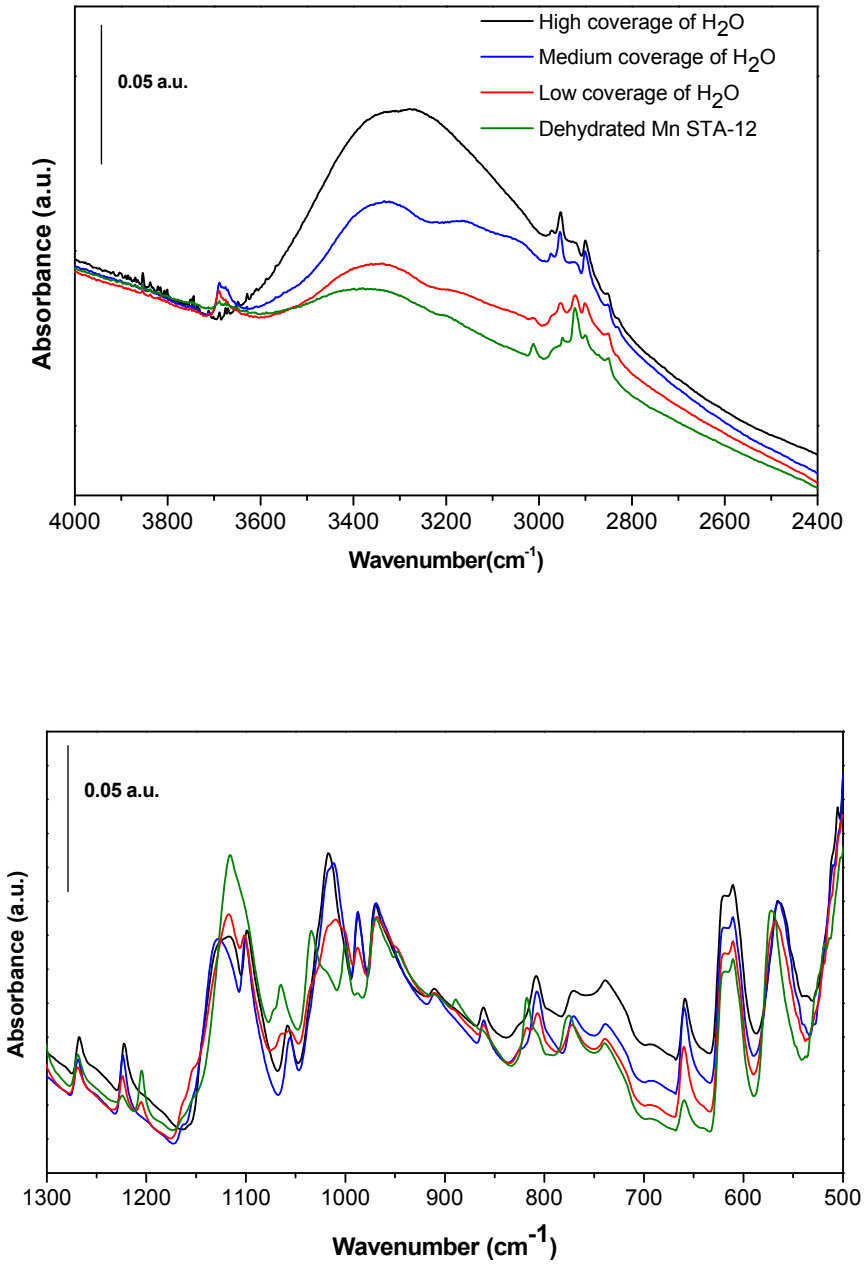

Figure 4.34 *– Effect of dehydration/hydration on IR spectra of Mn STA-12. (Top) OH stretching and bending region; (Bottom) framework bending region.*

The effect of dehydration at 298 K and subsequent rehydration has been followed by Infra-red spectroscopy (Figure 4.34). In order to allow for greater clarity in Figure 4.34, the data has been offset along the vertical scale, with the coverage of H_2O increasing from the bottom to the top. The spectra for Mn STA-12 have several differences to those produced for Co and Ni STA-12. The major differences include no band being present due to P=O at around 1200 cm^{-1}, and a weak intensity band at 3675 cm^{-1} attributed to –OH groups. Therefore, not very many free –OH groups are formed upon hydration. The two peaks at 3300 and 3100 cm^{-1} (due to symmetrical reorganisation of water in the pores) are present at medium coverage of water but with low intensities. It appears a hydrogen bonded physically adsorbed water network is not formed to the same extent as in Co and Ni STA-12.

The dehydration/rehydration mechanism in Mn STA-12 is therefore different to that for Co and Ni STA-12. The X-ray structural analysis indicates the rhombohedral symmetry is retained on dehydration, with a flexing of the piperazine rings taking place. The Infra-red study indicates several of the features present for Co and Ni STA-12 are either not present, or appear with only weak intensities. All of the water can be removed at room temperature, so the strength of the interactions of water with the framework are lower than those present in Ni STA-12, and are possibly similar to Co STA-12.

4.9 Dehydration of Fe STA-12

Thermal analysis of Fe STA-12 (Figure 4.35) indicates there is water loss in two steps, with 12 wt% lost below 373 K and 8 wt% lost between 373 K and 423 K. The total weight loss for water (20 wt%) is less than for Mn, Co and Ni STA-12, and the structure has a plateau after water loss up to 560 K (similar to Mn STA-12 – Figure 4.29). Above 560 K the structure decomposes, and at 1000 K the weight loss trace show a slight weight rise, attributed to formation of Fe pyrophosphate ($Fe_2P_2O_7$) via incorporation of oxygen from the flowing air in the experiment.

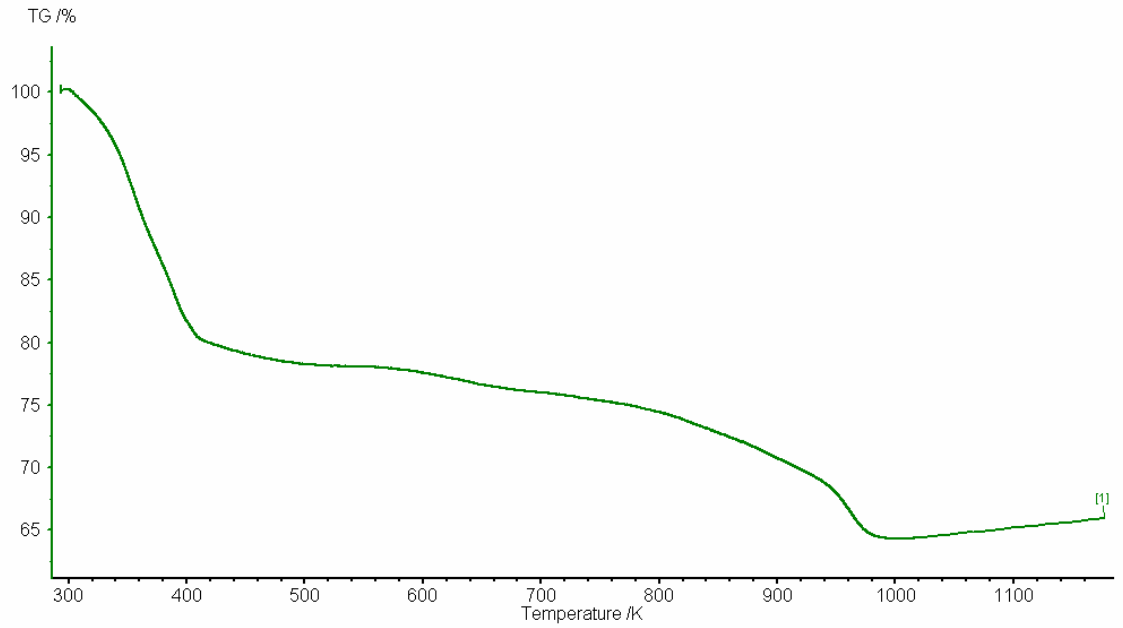

Figure 4.35 *- Thermogravimetric analysis of Fe STA-12 measured at 5K/min in air.*

There is no colour change on evacuation, with the sample remaining a brown colour. Laboratory powder diffraction data indicates the crystallinity is reduced as water is removed (peak broadening - Figure 4.36). The peaks shift to higher 2θ values and rhombohedral symmetry is retained (similar to Mn STA-12).

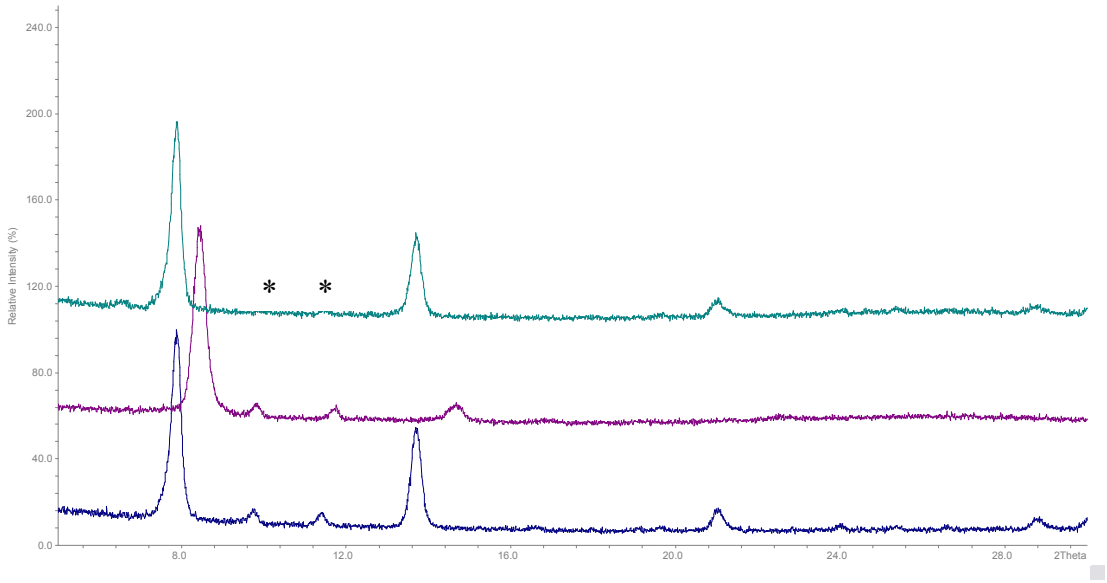

Figure 4.36 *- Laboratory powder X-ray diffractograms of Fe STA-12 (bottom to top) as-prepared, evacuated 373 K, rehydrated (Fe K_α radiation). Asterisks indicate impurity phase (identified in Figure 3.3, Chapter 3).*

Table 4.6 outlines the crystallographic data compared to as-prepared Fe STA-12. The main differences are the 1.64 Å reduction in the *a* cell parameter, the 0.43 Å reduction in the *c* cell parameter and the ~ 760 $Å^3$ reduction in the unit cell volume. The final Rietveld plot is shown in Figure 4.37 (more information on parameters and goodness of fit for Rietveld refinement in Appendix 5).

No nitrogen gas is adsorbed, and it appears Fe STA-12 is behaving in a similar way to Mn STA-12 on dehydration, with retention of the rhombohedral symmetry and the formation of some sort of amorphous surface layer which can be reversed by adsorption of water. Fe^{2+} has a smaller ionic radius than Mn^{2+}, but it is larger than both Co^{2+} and Ni^{2+} (Table 3.5 in Chapter 3). This means the size of ionic radii appears to govern the behaviour of the STA-12 frameworks during dehydration.

Table 4.6 - *Comparison of cell parameters of as-prepared and dehydrated Fe STA-12.*

Formula	$Fe_2(H_2O)_2L.5.4H_2O$	Fe_2L
Space Group	R-3	R-3
a (Å)	27.986(4)	26.347(29)
b (Å)	27.986(4)	26.347(29)
c (Å)	6.3976(14)	5.943(26)
α (°)	90	90
β (°)	90	90
γ (°)	120	120
V ($Å^3$)	4339.5(15)	3573(16)
Diffractometer	Lab (STOE)	Lab (STOE)
Temperature (K)	298	298
Wavelength (Å)	1.9361 (Fe K_α)	1.9361(Fe K_α)
R_{wp}	0.1183	0.0664

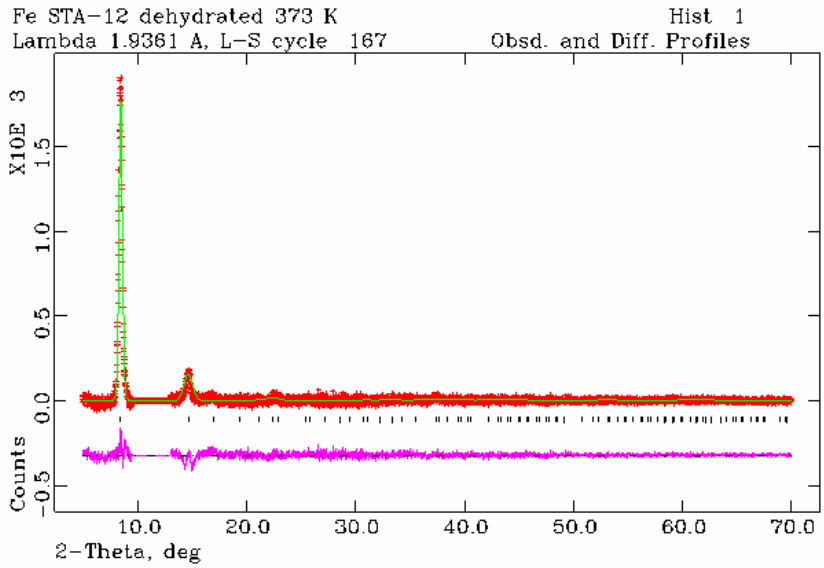

Figure 4.37 *- Rietveld refinement of dehydrated Fe STA-12 (Fe K_α radiation). Colour scheme as Figure 4.13.*

4.10 Conclusions of STA-12 dehydration studies

As outlined in Chapter 3 there is a significant amount of water present in the STA-12 structure. The water is physically adsorbed in the pores and coordinated to the metal cations, so a study of the dehydration of the Mn, Fe, Co and Ni forms is relevant to understanding structural changes taking place on thermal activation, which are important when considering adsorption (Chapter 5) and catalytic (Chapter 6) properties.

Ni STA-12 loses water in three steps, with the chemically-bound water on the cations removed in a stepwise fashion. The dehydrated phases evolve with increasing temperature, and it is possible to isolate three structures. A partially dehydrated rhombohedral structure where only the water in the pores is removed was formed at 323 K, while at higher temperatures (373 K and 423 K) two other lower symmetry structures were produced. The fully dehydrated structure was found to adsorb 15 wt% N_2 at p/p_o = 0.4, indicating a reasonable porosity (*ca.* 0.11 cm^3g^{-1}).

The structure produced at 373 K was found to be unstable in the intense X-ray beam of a synchrotron radiation source, but the 323 K and 423 K structures were solved.[3] The 423 K structure, the X-ray analysis of which indicated the symmetry had decreased to triclinic from rhombohedral, was found to have three crystallographically distinct Ni and P sites. UV-visible spectroscopic data confirmed the Ni atoms were present in distorted five-coordinated polyhedra, and structural rearrangement was shown to take place via the rotation of phosphonate groups to coordinate to the Ni^{2+} cations. This results in only one out of every three of the phosphonate groups pointing inwards towards the pore. The dehydration and rehydration mechanism was followed by Infra-red spectroscopy. At low coverage there was evidence the water molecules reacted with both the Ni^{2+} cations and P=O groups, forming a cyclic species with Ni-OH and hydrogen bonded P-OH.

Co STA-12 is observed from X-ray data to undergo a similar reversible structural distortion to Ni STA-12 on dehydration, although at a lower temperature. The X-ray data was not of good enough quality to allow for a structural solution, although UV-visible spectroscopy suggests the Co^{2+} cations are five-coordinate. Nitrogen adsorption indicated there was less wt% uptake and lower porosity compared to Ni STA-12. Infra-red spectroscopy was also used to follow the dehydration and rehydration mechanism. The

spectra were observed to be similar to those produced for Ni STA-12, indicating dehydration and rehydration of Co STA-12 proceeds in a similar way to Ni STA-12. There was also evidence for defect hydroxyl groups in the fully dehydrated solid.

Ni and Co STA-12 formed using the H_4L-Me ligand were observed from X-ray data to retain rhombohedral symmetry on dehydration. Higher amounts of nitrogen were adsorbed in the methyl ligand versions, due in part to methyl groups helping to retain the rhombohedral symmetry. A dehydrated form of Ni Me STA-12 with the same structure as fully dehydrated Ni STA-12 could not exist, as there is not enough space for the methyl groups. The distances between equatorial hydrogen atoms and the nearest framework atoms in the structure are, at 2.5 Å, just large enough for the hydrogen and the framework atom once the van der Waals radii are taken into account. When 50% of each ligand is present the structure is still rhombohedral on dehydration, although the X-ray powder diffraction peaks are very broad, indicating a lot of strain is present in the structure.

Mn STA-12 was observed to retain rhombohedral symmetry after thermal activation, with a 2.42 Å reduction in the cell via changes in the torsion angles present in the ligand. It does not adsorb nitrogen gas, which is unexpected as the crystallographic structure indicates there is pore space available. An amorphous surface layer seems to be forming on dehydration which can be reversibly removed by adsorption of water. Fe STA-12 was observed from X-ray data to act in a similar way to Mn STA-12, with a 1.64 Å reduction in the cell upon water loss. Like Mn STA-12, Fe STA-12 does not adsorb nitrogen, possibly for a similar reason.

Changing the metal cation present in STA-12 (Mn^{2+}, Fe^{2+}, Co^{2+} or Ni^{2+}) changes the dehydration properties of the structure. The size of the ionic radii appears to play a large part in the differences, with the frameworks with the largest cations (Mn^{2+} and Fe^{2+}) having quite different dehydration properties to the frameworks with the smallest cations (Co^{2+} and Ni^{2+}). Also, if the H_4L-Me ligand is used instead of H_4L, the stability of the rhombohedral structure is improved as water is removed. The potential therefore exists for the versions of STA-12 to have different adsorption (Chapter 5) and catalysis (Chapter 6) behaviour.

4.11 References

1) A. C. Larson and R. B. von Dreele, *Generalised crystal structure analysis system*, Los Alamos National Laboratory, USA, 1998

2) J. A. Groves, S. R. Miller, S. J. Warrender, C. Mellot-Draznieks, P. Lightfoot and P. A. Wright, *Chem. Commun.*, 2006, 3305

3) S. R. Miller, G. M. Pearce, P. A. Wright, F. Bonino, S. Chavan, S. Bordiga, I Margiolaki, N. Guillou, G. Férey, S. Bourelly and P. L. Llewellyn, *J. Am. Chem. Soc.*, 2008, **130**, 15967

4) P. D. C. Dietzel, B. Panella, M. Hirscher, R. Blom and H. Fjellvåg, *Chem. Commun.*, 2006, 959

5) A. N. Fitch, *J. Res. NIST*, 2004, **109**, 133

6) A. Altomare, R. Caliandro, M. Camalli, C. Cuocci, C. Giacovazzo, A. Grazia, G. Moliterni and R. Rizzi, *J. Appl. Crystallogr.*, 2004, **37**, 1025

7) Bruker AXS ltd, TOPAS V3.0: General Profile and Structure Analysis Software for Powder Diffraction Data. 2004

8) A. A. Coelho, *J. Appl. Crystallogr.*, 2003, **36**, 86

9) A. Boultif and D. Louer, *J. Appl. Crystallogr.*, 1991, **24**, 987

10) F. Bonino, S. Chavan, J. G. Vitillo, E. Groppo, G. Agostini, C. Lamberti, P. D. C. Dietzel, C. Prestipino and S. Bordiga, *Chem. Mater.*, 2008, **15**, 4957

11) M. Ciampolini, *Inorg. Chem.*, 1966, **5**, 35

12) S. Bauer, J. Marrot, T. Devic, G. Férey and N. Stock, *Inorg. Chem.*, 2007, **46**, 9998

13) E. V. Bakhmutova, X. Ouyang, D. G. Medvedev and A. Clearfield, *Inorg. Chem.*, 2003, **42**, 7046

14) N. Stock and T. Bein, *J. Solid State Chem.*, 2002, **167**, 330

15) V. Zima, J. Svoboda, L. Benesa, K. Melanova, M. Trchova and J. Dybal, *J. Solid State Chem.*, 2007, **180**, 929

16) A. Zecchina, G. Spoto and S. Bordiga, *Phys. Chem. Chem. Phys.*, 2005, **7**, 1627

17) A. Zecchina, F. Geobaldo, G. Spoto, S. Bordiga, G. Ricchiardi, R. Buzzoni and G. Petrini, *J. Phys. Chem.*, 1996, **100**, 16584

18) P. D. C. Dietzel, Y. Morita, R. Blom and H. Fjellvåg, *Angew. Chem. Int. Ed.*, 2005, **44**, 6354

19) K. Fujisawa, T. Kakizaki, Y. Miyashita and K. Okamoto, *Inorg. Chem. Acta*, 2008, **361**, 1134

20) P. D. C. Dietzel, R. Blom and H. Fjellvåg, *Eur. J. Inorg. Chem.*, 2008, 3624

Chapter 5: Gas and Vapour Adsorption

5.1 Introduction

In this work, the performance of STA-12 as an adsorbent for fuel related gases and probe molecules[1, 2] will be investigated. The adsorption of H_2, CO, CO_2, CH_4, CH_3CN, CH_3OH and hydrocarbons at low and ambient temperatures will be studied, using adsorption calorimetry and Infra-red spectroscopy. This will allow for characterisation of the adsorption sites and mechanisms.

5.2 Experimental and Characterisation Techniques

Carbon dioxide adsorption was performed at 196 K on samples pre-treated under vacuum at various temperatures. This was achieved by surrounding about 50 mg of sample with an ethanol/dry ice mixture. The measurements were carried out gravimetrically, using a Hiden Intelligent Gravimetric Analyser.

Adsorption of hydrocarbon molecules was undertaken using a glass line with greaseless taps. The organic liquids were first degassed by freeze/thaw cycles. The uptake of the various molecules at 298 K was calculated from observed pressure changes on the line, and a maximum uptake was measured at pressures below the saturated vapour pressure ($p/p_0 \approx 0.1$).

High resolution isotherms and differential heats of adsorption were measured in two ways by Prof Philip Llewellyn and co-workers at the University of Marseille, France. Low temperature isotherms at 77 K were measured along with simultaneous direct calorimetric measurements.[1] The low temperature calorimeter used at 77 K consisted of two thermopiles mounted in electrical opposition, and the system was immersed in a

liquid nitrogen cryostat. 50 mg of sample was placed in a cell connected to the calorimeter, and a continuous procedure of gas adsorption was used. The continuous dosing procedure was calibrated to be close to equilibrium, resulting in high resolution isotherms and differential heats of adsorption. Room temperature isotherms were measured at 303 K using a volumetric device coupled to a calorimeter. The system was placed in a thermostat regulated to ± 0.01 K. A discontinuous dosing procedure was used up to 15 bar, resulting in more widely spaced measurements of differential enthalpies.

The Infra-red spectroscopic measurements were performed at the University of Turin, Italy during a visit in July 2007 in collaboration with Prof Silvia Bordiga and co-workers. The measurements were undertaken in controlled atmospheres using environmental cells that allow thermal treatment under high vacuum ($<1 \times 10^{-3}$ Torr), dosing of gases (H_2, CO, CO_2) and vapours (CH_3OH, CH_3CN), and *in situ* spectra collection. FTIR spectra were collected in transmission mode on self supporting wafers. The spectra were recorded at a resolution of 2 cm^{-1} using a Bruker IFS 66 FTIR spectrometer. In the case of H_2 and CO adsorption, a Bruker Equinox-55 FTIR spectrometer equipped with an MCT detector with a sample compartment that had been modified *ad hoc* to accommodate a cryogenic IR probe was used. A detailed description of the experimental setup is outlined elsewhere.[3]

For X-ray powder diffraction studies of the interaction of acetonitrile and methanol with STA-12, the samples were sealed after adsorption in 0.7 mm quartz capillaries and analysed at room temperature using lab diffractometers as outlined in Chapter 3. Analysis of the unit cell parameters was undertaken with the GSAS program suite,[4] using the cell parameters and atomic coordinates for as-prepared Ni STA-12 as the starting point.[5] The positions of the adsorbed acetonitrile molecules in Ni STA-12 were found using Fourier mapping within the GSAS program suite,[4] with constraints on the bonds to maintain the linearity of the CH_3CN molecules.

5.3 Low temperature adsorption and investigation of interaction sites in STA-12

5.3.1 Hydrogen adsorption

Many governments have a 'hydrogen economy' as an aim for future energy needs. One of the major challenges to be overcome before the hydrogen economy can become a reality is how to store hydrogen safely and economically. The US department of energy has set stringent targets for hydrogen storage capacity for mobile applications that are yet to be met (6.0 wt% and 45 gL^{-1} by 2010, and 9.0 wt% and 81 gL^{-1} by 2015).[2] Physisorption of hydrogen gas onto porous materials has been looked at as a possible solution, with MOFs attracting considerable interest.

Most of the measurements for hydrogen storage have taken place at 77 K, which would create a technical challenge if used in fuel and energy delivery applications. Some interesting results using MIL-100 and MIL-101 (Chapter 1) have been obtained.[6] MIL-100 has an uptake of 3.3 wt% of H_2 at 25 bar pressure, with heats of adsorption ranging from -5.6 to -6.3 kJ mol^{-1}, while MIL-101 has an uptake of 6.1 wt% at 60 bar pressure, with heats of adsorption ranging from -9.3 to -10 kJ mol^{-1}. The thermodynamic requirement for an adsorbent capable of storing hydrogen at ambient temperature is calculated as a heat of adsorption of -15.1 kJ mol^{-1}. Both MIL-100 and MIL-101 can adsorb hydrogen at room temperature, but the uptakes are less than 1 wt% and the adsorption enthalpies are very low.

MIL-53 (Cr) (Chapter 1) has a wt% uptake at 77 K of 3.8 wt%, but does not adsorb hydrogen at room temperature. This indicates the presence of coordinatively unsaturated (CUS) metal sites in MIL-100 and MIL-101 is important, backed up by studies of H_2 adsorption on HKUST-1 and Ni CPO-27.[7] Using variable temperature Infra-red spectroscopy, HKUST-1 was measured with an adsorption enthalpy of -10.1 kJ mol^{-1} while Ni CPO-27 was measured at -13.5 kJ mol^{-1}. Both of these compare well to the measured adsorption enthalpies at 77 K for MIL-100 and MIL-101.

Studies of the correlation between surface area and pore size for hydrogen adsorption indicate some other important points have to be considered.[8] As well as CUS adsorption sites, a good adsorbent for H_2 has to have a high specific surface area and relatively small pore sizes to allow for high heats of adsorption.

5.3.2 H_2 adsorption and calorimetry

5.3.2.1 Ni STA-12

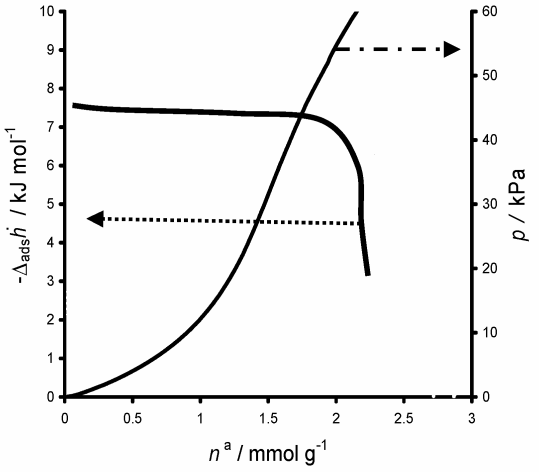

Figure 5.1 *– Adsorption isotherm and differential heat of adsorption for H_2 at 77 K on dehydrated Ni STA-12. Measurements undertaken by Prof P. L. Llewellyn at University of Marseille.*

The adsorption of H_2 at 77 K onto dehydrated Ni STA-12 displays a constant enthalpy of -7.5 kJ mol^{-1} up to 2 mmol g^{-1} loading (Figure 5.1). This is lower than the values observed for other MOFs with CUS metal sites, such as MIL-100 (-11 kJ mol^{-1}), MIL-101 (-9 kJ mol^{-1}),[6] Ni CPO-27 (-13.5 kJ mol^{-1})[7] or $NaNi_3OH(SIP)_2$ (-9.4 kJ mol).[9] The constant enthalpy with adsorption is different to other structures, where interactions change with increased loading. This indicates hydrogen is adsorbing on equivalent sites without significant $H_2 – H_2$ interactions.

Studies of the structure of dehydrated Ni STA-12 (Chapter 4) indicate there is *ca.* 5.2 mmol Ni^{2+} g^{-1}. This means the adsorption of hydrogen must be happening on only one out of the three crystallographically distinct Ni^{2+} cations, possibly due to problems with access (Figure 5.2). Therefore, hydrogen does not interact strongly enough with the Ni STA-12 framework to allow it to distort (as it does with water – Chapter 4).

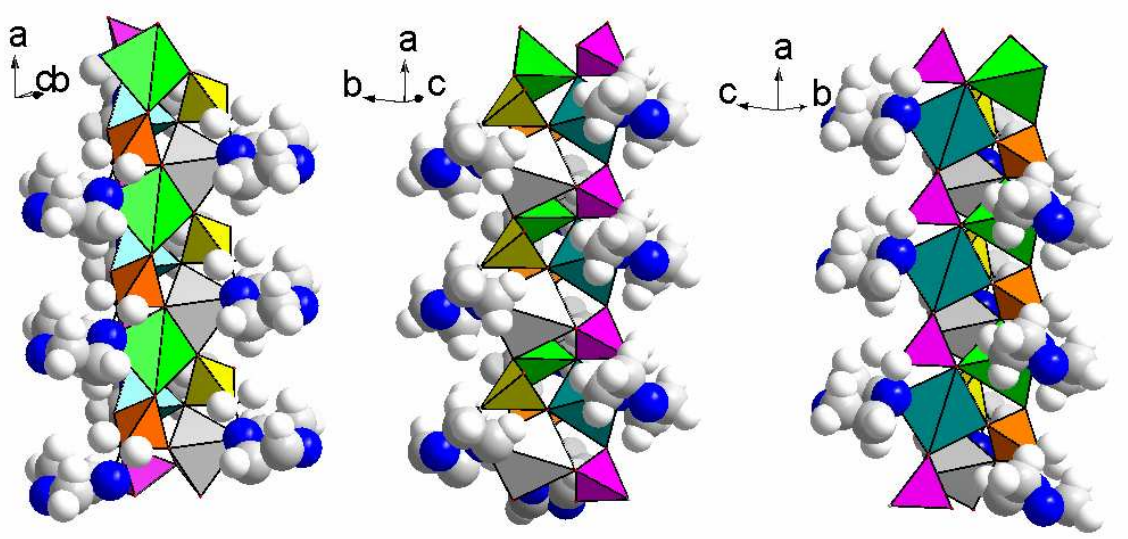

Figure 5.2 *– Structural diagrams showing different accessibility to the three crystallographically distinct Ni^{2+} cations in dehydrated Ni STA-12 - space filling for ligand atoms (Colour scheme - Ni(1) green; Ni(2) grey; Ni(3) dark blue-green; P(1) orange; P(2) purple; P(3) yellow).*

The adsorption of H_2 at low temperature is a well characterised Infra-red probe of adsorption sites. It is small enough to reduce steric interactions, and the effects on the resulting spectra are well understood (Chapter 2).[10, 11] The shift in the vibration frequency, with respect to the theoretical band at 4060 cm^{-1}, gives an indication of the strength of the interaction. The intensity of the band(s) also indicates the amount of each adsorption site(s) present.

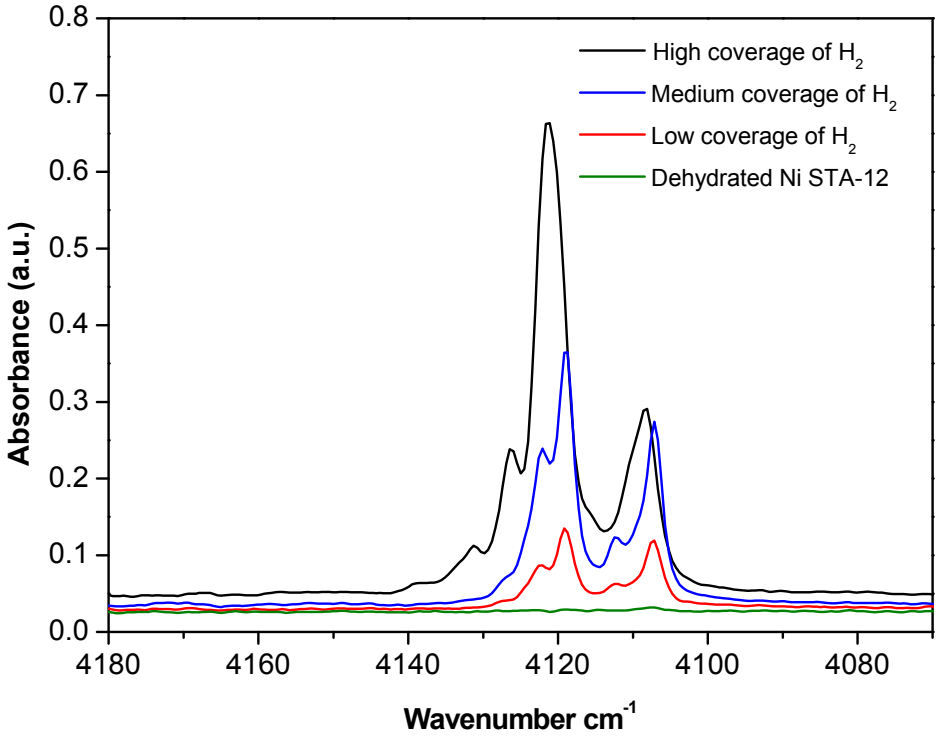

Figure 5.3 *– Background-subtracted Infra-red spectra of increasing coverage of H_2 adsorbed at 20 K on dehydrated Ni STA-12 – H_2 coverage increasing from bottom to top. Measurements undertaken in collaboration with Prof S. Bordiga at University of Turin.*

The adsorption of hydrogen onto dehydrated Ni STA-12 at 20 K shows an evolution of the spectra with increasing loading (Figure 5.3). The most reactive sites adsorb hydrogen first, forming two bands at 4107 cm^{-1} and 4119 cm^{-1}. These bands grow in intensity in a parallel way, indicating there are similar interaction energies. Increasing the coverage results in the appearance of two extra bands, on the high frequency side of these two main bands (4122 and 4112 cm^{-1}). An further increase in the loading results in these four bands turning into two bands at 4121 and 4108 cm^{-1}, along with formation of two new bands at 4132 and 4126 cm^{-1}.

The hydrogen is interpreted to be interacting with the Ni sites in a linear fashion, as a dipole is induced. It would be expected that only one band would be seen in the spectra, so the appearance of several bands indicates not all of the interaction sites are equivalent.

At low coverage, two bands being present means the accessible interaction sites are not the same as one another, and the evolution of these initial bands as the coverage increases indicates dipoles are induced in a complex fashion through multilayers.

The frequency shifts for the bands due to interaction of H_2 with Ni STA-12 are not as large as for other MOFs with CUS sites.[7] As the temperature is decreased, H_2 is first observed in the spectrum at 95 K, which is a significantly lower temperature than for HKUST-1 and Ni CPO-27.[7] H_2 can also be fully desorbed at 20 K, confirming the calorimetry results that there is weak interaction.

Similar spectral evolution is observed for H_2 adsorbed onto other MOFs.[7, 11, 12] In Ni CPO-27, the adsorption produces bands at 4035 and 4028 cm^{-1} due to interaction with Ni^{2+} sites.[17] The lower interaction energy and higher observed frequency for H_2 adsorption on Ni STA-12 indicates phosphonate oxygen atoms are partially shielding the Ni^{2+} cations (Figure 5.2), meaning access is affected differently by the ligands. Ni (1) and Ni (2) are impeded by the P=O group (P(3)). Therefore, uptake on Ni (3) can explain most of the low pressure adsorption of H_2 at 77 K (Figure 5.1).

5.3.2.2 Co STA-12

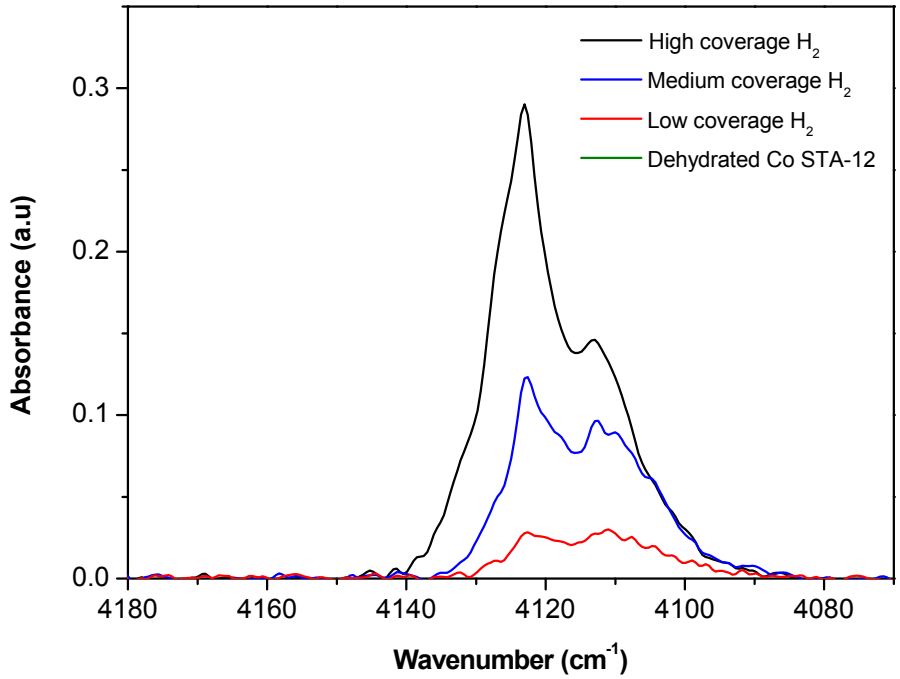

Figure 5.4 *– Background-subtracted Infra-red spectra of increasing coverage of H_2 adsorbed at 20 K on dehydrated Co STA-12 – H_2 coverage increasing from bottom to top. Measurements undertaken in collaboration with Prof S. Bordiga at University of Turin.*

Adsorption of H_2 at 20 K onto Co STA-12 also shows evolution of the Infra-red spectra (Figure 5.4). The most reactive sites adsorb hydrogen at low coverage, forming two bands at 4110 cm^{-1} and 4123 cm^{-1} which evolve in a parallel way. Compared to Ni STA-12 the spectral evolution is not as complex, the overall intensity is lower and the bands are present at higher frequency. These all indicate the adsorption of H_2 onto Co STA-12 takes place with lower adsorption energies, although hydrogen is interpreted to be interacting with the Co^{2+} sites in a linear fashion as interpreted for Ni STA-12.

5.3.3 Carbon monoxide adsorption

CO is one of the most used probes of the acidity of adsorption sites in Infra-red spectroscopy.[10] The interaction of CO with HKUST-1[11, 12] is driven by the presence of CUS Cu^{2+} cations in the structure after thermal activation. Only low equilibrium pressures were used, but two distinct copper sites were distinguished. These are a more polarizing but significantly less populated site (located at the external faces of the crystals) and the regular Cu^{2+} sites coordinated in the framework.

In a study to characterise the acidity present in MIL-100,[13] water and alcohols of various acidities were adsorbed, with CO used as a probe of the acid sites. The results indicated MIL-100 has acid – base properties that are different from those of zeolites. The acidity measurements indicate MIL-100 has a large number of Lewis acid sites, with two present per Cr trimer. The CO adsorption shows the acid sites are heterogeneous, which was ascribed to the effect of fluorine atoms in neighbouring trimers. CO adsorption also indicates Lewis acid sites can be converted to Brønsted acid sites by uptake of water or alcohols onto the CUS Cr cations.

A study of the interaction of CO with Ni CPO-27[14] indicated a stable monocarbonyl adduct was formed, which was measured to have a very high differential heat of adsorption of -58 kJ mol^{-1}. The CO was observed to coordinate directly to the CUS Ni sites, and despite the high differential heat of adsorption the CO was completely and reversibly removed at room temperature under high vacuum.

5.3.4 CO adsorption and calorimetry

5.3.4.1 Ni STA-12

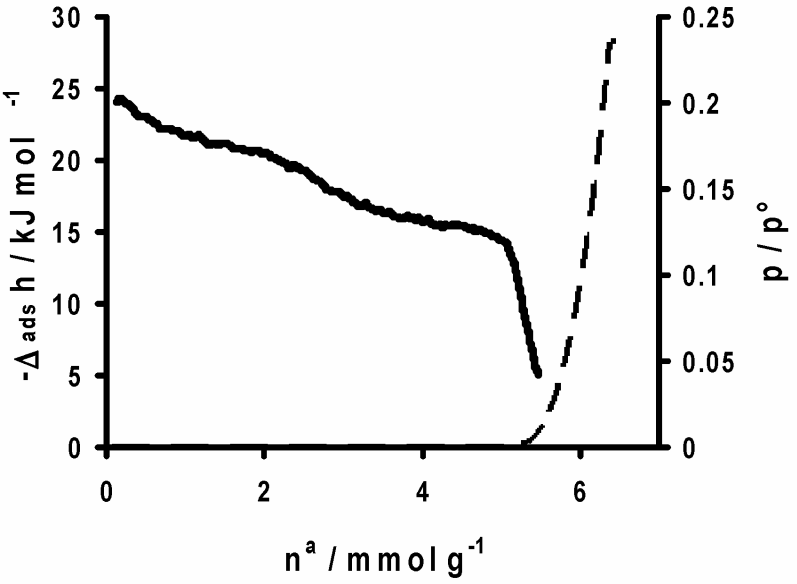

Figure 5.5 *– Adsorption isotherm (dashed line) and differential heat of adsorption (solid line) for CO adsorption at 77 K on dehydrated Ni STA-12. Measurements undertaken by Prof P. L. Llewellyn at University of Marseille.*

Adsorption of CO onto dehydrated Ni STA-2 at 77 K results in an uptake of 6 mmol g^{-1} at $p/p_o = 0.2$ (Figure 5.5). The adsorption enthalpies have an initial value of -24 kJ mol^{-1}, decreasing to -14 kJ mol^{-1} at a loading of 5 mmol g^{-1}. The adsorption enthalpy trace indicates two adsorption regimes are present, with ranges of -19 to -24 kJ mol^{-1} (0 - 2 mmol g^{-1}) and -14 to -17 kJ mol^{-1} (2 - 5 mmol g^{-1}). This can be interpreted as the adsorption sites being energetically heterogeneous.

The two adsorption regimes can be related to adsorption happening on all the Ni^{2+} cations. The higher energy adsorption step occurs up to 2 mmol g^{-1}, which is similar to the total H_2 uptake. This means the same sites responsible for H_2 adsorption are also responsible for the higher energy CO adsorption. The lower energy adsorption can then be related to CO adsorbing onto the less accessible Ni^{2+} cations. The stronger interaction energy of CO means the structure relaxes, allowing access to all of the Ni^{2+} cation sites. The brown-

yellow colour of dehydrated Ni STA-12 is replaced by a green colour after adsorption that is similar to the fully hydrated sample. Therefore, CO can change the electronic configuration of Ni STA-12 by adsorbing to the metal sites. The colour change is irreversible at 77 K, with the sample having to be warmed to room temperature under vacuum to desorb CO and restore the dehydrated colour.

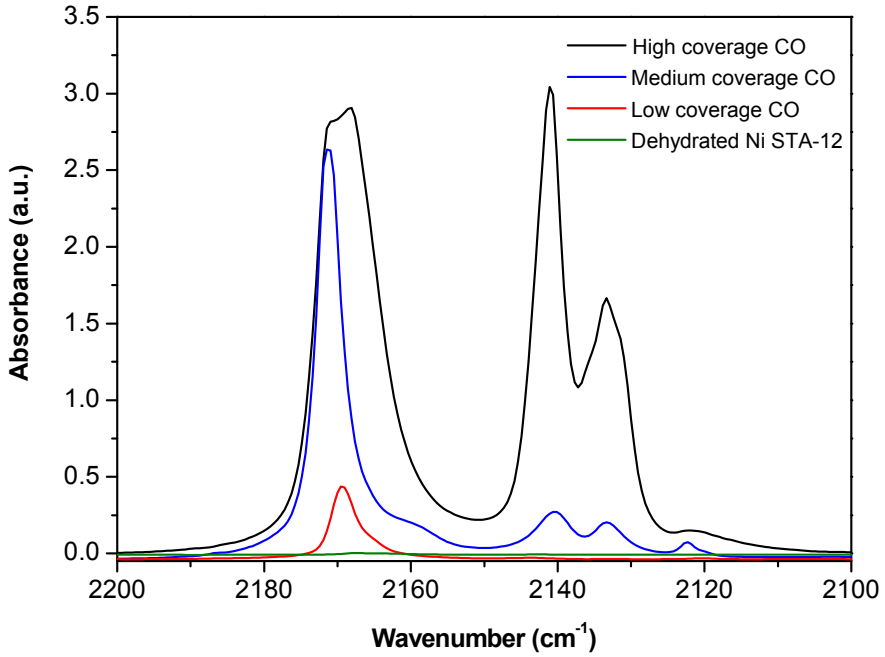

Figure 5.6 *- Background-subtracted Infra-red spectra of increasing coverage of CO adsorbed at 77 K on dehydrated Ni STA-12 – CO coverage increasing from bottom to top. Measurements undertaken in collaboration with Prof S. Bordiga at University of Turin.*

The effect of increasing the loading of CO at 77 K on the Infra-red spectra of dehydrated Ni STA-12 is shown in Figure 5.6. At low coverage, a band at 2170 cm^{-1} is observed along with a weak intensity band at 2122 cm^{-1}. The high frequency band is interpreted as ^{12}CO bound linearly through carbon to Ni^{2+}, but the frequency shift is less than for bare Ni^{2+} (the weak band at low wavenumber is interpreted as the related ^{13}CO species).[15] The

lower frequency shift is attributed to the steric effects of the ligands, explained previously for H_2 adsorption (Figure 5.2).

At higher loading a band at 2140 cm^{-1} appears from CO condensing in the pores. A band at 2133 cm^{-1} also appears, from interaction of CO with the P=O groups in dehydrated Ni STA-12.[10, 11] The red shift in the frequency is explained as the interaction taking place via electron donation from the O of the P=O into the 2π antibonding orbital of CO. This is a weak interaction, as it is only observed at low temperature (near 77 K). The band at 2170 cm^{-1} is stable at 77 K, and an increase in temperature is needed to remove it. Therefore, it corresponds to the adsorption, noted in the calorimetry measurements, that changes the sample colour.

5.3.4.2 Co STA-12

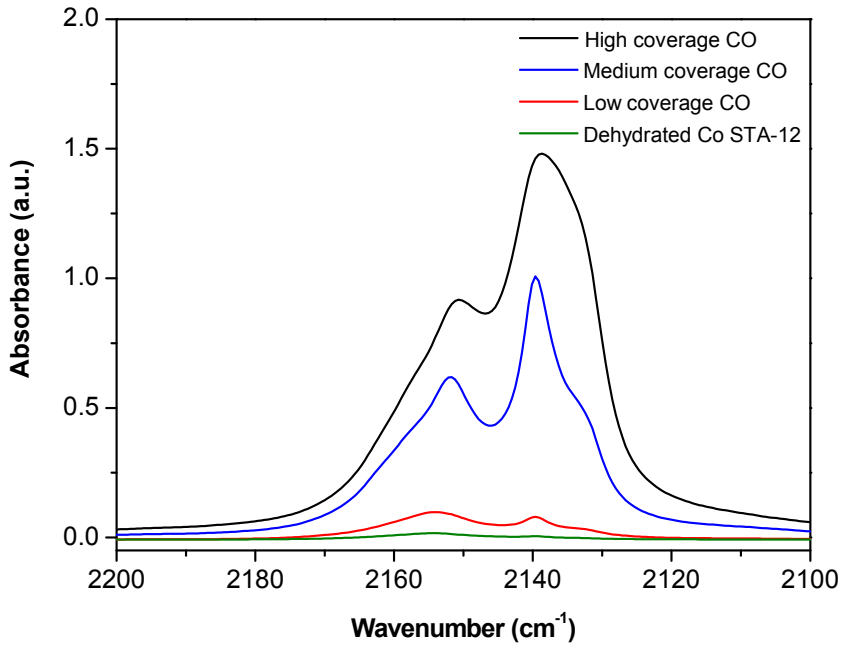

Figure 5.7 *- Background-subtracted Infra-red spectra of increasing coverage of CO adsorbed at 77 K on dehydrated Co STA-12 – CO coverage increasing from bottom to top. Measurements undertaken in collaboration with Prof S. Bordiga at University of Turin.*

A band at 2153 cm^{-1} is observed at low loading, and comparing to Ni STA-12, it can be interpreted as due to adsorption of CO linearly onto the Co^{2+} cation sites (Figure 5.7). The frequency shift, $\Delta\nu$, of + 13 cm^{-1} is not as high as for Ni STA-12, and the intensity of the peaks are lower. This indicates the interaction between CO and the metal cation sites is weaker in Co STA-12. CO condenses in the pores, producing a band at 2140 cm^{-1}, while a weak intensity band also develops at 2133 cm^{-1}. Comparing to Ni STA-12, this is interpreted as CO interacting with the P=O groups present in dehydrated Co STA-12.[10, 11] This interaction is also weaker than for Ni STA-12, as the intensity is less.

5.4 Ambient temperature adsorption and investigation of interaction sites in STA-12

5.4.1 Carbon dioxide and methane adsorption

Several studies have been undertaken into ambient temperature adsorption of CO_2, as it is considered to be a harmful greenhouse gas. Yaghi *et al*. have investigated the IRMOF-*n* series for CO_2 adsorption, comparing to HKUST-1 and some industrial adsorbents.[16] Nine IRMOFs were evaluated for adsorption at ambient temperature and pressures up to 35 bar. Most demonstrated Type I adsorption isotherms, especially in the low pressure regions. For IRMOF-3 and -6, which have alkyl and amino functionalisation on the ligands, the capacity for CO_2 was observed to be higher than the other samples. The isotherms take on a sigmoidal shape, as these samples have larger surface areas, leading to behaviour closer to a bulk fluid at high pressure. MOF-177 has a very high surface area (over 4,500 $m^2\ g^{-1}$) and porosity, and demonstrated adsorption of 33.5 mmol g^{-1}, which at the time was the highest reported CO_2 uptake for any porous material.

Férey *et al*. have investigated uptake of CO_2 by MIL-100 and MIL-101.[17] MIL-100 had an uptake of 18 mmol g^{-1} at 5 MPa and 303 K. This is lower than MOF-177, but the volume adsorbed was found to reach 280 $cm^3_{STP}\ cm^{-3}$ at 5 MPa. The enthalpy of adsorption for MIL-100, -63 kJ mol^{-1}, is the highest reported for adsorption of CO_2 on any porous material. MIL-101 adsorbed 40 mmol g^{-1} at 5 MPa and 303 K, leading to a volumetric adsorption of 390 $cm^3_{STP}\ cm^{-3}$. This is the highest recorded volumetric uptake of CO_2 for any porous material, but it is dependent on how MIL-101 is activated.

MIL-53 has also been investigated for CO_2 adsorption.[18-21] The striking feature of the adsorption isotherms was the presence of a step as the pressure increased above 6 bar. The enthalpy of adsorption was measured below the step (for the Al version) as -35 kJ mol^{-1}. Above the adsorption step the enthalpy decreased to a minimum slightly below the enthalpy of liquefaction (-17.2 kJ mol^{-1}). For Cr MIL-53, the initial adsorption enthalpy was measured at -32 kJ mol^{-1}, and a similar reduction was observed above the step. The step was attributed to strong interaction between CO_2 and the framework below 6 bar, causing the pores to close, indicating initial adsorption took place on the hydroxyl groups. As the gas pressure increased the pores opened up, resulting in a large increase in uptake and a reduction in the adsorption enthalpies.

Methane (CH_4) is also a UV active greenhouse gas, and Férey *et al*. have tested uptake in MIL-100, MIL-101,[6] MIL-53 and MIL-47.[18, 22] The adsorption isotherms at 303 K were observed to increase gradually with increasing pressure, but without total pore filling. At 3.5 MPa, 119 cm^3_{STP} cm^{-3} of methane was adsorbed onto MIL-100, which was less than Al MIL-53 (150 cm^3_{STP} cm^{-3}) and the US DOE target (180 cm^3_{STP} cm^{-3}). The activation method of MIL-101 did not affect the adsorption of methane, and saturation was not reached even at 8 MPa. The uptake of 13.6 mmol g^{-1} at 6 MPa was more than for MIL-100 (9.5 mmol g^{-1} at 6 MPa). The volume capacity (135 cm^3_{STP} cm^{-3}) was more than for MIL-100, but less than for MIL-53, and the results indicated CH_4 interacts weakly with the adsorbents due to the lack of a quadrupole on the molecule.[23]

5.4.2 Low pressure CO_2 adsorption

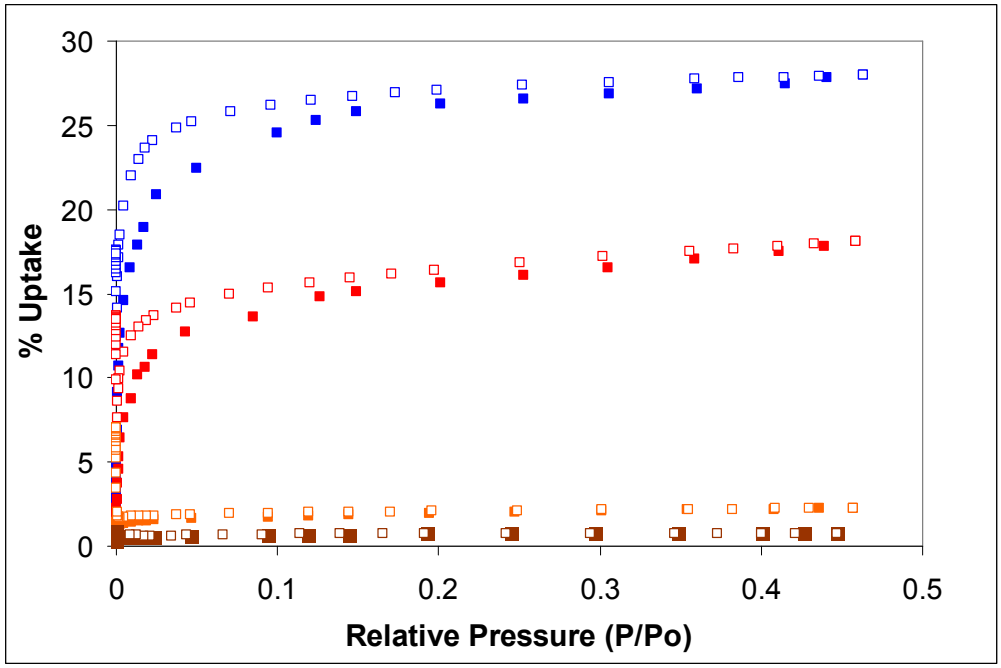

Figure 5.8 *– Low pressure adsorption (full squares) and desorption (empty squares) isotherms for CO_2 at 196 K on STA-12 - Mn (orange), Fe (brown), Co (red) and Ni (blue).*

In order for the maximum uptake of CO_2 at low pressure to be measured on the STA-12 structures, the isotherm data was collected at 196 K (Figure 5.8), which is near the condensation temperature for CO_2 (194 K). Neither Fe nor Mn STA-12 adsorbs any appreciable amount of CO_2. As outlined in Chapter 4, both of these structures can reversibly lose and uptake water but do not adsorb N_2 gas. The CO_2 molecule is a similar size to the N_2 molecule, and the quadrupole is similar. Therefore, the amorphous surface layer thought to form on dehydration in Fe and Mn STA-12 would not be expected to admit CO_2 molecules into the pores.

Co STA-12 adsorbs 15 wt% of CO_2 at p/p_0 = 0.2, and as the pressure increases a secondary slow uptake to 17 wt% (4.25 mmol g^{-1}) at p/p_0 = 0.5 is also observed. This is similar to the behaviour for N_2 adsorption (Chapter 4), and suggests the particle size of the sample is quite small or the structure is flexible. The CO_2 can be reversibly desorbed, with evidence of a slight hysteresis. Ni STA-12 is observed to adsorb CO_2 with a typical

Type I isotherm, and an uptake of 28 wt% (7 mmol g^{-1}) at $p/p_o = 0.4$. This is similar to the uptake of N_2 at 77 K (Chapter 4). A slight hysteresis is noticeable on desorption, indicating some reasonably strong interactions are taking place between CO_2 and Ni STA-12. It has been noted changing the metal in MIL-53[24] results in large differences in the dehydration and adsorption properties of the structure, and something similar is happening with STA-12.

5.4.3 CO_2 and CH_4 adsorption and calorimetry

5.4.3.1 Ni STA-12

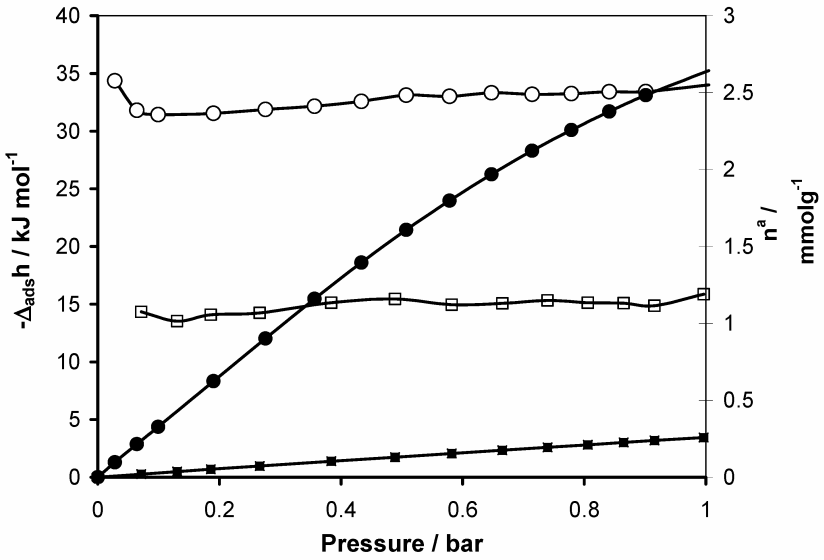

Figure 5.9 *– High resolution low pressure adsorption isotherms (solid symbols) and differential heats of adsorption (empty symbols) from 0 - 1 bar, measured for CO_2 (circles) and CH_4 (squares) at 303 K on dehydrated Ni STA-12. Measurements undertaken by Prof P. L. Llewellyn at University of Marseille.*

The enthalpies of adsorption for CO_2 are between -30 to -35 kJ mol^{-1} at 303 K, while those for CH_4 are between -14 to -16 kJ mol^{-1} (Figure 5.9). The low pressure data shows uptake of CO_2 is *ca.* 10 × that of methane at 1 bar. This is a higher ratio than for other large pore MOFs, such as MIL-100, MIL-101 and MOF-177,[17, 25] and is close to that

observed for some cationic zeolites.[1] Therefore, Ni STA-12 demonstrates good selectivity for adsorption from gas mixtures, which might be of use in pressure swing applications.

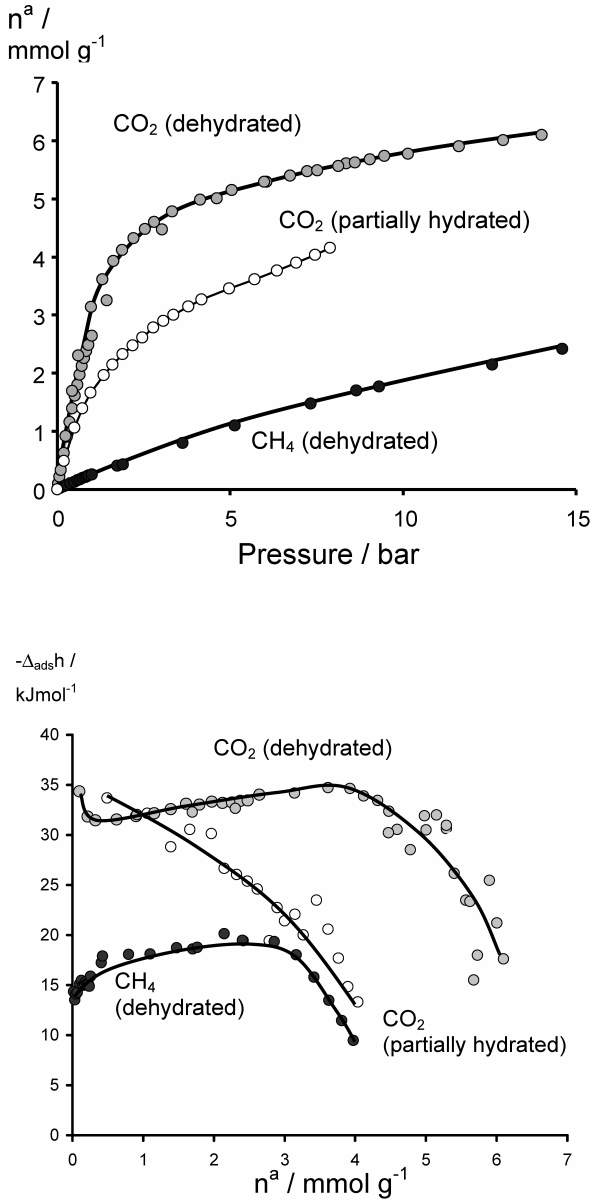

Figure 5.10 *– (Top) High pressure adsorption isotherms and (Bottom) differential heats of adsorption measured for CO_2 and CH_4 on Ni STA-12 at 303 K (CO_2: partially dehydrated – white circles, fully dehydrated – grey circles; CH_4: black circles). Measurements undertaken by Prof P. L. Llewellyn at University of Marseille.*

High pressure isotherms were measured for CO_2 adsorbed on both partially dehydrated (physisorbed water only removed) and fully dehydrated Ni STA-12 (Figure 5.10). The loading of CO_2 on fully dehydrated Ni STA-12 is 6 mmol g^{-1} at 15 bar, which compares well to the 7 mmol g^{-1} measured in the lab at low temperature and pressure. Loading of 6 mmol g^{-1} at 15 bar corresponds to roughly one adsorbed CO_2 molecule per Ni. This indicates the high pressure ambient temperature adsorption mechanism is similar to the low pressure adsorption mechanism close to the condensation temperature. The enthalpies of adsorption are -30 kJ mol^{-1} when the adsorption starts; reach a maximum of -35 kJ mol^{-1} at an uptake of 4 mmol g^{-1}, before decreasing at higher loadings.

The increase in the adsorption enthalpies as the uptake increases from 0.5 mmol g^{-1} to 4 mmol g^{-1} is interpreted as adsorption of CO_2 onto a homogeneous pore structure, with the increase in the enthalpies due to $CO_2 - CO_2$ interactions. The decrease in the enthalpies above 4 mmol g^{-1} is due to rearrangement of the first adsorbed molecules to allow complete filling of the pores.

The initial enthalpies of adsorption for CO_2 on fully dehydrated Ni STA-12 of between -30 and -35 kJ mol^{-1} are similar to those for zeolite NaY,[26] meaning some relatively polar centres are present in the framework. The adsorption enthalpies for CO_2 on fully dehydrated Ni STA-12 are greater than the -22 kJ mol^{-1} measured for MIL-47,[18] which has similar sized pores but no CUS metal sites. Ni CPO-27 has slightly higher enthalpies of adsorption in the region of -40 kJ mol^{-1}, as the structure does not undergo any distortion with water loss.[27] Greater enthalpies of adsorption are also observed for MIL-100 and MIL-101.[17]

Partially dehydrated Ni STA-12 has an uptake for CO_2 at 15 bar of 4 mmol g^{-1}. The initial adsorption enthalpies are similar to fully dehydrated Ni STA-12 (indicating some of the Ni^{2+} sites might be dehydrated), and a rapid decrease is observed as the loading increases. The chemisorbed water shields the Ni^{2+}, and CO_2 therefore interacts with hydroxyl and organic groups in the framework with lower energies that the CUS Ni^{2+} cation sites.

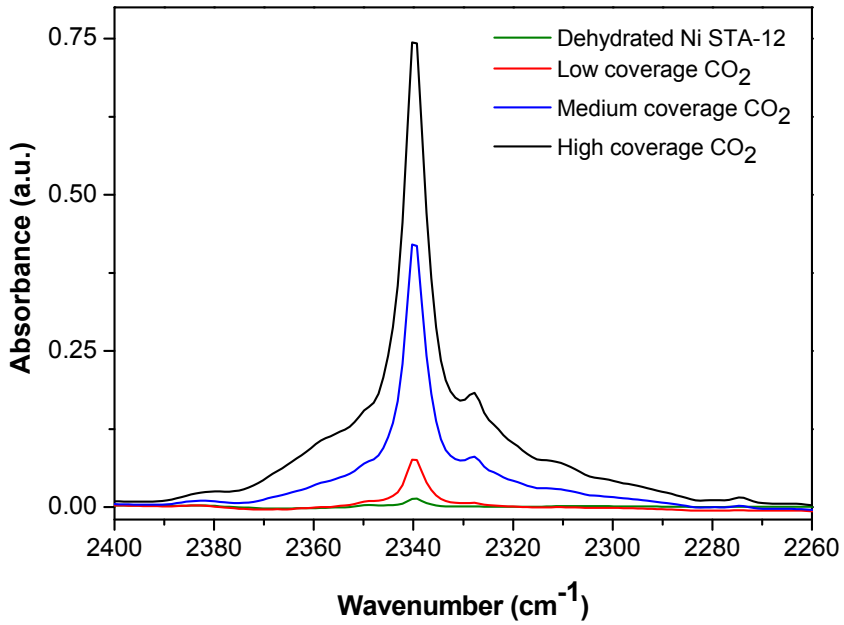

Figure 5.11 *– Background-subtracted Infra-red spectra of increasing coverage of CO_2 at 303 K on dehydrated Ni STA-12 – CO_2 coverage increasing from bottom to top. Measurements undertaken in collaboration with Prof S. Bordiga at University of Turin.*

The adsorption of CO_2 was studied with Infra-red spectra collected at 303 K on dehydrated Ni STA-12 (Figure 5.11). Only low equilibrium pressures (9 mbar) could be used as the ν_3 mode (asymmetric O=C=O stretch, Table 2.3 in Chapter 2) has a high extinction coefficient, and the spectra go off the scale very quickly.[28] The intense band at 2339 cm^{-1} is due to the ν_3 vibration of CO_2 bound linearly to Ni^{2+}, and the small blue frequency shift (+ 10 cm^{-1}) can be explained with reference to HKUST-1.[29] The CO_2 is interacting with the full NiO_4N unit, rather than just Ni^{2+} (which should give large blue frequency shifts as observed with oxides and zeolites[28]). Therefore, the shielding around the Ni^{2+}, discussed previously for low temperature adsorption, results in behaviour that is different from what might be expected.

CH_4 adsorption at high pressure onto fully dehydrated Ni STA-12 (Figure 5.10) results in initial adsorption enthalpies between -14 to -16 kJ mol^{-1}. These increase to -20 kJ mol as the uptake increases, with CH_4 – CH_4 interactions becoming more important. There is a

rapid decrease in the adsorption enthalpies at high pressures, indicating pore filling takes place via rearrangement of the first adsorbed molecules. The enthalpies are similar to those seen for MIL-53, MIL-47,[18] MIL-100 and MIL-101,[17] meaning the interaction of methane with Ni STA-12 is quite weak.

5.4.3.2 Co STA-12

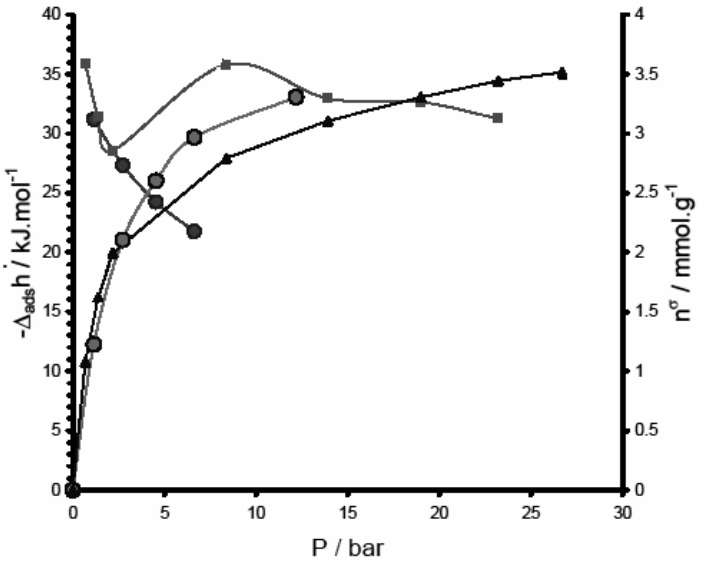

Figure 5.12 *- High pressure adsorption isotherms and differential heats of adsorption measured for CO_2 on Co STA-12 at 303 K (Dehydrated under vacuum: isotherm – grey circles; differential heats of adsorption – black circles; Dehydrated at 423 K: isotherm – black triangles; differential heats of adsorption - grey squares). Measurements undertaken by Prof P. L. Llewellyn at University of Marseille.*

CO_2 uptake on Co STA-12 dehydrated at 423 K is 3.5 mmol g^{-1} at 15 bar (Figure 5.12), which compares to the 4.25 mmol g^{-1} measured in the lab at low pressure and temperature. As with Ni STA-12, this indicates the adsorption mechanism is similar to that observed close to the condensation temperature. The enthalpies of adsorption are initially -30 kJ mol^{-1}, and they reach a maximum of -35 kJ mol^{-1} at a loading of 2.75 mmol g^{-1}. The enthalpies of adsorption on Co STA-12 dehydrated at 423 K are similar to those measured for Ni STA-12 and zeolite NaY,[26] indicating Co STA-12 also contains some relatively polar centres.

Co STA-12 dehydrated under vacuum has a loading of 3.5 mmol g^{-1} at 15 bar, indicating similar adsorption sites are present as in the dehydrated at 423 K phase. This means all the water can be removed at room temperature under high vacuum, as seen in Chapter 4. The initial adsorption enthalpies are similar to those observed for the fully dehydrated sample, but there is a rapid decrease with increasing coverage. This indicates maybe not all of the Co^{2+} sites have water removed under vacuum and there may be some residual water, which is suggested from Infra-red studies of dehydration at 298 K presented in Chapter 4 (Figure 4.24). The adsorption performance for CO_2 is less for Co STA-12 than for Ni STA-12, and this behaviour is similar to the observations for low temperature adsorption of N_2, H_2, CO and CO_2. Therefore, the decreased crystallinity of Co STA-12 compared to Ni STA-12 appears to affect the adsorption performance.

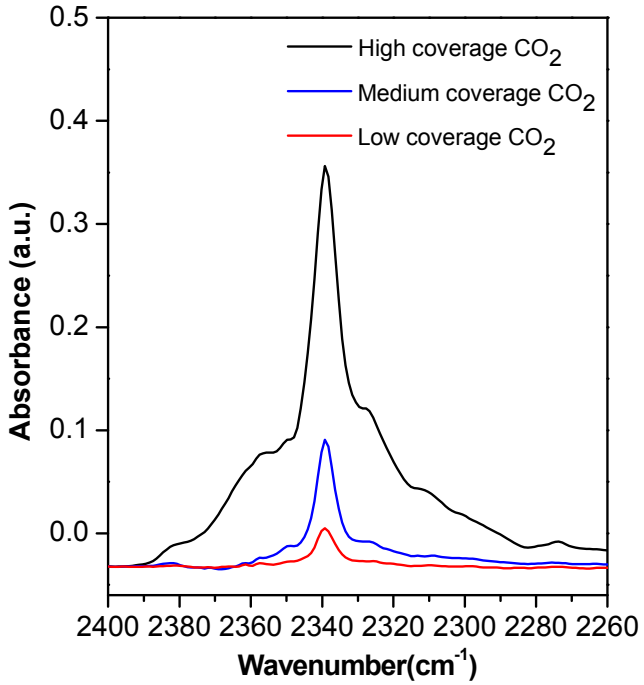

Figure 5.13 *- Background-subtracted Infra-red spectra of increasing coverage of CO_2 at 303 K on dehydrated Co STA-12 – CO_2 coverage increasing from bottom to top. Measurements undertaken in collaboration with Prof S. Bordiga at University of Turin.*

The high intensity band at 2339 cm^{-1} is from the ν_3 vibration of CO_2 bound linearly to Co^{2+} (Figure 5.13). The small blue shift (+ 10 cm^{-1}) can be explained as CO_2 interacting with the full CoO_4N unit. Therefore, the structural distortions taking place on dehydration of Co STA-12 (Chapter 4) appear to result in shielding around the metal cations in a similar way to Ni STA-12.

5.4.4 Acetonitrile adsorption

Acetonitrile is used as a probe molecule to evaluate different acid sites.[30, 31] The deuterated form (CD_3CN) is used, as this reduces the Fermi resonance overlaps in the resulting Infra-red spectra, allowing for easier interpretation of the C≡N stretching region (Chapter 2). The lone pair on the C≡N group acts as a Lewis base, and the study of ν(C≡N) is used to evaluate the acidity of adsorption sites. Bands blue shifted relative to free acetonitrile are interpreted as being due to interaction with acid sites.

5.4.5 CH_3CN adsorption

5.4.5.1 Ni STA-12

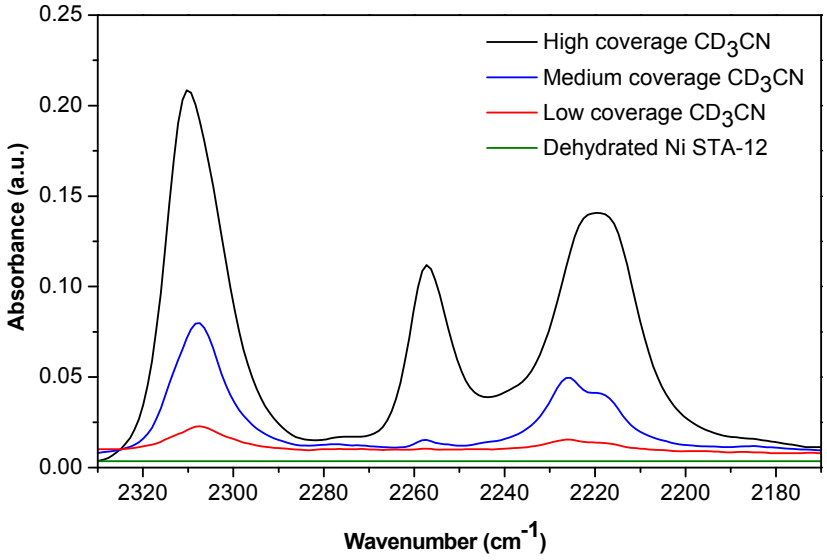

Figure 5.14 *– Background subtracted Infra-red spectra of CD_3CN adsorbed onto dehydrated Ni STA-12 at 303 K – CD_3CN coverage increasing from bottom to top. Measurements undertaken in collaboration with Prof S. Bordiga at University of Turin.*

Three bands are observed in the C≡N stretching region (Figure 5.14). One is blue frequency shifted (2310 cm^{-1}, $\Delta\nu$ = + 55 cm^{-1}) with respect to C≡N in free CD_3CN (2255 cm^{-1}), and one is red frequency shifted (2220 cm^{-1}, $\Delta\nu$ = -35 cm^{-1}). As outlined previously, blue shifted band in the C≡N region are due to interaction of CD_3CN with acid sites. The band at 2310 cm^{-1} can therefore be attributed to adsorption of acetonitrile onto medium strength Lewis acid Ni^{2+} sites.[31] The red frequency band at 2220 cm^{-1} is harder to explain. Red frequency shifted bands are rarely, if ever, seen in the C≡N stretching region of acetonitrile. Looking at the adsorption of H_2, CO and CO_2 onto Ni STA-12, as well as the metal cations, the P=O groups are also interaction sites. Therefore, interaction of C≡N with the P=O groups possibly produces the red shifted band.

Dosing of dry acetonitrile onto dehydrated Ni STA-12 using a glass line results in a colour change from brown/yellow to green, indicating the adsorption is able to change the electronic configuration of the nickel, as seen for CO adsorption. A sample exposed to

acetonitrile vapour was subsequently heated at 343 K under vacuum to try and remove any physically adsorbed molecules. The unit cell parameters from the X-ray analysis of the acetonitrile dosed sample compared to the unit cell parameters from Ni STA-12 measured at room temperature on a lab diffractometer [5] shows the structure returns to rhombohedral symmetry (Table 5.1). The parameters are similar to the fully hydrated as-prepared structure, but with a slight contraction in the cell volume by ~ 140 $Å^3$. Using Fourier maps the positions of the adsorbed acetonitrile molecules were located within the pores, and the atoms were allowed to refine, keeping restraints on to maintain the linearity of the adsorbed CH_3CN molecules. The atomic coordinates and cif file are presented in Appendix 7, while the final Rietveld plot is shown in Figure 5.15.

Table 5.1 *– Comparison of the atomic parameters of as-prepared Ni STA-12*[5] *and Ni STA-12 with adsorbed acetonitrile. The amount of adsorbed acetonitrile in the chemical formula was calculated using the acetonitrile occupancies scaled to two Ni (see Appendix 7).*

Formula	$Ni_2(H_2O)_2L.5.4H_2O$[5]	$Ni_2L.1.371CH_3CN$
Space Group	R-3	R-3
a (Å)	27.9486(4)	27.6408(12)
b (Å)	27.9486(4)	27.6408(12)
c (Å)	6.2302(1)	6.15530(32)
α (°)	90	90
β (°)	90	90
γ (°)	120	120
V ($Å^3$)	4214.6(1)	4072.68(33)
Diffractometer	Lab (STOE)	Lab (STOE)
Temperature (K)	298	298
Wavelength (Å)	1.5406 (Cu K_α)	1.5406 (Cu K_α)
R_{wp}	0.061	0.1093

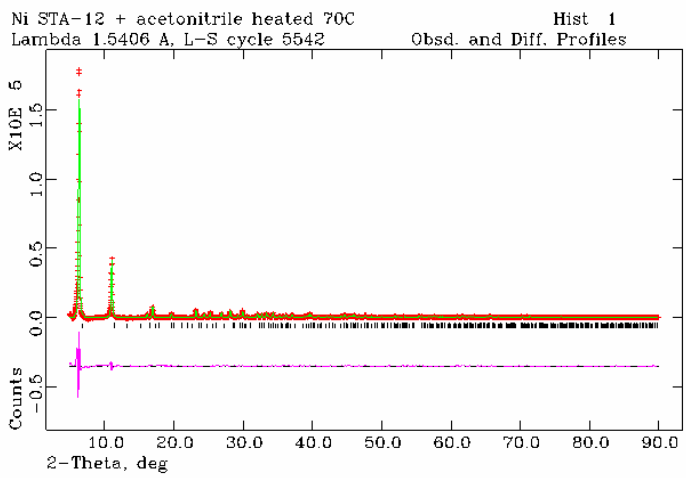

Figure 5.15 *– Rietveld refinement of dry acetonitrile adsorbed onto dehydrated Ni STA-12 (on glass line) at 298 K (Cu K_α radiation) – red: measured pattern, green: calculated pattern, purple: difference between measured and calculated patterns. (R_{wp} = 10.93 %, R_p = 7.53 %).*

The linear acetonitrile molecules coordinate via the nitrogen atoms to the Ni^{2+} sites, and point into the pore space, forcing the structure to adopt rhombohedral symmetry (Figure 5.16). Heating at 343 K under vacuum after adsorption removes most of the acetonitrile molecules not directly coordinated to the Ni^{2+} cations, although there is evidence that a small amount remains. The acetonitrile molecules bound to the Ni^{2+} cations have occupancies of *ca.* 0.5, meaning about half of the sites are coordinated. The remaining free pore space is about 5 Å in diameter.

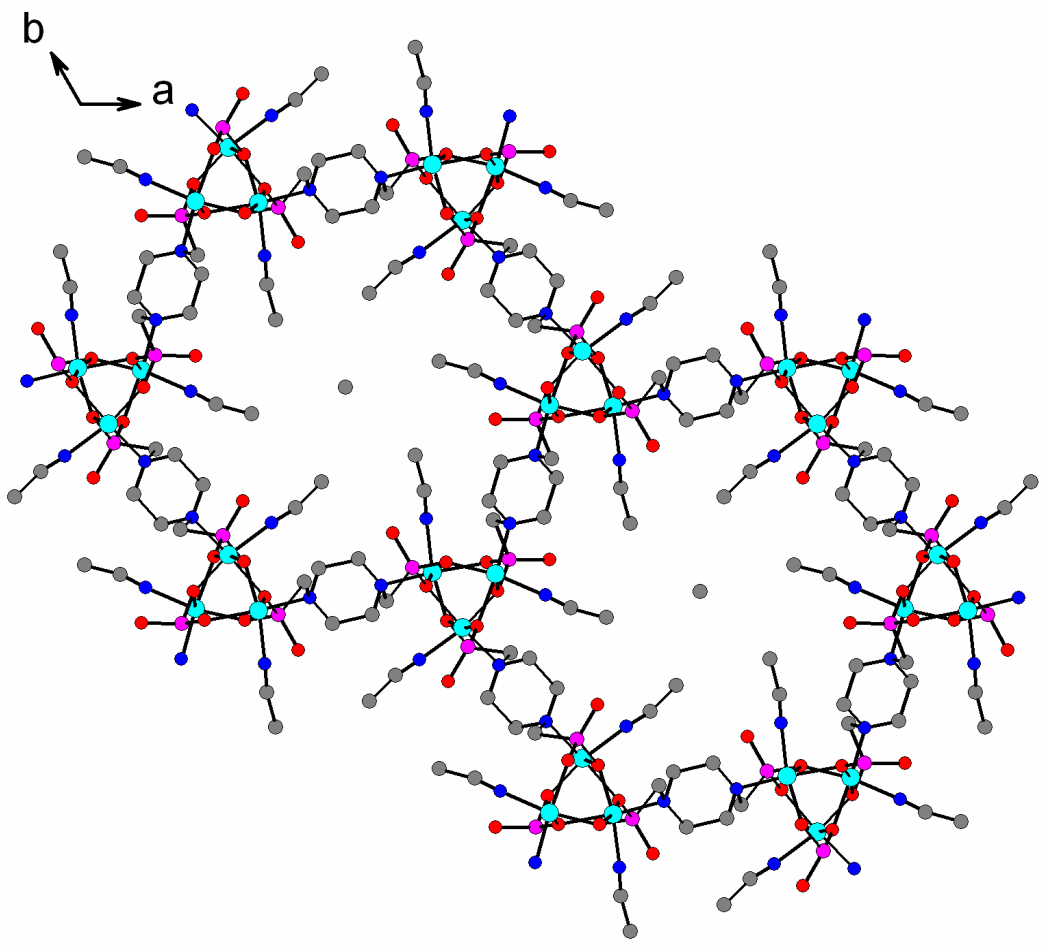

Figure 5.16 *– Ni STA-12, with coordinated acetonitrile molecules on the* Ni^{2+} *cations, looking down the direction of the large hexagonal pores. Ni atoms in light blue, phosphorous atoms in purple, oxygen atoms in red, nitrogen atoms in dark blue and carbon atoms in grey.*

5.4.5.2 Co STA-12

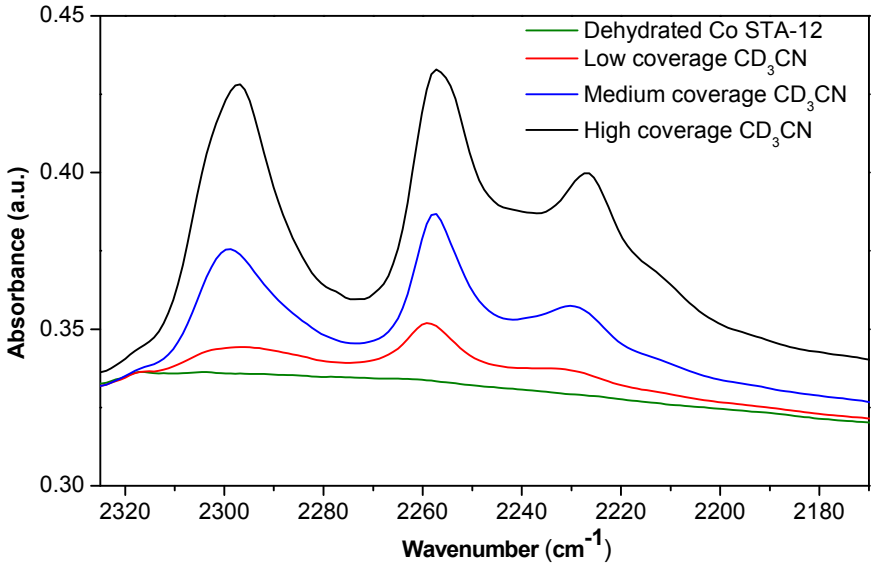

Figure 5.17 *– Selected region of background subtracted Infra-red spectra of CD_3CN adsorbed onto dehydrated Co STA-12 at 298 K, showing bands due to C≡N stretching - CD_3CN coverage increasing from bottom to top. Measurements undertaken in collaboration with Prof S. Bordiga at University of Turin.*

As for Ni STA-12, three bands are seen in the C≡N stretching region (Figure 5.17). One is blue frequency shifted (2300 cm^{-1}, $\Delta\nu$ = + 45 cm^{-1}) with respect to C≡N in free CD_3CN (2255 cm^{-1}), and one is red shifted (2225 cm^{-1}, $\Delta\nu$ = - 30 cm^{-1}). The blue frequency shifted band is interpreted as interaction with Co^{2+} sites, and the red shifted band is interpreted as the interaction with P=O groups. The intensity of the bands is less than for Ni STA-12, suggesting a lower uptake for acetonitrile.

Dosing of dry acetonitrile onto dehydrated Co STA-12 changes the electronic configuration of the solid by adsorbing to the Co^{2+} sites (colour change from blue to pink). X-ray analysis shows the structure returns to rhombohedral symmetry with unit cell parameters similar to the fully hydrated as-prepared structure (Table 5.2). Due to the reduced crystallinity of Co STA-12 compared to Ni STA-12, the CH_3CN molecule positions could not be determined. The final Rietveld plot is shown below in Figure 5.18.

Table 5.2 *- Comparison of the atomic parameters of as-prepared Co STA-12 and Co STA-12 with adsorbed acetonitrile.*

Formula	$Co_2(H_2O)_2L.5.4H_2O$	$Co_2L.xCH_3CN$
Space Group	R-3	R-3
a (Å)	28.0243(33)	28.0192(23)
b (Å)	28.0243(33)	28.0192(23)
c (Å)	6.2734(8)	6.2477(8)
α (°)	90	90
β (°)	90	90
γ (°)	120	120
V (Å^3)	4266.8(9)	4247.8(7)
Diffractometer	Lab (STOE)	Lab (STOE)
Temperature (K)	298	298
Wavelength (Å)	1.9361 (Fe K_α)	1.9361 (Fe K_α)
R_{wp}	0.1386	0.1161

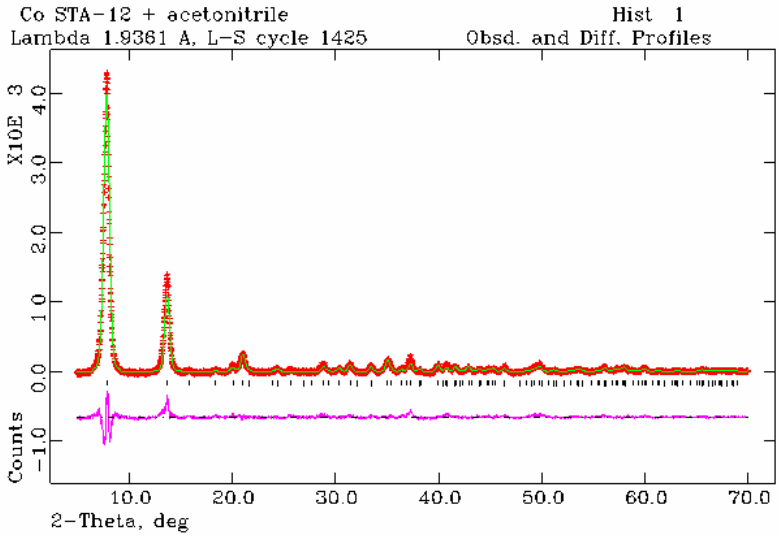

Figure 5.18 *- Rietveld refinement of dry acetonitrile adsorbed onto dehydrated Co STA-12 (on glass line) at 298 K (Fe K_α radiation). Colour scheme as Figure 5.15.*

5.4.6 Methanol adsorption

Methanol can act as an electron and proton donor, so the relative acidity/basicity and reactivity of adsorption sites can be investigated.[32] This is important when considering whether a material can be used as a catalyst, and also which type of reactions would be favoured. The adsorption of methanol along with water can also help to give insights into the relative activities of the interaction sites present in STA-12.

5.4.6.1 Ni STA-12

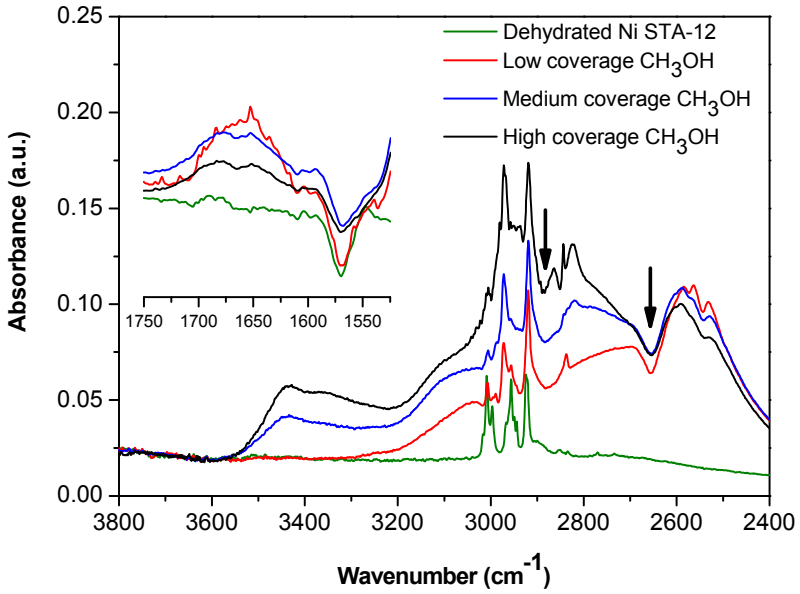

Figure 5.19 *– Infra-red spectra showing effect of adsorption of methanol at 303 K on dehydrated Ni STA-12 – high frequency region. CH_3OH coverage increasing from bottom to top. Measurements undertaken in collaboration with Prof S. Bordiga at University of Turin.*

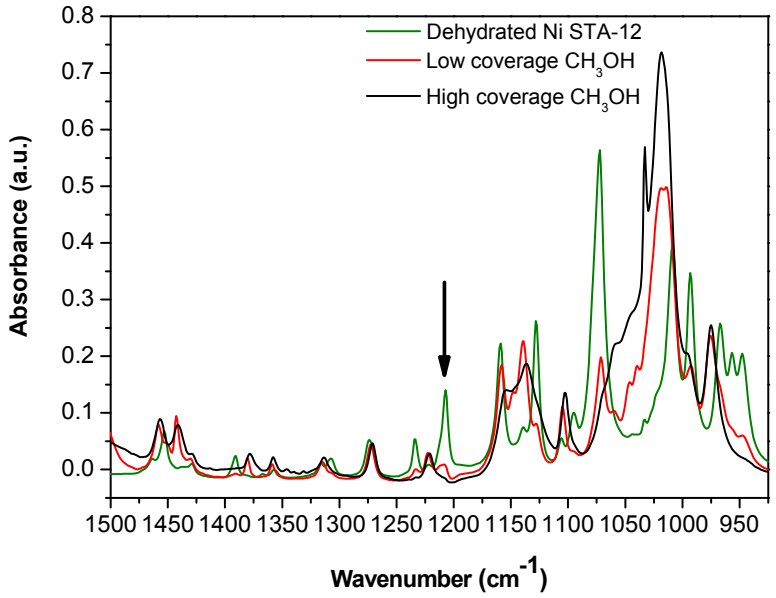

Figure 5.20 *– Infra-red spectra showing effect of adsorption of methanol at 303 K on dehydrated Ni STA-12 – low frequency framework region. Measurements undertaken in collaboration with Prof S. Bordiga at University of Turin.*

The effect of adsorption of methanol onto Ni STA-12 has been followed by Infra-red spectroscopy (Figures 5.19 and 5.20). At low loading, adsorption of CH_3OH results in the formation of a band at 2750 cm^{-1} similar to that formed on hydration (Chapter 4), interpreted as due to a hydrogen bonded hydroxyl group. The minima at 2650 and 2875 cm^{-1} (outlined by arrows in Figure 5.19) are due to interference from Fermi Resonance (Chapter 2), and there is no evidence for the formation of any bands due to free hydroxyls. In the bending region, there are bands at 1650 cm^{-1} and 1500 cm^{-1} from δ(OH).

As the loading of CH_3OH increases a weak intensity band at 3480 cm^{-1} appears, associated with -OH groups from methanol condensing in the pores. There are also changes in the C-H stretching region due to the symmetry of the structure increasing. The band at about 2925 cm^{-1}, associated with $-CH_3$ groups, increases in intensity as the number of methanol molecules increases.

At the highest loading of CH_3OH, the band at 2750 cm^{-1} decreases in intensity, along with the bands at 1650 and 1500 cm^{-1}. This indicates methanol is condensing in the pores of

the framework, resulting in reorganisation of the adsorbed molecules. In the framework region the band at 1207 cm^{-1} (outlined by arrow in Figure 5.20), assigned to the P=O groups in the dehydrated structure disappears (Chapter 4). This indicates methanol molecules are interacting and bonding with the P=O groups.

Dosing of dry methanol onto dehydrated Ni STA-12, using a glass line, results in a colour change from brown/yellow to green. This indicates the adsorption of methanol is able to change the electronic configuration of the solid, while X-ray analysis shows it returns to rhombohedral symmetry with very similar unit cell parameters to Ni STA-12 measured at room temperature on a lab diffractometer [5] (Table 5.3). It was not possible to locate the positions of the molecules in the structure by Fourier mapping, presumably because they were disordered. The final Rietveld plot is shown in Figure 5.21.

Table 5.3 *- Comparison of the atomic parameters of as-prepared Ni STA-12[5] and Ni STA-12 with adsorbed methanol.*

Formula	$Ni_2(H_2O)_2L.5.4H_2O$[5]	$Ni_2L.xCH_3OH$
Space Group	R-3	R-3
a (Å)	27.9486(4)	27.8655(12)
b (Å)	27.9486(4)	27.8655(12)
c (Å)	6.2302(1)	6.22912(31)
α (°)	90	90
β (°)	90	90
γ (°)	120	120
V ($Å^3$)	4214.6(1)	4188.81(33)
Diffractometer	Lab (STOE)	Lab (STOE)
Temperature (K)	298	298
Wavelength (Å)	1.5406 (Cu K_α)	1.5406 (Cu K_α)
R_{wp}	0.061	0.1521

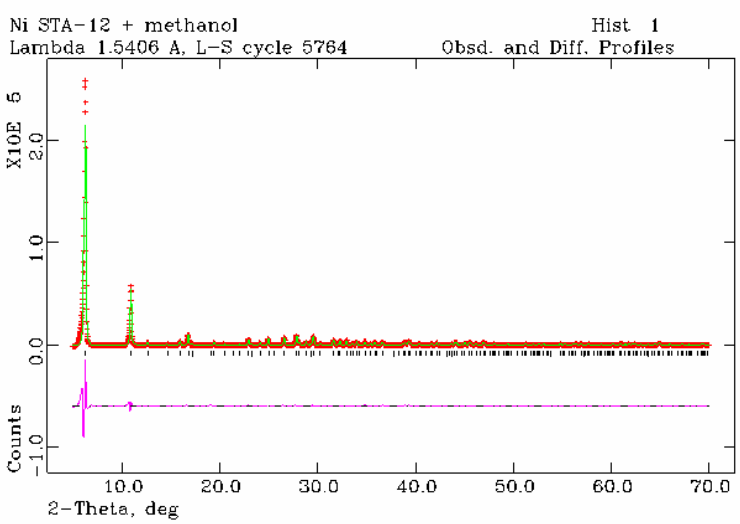

Figure 5.21 *– Rietveld refinement of dry methanol adsorbed onto dehydrated Ni STA-12 (on glass line) at 298 K (Cu K_α radiation). Colour scheme as Figure 5.15.*

The interpretation of the spectral changes taking place during adsorption of methanol onto Ni STA-12 is outlined in Scheme 5.1. A cyclic species similar to that observed for low loadings of water (Scheme 4.1 in Chapter 4), is produced at low loadings of methanol. Methanol interacts with the Ni^{2+} sites and the P=O groups, producing Ni-OCH_3 and P-OH species. There is evidence for a large amount of methanol in the pores at high loadings. These molecules will interact with the cyclic species, and interpretation of what takes place as methanol molecules hydrogen bond with the chemically bound molecules is presented in reference 33.

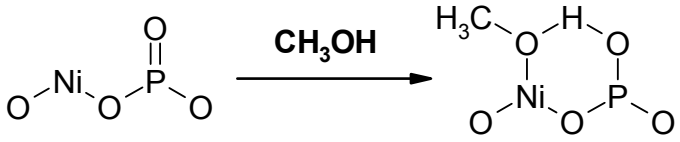

Scheme 5.1 *– Cyclic species formed by initial adsorption of methanol onto dehydrated Ni STA-12. Similar to cyclic water species outlined in Scheme 4.1 in Chapter 4.*

5.4.6.2 Co STA-12

Dosing of dry methanol onto dehydrated Co STA-12, using a glass line, changes the colour from blue to pink. This means the electronic configuration of the solid is changed, as observed for methanol adsorption onto Ni STA-12. X-ray analysis indicates the Co STA-12 structure returns to rhombohedral symmetry, with similar unit cell parameters to the as-prepared structure (Table 5.4). The R factors appear to indicate that the structure where methanol is adsorbed has a better fit than the as-prepared structure. This is most likely an artifice of the diffractometer, with the runs taking place on different days. Due to the reduced crystallinity of Co STA-12 compared to Ni STA-12 it was not possible to locate the positions of the molecules in the structure using Fourier mapping. The final Rietveld plot is shown in Figure 5.22.

Table 5.4 *- Comparison of the atomic parameters of as-prepared Co STA-12 and Co STA-12 with adsorbed methanol.*

Formula	$Co_2(H_2O)_2L.5.4H_2O$	$Co_2L.xCH_3OH$
Space Group	R-3	R-3
a (Å)	28.0243(33)	28.0573(17)
b (Å)	28.0243(33)	28.0573(17)
c (Å)	6.2734(8)	6.2821(4)
α (°)	90	90
β (°)	90	90
γ (°)	120	120
V (Å^3)	4266.8(9)	4282.8(5)
Diffractometer	Lab (STOE)	Lab (STOE)
Temperature (K)	298	298
Wavelength (Å)	1.9361 (Fe K_α)	1.9361 (Fe K_α)
R_{wp}	0.1386	0.0891

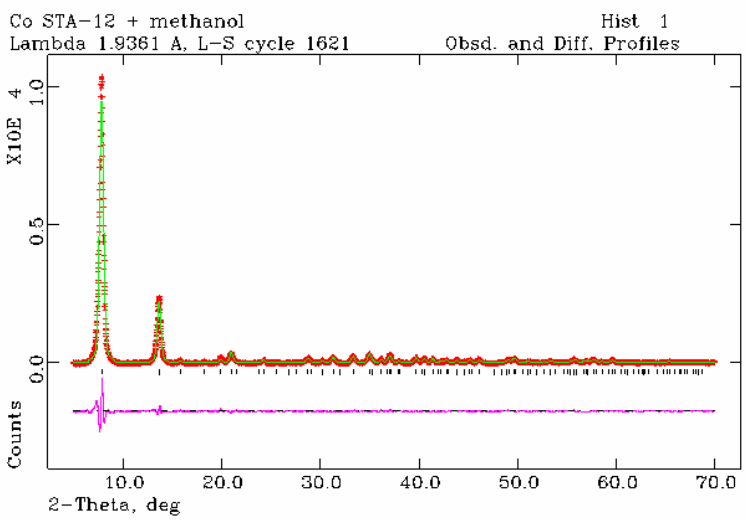

Figure 5.22 *- Rietveld refinement of dry methanol adsorbed onto dehydrated Co STA-12 (on glass line) at 298 K (Fe K_α radiation). Colour scheme as Figure 5.15.*

5.4.7 Methanol and water adsorption – Ni STA-12

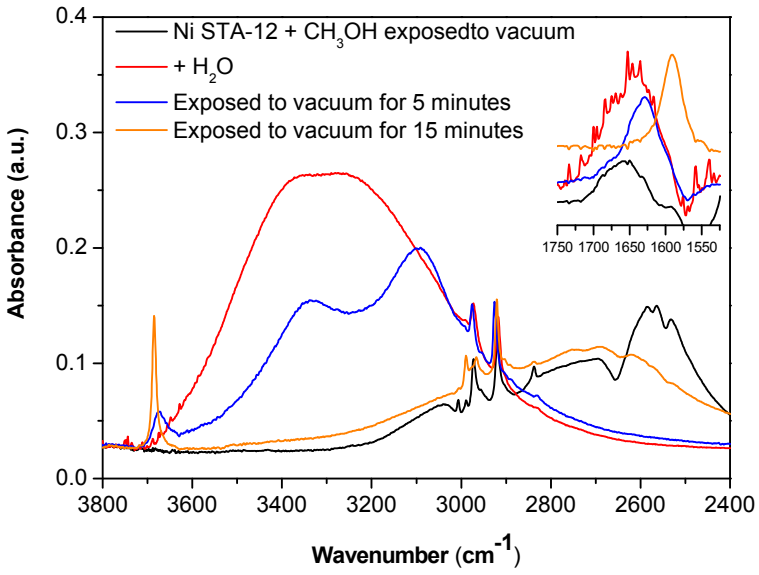

Figure 5.23 *- Infra-red spectra showing effect of interaction of methanol and water at 303 K on Ni STA-12 - high frequency region. Measurements undertaken in collaboration with Prof S. Bordiga at University of Turin.*

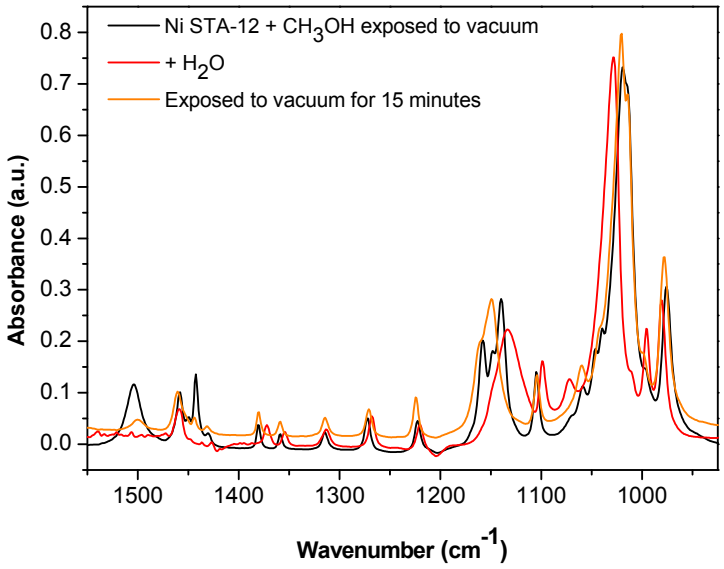

Figure 5.24 *- Infra-red spectra showing effect of interaction of methanol and water at 303 K on Ni STA-12 - low frequency framework region. Measurements undertaken in collaboration with Prof S. Bordiga at University of Turin.*

The effect of exposing Ni STA-12 with adsorbed methanol to a vacuum (< 1×10^{-3} Torr) and subsequent reaction with water has been followed by Infra-red spectroscopy (Figures 5.23 and 5.24).When Ni STA-12 with adsorbed methanol is placed under high vacuum for several hours, only a fraction of the molecules are removed. The main features in the spectrum are a reduction in the intensity of the band at 3480 cm^{-1}, interpreted as due to hydrogen bonded -OH groups in methanol, a slight decrease in the intensity of the band at 2925 cm^{-1} due to $-CH_3$ groups, and an increase in the intensity of the bands at 1650 and 1500 cm^{-1}. All these features are consistent with the presence of bound methoxy groups on the Ni^{2+} and P=O, along with some other hydrogen bonded –OH species.

When water vapour is dosed, several changes take place in the spectrum. There is the formation of a band centred at 3300 cm^{-1} from hydrogen-bonded water (similar to that seen in the Infra-red spectrum of as-prepared Ni STA-12 in Chapter 4), and a reduction in the intensities of the bands at 2750 cm^{-1} and 1500 cm^{-1}.

Subsequent evacuation at room temperature for 5 and 15 minutes results in further changes to the spectra. Two bands at 3350 and 3100 cm^{-1} form due to hydrogen bonded water in the pores, and a band appears at 3685 cm^{-1} associated with free -OH groups (similar to water adsorption onto Ni STA-12, seen in Chapter 4). CO was dosed onto the sample at low temperature to check if the free –OH was acidic. The peak did not change, suggesting the –OH is from Ni-OH. This means the methoxy (Ni-OCH_3) groups formed on direct adsorption of methanol (Scheme 5.1) are being displaced by the adsorbed water molecules. This indicates the Ni^{2+} and P=O sites have reasonable activities, and methanol is relatively weakly bound to the framework compared to water.

5.4.8 Hydrocarbon adsorption

Several hydrocarbons molecules have been investigated for their adsorption properties in MOFs.[2] Kitagawa *et al*. looked at the uptake of acetylene, which is important as a starting material for many chemical products.[34] The main issue for acetylene is its safe storage, as it is a highly flammable gas, and as a result adsorption onto microporous materials has been investigated. A MOF structure was synthesised with pores 4 × 6 Å using pyrazine-2,3-dicarboxylate as the organic linker, and the adsorption isotherms for acetylene reached saturation point with 42 $cm^3g^{-1}{}_{STP}$ adsorbed. This value is much higher than the safe volume density for storage of acetylene in a tank.

Investigation of n-alkane adsorption onto MIL-53 indicated the structure demonstrates good adsorption capacities,[35] and the alkane chain length influences the shape of the resulting isotherms. The ability of Al MIL-53 to both adsorb and separate alkyl aromatic molecules has also been studied.[36] Al MIL-53 has a preference for *ortho*-substituted isomers of C_8, C_9 and C_{10} alkyl aromatics, with molecular packing playing an important role. In MIL-47, conversely, there is a slight preference for *para*-substituted isomers.[37] In mixtures of C_8 alkyl aromatics at low pressure little difference was observed in the selectivity due to a lack of specific interaction sites on the non-polar pore surface of MIL-47.[38] At high pressure, it is possible to differentiate and separate the C_8 alkyl aromatic isomers due to molecular packing differences in the pores.

MIL-101 has been demonstrated to adsorb large aromatic molecules,[39] with a huge uptake for benzene (16.7 mmol g^{-1} at 303 K and p/p_o = 0.5). This is much higher than other porous materials under the same conditions, such as the mesoporous silica SBA-15 (3 mmol g^{-1}), HZSM-5 zeolite (1.9 mmol g^{-1}) and activated carbon (8 mmol g^{-1}). The result is believed to be the highest ever reported for benzene adsorption, and demonstrates the large adsorption capacity possessed by MIL-101.

5.4.8.1 Adsorption of hydrocarbons onto Ni STA-12 and Ni CPO-27

Table 5.5 *– Adsorption results at 298 K for aromatic hydrocarbons and cyclohexene onto dehydrated Ni STA-12 and Ni CPO-27 ($p/p_o \approx 0.1$).*

	Ni STA-12		**Ni CPO-27**	
Cyclohexene	7.8 wt%	0.95 mmol g^{-1}	3.49 wt%	0.42 mmol g^{-1}
Toluene	8.85 wt%	0.96 mmol g^{-1}	4.47 wt%	0.48 mmol g^{-1}
Mesitylene	5.8 wt%	0.48 mmol g^{-1}	2.4 wt%	0.23 mmol g^{-1}
***Ortho*-xylene**	6.2 wt%	0.58 mmol g^{-1}	9.76 wt%	0.92 mmol g^{-1}
***Meta*-xylene**	4.56 wt%	0.43 mmol g^{-1}	6.39 wt%	0.61 mmol g^{-1}
***Para*-xylene**	4.8 wt%	0.45 mmol g^{-1}	13.78 wt%	1.30 mmol g^{-1}

The adsorption performances of Ni STA-12 and Ni CPO-27 for various large cyclic hydrocarbons are presented in Table 5.5. Both Ni STA-12 and Ni CPO-27 adsorb mesitylene, confirming the pores contained in the dehydrated structures are *ca*. 10 Å in diameter. Also, the uptakes for large hydrocarbons are lower than expected. This demonstrates these molecules interact in a different way with the frameworks than small gas molecules, principally due to their large kinetic diameters and slow diffusion rates. There also may be some pore blocking effects taking place.

Some slight differences in the adsorption results for the xylene isomers could give an indication of the shape selectivity of Ni STA-12 and Ni CPO-27. Ni CPO-27 adsorbs slightly more xylenes than Ni STA-12, possibly indicating there are more favourable interactions for these molecules in the undistorted dehydrated structure. Ni CPO-27

shows a slight preference for *para*-xylene, while Ni STA-12 shows a slight preference for *ortho*-xylene. The slight preference for *ortho*-xylene by Ni STA-12 and *para*-xylene by Ni CPO-27 may result from steric factors. The pores are similar sizes, but the frameworks are quite different on dehydration. Different molecular packing could take place within the pores, favouring one xylene isomer over another.

MIL-47 has pores with a similar diameter to both Ni STA-12 and Ni CPO-27, so a comparison can be made between the xylene uptake results.[38, 39] MIL-47 has non-polar pore surfaces that can be thought of as covered in delocalised π electrons. It adsorbs > 25 wt% xylene molecules, with a preference for the *para*- isomer. The adsorption uptake for the xylene isomers is much higher than that measured for Ni STA-12 and Ni CPO-27, which indicates that either fewer steric factors are influencing the adsorptions or the experimental setup is better.

5.5 Conclusions about gas and vapour adsorption

STA-12 has been demonstrated to adsorb many different types of gas molecules, with reasonable performances for small molecules when compared to other MOFs with CUS metal sites. Low temperature adsorption of both H_2 and CO indicates the main adsorption takes place on the metal cations, with P=O as a secondary site.

The adsorption behaviour for H_2 on Ni STA-12 can be explained by the relative accessibility of the Ni^{2+} sites in the distorted dehydrated structure. Out of the three crystallographically distinct cations, Ni (3) is the most accessible and favourable for H_2 adsorption. The higher adsorption enthalpies for CO mean it adsorbs on all of the Ni^{2+} sites in a two stage process, resulting in a relaxing of the structure and the formation of an irreversible, linear Ni-CO adduct at 77 K. The performance for the adsorption of H_2 and CO onto Co STA-12 indicates the adsorption enthalpies are smaller, and the capacity is lower, even though there should be as many adsorption sites present as in Ni STA-12. This indicates the lower crystallinity of Co STA-12 compared to Ni STA-12 affects the adsorption performance.

CO_2 measurements at low temperature confirm Fe and Mn STA-12 do not adsorb gas, while the total uptakes for Ni and Co STA-12 are similar to those measured for N_2

adsorption. High pressure adsorption of CO_2 at room temperature demonstrates total uptakes comparable to the low temperature adsorption amounts and similar adsorption enthalpies for Ni and Co STA-12. Low pressure adsorption at room temperature indicates the metal cation sites and P=O groups are the adsorption sites, similar to that seen for H_2 and CO at low temperature. Comparison of the uptake of CO_2 and CH_4 on Ni STA-12 shows 10 × more CO_2 than CH_4 is adsorbed, which could be possibly exploited in pressure swing applications.

Adsorption of acetonitrile onto Ni and Co STA-12 demonstrates the interactions are large enough for the molecules to strongly bind to the metal cation sites, changing the symmetry from triclinic to rhombohedral with slight reductions in the cell parameters compared to the as-prepared structures. The metal cation sites are acting as medium Lewis acids, and the P=O groups are inferred to also be involved in the adsorption. The linear acetonitrile molecules have been shown to bind through N to the Ni^{2+} cations in Ni STA-12. The adsorbed molecules point into the pore space, reducing it to about 5 Å in diameter and forcing the structure to adopt rhombohedral symmetry.

The interaction of methanol with Ni STA-12 enables the reactivity of the Ni^{2+} cations and the P=O groups to be observed. The adsorption of methanol forms Ni-OCH_3 and P-OH groups in a cyclic species similar to that seen for adsorption of water. This results in the Ni STA-12 structure adopting rhombohedral symmetry similar to that observed in the as-prepared structure. Adsorption of water onto Ni STA-12 with adsorbed methanol results in displacement of the methoxy groups, and the formation of free Ni-OH.

The adsorption of large hydrocarbon molecules has also been measured for Ni STA-12, confirming the pores of the dehydrated structure are *ca*. 10 Å in diameter. The shape selectivity in the adsorption of xylene isomers was investigated as well, indicating Ni STA-12 has a slight preference for the *ortho*-isomer, which could be explained with reference to steric interactions in the pores. This means Ni STA-12 could have potential for molecular shape selectivity and separation.

5.6 References

1) P. L. Llewellyn and G. Maurin, *C. R. Chemie*, 2005, **8**, 283

2) R. E. Morris and P. S. Wheatley, *Angew. Chem. Int. Ed.*, 2008, **47**, 4966

3) G. Spoto, E. N. Gribov, G. Ricchiardi, A. Damin, D. Scarno, S. Bordiga, C. Lamberti and A. Zecchina, *Prog. Surf. Sci.*, 2004, **76**, 71

4) A. C. Larson and R. B. von Dreele, *Generalised crystal structure analysis system*, Los Alamos National Laboratory, USA, 1998

5) J. A. Groves, S. R. Miller, S. J. Warrender, C. Mellot-Draznieks, P. Lightfoot and P. A. Wright, *Chem. Commun.*, 2006, 3305

6) M. Latroche, S. Surblé, C. Serre, C. Mellot-Draznieks, P. L. Llewellyn, J-H. Lee, J-S. Chang, S. H. Jung and G. Férey, *Angew. Chem. Int. Ed.*, 2006, **45**, 8227

7) J. G. Vitillo, L. Regli, S. Chavan, G. Ricchiardi, G. Spoto, P. D. C. Dietzel, S. Bordiga and A. Zecchina, *J. Am. Chem. Soc.*, 2008, **130**, 8386

8) B. Schmitz, U. Müller, N. Trukhan, M. Schubert, G. Férey and M. Hirscher, *ChemPhysChem*, 2008, **9**, 2181

9) P. M. Forster, J. Eckert, B. D. Heiken, J. B. Parise, J. W. Yoon, S. H. Jhung, J-S. Chang and A. K. Cheetham, *J. Am. Chem. Soc.*, 2006, **128**, 16846

10) G. Spoto, S. Bordiga, A. Zecchina, D. Cocina, E. N. Gribov, L. Regli, E. Groppo and C. Lamberti, *Catalysis Today*, 2006, **113**, 65

11) S. Bordiga, L. Regli, F. Bonino, E. Groppo, C. Lamberti, B. Xiao, P. S. Wheatley, R. E. Morris and A. Zecchina, *Phys. Chem. Chem. Phys.*, 2007, **9**, 2676

12) S. Bordiga, J. G. Vitillo, G. Ricchiardi, L. Regli, D. Cocina, A. Zecchina, B. Arsta, M. Bjørgen, J. Hafizovic and K. P. Lillerud, *J. Phys. Chem. B*, 2005, **109**, 18237

13) A. Vimont, H. Leclerc, F. Maugé, M. Daturi, J-C. Lavalley, S. Surblé, C. Serre and G. Férey, *J. Phys. Chem. C*, 2007, **111**, 383

14) S. Chavan, J. G. Vitillo, E. Groppo, F. Bonino, C. Lamberti, P. D. C. Dietzel and S. Bordiga, *J. Phys. Chem. C.*, 2009, **133**, 3292

15) A. Zecchina, C. O. Areán, G. T. Palomino, F. Geobaldo, C. Lamberti, G. Spoto and S. Bordiga, *Phys. Chem. Chem. Phys.*, 1999, **1**, 1649

16) A. R. Millward and O. M. Yaghi, *J. Am. Chem. Soc.*, 2005, **127**, 17998

17) P. L. Llewellyn, S. Bourrelly, C. Serre, A. Vimont, M. Daturi, L. Hamon, G. De Weireld, J-S. Chang, D-Y. Hong, Y. K. Hwang, S. H. Jhung and G. Férey, *Langmuir*, 2008, **24**, 7245

18) S. Bourrelly, P. L. Llewellyn, C. Serre, F. Millange, T. Loiseau and G. Férey, *J. Am. Chem. Soc.*, 2005, **127**, 13519

19) P. L. Llewellyn, S. Bourrelly, C. Serre, Y. Filinchuk and G. Férey, *Angew. Chem. Int. Ed.*, 2006, **45**, 7752

20) C. Serre, S. Bourrelly, A. Vimont, N. A. Ramsahye, G. Maurin, P. L. Llewellyn, M. Daturi, Y. Filinchuk, O. Leynaud, P. Barnes and G. Férey, *Adv. Mater.*, 2007, **19**, 2246

21) P. L. Llewellyn, G. Maurin, T. Devic, S. Loera-Serna, N. Rosenbach, C. Serre, S. Bourrelly, P. Horcajada, Y. Filinchuk and G. Férey, *J. Am. Chem. Soc.*, 2008, **130**, 12808

22) N. Rosenbach, H. Jobic, A. Ghoufi, F. Salles, G. Maurin, S. Bourrelly, P. L. Llewellyn, T. Devic, C. Serre and G. Férey, *Angew. Chem. Int. Ed.*, 2008, **47**, 6611

23) R. Babarao and J. Jiang, *Langmuir*, 2008, **24**, 5474

24) F. Millange, N. Guillou, R. I. Walton, J-M. Grenéche, I. Margiolaki and G. Férey, *Chem. Commun.*, 2008, 4732

25) G. Férey, *Chem. Soc. Rev.*, 2008, **37**, 191

26) G. Maurin, P. L. Llewellyn and R. G. Bell, *J. Phys. Chem. B*, 2005, **109**, 16084

27) P. D. C. Dietzel, R. E. Johnsen, H. Fjellvåg, S. Bordiga, E. Groppo, S. Chavan and R. Blom, *Chem. Commun.*, 2008, 5125

28) B. Bonelli, B. Civalleri, B. Fubini, P. Ugliengo, C. Otero-Arean and E. Garrone, *J. Phys. Chem. B*, 2000, **104**, 10978

29) C. Prestipino, L. Regli, J. G. Vitillo, F. Bonino, A. Damin, C. Lamberti, A. Zecchina, P. L. Solari, K. O. Kongshaug and S. Bordiga, *Chem. Mater.*, 2006, **18**, 1337

30) F. Bonino, A. Damin, S. Bordiga, C. Lamberti and A. Zecchina, *Langmuir*, 2003, **19**, 2155

31) C. Pazé, A. Zecchina, S. Spera, G. Spano and F. Rivetti, *Phys. Chem. Chem. Phys.*, 2000, **2**, 5756

32) K. C. Szeto, K. P. Lillerud, M. Tilset, M. Bjørgen, C. Prestipino, A. Zecchina, C. Lamberti and S. Bordiga, *J. Phys. Chem. B*, 2006, **110**, 21509

33) S. R. Miller, G. M. Pearce, P. A. Wright, F. Bonino, S. Chavan, S. Bordiga, I. Margiolaki, N. Guillou, G. Férey, S. Bourelly and P. L. Llewellyn, *J. Am. Chem. Soc.*, 2008, **130**, 15967

34) R. Matsuda, R. Kitaura, S. Kitagawa, Y. Kubota, R. V. Belosludov, T. C. Kobayashi, T. Chiba, M. Takata, Y. Kawazoe and Y. Mita, *Nature*, 2005, **436**, 238

35) T. K. Trung, P. Trens, N. Tranchoux, S. Bourelly, P. L. Llewellyn, S. Loera-Serna, C. Serre, T. Loiseau, F. Fajula and G. Férey, *J. Am. Chem. Soc.*, 2008, **130**, 16926

36) L. Alaerts, M. Maes, L. Giebeler, P. A. Jacobs, J. A. Martens, J. F. M. Denayer, C. E. A. Kirschhock and D. E. De Vos, *J. Am. Chem. Soc.*, 2008, **130**, 14170

37) L. Alaerts, C. E. A. Kirschhock, M. Maes, M. A. van der Veen, V. Finsy, A. Depla, J. A. Martens, G. V. Baron, P. A. Jacobs, J. F. M. Denayer and D. E. De Vos, *Angew. Chem. Int. Ed.*, 2007, **46**, 4293

38) V. Finsey, H. Verelst, L. Alaerts, D. E. De Vos, P. A. Jacobs, G. V. Baron and J. F. M. Denayer, *J. Am. Chem. Soc.*, 2008, **130**, 7110

39) S. H. Jhung, J-H. Lee, J. W. Yoon, C. Serre, G. Férey and J-S. Chang, *Adv. Mater.*, 2007, **19**, 121

Chapter 6: Catalysis Over Large Pore MOFs

6.1 Introduction

In this work, the STA-12, CPO-27 and MIL-*n* samples will be tested for catalytic activity in test reactions. Acidity will be measured using selective oxidations, while basicity will be measured using Knoevenagel condensations, with the results interpreted in terms of substrate conversions and selectivities to the various products.

6.2 Selective oxidation reactions

6.2.1 Background

Selective oxidation reactions (examples in Scheme 6.1) producing epoxides, aldehydes, ketones and alcohols from alkene substrates are well known in homogeneous catalysis.[1, 2] The reactions involve the use of liquid phase hydroperoxides as oxidants, and metals such as Ti, Mo and V in the catalysts.

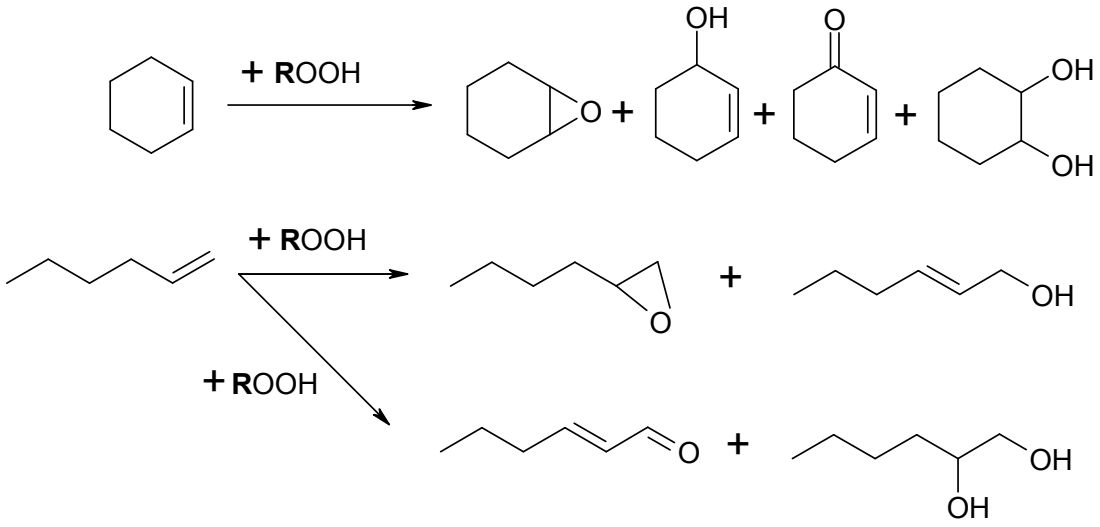

Scheme 6.1 *– Selective oxidation reactions of cyclohexene and 1-hexene. R = H or an organic functionality.*

As outlined previously, there have been several studies into the activity of microporous hybrid solids as oxidation catalysts. There have also been a substantial number of studies undertaken with zeotypes, especially titanium silicates.[3–6] These materials, including the well characterised structures TS-1 and Ti-β, have easily accessible metal sites and are also highly hydrophobic, so they are not deactivated by water. The main studies have looked at activity using short chain olefins as the substrates and either hydrogen peroxide (H_2O_2) or *tert*-butyl hydroperoxide as the oxidants (Table 6.1).

Table 6.1 *– Reaction data for oxidations carried out using Ti silicates as the catalysts.[6] Conditions - 323 K for 6 hours using H_2O_2 as the oxidant and methanol as the solvent.*

	Ti-ß Catalyst			**TS-1 Catalyst**		
Olefin	**Conversion (mol %)**	**Epoxide Select. (mol %)**	**TOF (h^{-1})**	**Conversion (mol %)**	**Epoxide Select. (mol %)**	**TOF (h^{-1})**
1-Hexene	11.9	3.9	6.14	14.3	94.7	13.5
2-Hexene	12.8	4.4	6.45	25.0	99.9	30.45
3-Hexene	11.0	10.0	5.13	-	-	-
1-Octene	9.0	6.1	4.32	11.1	80.3	10.43
1-Decene	7.1	5.9	3.66	7.9	79.5	8.58
4-Methyl-1-pentene	14.2	14.0	8.96	-	-	-
2-Methyl-2-pentene	17.2	0.6	10.01	3.9	76.7	3.94
Cyclohexene	17.7	0.0	10.01	-	-	-
1-Methyl-1-cyclohexene	12.8	0.9	7.46	-	-	-

Table 6.1 outlines some published data using TS-1 and Ti-β as oxidation catalysts.[6] TS-1 is observed to be the more active catalyst for short chain olefins, with higher mol % conversions than Ti-β. Conversely, with larger and bulkier olefins Ti-β is the more active catalyst. The pores of Ti-β are larger in size than TS-1, borne out by the

results obtained using cyclohexene and the related methyl derivative. The selectivity to epoxide products is very high in TS-1, meaning epoxide ring opening is not favoured, and the acidity is less than Ti-β.

Considering the olefins, those with the double bond in the α-position are slightly less reactive than those with the double bond in other positions, e.g. 1-hexene is less active than 2-hexene. Comparing straight chain olefins, the reactivity decreases as the carbon chain is lengthened. Also, bulkier olefin molecules exhibit almost no selectivity to epoxide products, possibly due to greater interaction with acid sites in Ti-β from slower diffusion. This results in further oxidation products being produced.

Studies have also been undertaken into Cr- and V-containing zeotypes. A comparison between CrAPO-5 and Ti-β by Chen *et al.* indicated CrAPO-5 was not selective to epoxide products.[4] When cyclohexene was used as the substrate there was a selectivity of over 80% for cyclohexanone, which is an important intermediate in the manufacture of nylon 6 and nylon 6,6. The activity of CrAPO-5 was found to be similar to Ti-β, indicating the Cr sites are similar to the Ti sites in Ti-β.

In the oxidation of 3-phenyl-2-propene-1-ol by *tert*-butyl hydroperoxide the activity of VAPO-5 was low, but the selectivity to the epoxide product was very high.[7] Re-using VAPO-5 as a catalyst several times in succession resulted in selectivity to the epoxide product reducing, along with the activity. Vanadium was discovered to be leaching into the reaction mixture, and comparison with a test reaction where an equivalent amount of vanadium acetate was used as the catalyst indicated most of the activity could be attributed to the leached vanadium.

Some other zeotypes with transition metals in the structures have been studied where O_2 in air is used as the oxidant for reasons of economy and to help promote framework stability. The autooxidation of cyclohexane to form cyclohexanone can proceed via a free radical chain reaction, where the first step is reaction of dioxygen to give a hydroperoxide. A series of Co and Mn substituted zeotypes (Co AlPO-5, -11, -18 and -36, and Mn AlPO-18 and -36) were tested using short chain alkane substrates.[8] The conversions of the reactants to ketone and aldehyde products were low (*ca.* 7 %) meaning polar products, such as carboxylic acids, which might leach metals from the framework were not formed. It was observed that the Mn-containing structures gave higher conversions than the Co-containing structures, and that the smaller pore AlPO-18 frameworks only allowed oxidation on C_1 and C_2 of the substrates.

The nature of the redox active metal sites were established via a combination of X-ray diffraction, EXAFS, UV-vis and IR spectroscopies.[9] It was discovered the Co and Mn cations had reversible redox behaviour between +2 and +3 oxidation states. The redox processes were also demonstrated to be reversible, using alternate oxidations in O_2 and reductions in H_2. The addition of free radical initiators and scavengers to the reactions allowed for the mechanisms to be elucidated. When the free radical initiators were added, the induction times for the reaction were reduced, and when the free radical scavengers were added the reactions did not take place. Therefore, oxidations in air over the Co and Mn zeotypes took place via free radicals, with a cyclic intermediate species involving a hydroperoxide forming at the active site.

6.2.2 Reactive intermediates in liquid phase selective oxidation reactions

When homogeneous catalysts oxidise C=C bonds, the peroxide oxidant complexes to the metal,[10] the O-O bond is weakened, and electron transfer forms the energetic alkoxy radical $RO^{\cdot}$. A short lived reactive transition state forms, the reactivity of which is dependent on the hydroperoxide and solvent used in the reaction.[11]

Any transition state must involve the solvent and also be reactive enough to allow for oxidative attack on the C=C bond. Several possible transition state structures have been proposed for Ti-silicates,[12–14] with these outlined in Figure 6.1. Liquid NMR studies of the reactivity of peroxotitanium complexes formed in the reaction of H_2O_2 and $Ti(OEt)_4$ suggested the most probable reactive intermediate species formed was the cyclic hydroperoxy.[15] It allows for fast abstraction of oxygen by the substrate and is not too bulky. It also allows the effects associated with using different solvents in the reactions to be explained (possible mechanism outlined in Scheme 6.2).

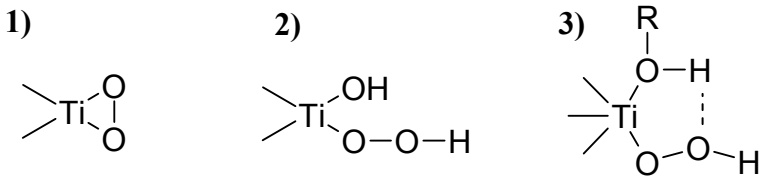

Figure 6.1 *– Possible peroxy intermediates formed in Ti-silicates – 1) tetrahedral metallodioxirane; 2) hydroperoxy; 3) cyclic hydroperoxy.*

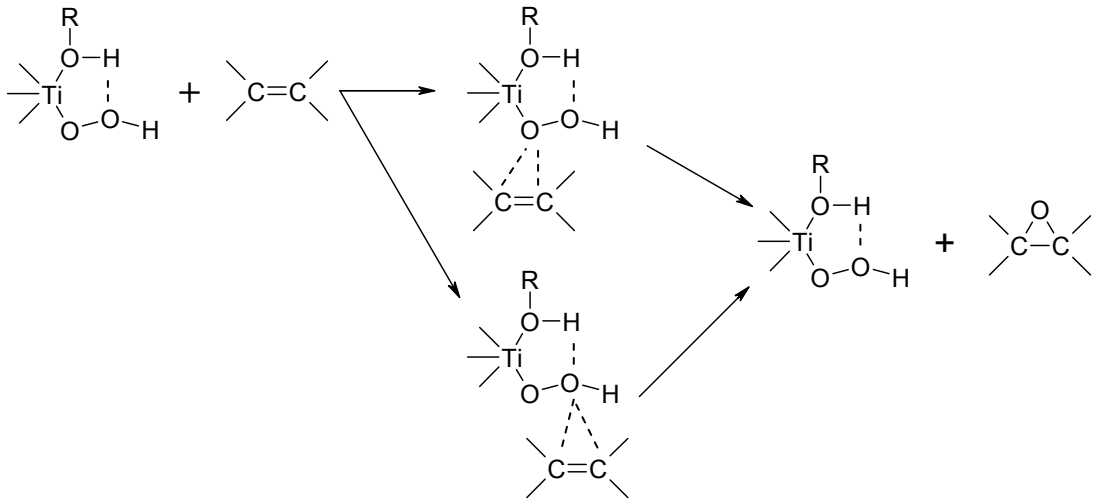

Scheme 6.2 *– Possible mechanism for formation of epoxide products when using Ti-silicates as catalysts with an alcohol solvent.*[14]

6.2.3 Selective Oxidation Reactions - Experimental and Characterisation Techniques

The selective oxidation reactions in this study were carried out using the same conditions as Corma *et al*.[6]

Oxidations using H_2O_2 – 1-hexene or cyclohexene (3.1 ml, 25 mmol), methanol (25 ml) and H_2O_2 (0.72 ml, 6.25 mmol, 30 wt% in H_2O) were mixed together. 0.2 g (0.5 mmol with 15 mol % active sites) of catalyst activated at 423 K was added (t = 0) and the reaction stirred for 6 hours at 323 K. The solid and liquid were separated using filtration, with the liquid analysed by GC and the solid by X-ray powder diffraction.

Oxidations using *tert*-butyl hydroperoxide – 1-hexene or cyclohexene (3.1 ml, 25 mmol), acetonitrile (8 ml) and *tert*-butyl hydroperoxide (0.62 ml, 6.25 mmol, 80% solution in di-*tert*-butylperoxide) were mixed together. 0.2 g (0.5 mmol with 15 mol % active sites) of catalyst activated at 423 K was added (t = 0) and the reaction stirred for 6 hours at 323 K. The solid and liquid were separated using filtration, with the liquid analysed by GC and the solid by X-ray powder diffraction.

Gas chromatography (GC) measurements were performed on the mixtures of liquid organics produced from the catalysis experiments. 1 μl of sample was injected onto an

HP-5 crosslinked 5% phenyl dimethylpolysiloxane capillary column fitted to a CE Instruments GC 8000 Top machine with a Flame Ionisation Detector (FID). Column temperature was kept constant at 403 K, with helium used as the carrier gas (flow rate - 25 ml min^{-1}). Data was plotted and analysed using a Fisons Instruments DP700 integrator. Each component of the organic mixtures was identified by comparison with known compounds, and toluene was used as an internal standard. Examples of the peak positions in the GC traces and the associated calculation of substrate conversions are presented in Appendix 8.

6.2.4 Reactions using STA-12 as catalysts

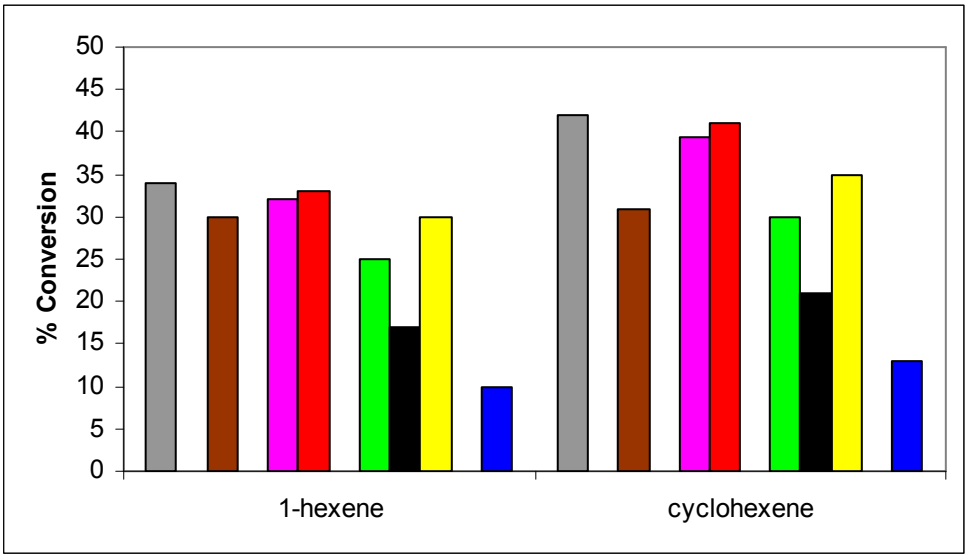

Figure 6.2 *– Results obtained for conversion of 1-hexene and cyclohexene over 6 hours of reaction using t-butyl hydroperoxide as the oxidant and STA-12 and CPO-27 as catalysts. Mn STA-12 - grey; Fe STA-12 - brown; Co STA-12 - pink; Co CPO-27 - red; Ni STA-12 - green; Ni STA-12 as-prepared - black; Ni CPO-27 - yellow; No catalyst present - blue.*

In the results (Figure 6.2), % conversion relates to the mol % of the original substrate that has been converted. The first noticeable feature of the results is that cyclohexene is slightly more reactive than 1-hexene, with greater conversion over the course of the reaction. This is due to cyclohexene not having the double bond present in the α-position, so it is more labile and reactive. The second noticeable feature is all of the

dehydrated MOF structures help to catalyse the oxidation reactions, with conversions increased 3 - 4 × compared to when no MOF is present.

Comparing the dehydrated STA-12 samples with each other, the reactivity increases Ni < Fe < Co < Mn. Fe, Co and Mn are good oxidation catalysts in homogeneous reactions, and this is translated into these heterogeneous reactions. This means even though the dehydrated versions of Co, Fe and Mn STA-12 are not as crystalline as dehydrated Ni STA-12, the activities are higher due to the metals present. Comparing Ni and Co STA-12 to Ni and Co CPO-27, the greater accessibility to the cation sites in dehydrated CPO-27 results in slightly higher activities.

The brown-yellow and blue colours of, respectively, dehydrated Ni and Co STA-12 disappear over the course of the reactions and are replaced by colours similar to those of the as-prepared structures. This indicates the metal sites are adsorbing and coordinating molecules from the reaction mixture. As-prepared Ni STA-12, where all the metal sites are coordinated by water, was tested for activity. The substrate conversion for as-prepared Ni STA-12 is higher than when no catalyst is present, but is not as high as when dehydrated Ni STA-12 is used as the catalyst.

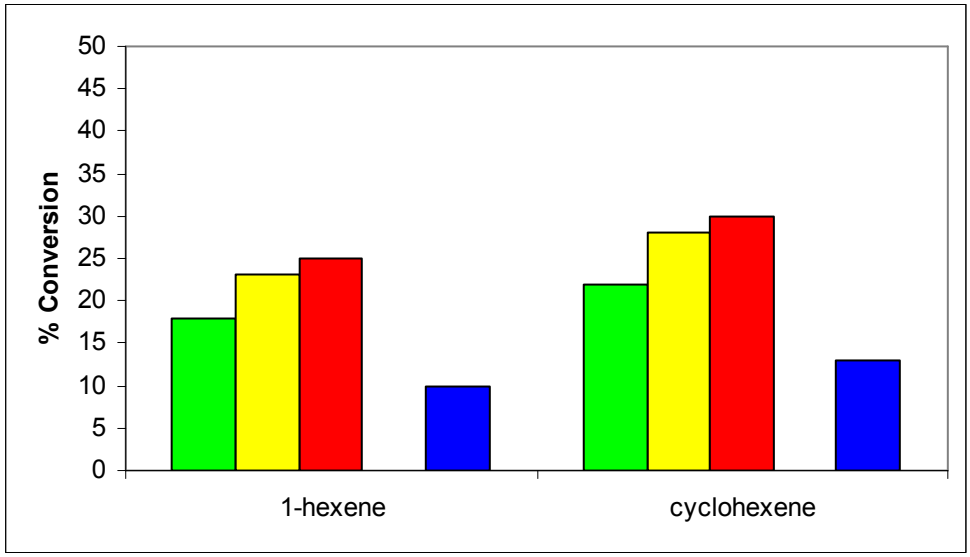

Figure 6.3 *– Results obtained for conversion of 1-hexene and cyclohexene over time using Ni STA-12 as the catalyst and t-butyl hydroperoxide as the oxidant. 2 hours contact - green; 4 hours contact - yellow; 6 hours contact - red; No catalyst present - blue.*

To understand the behaviour of Ni STA-12, the reaction has been run as a function of time (Figure 6.3). After 2 hours reaction time the substrate conversion is almost two-thirds of the total after 6 hours. After 4 hours, the substrate conversion is virtually the same as the total conversion after 6 hours. This indicates that as the reaction proceeds the active sites are adsorbing and coordinating molecules from the reaction mixture, reducing the activity of the catalyst over time. This means surface catalysis is dominating during the course of the reactions.

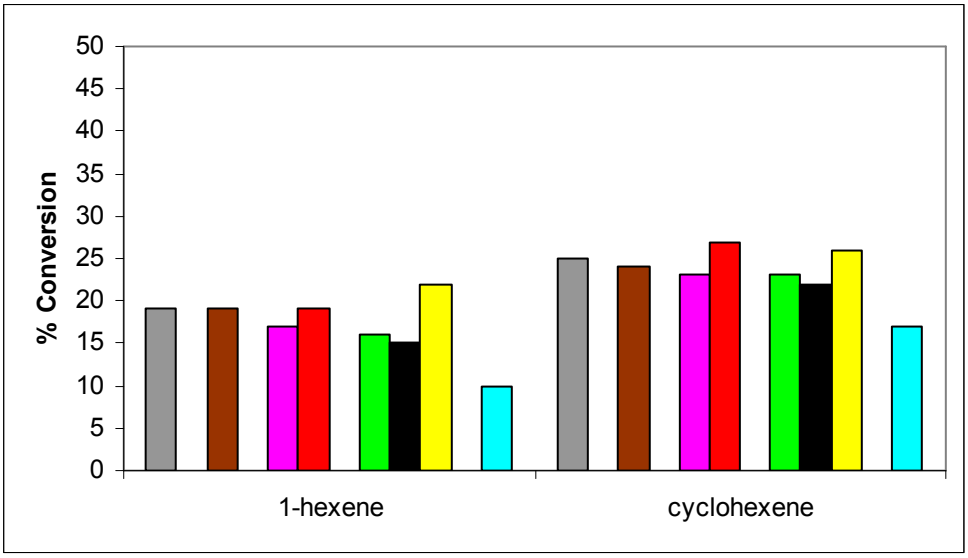

Figure 6.4 *- Results obtained for conversion of 1-hexene and cyclohexene over 6 hours of reaction using H_2O_2 as the oxidant and STA-12 and CPO-27 as catalysts. Mn STA-12 - grey; Fe STA-12 - brown; Co STA-12 - pink; Co CPO-27 - red; Ni STA-12 - green; Ni STA-12 as-prepared - black; Ni CPO-27 - yellow; No catalyst present - light blue.*

The conversions of the substrates were lower when H_2O_2 was used as the oxidant (Figure 6.4), although the MOFs still catalyse the reactions. The relationships between STA-12 and CPO-27 are similar to those observed when *tert*-butyl hydroperoxide is used as the oxidant, and there is no evidence of leaching or dissolution during the reactions. This means STA-12 and CPO-27 are stable in the presence of water.

The colours of dehydrated Ni and Co STA-12 change to similar colours to the as-prepared samples almost immediately on contact with the reaction mixture. There is water and methanol present, and these will probably coordinate to the metal sites.

Comparisons of dehydrated and as-prepared Ni STA-12 as catalysts indicate substrate conversions are very similar. The conversions do not change much over the course of the reaction, suggesting most of the active sites are coordinated by molecules from the beginning of the reaction and surface catalysis dominates.

In the oxidation of 1-hexene and cyclohexene, the epoxide, aldehyde/ketone and diol products were found to make up at least 70% of the total products. A comparison can be made between these three products to give an idea of the relative acidity of the catalysts, as outlined in Figures 6.5 and 6.6.

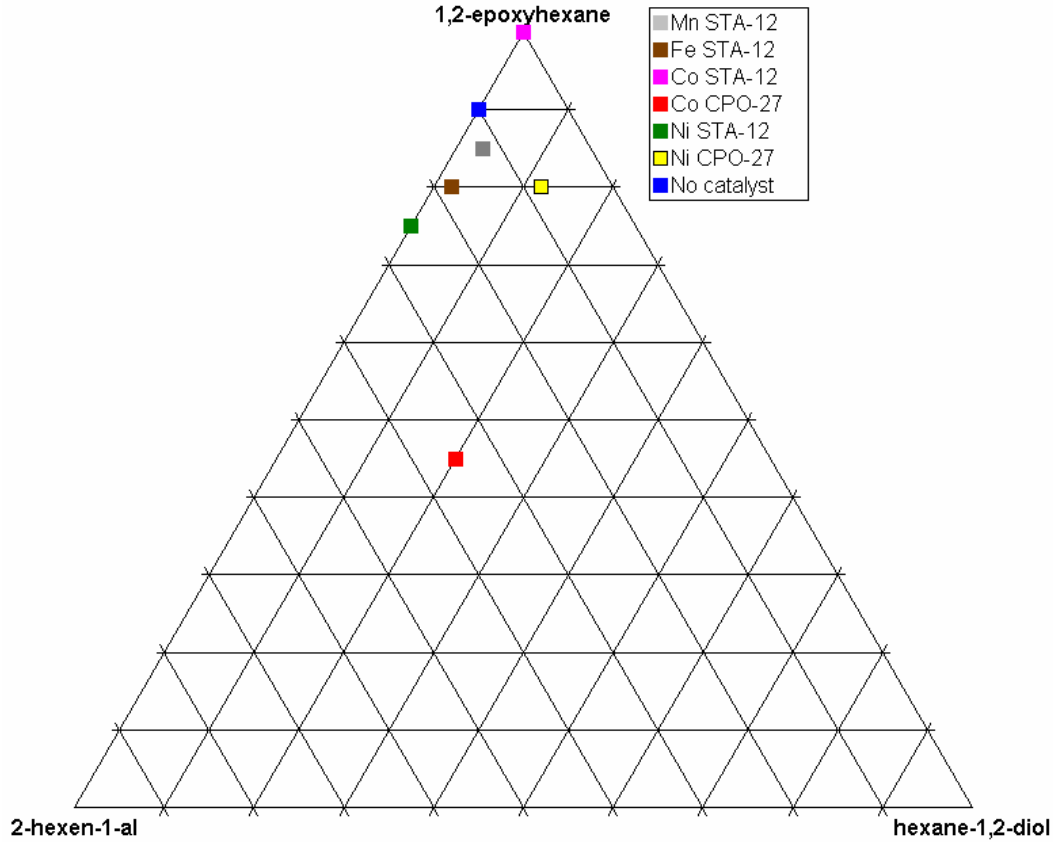

Figure 6.5 *- Triangular plot comparing epoxide, aldehyde and diol products in oxidation of 1-hexene with H_2O_2. Apices represent 100% of each product.*

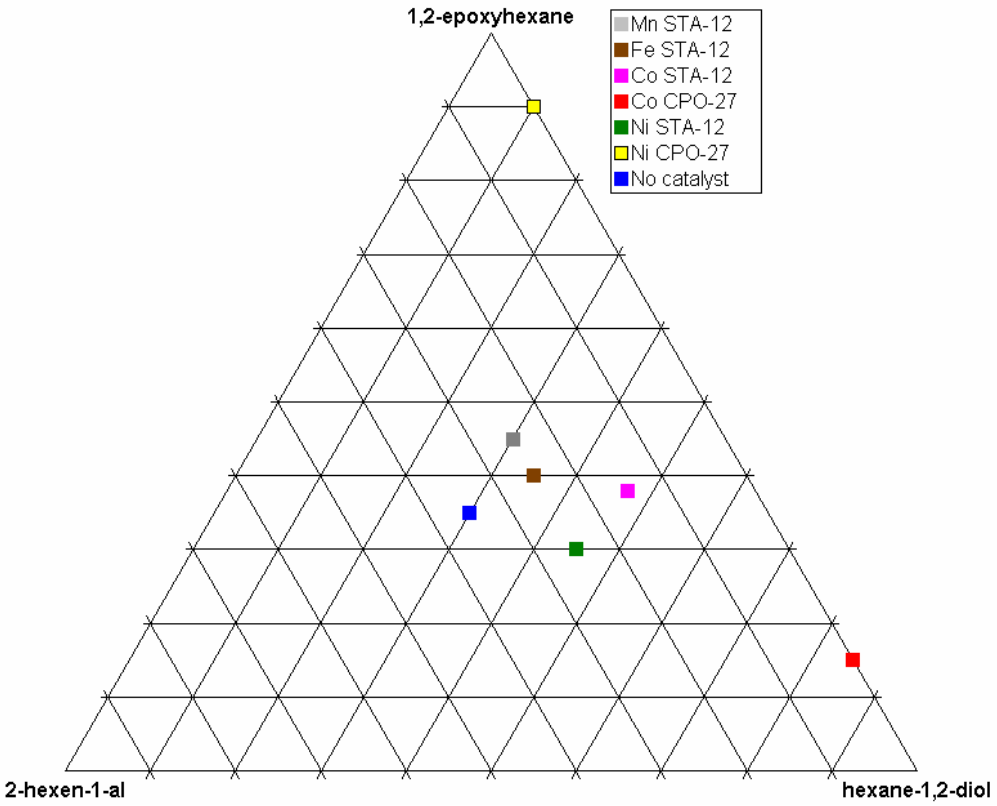

Figure 6.6 *– Triangular plot comparing epoxide, aldehyde and diol products in oxidation of 1-hexene with t-butyl hydroperoxide. Apices represent 100% of each product.*

When 1-hexene is used as the substrate, the STA-12 samples plot in one area of the triangular plots. The area is not far from the position for the products when no catalyst is present. Using H_2O_2 as the oxidant the points are near the epoxide apex (Figure 6.5), while when using t-butyl hydroperoxide as the oxidant the points are to the hexane-1,2-diol side of the middle (Figure 6.6). This suggests t-butyl hydroperoxide is more acidic than H_2O_2, as it favours breaking of the epoxide ring and further oxidation. The oxidation reaction mechanisms are different for Co and Ni CPO-27, as they do not plot with the STA-12 samples when using either of the oxidants. This is probably a feature of the differences in the structures, as CPO-27 is a carboxylate framework and STA-12 is a phosphonate framework.

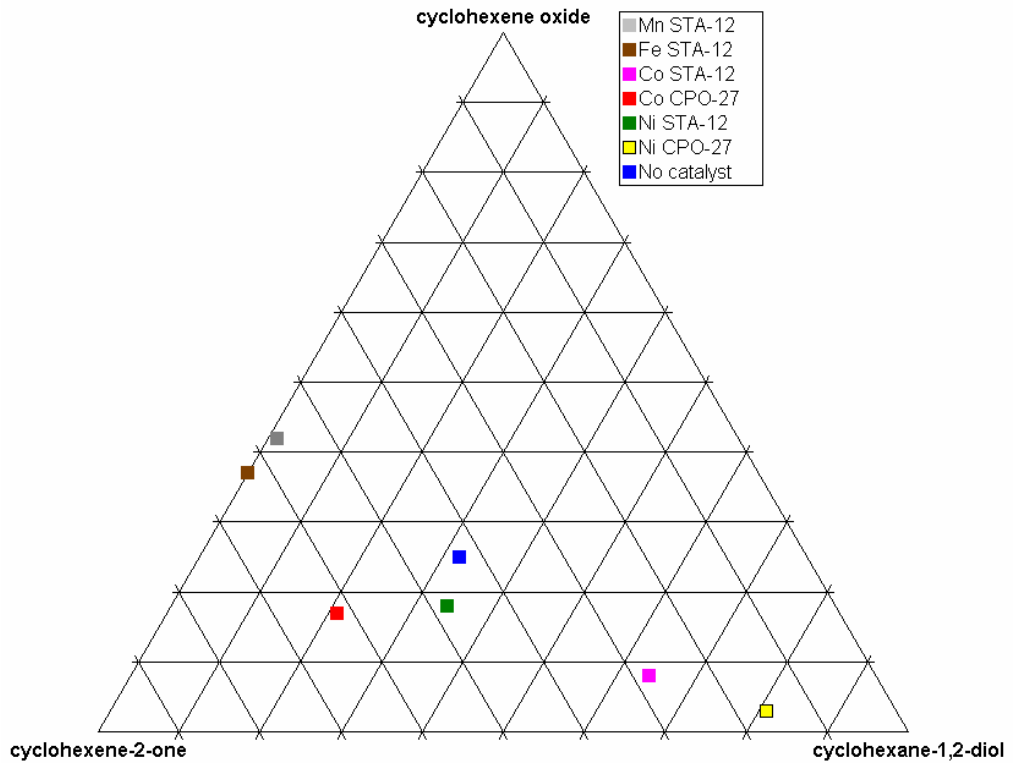

Figure 6.7 *– Triangular plot comparing epoxide, aldehyde and diol products in oxidation of cyclohexene with H_2O_2. Apices represent 100% of each product.*

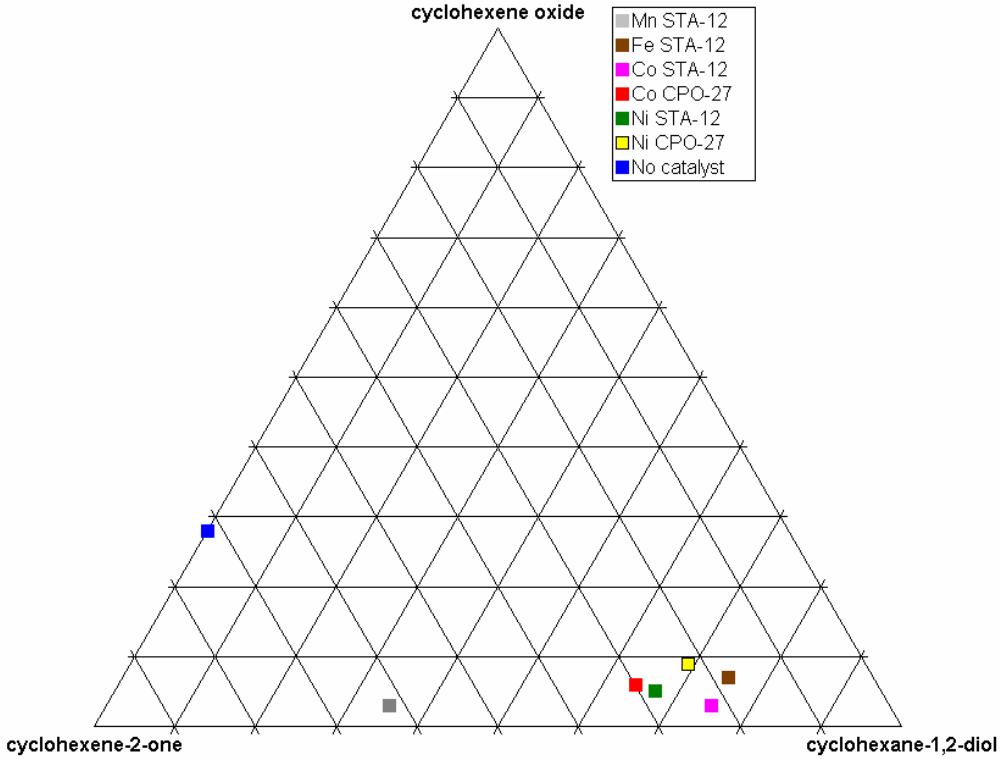

Figure 6.8 *– Triangular plot comparing epoxide, aldehyde and diol products in oxidation of cyclohexene with t-butyl hydroperoxide. Apices represent 100% of each product.*

Comparing the reactions of cyclohexene with and without catalysts (Figures 6.7 and 6.8), STA-12 shifts the product distributions towards the 100% diol apex when t-butyl hydroperoxide is used as the oxidant, creating a plot of points that indicate the presence of significant acidity (Figure 6.8). The product distribution is more spread out when H_2O_2 is used as the oxidant, and the points plot further from the diol apex (Figure 6.7). This indicates the acidity is less when using H_2O_2, similar to the observation for 1-hexene. The Co and Ni CPO-27 frameworks plot in similar parts of the triangular diagrams to the STA-12 structures, indicating the reaction mechanisms when cyclohexene is used as the substrate are similar, unlike what is observed with 1-hexene.

6.2.5 Reactions using mixed metal STA-12 as catalysts – using t-butyl hydroperoxide as oxidant

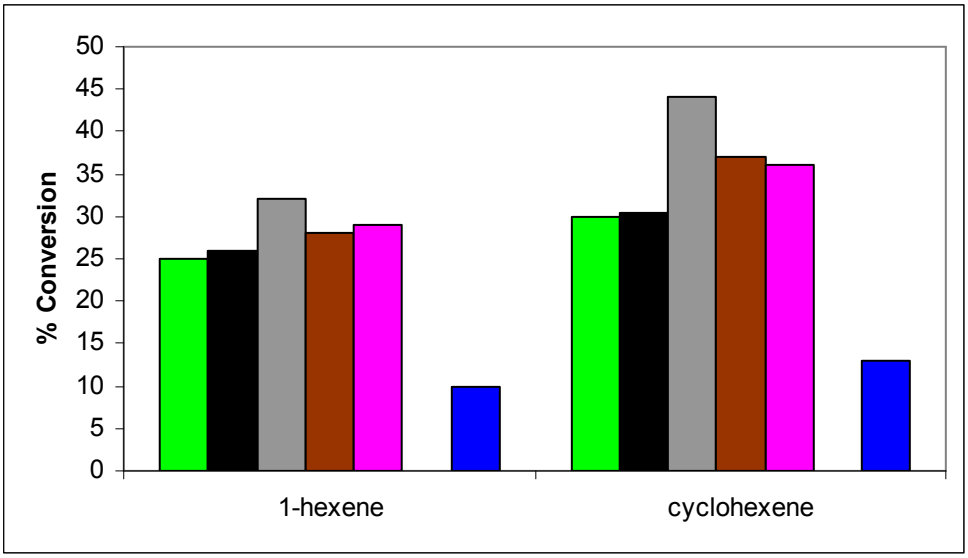

Figure 6.9 *– Results obtained for conversion of 1-hexene and cyclohexene over 6 hours of reaction using t-butyl hydroperoxide as the oxidant and mixed metal STA-12 as catalysts. Ni STA-12 - green; Ni STA-12 + 20% Mg - black; Ni STA-12 + 20% Mn - grey; Ni STA-12 + 20% Fe - brown; Ni STA-12 + 20% Co - pink; No catalyst present - blue.*

The results obtained indicate replacing 20% of the Ni with another divalent metal slightly increases the activity compared to pure Ni STA-12 (Figure 6.9). The

conversions increase in the order Mg < Co < Fe < Mn, which is similar to the results seen for pure Co, Fe and Mn STA-12. The differences in the conversions are not very large between the STA-12 structures, and this indicates surface catalysis is more important in these reactions due to coordination of the active sites by solvent and product molecules during the course of the reaction. Any differences that might have taken place due to the presence of more than one metal in the catalyst are as a result not observed or reduced. Comparing the three main reaction products to one another allows for an indication of whether having two metals present changes the distribution of the products (Figure 6.10 and 6.11).

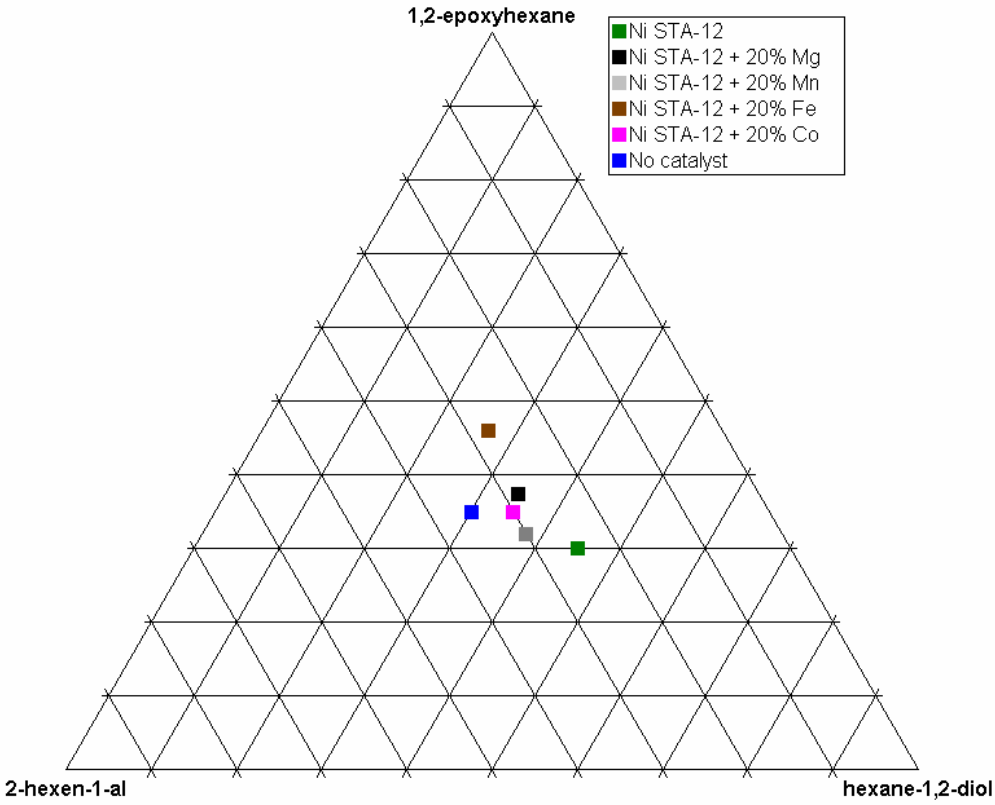

Figure 6.10 *– Triangular plot comparing epoxide, aldehyde and diol products in oxidation of 1-hexene using t-butyl hydroperoxide. Apices represent 100% of each product.*

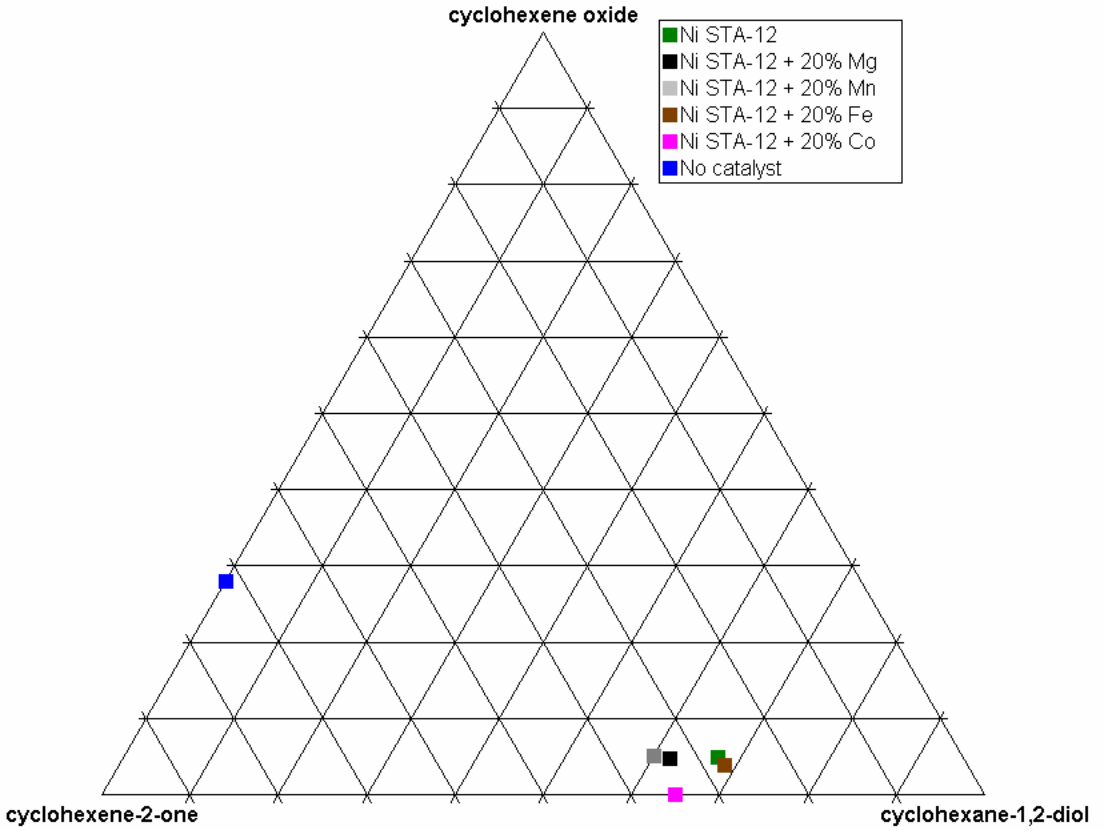

Figure 6.11 *- Triangular plot comparing epoxide, aldehyde and diol products in oxidation of cyclohexene using t-butyl hydroperoxide. Apices represent 100% of each product.*

The product distribution triangular plots indicate there is little difference between Ni STA-12 and the metal doped versions (Figures 6.10 and 6.11). The samples where Ni has been replaced cluster into a small area around the plot for pure Ni STA-12, indicating the final product distributions are related more to the bisphosphonate structure than the metals present.

6.2.6 Reactions using MIL-*n* structures as catalysts

The selective oxidation reactions were run using several MIL-*n* structures (structures outlined in Chapter 1 and syntheses outlined in Chapter 3) as catalysts, in order to compare to STA-12 (Figure 6.12). Only *tert*-butyl hydroperoxide was used as the oxidant due to vanadium-containing MIL-*n* MOFs dissolving in water. The MIL-53 samples were activated at 603 K, and the MIL-47 samples activated at 573 K to remove excess terephthalic acid from the pores. MIL-68 was activated at 523 K to

remove excess DMF from the pores, while MIL-100 was activated at 473 K to remove water from the Cr cations.

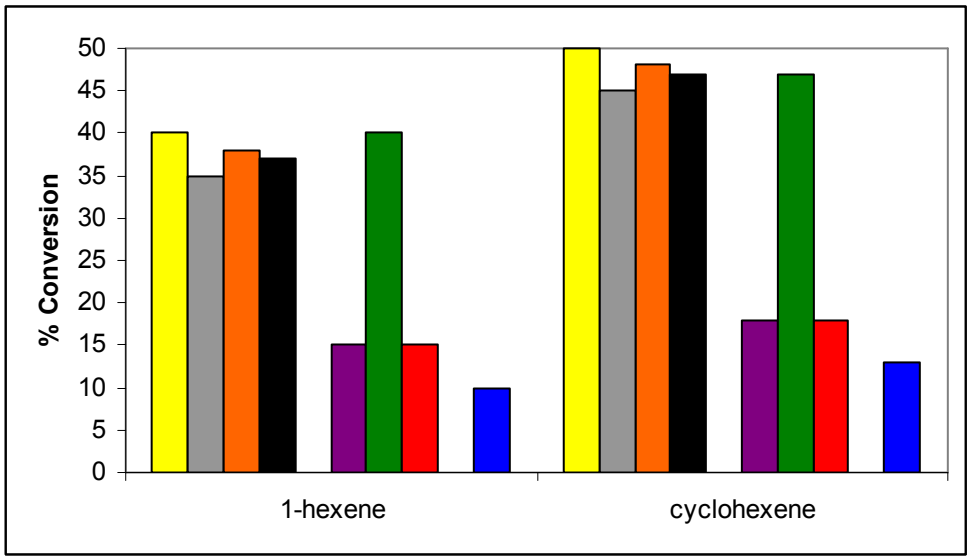

Figure 6.12 *- Results obtained for conversion of 1-hexene and cyclohexene over 6 hours of reaction using t-butyl hydroperoxide as the oxidant and MIL-n MOFs as catalysts. MIL-47 - yellow; MIL-47 re-use - grey; MIL-68 - orange; Vanadium acetylacetonate – black; Cr MIL-53 - purple; MIL-100 - green; Chromium acetylacetonate - red; No catalyst present - blue.*

Looking at the vanadium MIL structures (MIL-47 and MIL-68), the conversions are higher than STA-12. There are no CUS metal sites in either MIL-47 or MIL-68, so the activity would not be expected to be as high. The reaction mixtures turn orange during the six hours of reaction time, indicating vanadium is leaching and subsequently acting as a homogeneous catalyst. Vanadium acetylacetonate was tested as a homogenous source of vanadium, with an equivalent amount used equal to 5% of the metal present in 0.2 g of MIL-47. The activity was observed to be similar to MIL-47 and MIL-68, indicating most of the conversion is due to leached vanadium in the reaction. To test this, MIL-47 was recovered at the end of the reaction and used again. The resulting conversions were observed to be lower than when the structure was used the first time, indicating less vanadium is present. The stability issue for MIL-47 and MIL-68 is similar to that seen for VAPO-5,[7] and indicate possible problems using vanadium as an oxidation catalyst in microporous materials.

Looking at the chromium-containing structures, MIL-53 has lower conversions for 1-hexene and cyclohexene than MIL-100. MIL-53 has no CUS metal sites in the structure, and there is no evidence for chromium leaching. Surface Cr sites are probably the only active sites involved in catalysing the reaction, meaning the observed conversions are not much higher than chromium acetylacetonate.

MIL-100 has very large pores and significant numbers of CUS Cr sites. This accounts for the significantly higher activity compared to Cr MIL-53, STA-12 and CPO-27. MIL-100 is therefore the best catalyst tested in this work in terms of observed conversions of 1-hexene and cyclohexene in selective oxidation reactions. Comparison of the three main reaction products to one another allows for an indication of if there are any differences between the MIL-*n* structures (Figure 6.13 and 6.14).

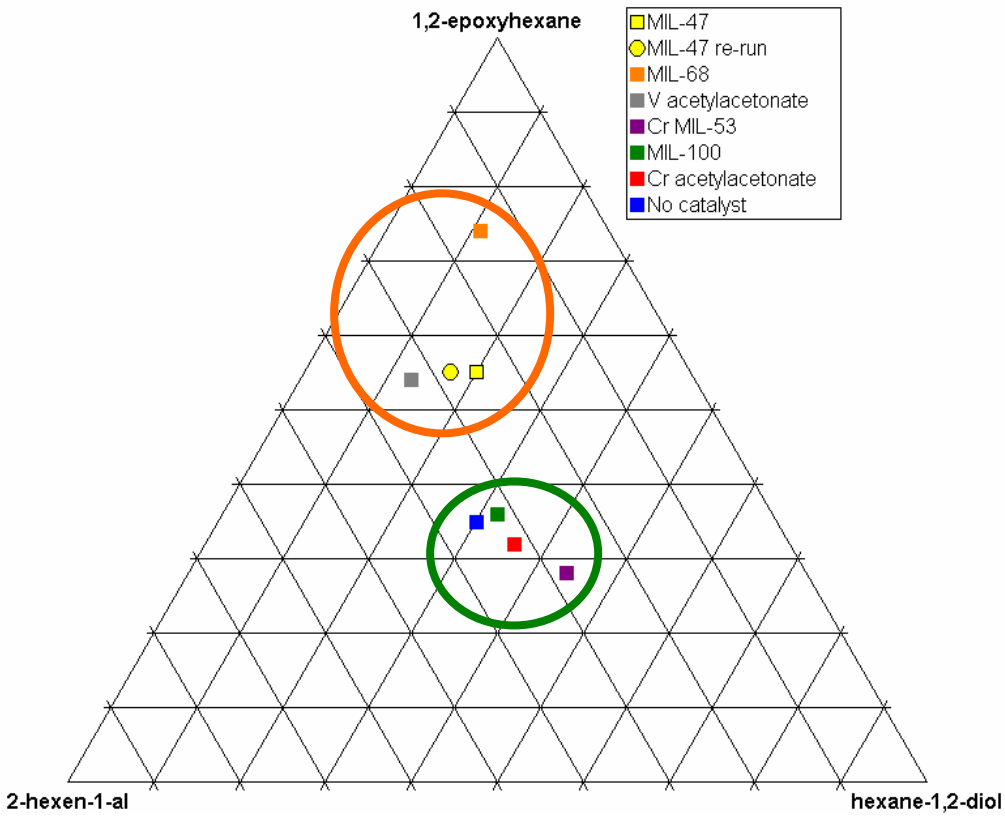

Figure 6.13 *- Triangular plot comparing epoxide, aldehyde and diol products in oxidation of 1-hexene. Orange circle - V containing structures, Green circle - Cr containing structures. Apices represent 100% of each product.*

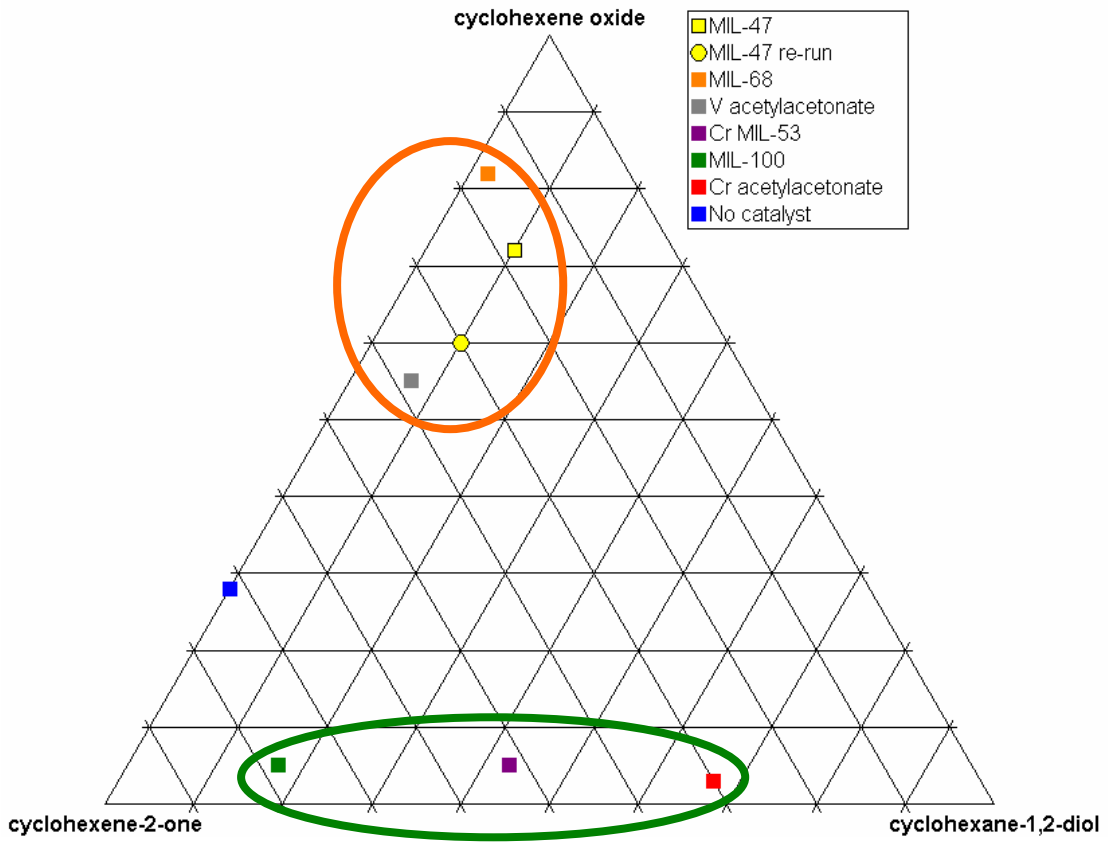

Figure 6.14 *- Triangular plot comparing epoxide, aldehyde and diol products in oxidation of cyclohexene. Orange circle - V containing structures, Green circle - Cr containing structures. Apices represent 100% of each product.*

The distributions of the three main products indicate a clustering in terms of the metal present (Figures 6.13 and 6.14). The vanadium-containing structures plot near the 100% epoxide apex, and the product distributions are similar to those for vanadium acetylacetonate. The chromium-containing structures plot lower down, in the case of 1-hexene near the centre of the triangular plot in a similar position to STA-12, and for cyclohexene near the bottom, in-between the 100% ketone and diol apices. This product distribution is similar to that observed for CrAPO-5 oxidising cyclohexene.[4] Comparison of the results obtained for the STA-12 and MIL-*n* structures (0.2 g catalyst, 25 mmol cyclohexene, 6.25 mmol H_2O_2, 25 ml methanol, 323 K and 6 hours) with those for POM loaded MIL-101[16] (0.02 g catalyst, 0.2 mol cyclohexene, 0.4 mol H_2O_2, 1.5 ml MeCN, 343 K and 6 hours) indicates POM loaded MIL-101 is a better oxidation catalyst than STA-12 and the MIL-*n* MOFs. There are even amounts of the ketone and diol products formed when using POM loaded MIL-101, along with virtually no epoxide. The product distribution would plot inside the green circle in the

triangular plot in Figure 6.14, indicating there is an influence on the reaction mechanism from the Cr in the structure.

6.3 Base catalysis – Knoevenagel condensation

6.3.1 Background to Knoevenagel condensation reaction

The Knoevenagel condensation reaction, first reported by E. Knoevenagel in 1898,[17] is a well known reaction catalysed in the presence of a base (Scheme 6.3). The reaction involves nucleophilic addition of an active hydrogen compound to a carbonyl group, followed by a dehydration reaction. The products are often alpha or beta conjugated enones.

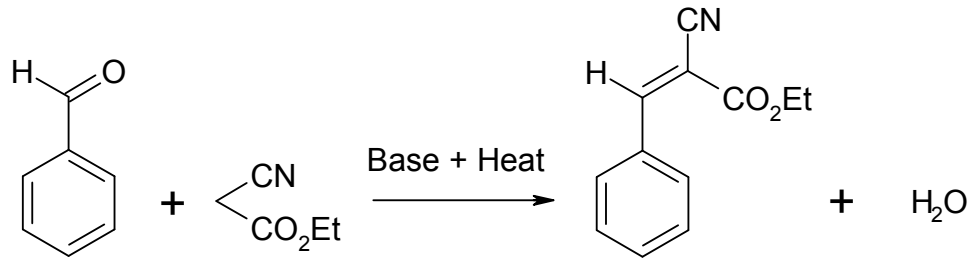

Scheme 6.3 *- Knoevenagel condensation reaction of benzaldehyde and ethyl cyanoacetate, producing ethyl trans-α-cyanocinnamate as the product.*

Knoevenagel condensations have important uses in a number of organic reactions. These include in the formation of charge transfer compounds such as the synthesis of 1,3-diethyl-5-(2-methoxybenzylidene)-2-thioxodihydropyrimidine-4,6-dione from 2-methoxybenzaldehyde and N,N-diethylthiobarbituric acid[18] (Scheme 6.4) and in the synthesis of the anti-malarial drug lumefantrine.[19]

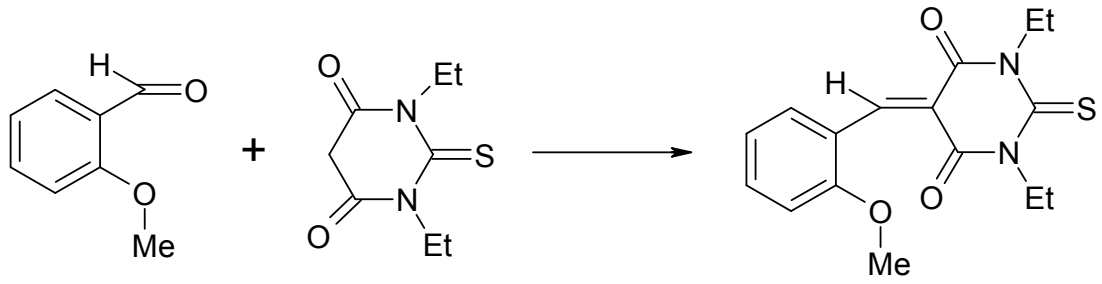

Scheme 6.4 *- Synthesis of 1,3-diethyl-5-(2-methxoybenzylidene)-2-thioxodihydropyrimidine-4,6-dione from 2-methoxybenzaldehyde and N,N-diethylthiobarbituric acid, using piperidine as the base and ethanol as the solvent.*

Previous work using porous materials as basic catalysts for Knoevenagel reactions has focused on zeolites, such as NaY and NaX,[20] and amine-grafted mesoporous solids, e.g. MCM-41.[21] Modification of MCM-41 with aminopropyltrimethoxysilane produced a catalyst with a significant percentage of functional amine groups within the mesopores.[21] This resulted in a high activity for the Knoevenagel condensation of benzaldehyde and ethyl cyanoacetate (Scheme 6.3), with a yield in excess of 99% after 1 hour of reaction. With longer reaction times (up to 24 hours), there was evidence the amine groups were leaching out of the solid, reducing the activity of the catalyst. Using zeolites NaY and NaX as catalysts for the same Knoevenagel reaction was investigated on a micro reactor scale.[20] Modification of the zeolite structure with 3-aminopropyl-trimethylsiloxane resulted in 80% conversion of benzaldehyde after 3 hours. An important part of this investigation involved the proposal of a mechanism for the catalytic reaction, involving coordination of benzaldehyde to the amine modified surface, followed by reaction with ethyl cyanoacetate to form the cinnamate product (Scheme 6.5).

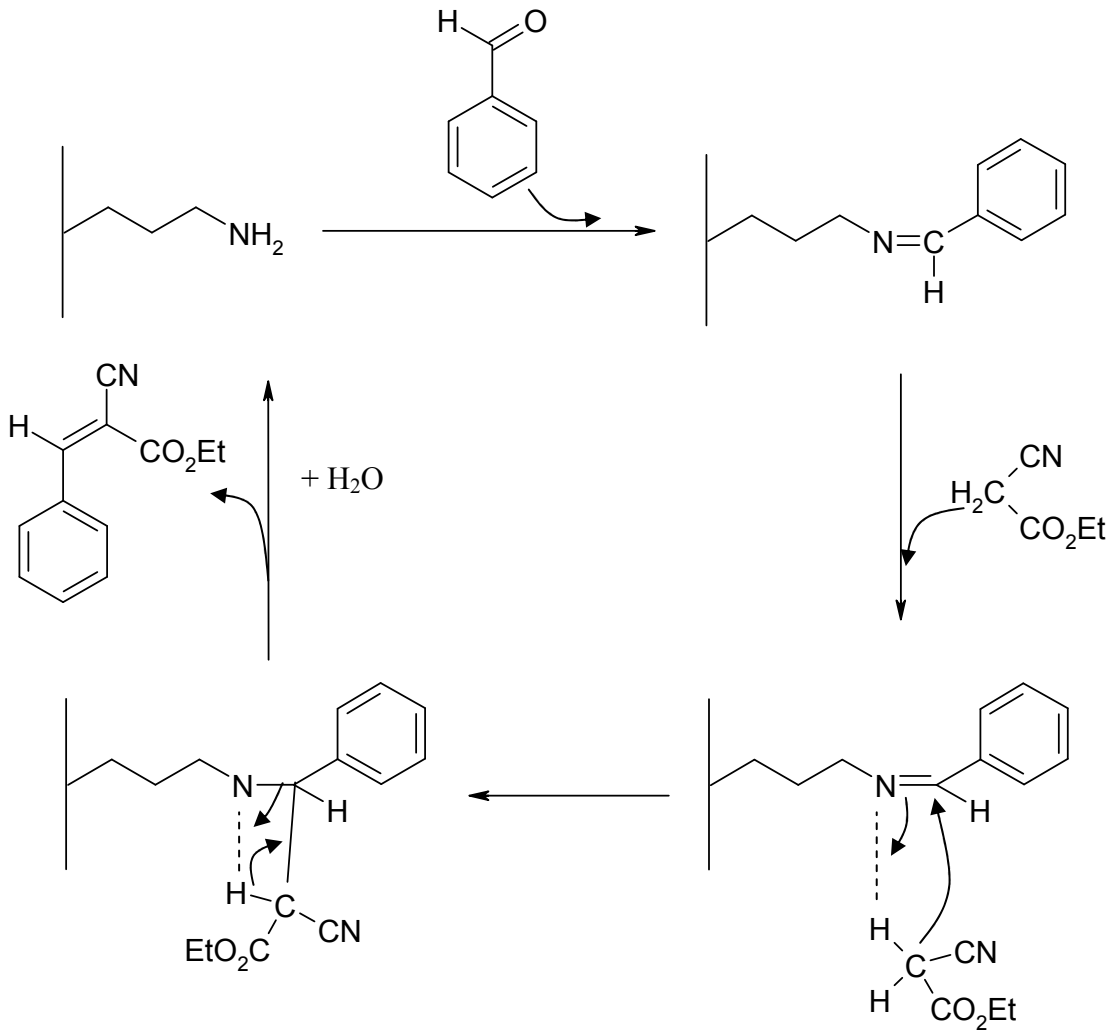

Scheme 6.5 *- Proposed reaction mechanism for Knoevenagel condensation catalysed by an amine-modified surface (adapted from reference 20).*

6.3.2 Modification of STA-12 with diamines

The work undertaken to modify MIL-101 into a basic catalyst by grafting of ethylene diamine onto the CUS Cr sites[23] has been used as a starting point to do the same with STA-12. As-prepared samples of STA-12 (0.1g) were immersed for various times in organic solutions comprising of toluene (15 ml) and a measured amount of either ethylene diamine or 1,3-diaminopropane (equivalent to 1 diamine molecule per 2 metal sites). The uptake of the diamines with time, calculated from CHN analyses, are compared in the graphs below (Figures 6.15 and 6.16).

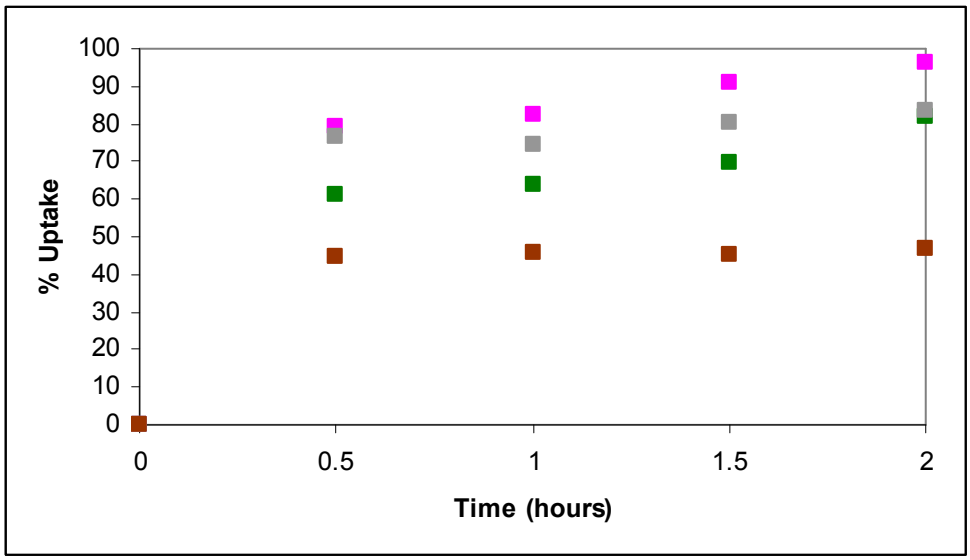

Figure 6.15 *- % Uptake of ethylene diamine over time by as-prepared STA-12 from organic solution. Mn STA-12 - grey; Fe STA-12 - brown; Co STA-12 - pink; Ni STA-12 - green.*

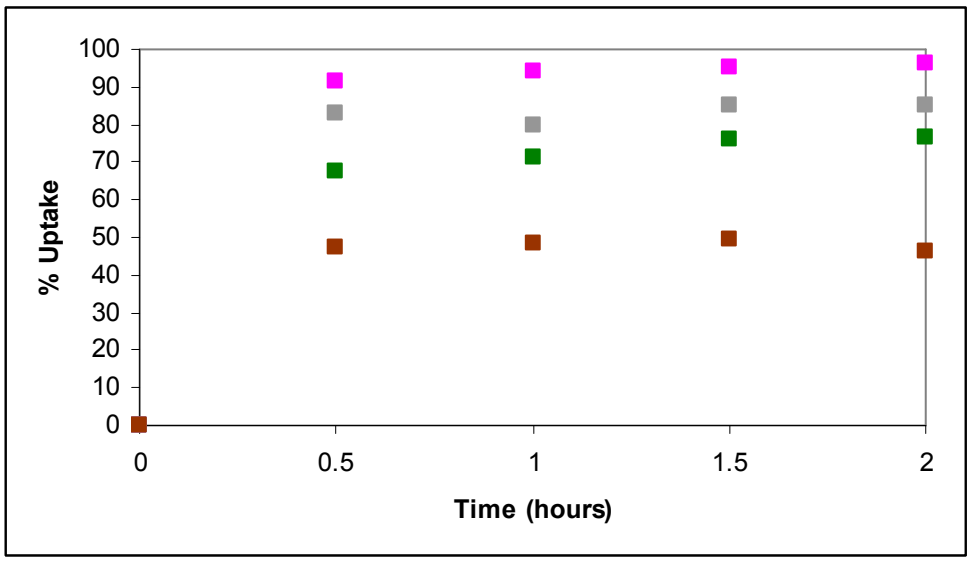

Figure 6.16 *- % Uptake of 1,3-diaminopropane over time by as-prepared STA-12 from organic solution. Colour coding same as Figure 6.15.*

The results indicate the different versions of STA-12 all have fast uptakes for ethylene diamine and 1,3-diaminopropane (Figures 6.15 and 6.16). The diamine molecules are attracted to the pores of as-prepared STA-12, which act as water rich tunnels. There is evidence they are displacing the chemically adsorbed water coordinated to the metal sites, as both Co and Mn STA-12 change colour, to red and brown respectively, while maintaining crystallinity after two hours of exposure to the organic solutions.
For ethylene diamine and 1,3-diaminopropane the order of highest uptake is the same, increasing from Fe < Ni < Mn < Co. There are similar final uptakes for both of the diamine molecules, indicating there are no significant steric differences upon adsorption.

6.3.3 Knoevenagel Reactions – Experimental and Characterisation Techniques

The Knoevenagel reactions in this study were carried out using the same conditions as Das *et al*.[21]

Knoevenagel condensation – benzaldehyde (2.03 ml, 20 mmol), ethyl cyanoacetate (2.13 ml, 20 mmol) and cyclohexane (10 ml) were mixed together. 0.1 g (0.03 mmol with 15 mol % active sites) of activated catalyst was added (t = 0) and the reaction stirred for 4 hours at 353 K. The solid and liquid were separated using filtration, with the liquid analysed by GC and the solid by X-ray powder diffraction.

Gas chromatography (GC) measurements were performed on the liquid mixtures in a similar way to the selective oxidation reactions, with toluene used again as an internal standard. Examples of the peak positions in the GC traces and the associated calculation of substrate conversion is presented in Appendix 9.

6.3.4 Results for Knoevenagel condensation reactions

6.3.4.1 Unmodified STA-12

Table 6.2 *– Catalytic results for unmodified STA-12 in Knoevenagel condensation of benzaldehyde and ethyl cyanoacetate.*

Catalyst	Conversion of benzaldehyde	Selectivity to ethyl *trans*-α-cyanocinnamate
Ni STA-12 – dehydrated 373 K	33.3 %	>99 %
Ni STA-12 – dehydrated 423 K	44.32 %	90.38%
Co STA-12 – dehydrated 423 K	39.1 %	>99 %
Fe STA-12 – dehydrated 423 K	38.7 %	>99 %
Mn STA-12 – dehydrated 423 K	39.1 %	>99 %
Ni CPO-27 – dehydrated 473 K	6.4 %	>99 %
Zeolite NaY – dehydrated 573 K	29.2 %	80 %
No catalyst present	1.9 %	>99 %

From the results in Table 6.2, when chemically bound water is present in Ni STA-12 the reaction results in less conversion to the ethyl *trans*-α-cyanocinnamate product than when no water is present. The results for fully dehydrated Ni STA-12 were also compared to those obtained for fully dehydrated Co, Fe and Mn STA-12. They indicate the basicity of the metal sites increase Fe < Co, Mn < Ni, and comparison of Ni in STA-12 and CPO-27 indicates STA-12 is the more basic framework.

Zeolite NaY was chosen as a control comparison, as it has been demonstrated to have basic properties. Conversion of benzaldehyde and selectivity to the cinnamate product

is lower for zeolite NaY than for the MOFs tested. This indicates the STA-12 structures have basicity that could be exploited for use in catalysis.

6.3.4.2 STA-12 modified with diamines

Table 6.3 *– Catalytic results for diamine modified STA-12 in Knoevenagel condensation of benzaldehyde and ethyl cyanoacetate.*

Catalyst	Conversion of benzaldehyde	Selectivity to ethyl *trans*-α-cyanocinnamate
Ni STA-12 – dehydrated 373K	33.3 %	>99 %
Ni STA-12 + ethylene diamine 0.5 hour	40.5 %	>99 %
Ni STA-12 + 1,3-diaminopropane 0.5 hour	63.2 %	>99 %
Ni STA-12 + 1,3-diaminopropane 1 hour	55.9 %	>99 %
Ni STA-12 + 1,3-diainopropane 1.5 hours	60.2 %	>99 %
Ni STA-12 + 1,3-diaminopropane 2 hours	47.9 %	>99 %
Ni STA-12 dehydrated 423 K + 1,3-diaminopropane	40.2 %	>99 %

The effect on the basic properties of STA-12 of modification with diamines has been tested with Ni STA-12 (Table 6.3). The activity for the Knoevenagel condensation reaction is increased with the addition of ethylene diamine and 1,3-diaminopropane. The highest activity was observed for Ni STA-12 in contact with the 1,3-diaminopropane and toluene solution for one and a half hours (75 % diamine uptake). The samples where Ni STA-12 had been in contact with toluene and ethylene diamine for longer than half and hour were unstable in the Knoevenagel condensation, with some structural dissolution taking place.

Different methods of adding the diamine molecules were also investigated, with 1,3-diaminopropane adsorbed onto a previously dehydrated sample of Ni STA-12. Using this in the Knoevenagel reaction results in a lower conversion rate compared to the samples where 1,3-diaminopropane was added to as-prepared Ni STA-12. This suggests water and diamines have to both be present to create the highest basicity.

Table 6.4 *- Catalytic results for re-use of diamine modified STA-12.*

Catalyst	**Conversion of benzaldehyde**	**Selectivity to ethyl *trans*-α-cyanocinnamate**
Ni STA-12 + ethylene diamine 0.5 hour Catalyst re-use	40.5 %	>99 %
Ni STA-12 + 1,3-diaminopropane 0.5 hour Catalyst re-use	61.3 %	>99 %
Ni STA-12 + 1,3-diaminopropane 1 hour Catalyst re-use	54.2 %	>99 %
Ni STA-12 + 1,3-diaminoporpane 1.5 hours Catalyst re-use	58.9 %	>99 %
Ni STA-12 + 1,3-dimainopropane 2 hours Catalyst re-use	42.5 %	>99 %

The re-usability of Ni STA-12 modified with diamines has been investigated (Table 6.4), and a slight decrease in the conversion of benzaldehyde was observed when using for a second time. This possibly indicates some of the diamine molecules are leaching out of the Ni STA-12 structure, and as a result catalytic reactions as functions of time were undertaken. Fully dehydrated Ni STA-12 and Ni STA-12 which had been in contact with 1,3-diaminopropane were used as the catalysts. The

reactions were run for 2 hours, and then the catalysts were filtered off. The reactions were subsequently continued in order to ascertain if any activity was still taking place.

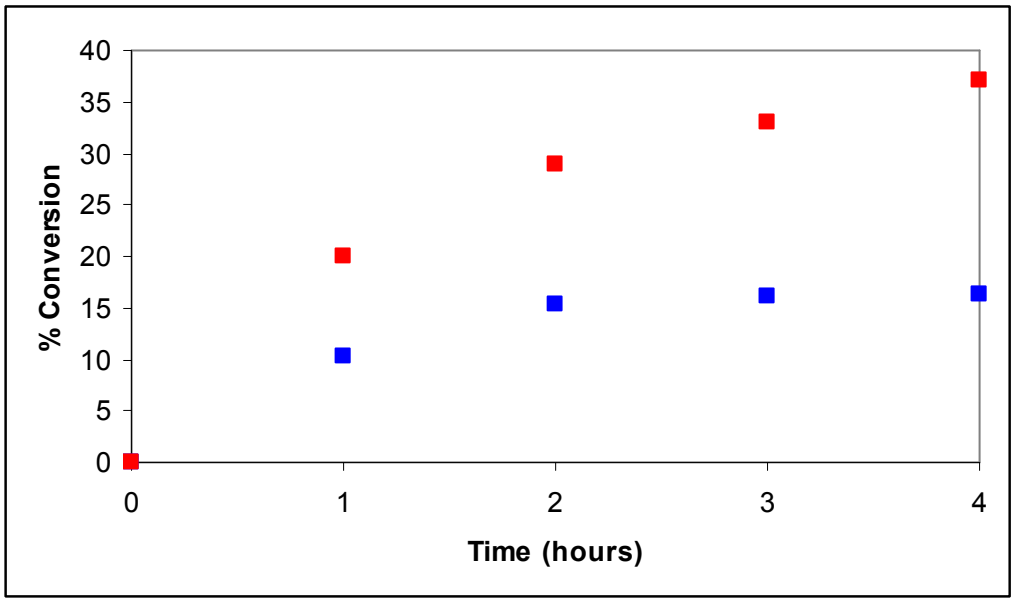

Figure 6.17 *– Conversion of Knoevenagel reaction versus time, with catalysts removed after 2 hours and reaction continued. Blue – Ni STA-12; Red - Ni STA-12 + 1,3-diaminopropane.*

Looking at the graph in Figure 6.17, there is still conversion of the substrates after removal of Ni STA-12 + 1,3-diaminopropane. Conversely, there is no conversion of the substrates when Ni STA-12 is removed. Therefore, the evidence indicates some of the diamine molecules must be leaching into the reaction mixture, and are contributing to the activity of the catalyst.

Comparing the results obtained for diamine modified Ni STA-12 with those for MIL-101 modified with ethylene diamine,[22] the selectivity to ethyl *trans*-α-cyanocinnamate is the same for both catalysts (>99 %). The reaction involving modified MIL-101 used 1 mmol of each reactants, 0.02 g of the catalyst, 25 ml cyclohexane and a 7 hour reaction time to give a benzaldehyde conversion of almost 98 %. Comparing this to the different reaction conditions used in this study (20 mmol of each reactant, 0.1g of catalyst, 10 ml cyclohexane and 4 hours of reaction time producing a highest benzaldehyde conversion of *ca.* 60 %), there is an indication modified MIL-101 is a

better basic catalyst than modified Ni STA-12. This is probably due to the fact more space is available in the framework after introduction of the diamine molecules.

6.4 Other catalytic reactions - Ni STA-12 + 20% Mn - CO activation

Mn STA-12 does not adsorb any gas molecules, so it is not possible to investigate it for use in gaseous reactions catalysed by manganese cations. As outlined in Chapter 3, however, 20% of the Ni can be replaced in Ni STA-12 by Mn, while maintaining the porosity. Therefore, it is possible to investigate the catalytic role of Mn supported in the framework of Ni STA-12.

Preliminary measurements of the activation of CO were undertaken in a controlled atmosphere using an environmental cell that allowed thermal treatment under high vacuum, dosing of gas and *in situ* spectra collection. FTIR spectra were collected in transmission mode on a self supporting wafer with a Bruker Equinox-55 FTIR spectrometer equipped with an MCT detector. The sample compartment was modified *ad hoc* to accommodate a cryogenic IR probe, and a detailed description of this experimental setup is outlined elsewhere.[23] Activation at 448 K results in the sample having the normal brown-yellow colour of dehydrated Ni STA-12. After adsorption of CO, the Infra-red spectrum is similar to that seen for CO onto Ni STA-12 (Chapter 5, Figure 5.6), and there is no evidence for any other major bands. Activation at 573 K, on the other hand, results in the sample turning black in colour, although it is still porous and adsorbs gas molecules. It appears the sample turns a black colour due to heating at high temperature under a high vacuum ($<1 \times 10^{-3}$ Torr). The Infra-red spectra for adsorption of CO are shown in Figure 6.18, with increasing coverage of CO in the direction of the bottom spectrum to the top spectrum.

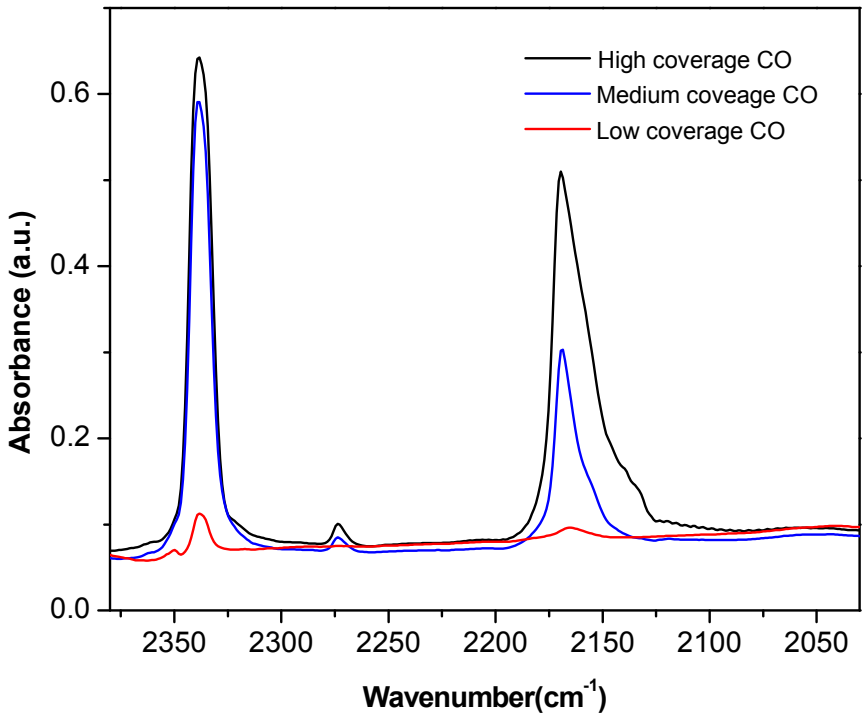

Figure 6.18 *- Background subtracted Infra-red spectra of the preliminary results for CO adsorption onto Ni STA-12 + 20% Mn activated at 573 K.*

Bands similar to adsorption onto Ni STA-12 are observed as well as the growth of a band at 2339 cm^{-1}, which is interpreted as due to the ν_3 vibration of CO_2 bound linearly to metal cations (Chapter 5, Figures 5.11 and 5.13). Therefore, activation of Ni STA-12 + 20% Mn at 573 K results in the CO gas molecules reacting to form CO_2. The high temperature and high vacuum activation step seems to result in at least some of the Mn atoms coming out of the framework, allowing them to take part in a catalytic reaction.

This reaction does not take place if the concentration of Mn in the structure is lower, indicating there is a critical threshold above which Mn^{2+} cations appear to leave the framework during high temperature treatment. If the concentration of Mn is increased to higher levels it would be expected that more activation of CO would take place, and a supported catalyst for Mn could in effect be formed.

6.5 Conclusions from catalysis

The MOFs synthesised during the course of this study are active as both acid and base catalysts in selective oxidation reactions and Knoevenagel condensations respectively. The activity of STA-12 was found to be significantly higher than when no catalyst was present, although when compared to some other large pore MOFs it was found to not be the best catalyst. STA-12 was also observed to be stable, with no evidence for dissolution in the presence of any of the reactants or solvents. In the selective oxidation reactions it was noted the activity of STA-12 was less than expected, and the framework had significant acidity with epoxide ring opening promoted. Investigations using as-prepared Ni STA-12 indicated when using H_2O_2 as the oxidant the sites are coordinated almost immediately on contact with the reaction mixture. When using t-butyl hydroperoxide as the oxidant, the substrate conversions were observed to slow over time, due to coordination of products and/or solvent during the reaction.

Investigations were undertaken, using the selective oxidation reactions, into mixed metal STA-12 samples, where set amounts of Ni are replaced by other divalent metals (Mg, Mn, Fe and Co – Chapter 3). The results indicated the activities increased only slightly compared to the pure Ni^{2+} material, meaning surface catalysis may be more important for the activity. The product distributions were similar to Ni STA-12, indicating the framework is a more important factor in the oxidation reactions than the metals present.

The STA-12 structures were compared with several Cr and V frameworks from the MIL-*n* series. The V-containing structures had good activities, but they were not stable, with the metals leaching into the reaction mixtures. Comparison with vanadium acetylacetonate indicated most of the activity could be attributed to leached metals acting as homogeneous catalysts. Considering the Cr-containing MIL-*n* structures, MIL-100 had the best activity. The very large pores, coupled with the significant number of CUS sites present allowed for a high catalytic activity. The product distribution for the MIL-*n* frameworks were different depending on the metal, the V-containing structures favouring epoxide formation, and the Cr-containing structures favouring epoxide ring opening and production of ketone rearrangement products, especially for cyclohexene.

In the Knoevenagel condensations, Ni STA-12 had the highest basic activity. As-prepared versions of the STA-12 structures were successfully modified with ethylene diamine and 1,3-diaminopropane from organic solution, with the physically bound water present in the pores acting as a water rich tunnel. Using the diamine modifed Ni STA-12 structures in the Knoevenagel condensation reaction increased the activity over the unmodifed structures, while it was demonstrated both water and the diamine molecules needed to be present to allow for the highest activity and basicity. Investigations of reactions over time where the catalyst was removed part way through indicated some of the diamine molecules were leached during the reaction, possibly accounting for some of the activity.

A sample of Ni STA-12 + 20% Mn was observed to have activity for converting CO to CO_2. Activation at a high temperature (573 K) under a high vacuum ($<1 \times 10^{-3}$ Torr) was interpreted to allow the Mn atoms to move out of the framework, forming catalytically active sites without destroying the porosity. This concept could in theory be extended to other reactions where Mn can be used as a catalyst, possibly using samples where the concentration of Mn is higher.

6.6 References

1) G. W. Parshall and S. D. Ittel, *Homogeneous Catalysis – the applications and chemistry of catalysis by soluble transition metal complexes*, *Wiley*, *New York*, 1992, **2nd ed.**, p. 137

2) R. A. Sheldon and J. A. van Doorn, *J. Catal.*, 1973, **31**, 427

3) J. D. Chen, H. E. B. Lempers and R. A. Sheldon, *Colloids and Surfaces A.*, 1995, **101**, 137

4) C. B. Khouw and M. E. Davis, *J. Catal.*, 1995, **151**, 77

5) I. W. C. E. Arends, R. A. Sheldon, M. Wallau and U. Schuchardt, *Angew. Chem. Int. Ed.*, 1997, **36**, 1144

6) A. Corma, P. Esteve, A. Martínez and S. Valencia, *J. Catal.*, 1995, **152**, 18

7) M. J. Haanepen, A. M. Elemans-Mehring and J. H. C. van Hooff, *Appl. Cat. A: General*, 1997, **152**, 203

8) J. M. Thomas, R. Raja, G. Sankar and R. G. Bell, *Nature*, 1999, **398**, 227

9) J. M. Thomas, *Top. Catal.*, 2001, **15**, 85

10) G. W. Parshall and S. D. Ittel, *Homogeneous Catalysis – the applications and chemistry of catalysis by soluble transition metal complexes*, *Wiley*, *New York*, 1992, **2nd ed.**, p. 240

11) R. A. Sheldon, J. A. van Doorn, C. W. A. Schram and A. J. de Jong, *J. Catal.*, 1973, **31**, 438

12) R. S. Reddy, J. S. Reddy, R. Kumar and P. Kumar, *J. Chem. Soc.*, *Chem. Commun.*, 1992, 84

13) W. Adam, A. Corma, T. I. Reddy and M. Renz, *J. Org. Chem.*, 1997, **62**, 3631

14) A. Corma and H. Garcia, *Chem. Rev.*, 2002, **102**, 3837

15) E. P. Talsi and D. E. Babushkin, *J. Mol. Catal. A: Chemical*, 1996, **106**, 179

16) N. V. Maksimchuk, M. N. Timofeeva, M. S. Melgunov, A. N. Shmakov, Y. A. Chesalov, D. N. Dybtsev, V. P. Fedin and O. A. Kholdeeva, *J. Catal.*, 2008, **257**, 315

17) E. Knoevenagel, *Berichte der deutschen chemischen Gesellschaft*, 1898, **31**, 2596

18) A. M. Asiri, K. A. Alamery, A. F. Jalbout and S. Zhang, *Molbank*, 2004, **M359**

19) U. Beutler, P. C. Fuenfschilling and A. Steinkemper, *Org. Process Res. Dev.*, 2007, **11**, 341

20) X. Zhang, E. S. M. Lai, R. Martin-Aranda and K. L. Yeung, *Appl. Catal. A*, 2004, **261**, 109

21) D. D. Das, P. J. E. Harlick and A. Sayari, *Catal. Commun.*, 2007, **8**, 829

22) Y. H. Hwang, D. Hong, J. Chang, S. H. Jung, Y. Seo, J. Kim, A. Vimont, M. Daturi, C. Serre and G. Férey, *Angew. Chem. Int. Ed.*, 2008, **120**, 4212

23) G. Spoto, E. N. Gribov, G. Ricchiardi, A. Damin, D. Scarno, S. Bordiga, C. Lamberti and A. Zecchina, *Prog. Surf. Sci.*, 2004, **76**, 71

Chapter 7: General Conclusions and Future Work

7.1 General Conclusions

The ligands N,N'-piperazinebis(methylene phosphonic acid) (H_4L), and the 2-methyl (H_4L-Me) and 2,5-dimethyl (H_4L 2,5-diMe) derivatives have been synthesised using a modified acid catalysed Mannich reaction. Several structures have been synthesised by hydrothermal treatments of gels with metal : ligand ratios of 2 : 1: STA-12 (with Mn, Fe, Co and Ni), Ni VSB-5, Co $H_2L.H_2O$ and Mg H_2L.

STA-12 is synthesised with both the H_4L and the H_4L-Me ligands, and Ni STA-12 (synthesised with H_4L) is the most crystalline version of the structure. Helical chains of metal octahedra are coordinated by the fully deprotonated ligand, forming large hexagonal shaped pores filled with physically bound water. The unit cell parameters and volume change when different metals are used in the structure, in line with the changes in the ionic radii, and when the H_4L-Me ligand is used the volume increases. Mixed metal STA-12 samples can be synthesised, with known amounts of Ni replaced by other divalent metals with retention of the structure and porosity.

Ni VSB-5 is formed in the reaction of Ni with the H_4L 2,5-diMe ligand. The framework is a Ni phosphate, indicating the ligand is breaking down under the reaction conditions. Co $H_2L.H_2O$ is formed when the starting pH of the gel for Co STA-12 is 5 instead of 7. The pH is not high enough to full deprotonate the ligand, and there is tetrahedral coordination of Co by phosphonate oxygens.

STA-12 undergoes complex dehydration behaviour, which can be followed by X-ray diffraction and spectroscopic methods. Ni and Co STA-12 exhibit similar behaviour, with the structure distorting with loss of water. The symmetry reduces from rhombohedral to

triclinic, and the porosity is created. Three different dehydrated structures have been identified for Ni STA-12, and these are where just the physically bound water is removed (dehydration at 323 K), where the physically bound water and two-thirds of the chemically bound water is removed (dehydration at 373 K) and where all of the water is removed (dehydration at ≥ 423 K). When all the water is removed the structure undergoes a topotactic rearrangement which results in the formation of three crystallographically distinct Ni and P sites. The Ni sites are five-coordinate, as interpreted from UV-visible spectroscopy. Infra-red spectroscopy suggests a cyclic species is formed upon hydration involving binding of water to the Ni^{2+} and P=O sites.

Dehydration of Ni and Co Me STA-12 results in retention of the rhombohedral symmetry, but with reduced crystallinity. Study of the STA-12 structure indicates there is just enough room for the methyl groups to be present on the ligand in the as-prepared structure. Upon dehydration the methyl groups prevent the structure from distorting, meaning the rhombohedral symmetry is retained, resulting in a slightly increased porosity when compared to the non-methyl ligand structure.

On dehydration Mn and Fe STA-12 exhibit similar behaviour, different to Ni and Co STA-12, which is attributed to the different ionic radii. The rhombohedral symmetry is retained, and the *a* cell parameter and the volume are significantly reduced. Structure solution of dehydrated Mn STA-12 indicated changes in the torsion angles in the ligand are responsible for the reduction in the cell and the retention of the symmetry. Unexpectedly, neither Mn nor Fe STA-12 adsorb nitrogen gas. It has been interpreted an amorphous surface layer is formed on dehydration that does not admit any molecules apart from water. In the as-prepared solids, Fe and Mn STA-12 take up ethylene diamine and 1,3-diaminopropane from organic solutions, indicating the pores are not blocked under those conditions.

Ni and Co STA-12 have been demonstrated to adsorb many different fuel related gas molecules at both low and ambient temperature. Compared to other MOFs with coordinatively unsaturated sites, Ni STA-12 has reasonable adsorption performances. Depending on the size of the adsorption enthalpies, the adsorbed species can adsorb on the most accessible Ni site in the distorted fully dehydrated structure, or can cause the structure to change to rhombohedral symmetry allowing adsorption on all the Ni^{2+} sites.

Infra-red spectroscopy of adsorbed species on Ni and Co STA-12 indicate the metal cation sites and the P=O groups are the main adsorption sites in the structure. Uptake of large aromatic molecules has also been demonstrated in Ni STA-12.

The MOFs synthesised in this work were demonstrated to be active as acid and base catalysts in selective oxidation and Knoevenagel reactions respectively. In the selective oxidation reactions, greatest activity was measured when t-butyl hydroperoxide was used as the oxidant and cyclohexene was used as the substrate. Examination of the relative amounts of the products formed showed STA-12 promoted epoxide ring opening, while control reactions indicated products and/or solvent were coordinating to the active sites over time reducing the activity and promoting surface catalysis. The results for Knoevenagel reactions indicate Ni STA-12 is more basic than Mn, Fe or Co STA-12. Modification of Ni STA-12 with the diamines ethylene diamine and 1,3-diaminopropane results in slightly higher activity for the Knoevenagel reactions, indicating the presence of the diamines increases the basicity of the structure.

7.2 Possible future work

There are several avenues of work that could be explored to further that presented in this thesis. At the end of Chapter 6 some preliminary work was presented looking at using Ni STA-12 + 20% Mn as a catalyst. Activating the structure at high temperatures appeared to result in the formation of a supported catalyst for Mn which could activate CO. Samples where there are higher concentrations of Mn present could be synthesised to try in this reaction, and further investigation could be undertaken to try and elucidate a mechanism for the CO activation.

The results indicate STA-12 catalyses both the selective oxidation and Knoevenagel reactions, but with activities that are not as high as other MOFs studied for the same reactions. Therefore, STA-12 could be tried in other acid and base catalysed reactions to see if there is any activity, for example in catalytic ene reactions which require Lewis acidity.[1] Preliminary work using the reaction in Figure 7.1 indicates there is some activity.[2]

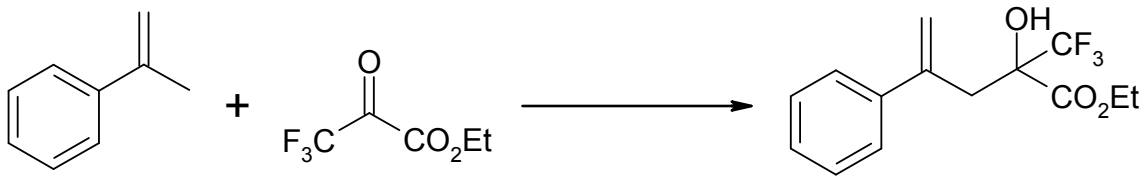

Figure 7.1 *– Intermolecular ene reaction between ethyl trifluoropyruvate and α-methyl styrene which requires a Lewis acid catalyst.*[2]

On the synthesis side, there are some reactions that have not been considered in this work. The Mn and Fe STA-12 hydrothermal reactions have not been run using the H_4L Me ligand. As both Ni and Co Me STA-12 can be formed, there should be no reason Mn and Fe Me STA-12 cannot be synthesised. Also, Mn, Fe and Mg have not been reacted with the H_4L 2,5-diMe ligand. Reaction of these metals with this ligand could potentially produce novel structures. The structure of Mg H_2L, which is the only novel structure synthesised in this work, has not been solved. If the structure was solved, it would be possible to understand how it could be related to STA-12, as the metal : ligand ratios are the same.

To complete the adsorption work the differential heats of adsorption of hydrogen and carbon monoxide could be measured for Co STA-12. This would provide a comparison to Ni STA-12, and allow for the conclusions about the adsorption performance of Co STA-12 to be confirmed. In the adsorption of large aromatics, it was observed Ni STA-12 adsorbed slightly different amounts of xylenes. Further insight might be gained into separation using the STA-12 framework by co-adsorbing mixtures.

7.3 References

1) M. L. Clarke and M. B. France, *Tetrahedron*, 2008, **64**, 9003

2) M. Gunn, Honours Project "The Synthesis of Metal-Organic Frameworks and their use in Catalysis", *University of St Andrews*, *St Andrews*, 2009

<u>Appendix 1</u> – Ni STA-12 as-prepared – Atomic coordinates (High resolution)
(*J. Am. Chem. Soc.*, 2008, **130**, 15967**)**

$\mathbf{R_{wp}}$ = 5.96 %, $\mathbf{R_p}$ = 4.11 %

Atom	x	y	z	Occupancy	Uiso
Ni1	0.30346	0.02706	0.7192	1	0.0033
P1	0.28239	-0.09025	0.90413	1	0.0087
N1	0.32491	0.11125	0.62297	1	0.0087
C1	0.27813	0.11977	0.64497	1	0.0087
C2	0.37743	0.15727	0.74477	1	0.0087
C3	0.34673	0.11697	0.39487	1	0.0087
O1	0.2987	-0.14328	0.84973	1	0.006
O2	0.22308	0.0059	0.7798	1	0.006
O3	0.41457	0.86378	0.4435	0.9	0.0847
O4	0.36924	0.7752	0.7184	0.9	0.0847
O5	0.37747	0.78262	0.1342	0.9	0.0847
O6	0.38653	0.05056	0.7313	1	0.06
O7	0.28755	-0.05516	0.7162	1	0.06

<u>Appendix 2</u> – Ni STA-12 as-prepared – Atomic coordinates (Lab resolution)
(*Chem. Commun.*, 2006, 3305**)**

$\mathbf{R_{wp}}$ = 6.1 %, $\mathbf{R_p}$ = 4.2 %

Atom	x	y	z	Occupancy	Uiso
Ni1	0.63786(19)	0.02840(21)	0.0517(7)	1	0.00534
P1	0.61355(32)	0.03959(32)	-0.4271(13)	1	0.00534
N1	0.5567(9)	0.0062(8)	-0.0294(31)	1	0.00534
C1	0.5468(11)	-0.0115(8)	-0.2700(32)	1	0.00534
C2	0.5180(10)	-0.0387(9)	0.084(4)	1	0.00534
C3	0.5437(9)	0.0568(9)	-0.014(4)	1	0.00534
O1	0.6141(6)	0.0947(5)	-0.4815(23)	1	0.00534
O2	0.6306(7)	0.0104(6)	-0.6308(26)	1	0.00534
O3	0.6611(6)	0.0472(7)	-0.2712(25)	1	0.00534
O4	0.6566(5)	0.1098(6)	0.1253(24)	1	0.00534
O5	0.1950(6)	0.0835(6)	0.1743(27)	0.9	0.00534
O6	0.0375(6)	0.0745(6)	0.1830(26)	0.9	0.00534
O7	0.1422(7)	0.1488(6)	0.4453(25)	0.9	0.00534

<u>Appendix 3</u> – Ni STA-12 dehydrated 323 K – Atomic coordinates
(*J. Am. Chem. Soc.*, 2008, **130**, 15967**)**

$\mathbf{R_{wp}}$ = 5.96 %, $\mathbf{R_p}$ = 4.11 %

Atom	x	y	z	Occupancy	Uiso
Ni1	0.3047	0.0281	0.7197	1	0.0212
P1	0.4232	0.0383	0.5693	1	0.0266
N1	0.32473	0.11337	0.61047	1	0.0345
C1	0.27993	0.12007	0.64447	1	0.0025
C2	0.37393	0.15377	0.75817	1	0.014
C3	0.34643	0.12027	0.38917	1	0.03
O1	0.4784	0.0916	0.4958	1	0.0628
O2	0.3866	0.053	0.7331	1	0.0228
O3	0.222	0	0.7964	1	0.0431
O4	0.323	0.0446	1.0409	1	0.0224

<u>Appendix 4</u> – Ni STA-12 fully dehydrated – Atomic coordinates
(*J. Am. Chem. Soc.*, 2008, **130**, 15967**)**

$\mathbf{R_{wp}}$ = 6.94 %, $\mathbf{R_p}$ = 5.85 %

Atom	x	y	z	Occupancy	Uiso
Ni1	0.8182(7)	-0.6730(4)	-0.22118(32)	1	0.0334(6)
Ni2	0.0450(7)	-0.75109(33)	-0.39003(31)	1	0.0334(6)
Ni3	0.4713(7)	-0.5537(4)	-0.30748(33)	1	0.0334(6)
P1	0.3439(16)	-0.6482(7)	-0.1803(7)	1	0.0334(6)
P2	0.5076(17)	-0.7994(7)	-0.4228(7)	1	0.0334(6)
P3	0.9585(17)	-0.5441(8)	-0.3450(7)	1	0.0334(6)
O1	0.5279(24)	-0.7115(11)	-0.819(13)	1	0.0334(6)
O2	0.1379(22)	-0.7065(12)	-0.2523(10)	1	0.0334(6)
O3	0.4453(26)	-0.5446(9)	-0.1723(12)	1	0.0334(6)
O4	0.3841(27)	-0.7089(9)	-0.3981(12)	1	0.0334(6)
O5	0.7293(21)	-0.7819(14)	-0.3597(11)	1	0.0334(6)
O6	0.5629(26)	-0.8296(12)	-0.5194(8)	1	0.0334(6)
O7	0.8173(27)	-0.5576(14)	-0.2758(11)	1	0.0334(6)
O8	0.1991(21)	-0.4861(12)	-0.2998(11)	1	0.0334(6)
O9	0.9675(26)	-0.6362(11)	-0.4316(9)	1	0.0334(6)
N1	-0.003(4)	-0.5746(18)	-0.0692(16)	1	0.0334(6)
N2	0.073(4)	-0.9162(19)	-0.4461(19)	1	0.0334(6)
N3	0.568(4)	-0.5098(23)	-0.4254(19)	1	0.0334(6)
C1	0.204(4)	-0.6307(20)	-0.0781(12)	1	0.0334(6)

Atom	x	y	z	Occupancy	Uiso
C12	-0.167(4)	-0.5949(23)	-0.0071(24)	1	0.0334(6)
C13	0.020(5)	-0.4739(27)	-0.0801(21)	1	0.0334(6)
C2	0.313(4)	-0.8976(14)	-0.4087(18)	1	0.0334(6)
C21	-0.102(5)	-0.9621(29)	-0.4113(21)	1	0.0334(6)
C22	0.049(5)	-0.9330(26)	-0.5477(25)	1	0.0334(6)
C3	0.819(4)	-0.4585(17)	-0.3841(18)	1	0.0334(6)
C31	0.425(4)	-0.4284(25)	-0.4093(23)	1	0.0334(6)
C32	0.534(5)	-0.5888(23)	-0.5071(28)	1	0.0334(6)

<u>Appendix 5</u> – STA-12 – Rietveld refinements

No refinement of *x*, *y*, *z* atomic coordinates

1) STA-12 as-prepared

Refinements – background, peak shape and unit cell using Ni STA-12as model

Mn STA-12 $\mathbf{R_{wp}}$ = 11.25 %, $\mathbf{R_p}$ = 6.84 %

Fe STA-12 $\mathbf{R_{wp}}$ = 11.83 %, $\mathbf{R_p}$ = 9.94 %

Co STA-12 $\mathbf{R_{wp}}$ = 13.86 %, $\mathbf{R_p}$ = 11.33 %

Co Me STA-12 $\mathbf{R_{wp}}$ = 14.72 %, $\mathbf{R_p}$ = 11.47 %

Ni Me STA-12 $\mathbf{R_{wp}}$ = 12.21 %, $\mathbf{R_p}$ = 8.68 %

2) STA-12 dehydrated

Refinements – background, peak shape and unit cell using Ni STA-12as model

Fe STA-12 $\mathbf{R_{wp}}$ = 6.64 %, $\mathbf{R_p}$ = 6.56 %

Co Me STA-12 $\mathbf{R_{wp}}$ = 12.51 %, $\mathbf{R_p}$ = 10.95 %

Ni Me STA-12 $\mathbf{R_{wp}}$ = 12.44 %, $\mathbf{R_p}$ = 11.03 %

Refinement – background, peak shape and unit cell using dehydrated Ni STA-12 model

Co STA-12 $\mathbf{R_{wp}}$ = 11.99 %, $\mathbf{R_p}$ = 9.34 %

3) STA-12 + adsorbed species

Refinements - Amount of adsorbed species present not determined

Co STA-12 + acetonitrile $\mathbf{R_{wp}}$ = 11.61 %, $\mathbf{R_p}$ = 10.24 %

Co STA-12 + methanol $\mathbf{R_{wp}}$ = 8.91 %, $\mathbf{R_p}$ = 7.63 %

Ni STA-12 + methanol $\mathbf{R_{wp}}$ = 15.21 %, $\mathbf{R_p}$ = 9.38 %

Appendix 6 - Mn STA-12 dehydrated 423 K - Atomic coordinates

R_{wp} = 10.29 %, R_p = 5.85 %

Atom	x	y	z	Occupancy	Uiso
Mn1	0.6413(7)	0.0461(8)	0.0582(30)	1	0.00809
P1	0.6294(14)	0.0587(16)	-0.475(5)	1	0.00809
O1	0.6603(21)	0.1109(20)	-0.630(8)	1	0.00809
O2	0.6066(19)	-0.0005(16)	-0.622(8)	1	0.00809
O3	0.6800(17)	0.0633(21)	-0.300(7)	1	0.00809
N1	0.5581(20)	0.0405(29)	-0.078(11)	1	0.00809
C1	0.5763(29)	0.0782(27)	-0.292(11)	1	0.00809
C2	0.526(4)	-0.010(4)	-0.205(10)	1	0.00809
C3	0.524(4)	0.0584(24)	0.091(14)	1	0.00809

Mn STA-12 dehydrated 423 K – cif file – on CD inside back cover.

Appendix 7 - Ni STA-12 + acetonitrile heated 343 K - Atomic coordinates

R_{wp} = 10.93 %, R_p = 7.53 %

Atom	x	y	z	Occupancy	Uiso
Ni1	0.63812	0.03111	0.05034	1	0.00395
P1	0.61436	0.03868	-0.43027	1	0.00395
O1	0.61466	0.0957	-0.49951	1	0.00395
O2	0.61898	0.009	-0.63309	1	0.00395
O3	0.66582	0.04757	-0.29431	1	0.00395
N1	0.55617	0.01015	-0.04808	1	0.00395
N2	0.6731	0.11846	0.02959	0.49623	0.00948
C1	0.55015	-0.01576	-0.26449	1	0.00395
C2	0.51877	-0.03804	0.048	1	0.00395
C3	0.5451	0.05284	0.00936	1	0.00395
C4	0.0	0.0	0.0	0.1875	0.01
C11	0.69423	0.16469	0.10517	0.49623	0.00948
C12	0.15406	0.04315	0.13986	0.49623	0.00948

Ni STA-12 + acetonitrile heated 343 K – cif file - on CD inside back cover.

<u>Appendix 8</u> - GC traces and calculations – Selective oxidation reactions

1) Ni STA-12 as-prepared – oxidant: t-butyl hydroperoxide, substrate: 1-hexene

Time	Product	Peak area	%
5.67	acetonitrile	8843301	
5.99	1-hexene	391940	
6.27	1,2-epoxyhexane	19609	24.43
6.67	2-hexene-1-al	18527	23.08
7.09	hexane-1-ol	28854	35.94
7.90	hexane-1,2-diol	13287	16.55

% Conversion = (19609 + 18527 + 28854 + 13287) / (19609 + 18527 + 28854 + 13287 + 391940)

= 0.170 × 100

= **17.0%**

2) Ni STA-12 as-prepared – oxidant: t-butyl hydroperoxide, substrate: cyclohexene

Time	Product	Peak area	%
5.68	acetonitrile	7023722	
5.99	cyclohexene	1309869	
6.81	cyclohexene oxide	27918	7.83
6.98	cyclohexanol	52664	14.77
7.46	cyclohexene-2-one	108529	30.43
8.41	cyclohexene-2-ol	6345	1.78
8.99	cyclohexane-1,2-diol	149225	41.84
10.01	2-hydroxycylohexanol	11950	3.35

% Conversion = (27918 + 52664 + 108529 + 6345 + 149225 + 11950) / (27918 + 52664 + 108529 + 6345 + 149225 + 11950 + 1309869)

= 0.214 × 100

= **21.4 %**

3) Ni STA-12 as-prepared – oxidant: H_2O_2, substrate: 1-hexene

Time	Product	Peak area	%
5.61	methanol	5908364	
5.79	1-hexene	60688	
6.31	1,2-epoxyhexane	4851	44.59
6.66	2-hexene-1-al	3864	35.52
7.09	hexane-1-ol	2163	19.89

% Conversion = (4851 + 3864 + 2163) / (4851 + 3864 + 2163 + 60688)

= 0.152 × 100

= **15.2%**

4) Ni STA-12 as-prepared – oxidant: H_2O_2, substrate: cyclohexene

Time	Product	Peak area	%
5.61	methanol	4391939	
6.02	cyclohexene	901304	
6.82	cyclohexene oxide	18637	19.80
6.97	cyclohexanol	34652	36.81
7.46	cyclohexene-2-one	17782	18.89
8.64	cyclohexene-2-ol	1770	1.88
8.98	cyclohexane-1,2-diol	20914	22.22
9.22	2-hydroxycylohexanol	369	0.40

% Conversion = (18637 + 34652 + 177872 + 1770 + 20914 + 369) / (18637 + 34652 + 177872 + 1770 + 20914 + 369 + 901304)

= 0.22 × 100

= **22.0%**

<u>Appendix 9</u> - GC traces and calculations – Knoevenagel reactions

Ni STA-12 fully dehydrated

Time	Product	Peak area
5.62	cyclohexane	247203
5.98	ethyl-*trans*-α-cyanocinnamate	4900856
7.43	ethyl cyanoacetate	3314523
7.82	benzaldehyde	6138045

% Conversion = 4900856 / (4900856 + 6138045)

= 0.4432

= **44.32%**